UNIVERSITY OF CALIFORNIA SAN DIEGO

Metal-Semiconductor Compound Contacts to Nanoscale Transistors

A dissertation submitted in partial satisfaction of the requirements for the degree of Doctor of Philosophy

in

Electrical Engineering (Applied Physics)

by

Renjie Chen

Committee in charge:

Professor Shadi A. Dayeh, Chair
Professor Peter M. Asbeck
Professor Prabhakar R. Bandaru
Professor Yu-Hwa Lo
Professor Shirley Meng

2018

The Dissertation of Renjie Chen is approved, and it is acceptable in quality and form for publication on microfilm and electronically:

_____

_____

_____

_____

_____
Chair

University of California San Diego

2018

DEDICATION

To my beloved parents and fiancée

TABLE OF CONTENTS

LIST OF FIGURES

LIST OF TABLES

ACKNOWLEDGMENTS

Impossible is to finish my Ph.D. study and this thesis, without the enormous help and support from many people around me. I would like to take this opportunity to express my sincere gratitude and appreciation to all of them.

First of all, I'm extremely thankful to my advisor Prof. Shadi A. Dayeh for his great support, abundant guidance, and continual encouragement over the course of my Ph.D. researches. He acts both as a mentor and as a friend to all our group members, and dedicates a lot time and efforts to discuss, advise, and support each of us. With him being a role model, our hardworking leads to exciting outcomes, and the pressures transfers to honors and awards. It has been such a great opportunity and a uniquely fulfilling experience for me to work under his supervision.

I am also highly grateful to the members of my thesis committee, Prof. Peter M. Asbeck, Prof. Prabhakar R. Bandaru. Prof. Yu-Hwa Lo, and Prof. Shirley Meng. Their flexibility and understanding, as well as their valuable inputs and suggestions were of immense value to the completion of this thesis. It was the "Solid State Electronics" class taught by Prof. Lo that started my first quarter of graduate study at UC San Diego. Later, I also took two courses of "Electronic Devices" and "Nanoelectronics" with Prof. Asbeck. All those courses helped me to successfully pass the preliminary exam. I'm also very appreciative of the precious feedbacks from Prof. Bandaru and Prof. Meng during my qualifying exam and final defense, and their great support over the past five years. I would also like to express my especial thanks to Prof. S. S. Lau for many valuable inputs and discussions during my Ph.D. researches.

Moreover, the Center for Integrated Nanotechnologies (CINT) is the place that witnessed nearly four-years of my Ph.D. researches and exposed me to quite a few world-class research facilities, such as JEOL e-beam writer, FEI transmission electron microscopes, and etc. At CINT, I was also able to meet and frequently discuss with many prominent research scientists. I'm very grateful to Dr. Katie Jungjohann, Dr. Bill Mook and Dr. Yang Liu, for their training, support, and discussions on TEM operations, and their collaborations on several research papers. I'm also very thankful to Dr. Jinkyoung Yoo and Dr. Nan Li for their continual support and guidance to me at both Sandia national labs and Los Alamos national lab. Special thanks to all the staff members of the integration lab (cleanroom), John Nogan, Tony James, Doug Pete, Denise Webb, Will Ross, and Joseph Lucero.

I am very fortunate to have many brilliant labmates and senior group alumni. It was Dr. Xing Dai who introduced me to my Ph.D. group, and both Dr. Xing Dai and Dr. Binh-Minh Nguyen gave me enormous support, training, and guidance at the early stage of my Ph.D. research. I appreciate so much the precious discussion with Dr. Wei Tang on many phone calls, during which Wei shared with me all his experience on the *in-situ* heating TEM observation. Also, I would like to thank Dr. Yoontae Hwang for his training on fabricating the neuronal probe devices. Moreover, other group members, Ren Liu, Yun-Goo Ro, Atsunori Tanaka, Woojin Choi, Sang Heon Lee, Mehran Ganji, Lorraine Hossain, Keundong Lee, Hongseok Oh, Namseok Park, Siarhei Vishniakou, Ahmed El-Thakeb, Farid Azzazy, Cory Heath, Supanee Sukrittanon, have given me great supports both in experiments and in daily life.

Many friends at UC San Diego or CINT are greatly acknowledged for their friendship and encouragement including Weichuan Yao, Lujiang Yan, Sheng Liu, Chun-Chieh Chang, Enzhi Xu, Wenlong Yu, Erdong Song, Peter Liu, Yuanmu Yang, Miller Li, Changyi Li, and Geyuan Liu.

I would like also to acknowledge financial support from the ECE department, National Science Foundation, C-DEN Center Fellowship and the IEEE EDS PhD Student Fellowship.

Last but not the least, I would like to express my deep appreciation and thankfulness to my parents, Jianyong and Ying, and to my fiancée, Huan. Their profound love, care, patience, sacrifice, support, trust, belief, and encouragement have enabled me to sustain the pressures and challenges I met in the 5 years of my PhD program, and promoted my will and persistence to excel in my studies.

The list does not mean to be exhaustive and I would like to thank all other people who have helped me but are not mentioned above.

Part of chapter 1 has been submitted for publication as an invited book chapter of *Springer Publisher* 2018. R. Chen, S. A. Dayeh. The dissertation author is the first author of this paper.

Most of chapter 2 was published in *Nano Letters* 2015. R. Chen, S. A. Dayeh. The dissertation author is the first author of this paper.

Most of chapter 3 was published in *Nano Letters* 2017. R. Chen, K. L. Jungjohann, W. M. Mook, J. Nogan, S. A. Dayeh. The dissertation author is the first author of this paper.

Most of chapter 4 was published in *Small* 2017. R. Chen, S. A. Dayeh. The dissertation author is the first author of this paper.

Most of chapter 5 was published in *Applied Physics Letters* 2017. R. Chen, B.-M. Nguyen, W. Tang, Y. Liu, J. Yoo, S. A. Dayeh. The dissertation author is the first author of this paper.

VITA

2010	B.S., Material Physics, Wuhan University, China
2013	M.S., Applied Physics, Nanyang Technological University, Singapore
2018	Ph.D., Electrical Engineering, University of California San Diego, CA

PUBLICATIONS

1. **R. Chen**, S. A. Dayeh, "Size and Orientation Effects on the Kinetics and Structure of Nickelide Contacts to InGaAs Fin Structures", *Nano Letters* **2015**, *15* (6), 3770–3779

2. **R. Chen**, K. L. Jungjohann, W. M. Mook, J. Nogan, and S.A. Dayeh, "Atomic Scale Dynamics of Contact Formation in the Cross-section of InGaAs Nanowire Channels" *Nano Letters* **2017**, *17* (4), 2189-2196

3. **R. Chen**, and S. A. Dayeh, "Recordings and Analysis of Atomic Ledge and Dislocation Movements in InGaAs to Nickelide Nanowire Phase Transformation" *small* **2017**, *13*, 1604117

4. **R. Chen**, B. M. Nguyen, W. Tang, Y. Liu, J. Yoo, and S. A. Dayeh, "In-situ Control of Synchronous Germanide/Silicide Reactions with Ge/Si Core/Shell Nanowires to Monitor Formation and Strain Evolution in Abrupt 2.7nm Channel Length", *Applied Physics Letters* **2017**, *110*, 213103

5. **R. Chen**, X. Dai, K. L. Jungjohann, W. M. Mook, J. Nogan, C. Soci, S. A. Dayeh, "(Invited) The Dynamics of Nickelidation for Self-Aligned Contacts to InGaAs Channels", *ECS Transactions* **2017**, *14*, 819

6. **R. Chen**, and S. A. Dayeh, "(Invited book chapter) Metal-Semiconductor Compound Contacts to Nanowire Transistors" *Springer* **2018**, submitted

7. S. A. Dayeh, W. Tang, B. M. Nguyen, X. Dai, Y. Liu, Y. Hwang, X. Liu, and **R. Chen**," (Invited) Nanoscale Heterogeneous Reactions and Interfaces in Ge/Si and for III-V on Si Integrated Devices", *ECS Transactions* **2013**, *58*(7), 115-125

8. W. Tang; B. M. Nguyen; **R. Chen**; and S. A. Dayeh, "(Invited) Solid-state Reactions of Nickel Silicide, Germanide, and Alloyed Contacts to Semiconductor Nano-Channels"**,** *Semiconductor Science and Technology* **2014**, *29*, 054004

9. A. Tanaka, **R. Chen**, K. L. Jungjohann, and S. A. Dayeh, "Strong Geometrical Effects in Submillimeter Selective Area Growth and Light Extraction of GaN Light Emitting Diodes on Sapphire", *Scientific Reports* **2015**, *5*, 17314

10. Y. Shen, **R. Chen**, X. Yu, Q. Wang, K. L. Jungjohann, S. A. Dayeh, and T. Wu, "Gibbs–Thomson Effect in Planar Nanowires: Orientation and Doping Modulated Growth", *Nano Letters* **2016,** *16* (7), 4158-4165

11. S. A. Dayeh, A. Tanaka, W. Choi, and **R. Chen**, "(Invited) Strain Engineered Crack-Free GaN on Si for Integrated Vertical High Power GaN Devices with Si CMOS", *ECS Transactions* **2016**, *75*(8), 711-723

12. A. Tanaka, W. Choi, **R. Chen**, S. A. Dayeh, "Si Complies with GaN to Overcome Thermal Mismatches for the Heteroepitaxy of Thick GaN on Si", *Advanced Materials*, **2017**, *29*, 1702557

13. R. Liu, **R. Chen**, A. T. E. Youssef, S. H. Lee, S. Hinckley, M. L. Khraiche, J. Scott, D. Pre, Y. Hwang, A. Tanaka, Y. G. Ro, A. K. Matsushita, X. Dai, C. Soci, S. Biesmans, A. James, J. Nogan, K. L. Jungjohann, D. V. Pete, Y. Zou, A. Bang, and S. A. Dayeh, "High Density Individually Addressable Nanowire Arrays Record Intracellular Activity from Primary Rodent and Human Stem Cell Derived Neurons", *Nano Letters* **2017**, *17* (5), 2757–2764

14. S. A. Dayeh, **R. Chen**, Y. G. Ro, and J. Sim, "(Invited) Issues for the Doping of Semiconductor Nanowires During Growth", *Materials Science in Semiconductor Processing* **2017,** 62, 135-155

15. R. La, R. Liu, W. Yao, **R. Chen**, M. Jansson, J. L. Pan, I. A. Buyanova, J. Xiang, S. Aa Dayeh, C. W. Tu, "Self-catalyzed core-shell GaAs/GaNAs nanowires grown on patterned Si (111) by gas-source molecular beam epitaxy", *Applied Physics Letters* **2017**, *111*, 072106

CONFERENCES

1. Oral presentation, “Atomic Scale Dynamics of Contact Formation in the Cross-Section and Along InGaAs Nanowire Channels”, Materials Research Society (MRS) Spring Meeting, **Apr. 2018**, Phoenix, AZ

   This presentation lead to an MRS Graduate Student Award: Silver Medal.

2. Invited talk, “Recording and Analysis of the Atomic Scale Dynamics of Contact Formation in the Cross-Section and Along InGaAs Nanowire Channels”, CINT Annual Meeting (Sandia National Laboratories and Los Alamos National Laboratory), **Sep. 2017**, Santa Fe, NM

3. Oral presentation, “Recording and Analysis of the Atomic Scale Dynamics of Contact Formation in the Cross- Section and Along InGaAs Nanowire Channels”, 59th Electronic Materials Conferences (EMC), **Jun. 2017**, South Bend, IN

4. Two posters, (1) “Direct Observation of Alloyed Contact Formation in Nanowire Cross-Section”, (2) “In-situ TEM Observation of Nickelide Contact Formation in InGaAs Nanowire Channels”, Conference on Frontiers of Characterization and Metrology for Nanoelectronics, **Mar. 2017**, Monterey, CA

5. Oral presentation, “Ex-situ and In-situ TEM Studies of Nickelide reaction in InGaAs Fins”, 43rd Conference on the Physics and Chemistry of Surfaces and Interfaces (PCSI-43), **Jan. 2016**, Palm Springs, CA

6. Poster, “Advanced Nanoscale Fabrication for Versatile in-situ TEM Studies of Metal-semiconductor Reactions and Interfaces”, CINT Annual Meeting (Sandia National Laboratories and Los Alamos National Laboratory), **Sep. 2015**, Santa Fe, NM

7. Two oral presentation, (1) “Size and Orientation Effects on the Kinetics and Structure of Nickelide (Ni-InGaAs) Contact to InGaAs Fin Channels”, (2) “High Density Intra-cellular 3D Neuronal Nano-Probes”, 57th Electronic Materials Conferences (EMC), **Jun. 2015**, Columbus, OH

8. Oral presentation, “Kinetics and Structure of Nickelide Contact Formation to InGaAs Fin Channels”, Materials Research Society (MRS) Spring Meeting, **Apr. 2015**, San Francisco, CA

9. Poster, “Nickelide Contact Formation to InGaAs FinFETs”, CINT Annual Meeting (Sandia National Laboratories and Los Alamos National Laboratory), **Sep. 2014**, Santa Fe, NM

10. Oral Presentation, “Structure, Kinetics and Dynamics of Nickelide Contact Formation to InGaAs Fin structures”, 56th Electronic Materials Conferences (EMC), **Jun. 2014**, Santa Barbara, CA

ABSTRACT OF THE DISSERTATION

Metal-Semiconductor Compound Contacts to Nanoscale Transistors

by

Renjie Chen

Doctor of Philosophy in Electrical Engineering (Applied Physics)

University of California San Diego, 2018

Professor Shadi A. Dayeh, Chair

Semiconductor nanowires (NWs) and Fin structures are promising building blocks for next generation ultrascaled devices for electronic and optoelectronic applications. The detailed understanding of and control over the phase transformation that accompanies the formation of their compound contacts for lithography-free self-aligned gate design can accelerate the development of these ultra-scaled devices. Numerous aspects of nanoscale metallization technology were shown to exhibit significantly different behavior from their

bulk counterparts. And up to now, the majority of the studies that explored nanoscale contact metallurgy focused on nanostructures of elemental semiconductors, i.e., Si and Ge NWs, and detailed contact reactions have not been uncovered in III–V NW channels or heterostructured NW channels at atomic resolution.

In the first and the major part of this thesis, I will focus on the narrow band gap, high electron mobility III−V semiconductor, InGaAs, motivated by its potential in sub-10 nm metal-oxide-semiconductor field-effect transistors (MOSFETs). In chapter 2, we reported the first study on the solid-state reaction between Ni and $In_{0.53}Ga_{0.47}As$ nanochannels to reveal the reaction kinetics, formed crystal structure, and interfacial properties. In chapter 3 and 4, we developed a deeper understanding of this contact metallization process by utilizing the *in-situ* heating transmission electron microscopy (TEM) technique, and observed at atomic resolution the detailed ledge formation and movement behaviors in both the NW cross-section and along the NW channel.

In the second part, I will use the Ge/Si core/shell NW as a model system to talk about the compound contact formation in semiconductor heterostructures. In chapter 5, we managed to control the synchronous core/shell interface during the solid-state reactions between Ni and Ge/Si core/shell nanowires, and measured the strain evolution in ultra-short channels using *in-situ* TEM. These elevated compressive strains are expected to result in a non-homogeneous energy band structure in Ge/Si core/shell NWs below 10 nm and potentially benefit their transistor performance.

Finally, as appearing in chapter 6, I will introduce the ongoing electrical measurements of contact resistance for InGaAs transistors, and adapt the solid-phase-

regrowth method to future reduce the contact resistance with locally introduced dopants. I will also talk about the collaborated work in fabricating the AlGaN/GaN Fin MOS-HEMTs for intrinsically linear power amplification devices.

Chapter 1: Introduction

Semiconductor nanowires[1-4] and Fins[5,6] are promising building blocks for next generation ultrascaled devices for electronic[7-9] and optoelectronic[10-12] applications. As these devices scale at a few nanometer regimes, their contact access resistance starts to limit their performance. Therefore, an important aspect for the development, maturity, and efficiency of these ultrascaled devices is the detailed understanding of and control over the phase transformation that accompanies the formation of their compound contacts for lithography-free self-aligned gate design.[13,14] The term of "compound" here refers to the formed phases that have a fixed stoichiometry between metal and semiconductor elements. This is to be distinguished from the broader term, "alloy," that generally refers to phases that may include non-stoichiometric or amorphous structure. This distinction is important because the formation of a low resistance, crystalline and thermally stable compound metallic contact to a semiconductor channel is most preferred for realizing reliable functionality in ultrascaled semiconductor transistors. Usually, the phase of compound contact and its interfacial property with semiconductor nanowire (NW) can largely affect the band alignment and charge-injection in NW channels.[15] This necessitates a comprehensive understanding of the metal-semiconductor solid-state reactions, including the formed compound phases, reaction kinetics, and their correlation to the resulting device performances.

1.1 Phases of Metal-Semiconductor Compound Contacts

The development of these high fidelity contacts should start with an understanding of the phases of the naturally or thermally formed metallic compound contacts at the metal-semiconductor junction. Ideally, a crystalline compound with a low-resistivity phase is preferred as a contact to a NW transistor. It has also been noticed that atomically abrupt interfaces between metallic contacts and semiconductors can help reduce the surface Fermi-level pinning and control the Schottky barrier height (SBH),[16] which is especially critical for small band-gap and covalently bonded semiconductors (e.g. Ge, III-V, etc.) that have small electronegativity difference and a generally low index of interface behavior[17] with high density of surface and metal-induced gap states. Moreover, the interfacial correlations (details of bonding and atomic sites at the interface) between the compound contact and the semiconductor nanowire channel can further tune the electrical characteristics by residual interfacial strains. We are motivated to understand the phases and interfacial relationships for those compound contacts to be able to control and lower the specific contact resistance in self-aligned contacts to III-V semiconductor nanoscale channels.

Several precedent reviews[18-22] have extensively discussed the solid-state reactions between various metals and semiconductor NWs and it is beyond the scope of this thesis to cover all the compound contacts to NWs with different metal-semiconductor combinations. To this end, I will focus my discussions on few study cases that are of practical importance for integrated circuit applications and provide in-depth discussions on the phase selection rules in low-dimensional NW semiconductor channels.

1.1.1 Metal Silicide in Si Nanowires

Metal silicides have long been used as the standard contacts to conventional Si CMOS devices, particularly due to two main attributes: (1) The electron and hole barrier heights are nearly symmetric so that excellent contacts could be achieved to both n-MOSFETs and p-MOSFETs, respectively, using a single metal deposition and a single compound contact, and (2) the remaining un-reacted metal could be selectively etched leaving the reacted compound contact to be self-aligned to the gate without a lithographic step requirement. The semiconductor manufacturing lines witnessed the transition from $TiSi_2$, to $CoSi_2$, and to NiSi technology due to the considerations of contact resistance and dimensional scaling.[23,24] NiSi has demonstrated its superior properties to other candidates, such as reduced thermal budget, low resistivity, less Si consumption for ultra-thin device layer, and controlled silicide formation by Ni diffusion.[25-27] Therefore, nickel silicide showed great promise to serve as a standard contact to Si NW transistors, and has been most widely studied.

In the nickel silicide reaction on thin film or bulk Si structures, δ-Ni_2Si is the single phase that is formed at a low temperature of about 200 °C, and transforms to a NiSi phase at temperatures above 350 °C, and finally converts into a $NiSi_2$ phase above 750 °C.[28] However, in Si NW channels, the phase sequences are dramatically different. As shown in **Figure 1.1** (a), several phases exist simultaneously upon thermal annealing of Ni pad on top of a Si NW, including $NiSi_2$ as the leading and interfacial phase in direct contact with the pristine Si NW, followed by θ-Ni_2Si, δ-Ni_2Si, and $Ni_{31}Si_{12}$.[29] This phase sequence is generally observed under a broad range of reaction temperatures, 300~650°C, with some minor differences (presence or absence) in some of the Ni-rich intermediate phases.[30-32]

The leading phase, $NiSi_2$, has the same crystal family as pristine Si with very similar lattice constant, leading to nearly zero volume changes after $NiSi_2$ phase formation. This $NiSi_2$ phase grows on the low-energy Si (111) facets independent of the growth orientation of Si NW (as shown in **Figure 1.1** (b)-(c)), and the interfacial correlation is $NiSi_2$(111)||Si(111) and $NiSi_2$[-110]||Si[-110] is applicable to the various studied orientations. Naturally, more Ni-rich silicide phases appear near the Ni contact pad/metal reservoir. It is worth noting that $NiSi_2$ is the phase that is thermodynamically favored to form at high temperature when Ni reacts with planar thin film or bulk Si, and that θ-Ni_2Si is stable above 825 °C according to the Ni/Si phase diagram. In the following part of this section, two questions will be addressed: (1) why are the phase sequences quite different in NWs than in bulk and planar films, and (2) can the phase sequences formed in Si NW be manipulated?

To address these questions and to understand the coexistence of multiple phases (including high-temperature phases, $NiSi_2$ and θ-Ni_2Si) instead of expected NiSi phase at reaction temperatures of 300 ~ 650 °C, one need to consider the different thermodynamic treatments in two extremes of relative material abundance of the binary solid-state reactants. As we know, the driving force of silicide reaction is the total reduction of system Gibbs free energy:

$$\Delta G_f = \Delta H_f - T\Delta S_f \qquad (1\text{-}1)$$

Where ΔG_f, ΔH_f, and ΔS_f are the free energy, enthalpy, and entropy of formation, respectively at a given reaction temperature.

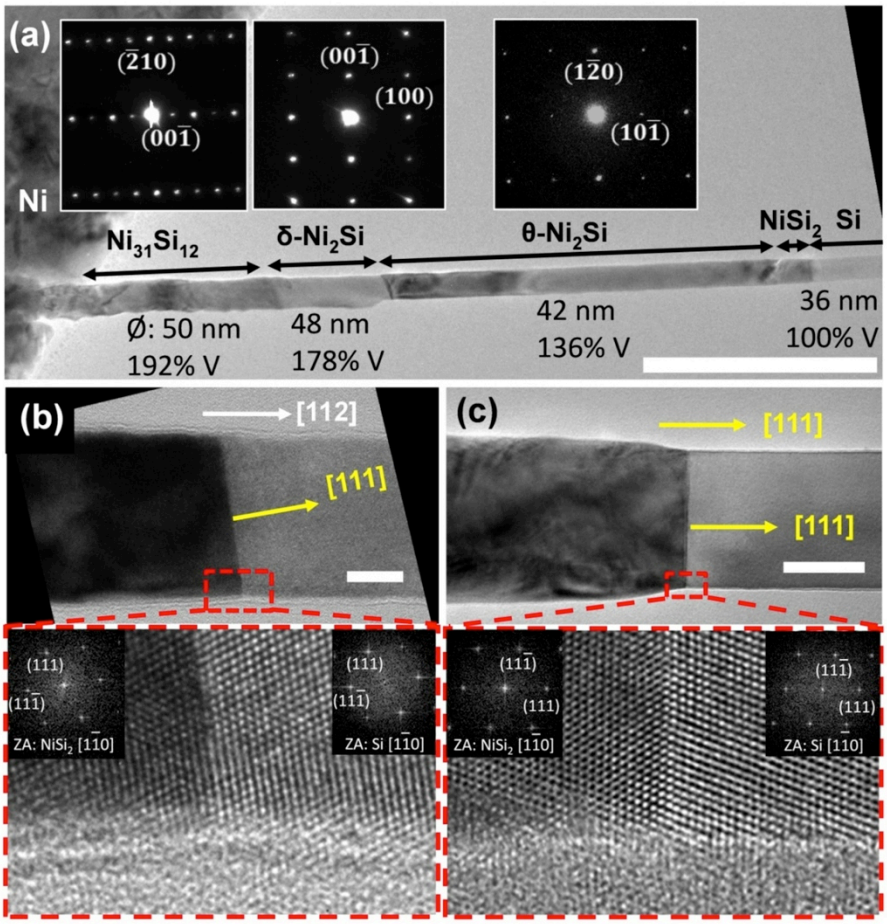

Figure 1.1. TEM images of nickel silicide formation in a Si NW. (a) TEM image showing the phases that co-exist during solid-station reaction between Ni pad and Si NW at 425 °C. The inserted diffraction patterns (from left to right) represent $Ni_{31}Si_{12}$, δ-Ni_2Si, and θ-Ni_2Si phases with their zone axes of [120], [010], and [212] respectively. Scale bar is 400 nm. (b) and (c) TEM images with higher magnification at $NiSi_2$ and Si interfaces. Despite the Si NW growth orientations of [112] or [111], the reaction front is on a Si (111) plane. Scale bars are 20 nm and 50 nm respectively. Reproduced with permission from Ref [29]. Copyright 2012 American Chemical Society.

Usually, the term $-T\Delta S_f$ is negligible compared to ΔH_f for solid-state reactions at low temperatures, and therefore the system free energy is largely determined by the enthalpy term.[33] In the silicide reaction between Ni and Si bulk or thin film, Si is considered unlimited, and the Ni_2Si has the smallest formation enthalpy (-141 kJ/mol) and therefore the largest driving force to nucleate at a low reaction temperature. While, $NiSi_2$ has the largest formation enthalpy (-2 kJ/mol) and hence the $NiSi_2$ phase formation in thin film or bulk reactions is perceived as nucleation controlled, which can only occur at a temperature of above 750 °C. On the contrary, Ni is considered as an excess reservoir in the silicide reaction with NWs, and several phases, including $NiSi_2$, Ni_2Si, and $Ni_{31}Si_{12}$, have small enough enthalpies that allow the formation of multiple phases simultaneously during the silicide reaction. This also indicates that nucleation is no longer the limiting step in determining the leading phase of $NiSi_2$, and kinetic competitive growth models suggest that the faster growth rate will separate the leading phase with the others.[34] At the same time, we should also consider the existence of θ-Ni_2Si phase, which is a high temperature phase that is stable above 850 °C. In situ X-ray diffraction studies of Ni-Si substrate reaction show that θ-Ni_2Si is a transient phase, which may appear at low temperatures but is later consumed by δ-Ni_2Si phase with temperature increase,[35] which is in agreement with the observations made on the reaction of Ni with Si NWs.[29] Another experiment to test the stability of θ-Ni_2Si phase suggests that high temperature formed θ-Ni_2Si phase transformed into δ-Ni_2Si and ε-Ni_3Si_2 during cooling down below 825 °C, while on the other hand, low temperature (460 °C) formed θ-Ni_2Si phases didn't decompose even during cooling down to room temperature.[36] These observations suggest that, although θ-Ni_2Si is a high

temperature stable phase, it also retains a certain type of stability at low temperatures, likely due to high kinetic barriers for phase transformation.

Our group has demonstrated that the primary reason for the formation of $NiSi_2$ at low temperature is mass-transport limitation of Ni through the surface native oxide layer to the reaction-interface. As I will demonstrate later in Chapter II that treats the reaction kinetics and thermodynamics in metal compound reactions, the Ni diffusion is a surface rather than volume dominant process and that the presence of the oxide can impede such diffusion. In an experiment conducted by my colleague Wei Tang, he observed that the Ni supply could be limited by the presence of a native SiO_2 layer on the Si surface (as demonstrated on planar Si layer and shown in **Figure 1.2**). It was found that under the thermal annealing at 300 °C the nickel silicide formed δ-Ni_2Si phase if without a native SiO_2 layer in between Ni and Si substrate (**Figure 1.2** (b)), while the $NiSi_2$ phase formed with the presence of a native SiO_2 layer at the interface, due to the limited Ni supply and subsequently the formation of a Si-rich silicide phase. At temperature of 350 °C, three different silicide phases, including δ-Ni_2Si, NiSi, and $NiSi_2$, were observed underneath the native SiO_2 covered Si surface, as shown in **Figure 1.2** (c). This is because the diffusion of Ni atoms through the native SiO_2 layer was facilitated at slightly higher temperatures and several silicide phases with different stoichiometric values could simultaneously form depending on the integrity of the native SiO_2 layer at the Ni/Si contact interface. While increasing the annealing temperature to around 400 °C ~ 600 °C (**Figure 1.2** (d)), NiSi was the only phase formed with and without the native SiO_2 layer at the Ni/Si contact interface. Further increase of the annealing temperature to 800 °C and above would lead to only the $NiSi_2$ phase.

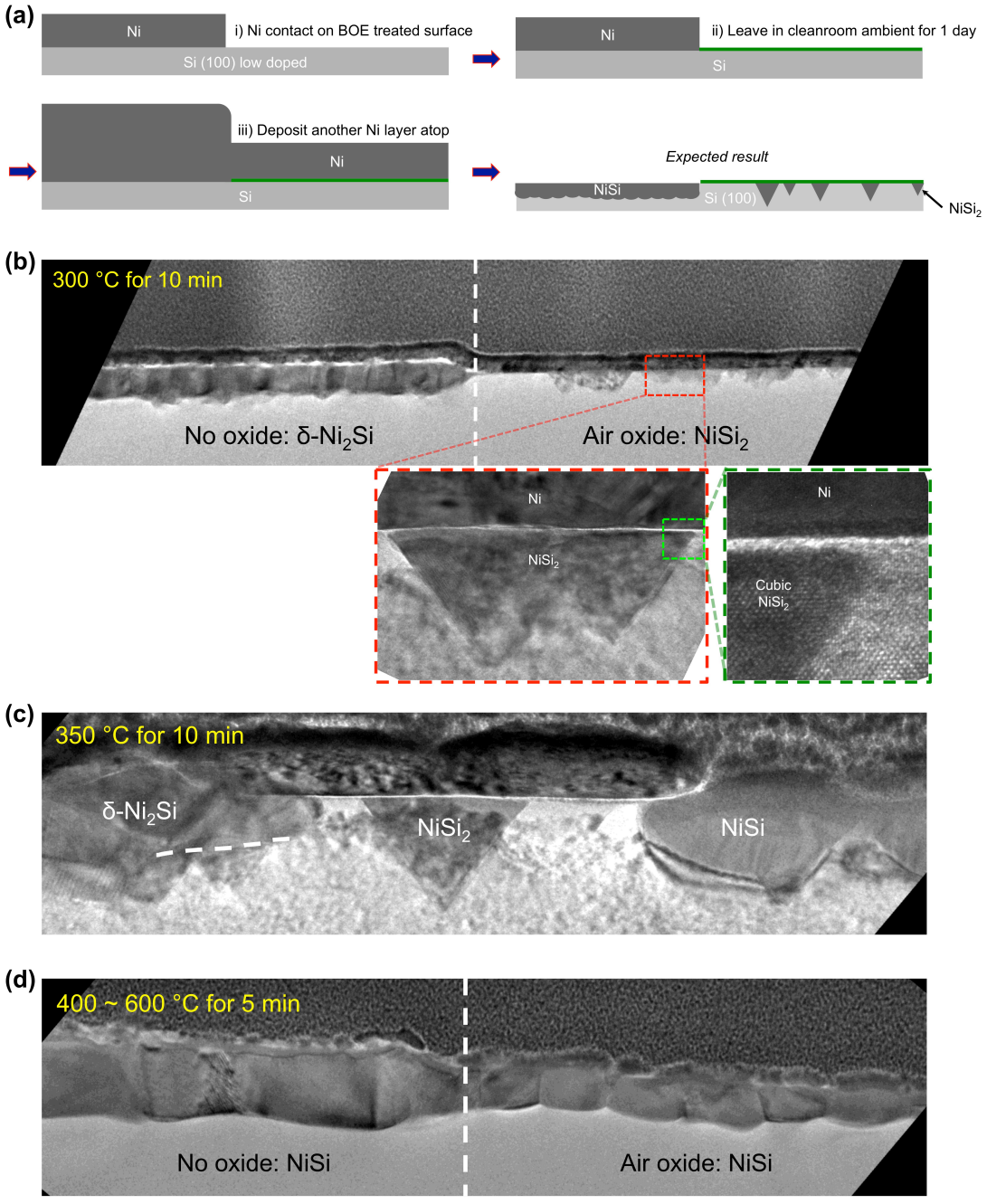

Figure 1.2. Nickel silicide formation at different temperatures with limited Ni supply by the presence of a native SiO_2 layer. (a) Schematics of an air-oxidized native oxide layer on part of the Si surface underneath the Ni contact. (b)-(d) The formed nickel silicide phase at different temperatures.

Many studies were carried out to control the phase formations in Si NW templates.[30,37,31,38,39,32] These studies were driven with the desire to eliminate the Ni-rich silicide phases (e.g. $Ni_{31}Si_{12}$) that generally have higher resistivity which compromises the series resistance in NW transistors. A dielectric shell (SiO_2[30,37] or Al_2O_3[32]) coating can exert a compressive stress to the silicide core and suppress the formation of phases that have high volume expansion ratios. This has been attributed to the fact that high compressive stresses squeeze the interstitial sites through which Ni diffuses, increasing the activation barrier of Ni diffusion for volume-mediated diffusion. Another possibility based on the above discussions is that the presence of these oxides serves to retard Ni diffusion to the reaction interface. As shown in **Figure 1.3** (a)-(d), an ALD Al_2O_3 layer with a thickness of 22nm on a Si nanowire with a diameter of ~50nm can effectively exclude $Ni_{31}Si_{12}$ phase in the formed nickel silicide sequence. Importantly, the leading silicide phase in direct contact with pristine Si determines the SBH and consequently charge injection/extraction, and therefore a better control of the leading phases could potentially fulfill various device functionalities. Since coexistence of multiple nickel silicide phases in NW is thermodynamically preferred, the leading phase adjustment relies on the kinetic competitions.[31,39] It has been found that $NiSi_2$ growth rate is limited by interfacial reactions, and remains constant at a given temperature despite of the NW size. On the contrary, θ-Ni_2Si growth is diffusion limited and the diffusion rate can significantly increase in Si NWs with smaller diameter. At a high reaction temperature, where stable θ-Ni_2Si phase is favored, there exists in principle a transition diameter, below which θ-Ni_2Si would be favored over $NiSi_2$ as the leading phase. Chen and et al[31] derived this critical diameter of 234 nm, by extracting the diffusivity (D) of Ni in θ-Ni_2Si and the reaction

constant (k) at $NiSi_2$/Si interface and setting the average growth rates of these two phases to be equal. **Figure 1.3** (e)-(g) demonstrate the feasibility of formation of θ-Ni_2Si as leading phase in a small (33 nm in diameter) Si NW at reaction temperature of 800 °C.

Thus far, the most preferred low-resistivity NiSi phase in bulk Ni-Si reaction was not yet observed in Ni-Si NW reaction, and was only reported in point contact reaction in Si NWs.[40,41] In order to manipulate the NiSi phase formation, Chen and et al[32] inserted a very thin layer of Pt in between Ni pad and Si NW, schematically shown in **Figure 1.3** (h). Pt has a higher solubility in NiSi phase than that in $NiSi_2$,[42] because the PtSi and NiSi share the same crystal structure with similar lattice constants and could potentially form a solid solution.[43] Therefore, Pt promotes the NiSi phase formation rather than $NiSi_2$, and by combing the constraining dielectric shell (to suppress Ni-rich silicide phases), a single NiSi phase was experimentally observed as shown in **Figure 1.3** (i)-(j).

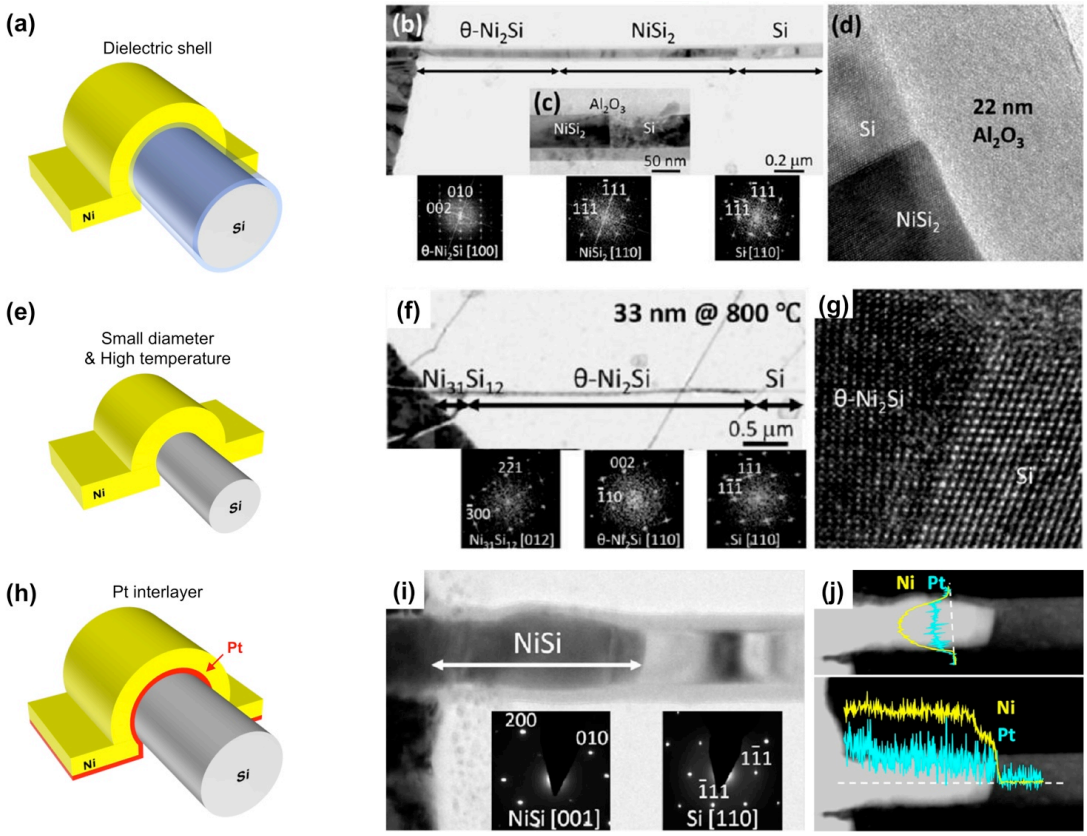

Figure 1.3. Manipulation of nickel silicide phases in Si NW templates. (a) Schematic of reaction between Ni and Si NW with dielectric shell coating. (b)-(d) TEM images of nickel silicide growth in a Si NW with a thick (22 nm) Al_2O_3 shell at 800 °C for 30s. The leading phase is $NiSi_2$, and the $Ni_{31}Si_{12}$ phase with highest volume change is suppressed. (e) Schematic of reaction between Ni and Si NW with small diameter at high temperature. (f)-(g) TEM images of nickel silicide growth in a thin (33nm) Si NW at 800 °C for 30s. The leading phase is θ-Ni_2Si in this case. (h) Schematic of reaction between Ni and Si NW with a thin Pt interlayer. (i)-(j) TEM image and elemental mapping of nickel silicide growth in a ~ 70 nm Si NW with 5 nm Pt interlayer and a thick Al_2O_3 shell, at 450 °C for 2.5h. The leading phase and the only phase is NiSi. TEM images are reproduced with permission from Ref [31,32]. Copyright 2012, 2013 American Chemical Society.

1.1.2 Metal Germanide in Ge Nanowires

Benefiting from the intrinsically higher hole-mobility, Ge NWs hold a great promise in PMOS devices, together with GeSi alloy[44] or Ge/Si core/shell[45] NWs. Similar to the case of Si, Ni is also the promising candidate for contact to p-type Ge, due to the small SBH and the ease of formation of Ni_xGe compounds. By virtue of being a group-IV semiconductor, Ge has the same diamond lattice structure as Si, and many similarities exist between metal-germanide reactions and metal-silicide ones. In this section, we will review the different behaviors of metal germanide phase formation in Ge NWs.

Firstly, no conclusive phase sequences have been observed in Ni reacting with Ge NWs over a broad reaction temperature range, and different Ni germanide phases have been reported at different reaction temperatures. Dellas et al[46] carried out the solid-state reaction between a Ni pad and a Ge NW at the temperature range of 300 ~ 400 °C. The formed polycrystalline Ni_xGe phase (shown in **Figure 1.4** (a)) was found to match Ni_2In prototype structure (hexagonal crystal structure) with the $P6_3/mmc$ space group. They pointed that the stoichiometry of Ni_xGe may deviate from x=2 due to vacancies on one of the Ni sub-lattices,[47] leading to similar lattice constants for several germanide phases (Ni_2Ge, Ni_5Ge_3, $Ni_{19}Ge_{12}$, $Ni_{17}Ge_{12}$, and Ni_3Ge_2).[48] In comparison, their experimentally observed diffraction data was most consistent with Ni_3Ge_2 phase. They also reported that this germanide phase was independent of Ge NW growth orientations, and that further increase of reaction temperatures above 450 °C would lead to a decomposition and discontinuity in germanide segment, the reasons of which were not clear. Tang et al[49] reported the Ni germanide reaction in <111> Ge NWs at the temperature range of 400 ~ 500 °C, and observed a single crystalline orthorhombic Ni_2Ge phase (shown in **Figure 1.4**

(b)). They found an abrupt interface between Ni_2Ge and Ge NW, and the interfacial correlation was Ni_2Ge (100) || Ge $(1\bar{1}\bar{1})$, and Ni_2Ge $[0\bar{1}1]$ || Ge $[01\bar{1}]$. At the reaction temperature of 650 °C, the same group reported cubic Ni_3Ge phase (shown in **Figure 1.4** (c)) with same cubic structure to Ge.[21] Their observations have shown very similar lattice constant between Ni_3Ge and Ge with only ~ 1.5% lattice mismatch, which was different from the conventional lattice constant for cubic Ni3Ge phase.[50,51] Similar to Si NWs, oxide confinement was also found to suppress the formation of Ni-rich germanide that had large volume expansions. An Al_2O_3 shell coating led to the formation of orthorhombic NiGe phase (shown in **Figure 1.4** (d)) in adjacent to pristine Ge NW followed by Ni_2Ge phase, at reaction temperature of 450 °C.

Secondly, the nickel germanide reaction is usually accompanied with segregation of Ni_xGe nanoparticles. Tang et al[21] found that the segregation of Ni_xGe nanoparticles could be caused by two factors, the instable native oxide, GeO_x, and the large lattice mismatch. As shown in **Figure 1.4** (e), with elongated reaction time Ni_xGe nanoparticles gradually formed at the surface of a germanide segment. When confined by the Al_2O_3 shell, Tang et al. have shown these segregated nanoparticles could be effectively suppressed, as shown in the NW cross-section in **Figure 1.4** (f), except the bottom surface on substrate where the Al_2O_3 shell was not conformal. It's worth noting that the germanide phase here with an Al_2O_3 shell confinement was found to be NiGe as validated in **Figure 1.4** (g), and had a large lattice mismatch of 77.7% with the Ge interface. This large lattice mismatch is another contributor to the formation of segregated nanoparticles at the non-coated surface. One possible way to eliminate the segregation is to introduce a Ni point-contact on the Ge NW, benefiting from the smaller Ni flux through the limited contact area.[21]

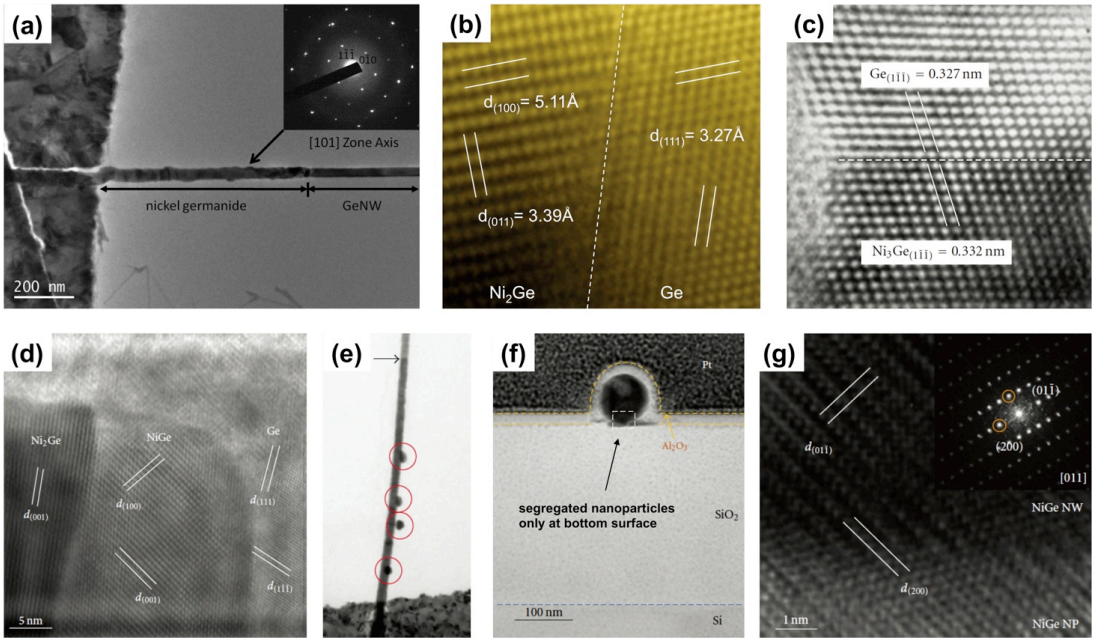

Figure 1.4. Different Ni_xGe/Ge NW interfaces at different reaction temperatures. (a) Ni_3Ge_2 phase formed at 400°C for 2min anneal. Reprinted with permission from Ref [46]. Copyright 2010 American Institute of Physics. (b) Ni_2Ge phase formed at 500°C for 60s anneal. (c) Ni_3Ge phase formed at 650°C. (d) NiGe phase formation at 450°C, with Al_2O_3 shell confinement. (e) Segregation of Ni_xGe nanoparticles upon thermal anneals. (f) Cross-sectional TEM of germanide nanowire coated with Al_2O_3 shell. There are segregated nanoparticles underneath the nanowire, the region that is not covered by Al_2O_3. (g) HRTEM image of the germanide phase in (f), which is NiGe. (b)-(g) are reproduced with permission from Ref [21]. Copyright 2011 Jianshi Tang et al.

1.1.3 Metal and III-V Compound Contacts

Continued progress in increasing transistor density incurs power-dissipation constraints in MOSFET scaling,[52] which may substantially elevate the packaging and cooling cost and make the chips impractical for many applications. One possible way to lower the power consumption is to reduce the operation voltage, which would in return compromise the logic gate switching speeds.[53] A possible solution is to introduce a channel material in which the charge carriers travel faster than in conventional Si channels, allowing a lower operation voltage without sacrificing device performances. Therefore, III-V compound semiconductors, especially $In_xGa_{1-x}As$ ($0 \leq x \leq 1$), are regarded as potential replacement candidates due to their high electron mobility.[22]

In order to take full advantages of the mobility enhancement, the contact requirements become very stringent for III-V transistors.[54] There are several general considerations for the metal contacts to III-V transistors. Since more than two elements are involved in the solid-state reactions between contact metal(s) and III-V compound semiconductors, fundamental studies become more difficult in these multi-compound reactions. Simultaneously, a technical concern arises for the instability of the compound contact to III-V materials under elevated thermal processes,[55] and therefore the electronic properties of compound contacts need to be carefully coordinated with the studies of their morphologies and phases. Despite the well-established contact theory in planar III-V channels,[55,56] only a few detailed studies have been carried out on compound contacts in III-V nanostructures.

Chueh et al.[57] were the first to demonstrate the fabrication of Ni_xInAs compound contact in vapor-liquid-solid (VLS) grown InAs NWs, by reacting Ni pad with <110> oriented InAs nanowires at 220 ~ 300 °C. The Ni_xInAs/InAs heterojunctions showed an atomically abrupt interface, with the epitaxial relationship of $Ni_xInAs(\bar{1}\bar{1}0)$ || InAs $(\bar{1}\bar{1}0)$, and Ni_xInAs [001] || InAs [112]. Their EDS analysis gave a Ni:In:As atomic ratio of 58:22:20, suggesting the ternary phase as Ni_3InAs. Limited by the InAs NW growth orientation and the TEM viewing zone axes, details on the crystal structure and lattice constant of Ni_3InAs phase were not reported. In their following studies, a Ni:In:As atomic ratio of 49:25:26 was found in the reaction of Ni with planar InAs,[58] and the Ni_2InAs stoichiometry was also found in NW channels.[59]

Later, Schusteritsch et al.[60] presented a first-principle calculation for the composition of this Ni_xInAs compound contact. They used *ab initio* random structure searching (AIRSS) approach to determine the value of *x*, and found that the Ni_3InAs phase has the lowest formation enthalpy among others (x=1~6). For the different possible crystal structures of Ni_3InAs, their calculations showed that an orthorhombic structure with Pmmn space group gave the lowest formation energy, which was not observed in the limited experimental data.[61] The possible reason of the difference between first-principle simulation and experimental observations, as they also pointed out in the paper, can be deduced from our discussions in the Si NW section 5.2.1 above, as the phase selection is not only determined by thermodynamics but also by kinetic competition, volume expansion, lattice mismatch, etc.

In fact, the stoichiometry has long been an argument in Ni_xGaAs compound contact to GaAs thin film structures.[62-66] Ni_xGaAs was observed as hexagonal lattice system, adopting NiAs (B8) crystal structure, with the value of *x* ranging in principle from 2 to 4 and the experimentally observed range to be within 2 to 3. As shown in **Figure 1.5**, Ni atoms occupy the corner sites (0, 0, 0) and the edge sites (0, 0, 1/2), forming the hexagonal frame. Ga and As atoms occupy the (1/3, 2/3, 3/4) site and (2/3, 1/3, 1/4) site respectively. There are still another two empty sites (1/3, 2/3, 1/4) and (2/3, 1/3, 3/4) that Ni can selectively occupy resulting in the possible stoichiometry of *x* from 2 to 4. Following experimental results presented in Chapter 2-4, we will show that stoichiometry of x=2 is the most commonly observed crystalline phase in $In_{0.53}Ga_{0.47}As$, as further squeezing of Ni in between the closely packed atoms becomes impractical.

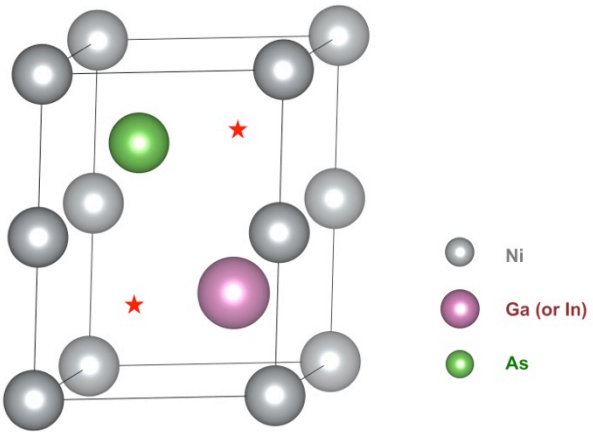

Figure 1.5. Lattice structure of Ni_xGaAs. In principle, the stoichiometry can have a range of x = 2~4. The schematic shows Ni_2GaAs, and extra Ni atoms can occupy one or both of the "★" sites to form Ni_3GaAs or Ni_4GaAs respectively.

1.2 Kinetics of the Solid-State Reaction Between Metal and Semiconductor Nanowires

The implementation of metal-semiconductor compounds as standard contacts to NW field-effect transistors (FETs) urges understanding and control over the dynamic processes in this metal-semiconductor solid-state reaction beyond the knowledge of phases discussed in section 1.1. On one hand, the kinetics in NW reactions can be quite different from that in thin film or bulk reactions, where the surface-to-volume ratio is tremendous. Size-effects, defects, and stain-effects can all play a role – or become dominant effects – in these nanoscale reactions. One the other hand, a well-controlled kinetic process is a prerequisite for realizing tunable channel lengths and ultimately ultra-short channel devices.

1.2.1 The Diffusion Paths of Metal Atoms: Through the Body or Surface

Ni is the dominant diffusion species in this silicide reaction, and there are generally two diffusion paths: through the entire NW cross-section (volume diffusion) or through the few atomic layers at the surface of the NW (surface diffusion). Appenzeller et al[67] were among the first to discuss the kinetics of the Ni-Si NW reaction and to deduce the Ni diffusion path during the silicide formation process. They found a strong size effect on the silicide growth rate, and plotted the silicide length ($L_{silicide}$) versus R^{-1} and R^{-2}. Based on their experimental observation that the $L_{silicide} \sim R^{-2}$ plot passed the origin point, they deduced a Ni volume diffusion dominant kinetics, with the assumption that the amount of diffused Ni (measured by the volume of reacted Ni silicide segment $L_{silicide} \cdot \pi R^2$) was

constant and that the silicide length should approach zero for infinitely large NW ($R^{-2} \approx 0$) under a short reaction time. Later, Katsman et al[68] argued that the extracted volume diffusion coefficient was much higher than realistic at the low reaction temperature of 280 °C. They re-plotted the Appenzeller's data with $L_{silicide} \sim R^{-1/2}$ coordination following their own surface diffusion model, and fitted the plot with linear approximation. This fitted line didn't pass through zero either, while they extrapolated this intercept as a transition diameter R_0, above which the interfacial diffusion (at silicide/Si interface) started to play a role.

Besides the Ni diffusion paths, there are also other limiting steps for the reaction kinetics. Lu et al[40] studied the nickel silicide reaction in [111] oriented Si NWs by point contact with Ni NWs. The silicide phase found in this study was nickel-mono-silicide, NiSi, which exhibited a linear dependence of $L_{silicide}$ with time, t, instead of the conventional $L_{silicide} \propto t^{1/2}$ dependence for a diffusion dominant process. The authors ruled out the phase growth on the silicide/Si interface as the rate-limiting step, as their observed epitaxial growth rate was much faster than the diffusion speed. Therefore, they concluded that this point contact reaction was limited by the rate Ni dissolution into Si NW at the contact interface. Dellas et al[69] investigated the silicide reaction at higher temperatures (400 ~ 500 °C), and found a NW orientation dependent reaction kinetics. They attribute this effect to the differences in dominant phase formed in different NW growth directions, and [111] oriented (or [112] oriented) NW had a linear $L_{silicide} \propto t$ (or hyperbolic $L_{silicide} \propto t^{1/2}$) kinetics due to the formed $NiSi_2$ phase (or θ-Ni_2Si phase). Chen et al[31] extended the discussions on kinetics of different silicide phases, and demonstrated the first phase

selection by kinetic competition for small NWs at a high reaction temperature (800 °C) as discussed in section 1.1.1.

All these debated aspects for the metal-semiconductor compound contact formation starve for a standard model that can quickly determine the rate-limiting steps and guide the extrapolation of relevant parameters. In Chapter 2, we will provide a mono-compound phase model that depicts the kinetic steps involved in the metal-semiconductor reactions, and provide a case study of nickelide reaction in InGaAs NWs.

1.2.2 Atomic Scale Dynamics: Ledge Nucleation and Movement

The dynamic process during metal-semiconductor reaction is reflected by the ledge (a moving step-line of atoms at the growth interface) nucleation and movement at atomic scale. Generally, a ledge or a train of ledges form on the compound contact/semiconductor interface, and propagate through the entire cross-section of NWs. In-situ heating TEM technique provides the platform to observe these ledge (or called step) events with atomic resolutions.[70]

In the study of $CoSi_2$ formation in Si NWs, Chou et al[71] prepared the [111] oriented Si NWs with point contact of Co NWs, and annealed the sample inside TEM chamber at 800 °C with real-time video recordings. They observed repeating events of the nucleation and stepwise growth mode during the epitaxial $CoSi_2$ phase formation, which has the same crystal structure and close lattice constant with pristine Si. Shown in **Figure 1.6** (a) – (d) are the HRTEM images near $Si/CoSi_2$ interface, with the step movements

labeled on the figures. By recording these repeating nucleation and growth events, they plotted the $CoSi_2$ atomic layers as a function of time in **Figure 1.6** (e), and several information can be interpreted from this plot. First, the vertical lines in this plot represent the steps of newly formed $CoSi_2$, and the height of each vertical transition is constantly that of one atomic layer of $CoSi_2$ (111) plane, indicating the layer-by-layer growth nature of $CoSi_2$ phase. Second, these vertical lines are not perfectly in parallel with y-axis but are sloped with a certain width that corresponds to the growth time of each $CoSi_2$ atomic layer with the average value of ~ 0.17 s. Third, the horizontal segment in between vertical lines is the stagnation period before the nucleation of another step, which is called incubation time of nucleating a step. Taking into account the incubation time for nucleating every step, the average growth rate of $CoSi_2$ along the axial direction is 0.0365 nm/s. The radial growth rate (step velocity) is about 135nm/s, calculated by the average step growth time and NW diameter, which is about 3700 times faster than the axial growth rate. This also indicates that interfacial reaction was not the rate-limiting step in this cobalt silicide growth. Fourth, the stair-step plot in **Figure 1.6** (e) can be treated as the microcosmic view of a conventional $L_{silicide} \sim t$ relationship (discussed in section 1.2.1), in which a linear dependence was found over a long reaction time. The authors attribute this linear time dependence to a Co source supply limited reaction. Moreover, each step of $CoSi_2$ showed a homogeneous nucleation behavior in the center of Si NW atop the $CoSi_2$/Si interface instead of the heterogeneous nucleation at the triple point of oxide shell, Si, and $CoSi_2$.

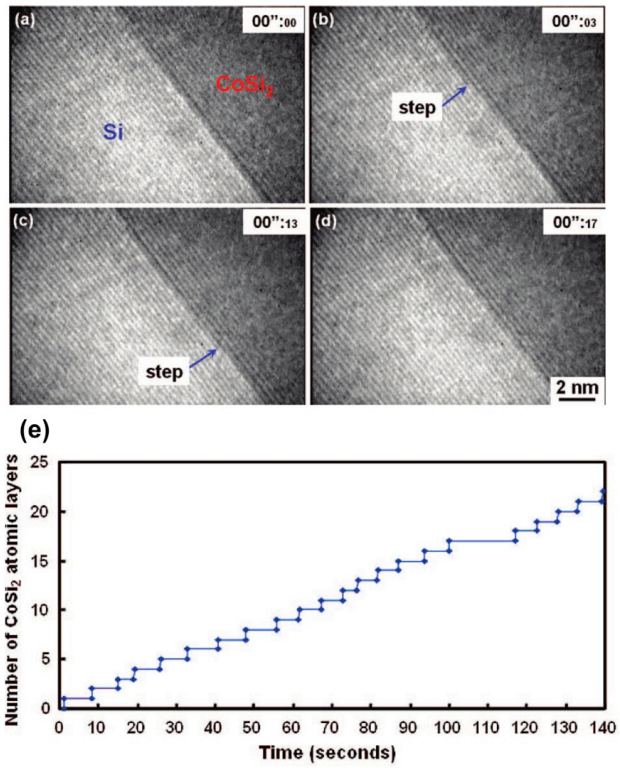

Figure 1.6. (a) – (d) In situ HRTEM image sequences of growing $CoSi_2$/Si epitaxial interfaces within a [111] oriented Si NW. (e) Plot of $CoSi_2$ atomic layers as a function of time to show the nucleation time and growth time of each step. Reproduced with permission from Ref [71]. Copyright 2008 American Chemical Society.

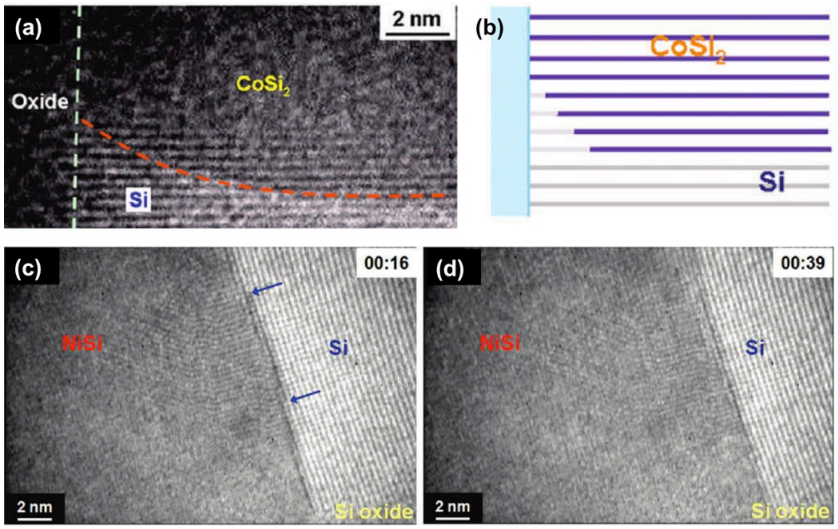

Figure 1.7. (a) – (b) HRTEM image and schematics of the $CoSi_2$/Si epitaxial interfaces at the oxide/Si/ $CoSi_2$ triple point. (c) – (d) In situ HRTEM image sequences of growing NiSi/Si epitaxial interfaces within a [111] oriented Si NW. Reproduced with permission from Ref [41]. Copyright 2009 American Chemical Society.

Though homogeneous nucleation was seldom expected in theory, the authors explained the nucleation behavior here that the energy of oxide/silicide interface is higher than that of oxide/Si interface reducing the nucleation frequency at the triple points. They provided further experimental evidence[41] in **Figure 1.7** (a) – (b) that the steps slowed down as approaching the oxide/Si/$CoSi_2$ triple points due to the high energy barrier. Their in-situ TEM study of Ni point contacted Si NW showed similar homogeneous nucleation of steps, as shown in **Figure 1.7** (c) – (d).

1.2.3 Modified Kinetic Process by Nanoscale Defects

Through the discussions above on kinetics of the solid-state reactions between metal and pristine semiconductor NWs, we argued that several factors can potentially dominate the rate limiting steps of compound contact growth, such as NW sizes, surface oxide, reaction temperature and formed phases. In the following paragraphs, we will discuss another important factor that may modify the nucleation and growth behaviors of compound contacts in NW channels: defects.

In advanced semiconductor technology nodes, defects are intentionally built into the device to tailor the stress in Si channel. The stress memorization technology[72] is one example that utilizes stacking faults to exert tensile strain in the channel by inducing missing planes in the source/drain regions. In other instances, defects can be unintentionally introduced to the S/D regions during dopant implantation and subsequent thermal activation anneal.[73] Therefore, understanding the interactions between metal-semiconductor

reactions and defects become important in controlling compound contact formation in defect-engineered nanochannels.

My senior group member, Wei Tang, has previously investigated the nickelide silicide nucleation and growth in the presence of defects in Si NWs.[74] The Si NWs are grown at different conditions,[75] to intentionally introduce two types of defects: (1) twin boundary (TB) along the axial direction of the NW with a high growth rate/SiH_4 partial pressure and (2) Si nanoparticles on the NW surface forming the grain boundary (GB) with high growth temperature. It has been found that the $NiSi_2$ prefers the heterogeneous nucleation at the defect sites in order annihilate the high-energy interfaces.

As shown in **Figure 1.8**, the $NiSi_2$ phase grows on the Si (111) plane in a layer-by-layer manner, and the growth fronts move asynchronously at two sides of the TB. The steps nucleate at the TB but never propagate across it, because the high energy-barrier of forming new $NiSi_2/NiSi_2$ TB prevents so. The lagging interface can catch up with the leading interface because the $NiSi_2$/Si corner at TB is a preferable hetero-nucleation site, so on the average asynchronous step height does not grow significantly, given that Ni supply is equally available for both halves of the bi-crystal. With the presence of GBs on the NW surface as shown in **Figure 1.9**, the heterogeneous nucleation is further facilitated and the steps are found to start from the GB and propagate towards the TB, in both leading and lagging interfaces, indicating that the GB is more energetically preferred nucleation site.

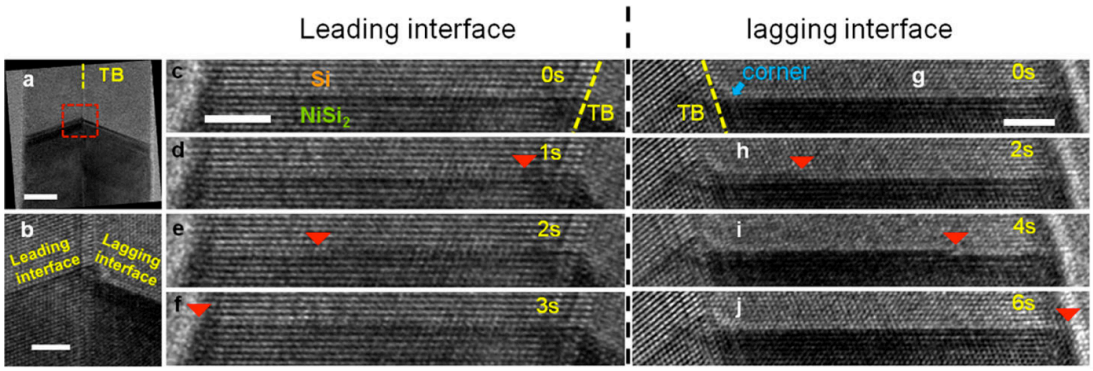

Figure 1.8. (a) and (b) $NiSi_2$ growth in Si NW with a TB. (c−f) and (g-j) HRTEM sequences showing the nucleation and propagation of $NiSi_2$ steps at the leading interface and at the lagging interface, respectively. Scale bar is 10 nm for (a) and 3nm for all the rests. Reprinted with permission from Ref [74]. Copyright 2013 American Chemical Society.

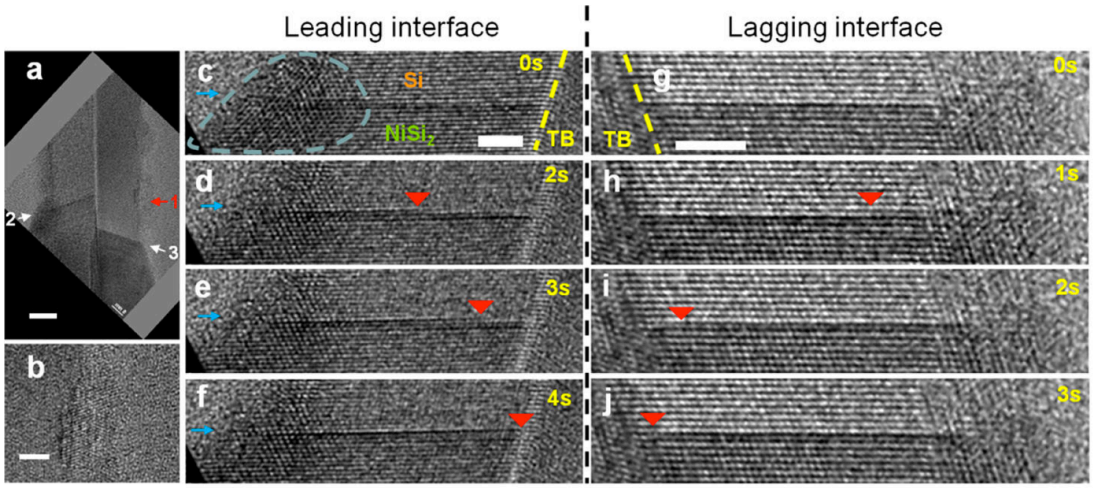

Figure 1.9. (a) $NiSi_2$ growth in Si NW with TB running along its central axis and GBs present at its surface. (b) Zoom-in HRTEM image of a cluster of surface grains. (c−f) and (g-j) HRTEM sequences showing the nucleation and propagation of $NiSi_2$ steps at the leading interface and at the lagging interface, respectively. Scale bar is 10 nm for (a) and 3nm for all the rests. Reprinted with permission from Ref [74]. Copyright 2013 American Chemical Society.

These observations are related to the effectiveness of nucleation barrier reductions in $NiSi_2$ phase formation, and this reduction can be evaluated at the three possible heterogeneous nucleation sites: (1) TB (2) "corner", and (3) surface GB, by calculating[74]:

$$\frac{\Delta G^*_{\text{hetero}}}{\Delta G^*_{\text{homo}}} = \frac{(\pi - \theta) + \sin\theta\cos\theta}{\pi} \tag{1-2}$$

where $\Delta G^*_{\text{hetero}}$ and ΔG^*_{homo} are the heterogeneous and homogeneous nucleation barriers respectively. And θ is the contact angle. The values of $\Delta G^*_{\text{hetero}} / \Delta G^*_{\text{homo}}$ can be calculated for TB, "corner", and GB as 0.93, 0.90, and 0.83 respectively. This indeed proves that the nucleation is more preferred on GB, than "corner", and than TB sites.

1.3 Electrical Properties of Metal-Semiconductor Compound Contacts

Thus far, we discussed the phases of the metal-semiconductor compound contacts and the kinetics during the solid-state reaction processes but the end goal of these metallurgical studies is to achieve a robust control over the electrical properties of the compound contacts and the resulting NW or Fin FETs performances. It has been found that the S/D series resistance increasingly becomes the limiting factor for integrating nanostructures into high-performance electronics and the dominant performance degradation component below 10nm node.[76] Therefore, understanding the electrical properties of the nanoscale electrical contacts, especially compound contacts, is a key step for fulfilling the leap from laboratory to real-world technology.[77]

1.3.1 Band-Alignment and Charge Injection

The charge injection from metal-compound contacts into semiconductors is largely dominated by the band alignment at the contact-semiconductor interface. Due to the different contact geometry and size effects, NW transistors exhibit distinct band-alignment and charge-injection properties than their bulk counterparts.[77] Here, we will discuss several theoretical studies of the nanoscale contacts.

For planar-geometry contacts (**Figure 1.10** (a)), metal is deposited on the semiconductor surface followed by thermal anneal to form the compound interfacial layer. For nanoscale contacts, there are generally two categories: end-bonded contacts and side contacts.[77] The end-bonded contact (**Figure 1.10** (b)) refers to the case that the metal or metallic contact has an abrupt interface with semiconductor in axial direction of nanochannels, in which atomic bonds form between the contact and the semiconductor. The compound formations in NW channels through metal diffusions as we discussed above all belong to this category. The side contact (**Figure 1.10** (c)) refers to the metal embedded geometry in the NW radial direction. A simple deposition of metals on top of the NW is considered as in this category, in which a weak bond forms in between metal and NW. It has also been found that a metal that reacts with semiconductor at high temperature can readily form a thin layer of metal-semiconductor compound at the surface of NW upon deposition at room temperature, due to the latent heat during the condensation of metal-vapor.[78] This also forms a side contact, but with strong bonds (atomic bonds) between compound contact and semiconductor.

In the planar-geometry contact,[79] the ideal model suggests that the electron SBH is given by:

$$\phi_b = \Phi - \chi \tag{1-4}$$

where Φ is the work function of metal compound contact, and χ is the semiconductor electron affinity as illustrated in **Figure 1.10** (d). The electrical charge flow across the contact-semiconductor interface equals the contact work function with semiconductor Fermi-level and causes the conduction and valence band-edge bending near the interface. This band-edge bending is associated with a depletion (or accumulation) of charge carriers. In the case of depletion, the width of this space-charge region is given by:

$$W = \sqrt{\frac{2\varepsilon\phi_b}{Nq}} \tag{1-5}$$

where ε is the dielectric constant of semiconductor, N is the dopant density, and q is the electron charge. In the presence of a Schottky barrier, the transport mechanisms are thermionic emission, tunneling through the barrier, and the electron-hole recombination in the depletion region. Usually, the electron-hole recombination current is much smaller than the other two, and the mixed thermally excited and tunneling current density can be expressed as:[80]

$$J_t = \frac{A^* T}{k} \int_0^\infty \tau(E) \cdot e^{-(E+q\varphi_s)/kT} dE \times \left[1 - e^{-qV_f/kT}\right] \tag{1-6}$$

where A^* is the Richardson constant, k is the Boltzmann constant, T is temperature, and E is the conduction band edge energy. $\tau(E)$ is the tunneling probability for carriers, V_f

is the applied forward bias, and $q\varphi_s$ is the potential energy of the charge carriers relative to the Fermi level. And therefore the contact resistivity can be calculated as:[81]

$$\rho_c = \left(\frac{\partial J}{\partial V} \right)^{-1} \Bigg|_{V=0} \tag{1-7}$$

In the end-bonded contact, the depletion width was found to be larger than that in planar contact with the same doping density and SBH.[82] This is related to the rapid change in the dielectric constant dictating a strongly varying size-dependent fringing field in between the metal contact and the semiconductor NW surface. In small NWs, the strong fringing field makes the electric field lines near the contact interface incline to the ambient around the NW, causing a week electric field inside the NW. The reduced electric field screening in the small NWs results in larger depletion width, smaller tunneling current and consequently larger contact resistivity. Shown in **Figure 1.11** are the simulation results of band-edge diagrams and contact resistivity changes versus NW radius, comparing the end-bond contacts in NW (NW-3D contact and NW-1D contact) to planar-geometry contact.[82] It can be found that the contact resistivity of NW-1D contact is less vulnerable to change of NW size than that of NW-3D contact, indicating the advantages of forming metal-semiconductor compounds contacts inside the NW channels. In principle, high contact doping can reduce the depletion width and bring down the contact resistivity.

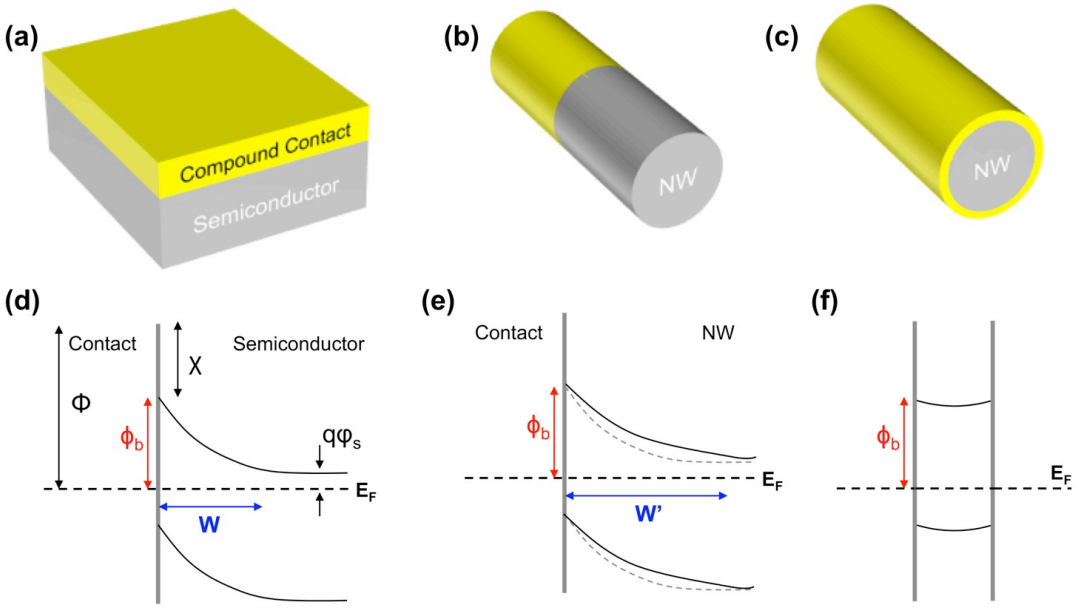

Figure 1.10. Schematics illustration for the energy band-edge alignment diagrams for (a, d) Planar-geometry contact, (b, e) end-bonded contact, and (c, f) side contact.

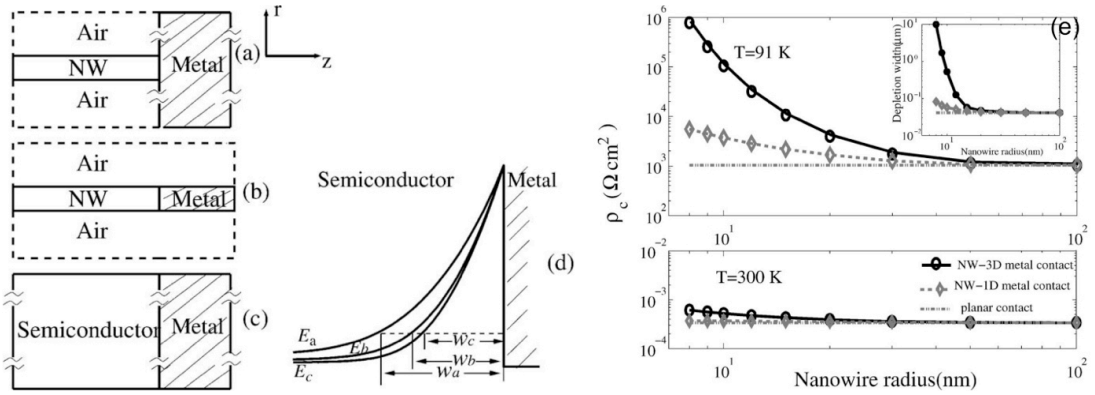

Figure 1.11. Schematic illustrations of different contact geometries to NWs: (a) NW-3D metal contact, (b) NW-1D metal contact, and (c) planar contact. (d) Simulated energy band-edge diagrams for different contact geometries. (e) Contact resistivity vs NW radius for different contact geometries at temperatures equal to 91 and 300 K, respectively. Reproduced with permission from Ref [82]. Copyright 2008 American Institute of Physics.

In the side contact, the band realignment due to charge transfer is weak due to the limited available depletion width in the NW cross-section. Theoretical studies[83] of the side contact to NW device suggested that the nanoscale dimension of the NWs prevents the energy band-edge from reaching their asymptotic value and instead presents only a weak band bending. Shown in the **Figure 1.12** are the simulated results of band bending and contact resistance for a heavily doped Si NW ($1\times10^{19}cm^{-3}$) with side contact. The results indicate that the conventional strategy of heavily doping the semiconductor to obtain Ohmic contacts breaks down as the NW diameter is reduced. A dramatical increase of contact resistance is expected for small NWs, as shown in **Figure 1.12** (c). By modeling the density of states using 1-D equation in NW structures, the authors found that the quasi-1D system (NWs) requires almost 2 orders of magnitude larger density of pinning states compared with the bulk interface for the same effect of Fermi-level pinning, meaning that NWs are generally free of contact Fermi-level pinning for very small diameters. This in principle applies for end-bonded contacts as well.

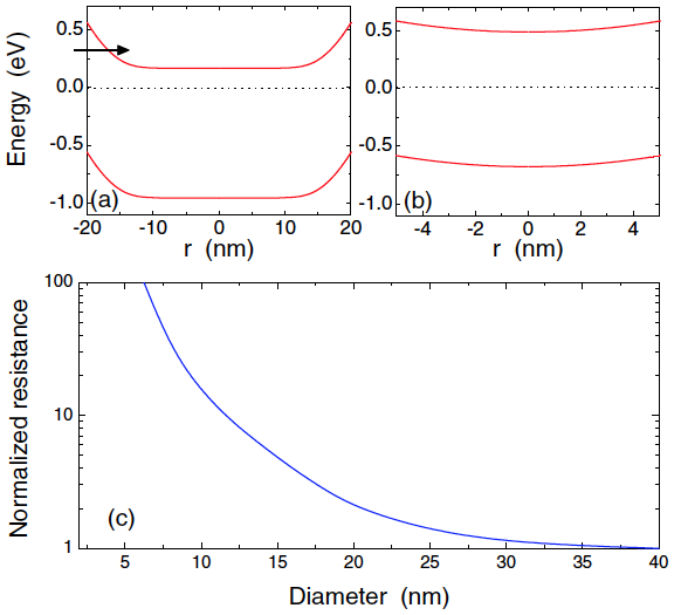

Figure 1.12. Simulated energy band-edge bending across Si NWs (doping of $1\times10^{19}cm^{-3}$) with side contact for diameters of (a) 40nm and (b) 10 nm. (c) The normalized resistance as a function of NW diameter. Reprinted with permission from Ref [83]. Copyright 2006 American Physical Society.

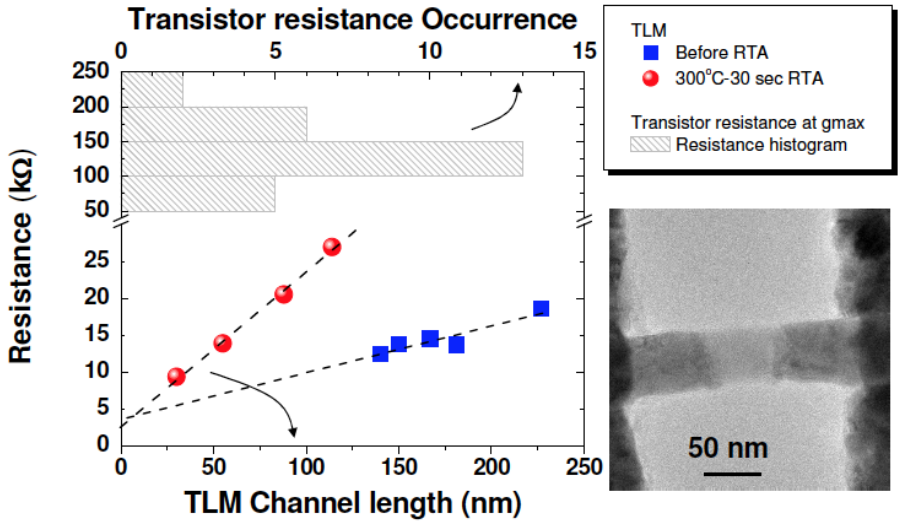

Figure 1.13. NW resistance as a function of non-reacted semiconductor channel lengths. The contact resistance in Ge/Si core/shell NWs is extracted to be below 10 kΩ, which is much smaller than the typical resistance of the NW FET operating at maximum transconductance (histogram peaks at 100–150 kΩ). Reprinted with permission from Ref [84]. Copyright 2014 American Chemical Society.

In experimental measurements, the contact resistance between the compound contact and the semiconductor is sometimes misinterpreted. This is because the conventional 4-probe technique can only contact resistance between metal/compound interface, but not the important compound/semiconductor interface. Transmission line measurement (TLM) is therefore a more preferred method, by patterning multiple metal pads with various spacing on a single NW channel followed by a short thermal annealing to form compound contact. An example is shown in **Figure 1.13** for TLM results on Ge/Si core/shell NWs with patterned Ni pads.[84] The fabrication was conducted on a 50 nm thick SiN_x membrane, so that after thermal annealing, the unreacted semiconductor NW segments can be precisely measured under TEM. As shown in **Figure 1.13**, the contact resistance between $NiGe_xSi_y$ and Ge/Si NW is below 10 kΩ, which is significantly smaller than typical resistance values of a NWFET device made on the same type of NWs and operating at maximum transconductance. This suggested that the contact resistance was negligible in these Ge/Si core/shell NWFET performance analysis and mobility extraction.

1.3.2 Ultra-short channel devices

Enhanced NW FET performance is enabled with ever-smaller channel lengths that can provide high on-current drives. The transistor channel length is usually defined by the metal gate width (in a gate-first self-aligned process) or the distance between its S/D electrodes, both of which requires expensive e-beam lithography tools or sophisticated photolithography techniques. The metal-semiconductor compound contact formation provides a lithography-free method to achieve ultra-short channel lengths in NW channels

with controlled metal-semiconductor reactions. **Figure 1.14** summarizes the prominent researches that demonstrated ultra-short NW channels with two terminal contacts. The most commonly used way was to monitoring the metal-semiconductor NW reactions *in situ* inside a TEM or SEM chamber, and the ultra-short channels have been achieved in Si,[85] Ge,[86] and Ge/Si core/shell[20] NWs.

Joule heating assisted nickel silicide reaction is shown in **Figure 1.14** (d)-(e), with the channel length monitored by the current measurements across the NW.[87] During this process, voltage V_1 and V_2 were applied on the metal strip at one side of the NW, and the joule heat peaked at the strip center and induced the Ni diffusion into the Si NW. The voltage drop across the NW, equaling to $(V_1+V_2)/2$, introduced a current flow that was recorded to monitor the silicide reaction process. Silicide could also form at the other end of the Si NW by applying V_1 and V_2 on the opposite metal strip. Due to the Schottky barrier between silicide and Si, the recorded current through Si NW was low (dominated by thermionic emission) in long channels and increased slowly as channel length decreased. When the channel length was below 50nm, the device showed a dramatic current increase due to the carriers effectively tunneling through Schottky barrier. With carefully monitored channel current, an ultra-short channel length of 8nm was achieved.

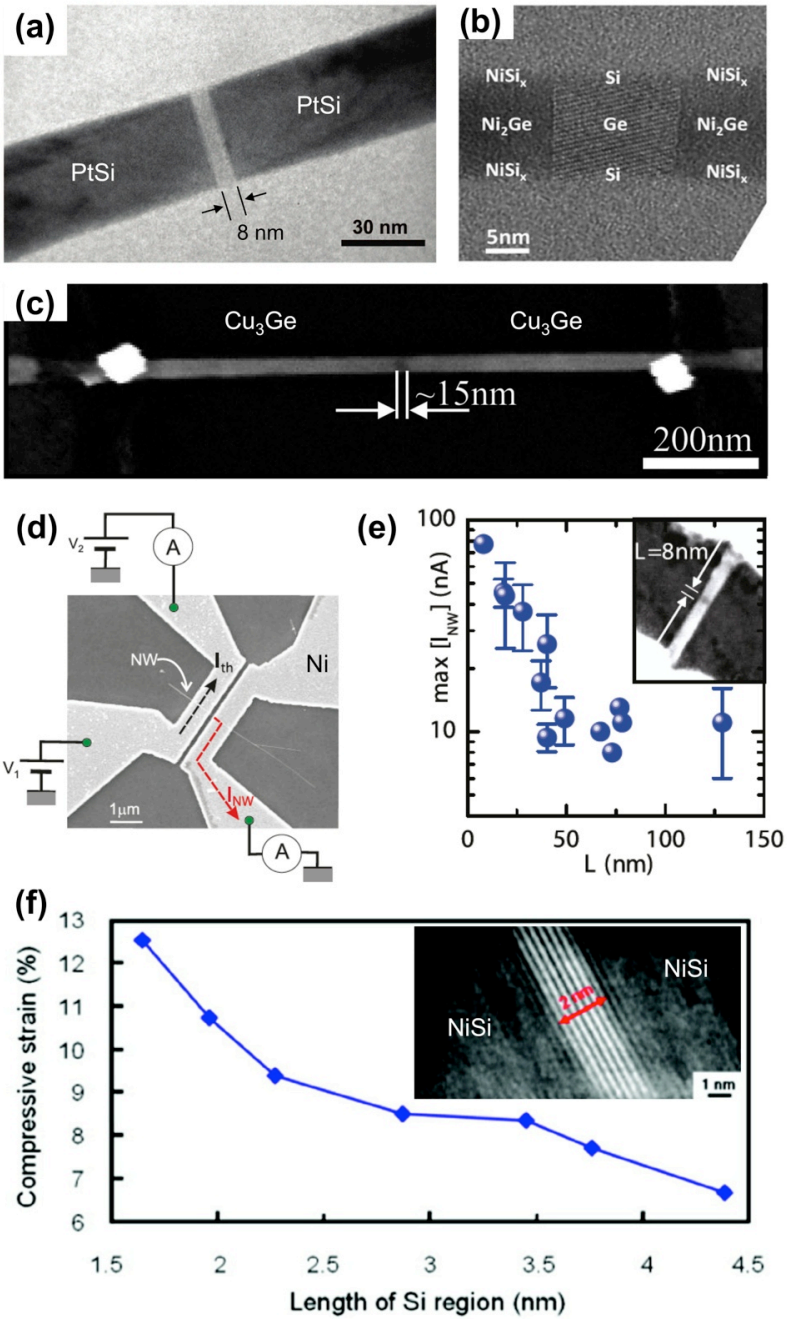

Figure 1.14. (a) PtSi/Si/PtSi NW with Si length of 8nm. Reprinted with permission from Ref [85]. Copyright 2008 American Chemical Society. (b) ultra-short channel formed in Ge/Si core/shell NW. Reprinted with permission from Ref [20]. Copyright 2014 IOP Publishing. (c) $Cu_3Ge/Ge/Cu_3Ge$ NW with Ge length of 15nm. Reprinted with permission from Ref [86]. Copyright 2009 American Chemical Society. (d) and (e) Joule-heating assisted nickel silicide formation in Si NW with ultra-short channel length of 8nm. Reproduced with permission from Ref [87]. Copyright 2011 American Chemical Society. (f) NiSi/Si/Si NW formed by anneal point-contacted Ni to Si NW. The channel strain was measured in those ultra-short channels. Reproduced with permission from Ref [40]. Copyright 2007 American Chemical Society.

To characterize the performance of the ultra-short channel device, my senior group members monitored the Ni-Si NW reactions in TEM chamber through *in situ* heating, until reaching a channel length of 17nm. Then, 10nm HfO_2 was deposited on top as a gate dielectric, followed by the Ti gate deposition. The ultra-short channel device shows higher on-currents than those with longer channel lengths, but with higher off-state current too because of the much larger NW diameter compared with the channel length (**Figure 1.15** (b)), which enforced stronger short channel effects. The dependence of maximum transconductance, g_m, versus the channel length, L_G, is shown in **Figure 1.15** (c), and the performance gain with down-scaled transistor channels starts to saturate below 100nm. This is because the Ni-silicide/Si SB contact resistance starts to dominate the on-state conduction at short channel lengths. **Figure 1.15** (c) inset shows an energy band-edge diagram of a Si NW SB FET in the on-state with a large potential drop across the contact SB and comparatively much smaller effective carrier-driving potential drop along the channel. This suggests that the SB contact engineering is vital to best fulfill the advantages of short channel SB-FETs.

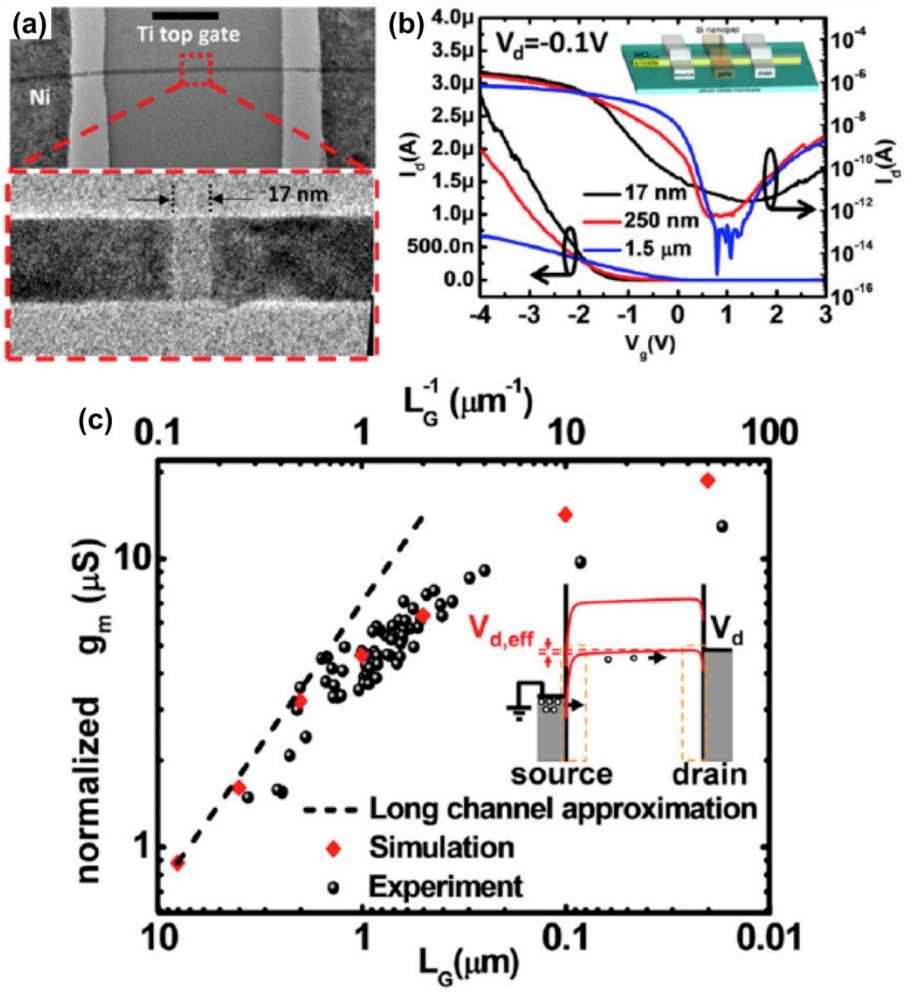

Figure 1.15. (a) TEM image of a Si NW FET device with 17 nm channel length. Scale bar is 1 μm. (c) I_d–V_g characteristics of Si NW FETs with different channel lengths at V_d=−0.1V at linear (left y-axis) and log (right y-axis) scales. Inset is a schematic of the ultra-short channel Si NW FET device. (d) Channel length-dependent device performance. Inset is the energy band-edge diagram of Si NW SBFET in on-state. Reproduced with permission from Ref [29]. Copyright 2012 American Chemical Society.

1.4 Conclusions

In this chapter, we the discussed compound contacts to NW transistors that are formed by solid-state reactions between metal and semiconductor NWs. We introduced the observed phases of compound contacts formed in Si, and Ge NWs, the kinetic processes during these solid-state reactions, and their electrical characteristics. These comprehensive summaries demonstrate the promise of compound contacts in nanoscale electronics. At the same time, people are seriously trying to improve the contact to III-V devices, because engineers always want to integrate the high-mobility III-V transistors onto the current Si circuits. However, despite the contact studies on III-V bulk or thin film structures, seldom researches have been conducted in the NW for Fin channels. In the following chapters, I will introduce the contact studies in InGaAs NWs, especially the observations made in real time.

Part of chapter 1 was invited for publication as a book chapter of *Springer Publisher* 2018. R. Chen, S. A. Dayeh. The dissertation author is the first author of this paper.

1.5 References

1. Cui Y, Lieber CM (2001) Functional nanoscale electronic devices assembled using silicon nanowire building blocks. science 291 (5505):851-853

2. Duan X, Huang Y, Cui Y, Wang J, Lieber CM (2001) Indium phosphide nanowires as building blocks for nanoscale electronic and optoelectronic devices. Nature 409 (6816):66-69

3. Huang Y, Duan X, Cui Y, Lauhon LJ, Kim K-H, Lieber CM (2001) Logic gates and computation from assembled nanowire building blocks. Science 294 (5545):1313-1317

4. Huang Y, Duan X, Wei Q, Lieber CM (2001) Directed assembly of one-dimensional nanostructures into functional networks. Science 291 (5504):630-633

5. Ieong M, Doris B, Kedzierski J, Rim K, Yang M (2004) Silicon device scaling to the sub-10-nm regime. Science 306 (5704):2057-2060

6. Ferain I, Colinge CA, Colinge J-P (2011) Multigate transistors as the future of classical metal–oxide–semiconductor field-effect transistors. Nature 479 (7373):310

7. Dayeh SA, Aplin DP, Zhou X, Yu PK, Yu ET, Wang D (2007) High Electron Mobility InAs Nanowire Field‐Effect Transistors. small 3 (2):326-332

8. Dayeh SA, Susac D, Kavanagh KL, Yu ET, Wang D (2008) Field dependent transport properties in InAs nanowire field effect transistors. Nano letters 8 (10):3114-3119

9. Dayeh SA, Soci C, Bao X-Y, Wang D (2009) Advances in the synthesis of InAs and GaAs nanowires for electronic applications. Nano Today 4 (4):347-358

10. Gudiksen MS, Lauhon LJ, Wang J, Smith DC, Lieber CM (2002) Growth of nanowire superlattice structures for nanoscale photonics and electronics. Nature 415 (6872):617-620

11. Barrelet CJ, Greytak AB, Lieber CM (2004) Nanowire photonic circuit elements. Nano Letters 4 (10):1981-1985

12. Yan R, Gargas D, Yang P (2009) Nanowire photonics. Nature Photonics 3 (10):569-576

13. Wu Y, Xiang J, Yang C, Lu W, Lieber CM (2004) Single-crystal metallic nanowires and metal/semiconductor nanowire heterostructures. Nature 430 (6995):61-65

14. Requist R, Baruselli PP, Smogunov A, Fabrizio M, Modesti S, Tosatti E (2016) Metallic, magnetic and molecular nanocontacts. Nature nanotechnology 11 (6):499-508

15. Kikuchi A, Ohshima T, Shiraki Y (1988) Schottky barrier height of single‐crystal nickel disilicide/silicon interfaces. Journal of Applied Physics 64 (9):4614-4617. doi:10.1063/1.341239

16. Zhou Y, Ogawa M, Han X, Wang KL (2008) Alleviation of Fermi-level pinning effect on metal/germanium interface by insertion of an ultrathin aluminum oxide. Applied Physics Letters 93 (20):2105

17. Sze SM, Ng KK (2006) Physics of semiconductor devices. John wiley & sons,

18. Chen L-J, Wu W-W (2015) Metal silicide nanowires. Japanese Journal of Applied Physics 54 (7S2):07JA04

19. Lin Y-C, Huang Y (2013) Nanoscale Contact Engineering for Si Nanowire Devices. Silicon and Silicide Nanowires: Applications, Fabrication, and Properties:413

20. Tang W, Nguyen B-M, Chen R, Dayeh SA (2014) Solid-state reaction of nickel silicide and germanide contacts to semiconductor nanochannels. Semiconductor Science and Technology 29 (5):054004

21. Tang J, Wang C-Y, Xiu F, Zhou Y, Chen L-J, Wang KL (2011) Formation and device application of Ge nanowire heterostructures via rapid thermal annealing. Advances in Materials Science and Engineering 2011:316513

22. Del Alamo JA (2011) Nanometre-scale electronics with III-V compound semiconductors. Nature 479 (7373):317-323

23. Nishi Y, Doering R (2000) Handbook of semiconductor manufacturing technology. CRC Press,

24. Chen LJ (2004) Silicide technology for integrated circuits, vol 5. Iet,

25. Lavoie C, d'Heurle F, Detavernier C, Cabral C (2003) Towards implementation of a nickel silicide process for CMOS technologies. Microelectronic Engineering 70 (2):144-157

26. Ahn C-G, Kim T-Y, Yang J-H, Baek I-B, Cho W-j, Lee S (2008) A two-step annealing process for Ni silicide formation in an ultra-thin body RF SOI MOSFET. Materials Science and Engineering: B 147 (2):183-186

27. Zhang Z, Pagette F, D'emic C, Yang B, Lavoie C, Zhu Y, Hopstaken M, Maurer S, Murray C, Guillorn M (2010) Sharp reduction of contact resistivities by effective Schottky barrier lowering with silicides as diffusion sources. IEEE Electron Device Letters 31 (7):731-733

28. Tu K-N, Alessandrini EI, Chu W-K, Krautle H, Mayer JW (1974) Epitaxial growth of nickel silicide NiSi2 on silicon. Japanese Journal of Applied Physics 13 (S1):669

29. Tang W, Dayeh SA, Picraux ST, Huang JY, Tu K-N (2012) Ultrashort Channel Silicon Nanowire Transistors with Nickel Silicide Source/Drain Contacts. Nano Letters 12 (8):3979-3985

30. Lin Y-C, Chen Y, Xu D, Huang Y (2010) Growth of Nickel Silicides in Si and Si/SiOx Core/Shell Nanowires. Nano Letters 10 (11):4721-4726

31. Chen Y, Lin Y-C, Huang C-W, Wang C-W, Chen L-J, Wu W-W, Huang Y (2012) Kinetic Competition Model and Size-Dependent Phase Selection in 1-D Nanostructures. Nano Letters 12 (6):3115-3120

32. Chen Y, Lin Y-C, Zhong X, Cheng H-C, Duan X, Huang Y (2013) Kinetic Manipulation of Silicide Phase Formation in Si Nanowire Templates. Nano Letters 13 (8):3703-3708

33. Pretorius R (1996) Prediction of silicide formation and stability using heats of formation. Thin solid films 290:477-484

34. d'Heurle F, Gas P (1986) Kinetics of formation of silicides: A review. Journal of materials research 1 (01):205-221

35. Mangelinck D, Hoummada K, Blum I (2009) Kinetics of a transient silicide during the reaction of Ni thin film with (100) Si. Applied Physics Letters 95 (18):1902

36. Van Bockstael C, Detavernier C, Van Meirhaeghe R, Jordan-Sweet J, Lavoie C (2009) In situ study of the formation of silicide phases in amorphous Ni–Si mixed layers. Journal of Applied Physics 106 (6):064515

37. Ogata K, Sutter E, Zhu X, Hofmann S (2011) Ni-silicide growth kinetics in Si and Si/SiO2 core/shell nanowires. Nanotechnology 22 (36):365305

38. Lin Y-C, Chen Y, Chen R, Ghosh K, Xiong Q, Huang Y (2012) Crystallinity Control of Ferromagnetic Contacts in Stressed Nanowire Templates and the Magnetic Domain Anisotropy. Nano Letters 12 (8):4341-4348. doi:10.1021/nl302113r

39. Chen Y, Huang Y (2013) Phase control in solid state silicide nanowire formation. physica status solidi (c) 10 (12):1666-1669

40. Lu K-C, Wu W-W, Wu H-W, Tanner CM, Chang JP, Chen LJ, Tu KN (2007) In situ Control of Atomic-Scale Si Layer with Huge Strain in the Nanoheterostructure NiSi/Si/NiSi through Point Contact Reaction. Nano Letters 7 (8):2389-2394. doi:10.1021/nl071046u

41. Chou Y-C, Wu W-W, Chen L-J, Tu K-N (2009) Homogeneous Nucleation of Epitaxial CoSi2 and NiSi in Si Nanowires. Nano Letters 9 (6):2337-2342. doi:10.1021/nl900779j

42. Loomans M, Chi D, Chua S (2004) Monosilicide-disilicide-silicon phase equilibria in the nickel-platinum-silicon and nickel-palladium-silicon systems. Metallurgical and Materials Transactions A 35 (10):3053-3061

43. Liu J, Chen H, Feng J (2000) Enhanced thermal stability of NiSi films on Si (111) substrates by a thin Pt interlayer. Journal of Crystal growth 220 (4):488-493

44. Lew KK, Pan L, Dickey EC, Redwing JM (2003) Vapor–liquid–solid growth of silicon–germanium nanowires. Advanced Materials 15 (24):2073-2076

45. Lauhon LJ, Gudiksen MS, Wang D, Lieber CM (2002) Epitaxial core–shell and core–multishell nanowire heterostructures. Nature 420 (6911):57-61

46. Dellas N, Minassian S, Redwing J, Mohney S (2010) Formation of nickel germanide contacts to Ge nanowires. Applied Physics Letters 97 (26):263116

47. Ellner M, Gödecke T, Schubert K (1971) Zur struktur der mischung Nickel-Germanium. Journal of the Less Common Metals 24 (1):23-40

48. Pearson WB, Villars P, Calvert LD (1985) Pearson's handbook of crystallographic data for intermetallic phases, vol 1. American Society for Metals,

49. Tang J, Wang C-Y, Xiu F, Hong AJ, Chen S, Wang M, Zeng C, Yang H-J, Tuan H-Y, Tsai C-J (2010) Single-crystalline Ni2Ge/Ge/Ni2Ge nanowire heterostructure transistors. Nanotechnology 21 (50):505704

50. Bhan S, Kudielka H (1978) Ordered bcc-phases at high temperatures in alloys of transition metals and B-subgroup elements. Zeitschrift fur Metallkunde 69:333-336

51. Suzuki T, Oya Y, Ochiai S (1984) The mechanical behavior of nonstoichiometric compounds Ni3Si, Ni3Ge, and Fe3Ga. Metallurgical Transactions A 15 (1):173-181

52. Frank DJ (2002) Power-constrained CMOS scaling limits. IBM Journal of Research and Development 46 (2.3):235-244

53. Theis TN, Solomon PM (2010) In quest of the “next switch”: prospects for greatly reduced power dissipation in a successor to the silicon field-effect transistor. Proceedings of the IEEE 98 (12):2005-2014

54. Dimoulas A, Toriumi A, Mohney SE (2009) Source and drain contacts for germanium and III–V FETs for digital logic. MRS bulletin 34 (07):522-529

55. Sands T, Palmstrøm C, Harbison J, Keramidas V, Tabatabaie N, Cheeks T, Ramesh R, Silberberg Y (1990) Stable and epitaxial metal/III-V semiconductor heterostructures. Materials Science Reports 5 (3):99-170

56. Murakami M, Koide Y (1998) Ohmic contacts for compound semiconductors. Critical reviews in solid state and materials sciences 23 (1):1-60

57. Chueh Y-L, Ford AC, Ho JC, Jacobson ZA, Fan Z, Chen C-Y, Chou L-J, Javey A (2008) Formation and Characterization of NixInAs/InAs Nanowire Heterostructures by Solid Source Reaction. Nano Letters 8 (12):4528-4533

58. Liu C-H, Chen S-Y, Chen C-Y, He J-H, Chen L-J, Ho JC, Chueh Y-L (2011) Kinetic growth of self-formed In2O3 nanodots via phase segregation: Ni/InAs system. ACS nano 5 (8):6637-6642

59. Chen S-Y, Wang C-Y, Ford AC, Chou J-C, Wang Y-C, Wang F-Y, Ho JC, Wang H-C, Javey A, Gan J-Y (2013) Influence of catalyst choices on transport behaviors of InAs NWs for high-performance nanoscale transistors. Physical Chemistry Chemical Physics 15 (8):2654-2659

60. Schusteritsch G, Hepplestone SP, Pickard CJ (2015) First-principles structure determination of interface materials: The Ni x InAs nickelides. Physical Review B 92 (5):054105

61. Oxland R, Chang S, Li X, Wang S, Radhakrishnan G, Priyantha W, van Dal M, Hsieh C, Vellianitis G, Doornbos G (2012) An Ultralow-Resistance Ultrashallow Metallic Source/Drain Contact Scheme for III–V NMOS. Electron Device Letters, IEEE 33 (4):501-503

62. Ogawa M (1980) Alloying reaction in thin nickel films deposited on GaAs. Thin Solid Films 70 (1):181-189

63. Lahav A, Eizenberg M, Komem Y (1986) Interfacial reactions between Ni films and GaAs. Journal of Applied Physics 60 (3):991-1001

64. Palmstrom C (1988) Lateral diffusion in Ni-GaAs couples investigated by transmission electron microscopy. J Mater Res 3 (6)

65. Guérin R, Guivarc’ h A (1989) Metallurgical study of Ni/GaAs contacts. I. Experimental determination of the solid portion of the Ni‐Ga‐As ternary‐phase diagram. Journal of applied physics 66 (5):2122-2128

66. Guivarc’h A, Guérin R, Caulet J, Poudoulec A, Fontenille J (1989) Metallurgical study of Ni/GaAs contacts. II. Interfacial reactions of Ni thin films on (111) and (001) GaAs. Journal of applied physics 66 (5):2129-2136

67. Appenzeller J, Knoch J, Tutuc E, Reuter M, Guha S (2006) Dual-gate silicon nanowire transistors with nickel silicide contacts. Electron Devices Meeting (IEDM):1-4

68. Katsman A, Yaish Y, Rabkin E, Beregovsky M (2010) Surface Diffusion Controlled Formation of Nickel Silicides in Silicon Nanowires. Journal of Elec Materi 39 (4):365-370

69. Dellas NS, Abraham M, Minassian S, Kendrick C, Mohney SE (2011) Kinetics of reactions of Ni contact pads with Si nanowires. Journal of Materials Research 26 (17):2282-2285

70. Chen L, Wu W (2010) In situ TEM investigation of dynamical changes of nanostructures. Materials Science and Engineering: R: Reports 70 (3):303-319

71. Chou Y-C, Wu W-W, Cheng S-L, Yoo B-Y, Myung N, Chen LJ, Tu KN (2008) In-situ TEM Observation of Repeating Events of Nucleation in Epitaxial Growth of Nano $CoSi_2$ in Nanowires of Si. Nano Letters 8 (8):2194-2199

72. Lim K-Y, Lee H, Ryu C, Seo K-I, Kwon U, Kim S, Choi J, Oh K, Jeon H-K, Song C Novel stress-memorization-technology (SMT) for high electron mobility enhancement of gate last high-k/metal gate devices. In: Electron Devices Meeting (IEDM), 2010 IEEE International, 2010. IEEE, pp 10.11. 11-10.11. 14

73. Yamaguchi T, Kashihara K, Kudo S, Tsutsumi T, Okudaira T, Maekawa K, Hirose Y, Asai K, Yoneda M (2010) Characterizations of NiSi2-Whisker Defects in n-Channel Metal–Oxide–Semiconductor Field-Effect Transistors with< 110> Channel on Si (100). Japanese Journal of Applied Physics 49 (12R):126503

74. Tang W, Picraux ST, Huang JY, Gusak AM, Tu K-N, Dayeh SA (2013) Nucleation and Atomic Layer Reaction in Nickel Silicide for Defect-Engineered Si Nanochannels. Nano Letters 13 (6):2748-2753

75. Dayeh S, Gin A, Picraux S (2011) Advanced core/multishell germanium/silicon nanowire heterostructures: Morphology and transport. Applied Physics Letters 98 (16):163112

76. King T-J (2005) Taking silicon to the limit: Challenges and opportunities. Electrochemical Society Interface:39

77. Léonard F, Talin AA (2011) Electrical contacts to one-and two-dimensional nanomaterials. Nature Nanotechnology 6 (12):773-783

78. Chen R, Jungjohann KL, Mook WM, Nogan J, Dayeh SA (2017) Atomic Scale Dynamics of Contact Formation in the Cross-Section of InGaAs Nanowire Channels. Nano letters 17 (4):2189-2196

79. Taur Y, Ning TH (2013) Fundamentals of modern VLSI devices. Cambridge university press,

80. Crowell C, Rideout V (1969) Normalized thermionic-field (TF) emission in metal-semiconductor (Schottky) barriers. Solid-State Electronics 12 (2):89-105

81. Berger H (1972) Contact resistance and contact resistivity. Journal of the Electrochemical Society 119 (4):507-514

82. Hu J, Liu Y, Ning C-Z, Dutton R, Kang S-M (2008) Fringing field effects on electrical resistivity of semiconductor nanowire-metal contacts. Applied Physics Letters 92 (8):083503

83. Léonard F, Talin AA (2006) Size-dependent effects on electrical contacts to nanotubes and nanowires. Physical review letters 97 (2):026804

84. Nguyen B-M, Taur Y, Picraux ST, Dayeh SA (2014) Diameter-independent hole mobility in Ge/Si core/shell nanowire field effect transistors. Nano letters 14 (2):585-591

85. Lin Y-C, Lu K-C, Wu W-W, Bai J, Chen LJ, Tu KN, Huang Y (2008) Single Crystalline PtSi Nanowires, PtSi/Si/PtSi Nanowire Heterostructures, and Nanodevices. Nano Letters 8 (3):913-918

86. Burchhart T, Lugstein A, Hyun Y, Hochleitner G, Bertagnolli E (2009) Atomic scale alignment of copper-germanide contacts for ge nanowire metal oxide field effect transistors. Nano letters 9 (11):3739-3742

87. Mongillo M, Spathis P, Katsaros G, Gentile P, Sanquer M, De Franceschi S (2011) Joule-assisted silicidation for short-channel silicon nanowire devices. ACS nano 5 (9):7117-7123

Chapter 2: Size and Orientation Effects on the Kinetics and Structure of Nickelide Contacts to InGaAs Fin Structures

2.1 Introduction

Advanced semiconductor devices that employ geometric scaling for performance enhancement encounter size effects, which emerge at nanometer scales, and crystal orientation effects that can dominate their physical properties and govern their performance.[1,2] As been discussed in chapter 1, an important aspect of ultra-scaled devices is the phase transformation that accompanies the formation of metal-semiconductor compound contacts to semiconductor channels which has critical fabrication and low resistance ohmic contact requirements.[3] These compound contacts are particularly important for new channel materials or materials with renewed interest in nanoscale architectures, such as Indium Gallium Arsenide (InGaAs)[4] in a Fin or nanowire geometry, which has been touted as a replacement channel material for sub-10 nm technology nodes.[5,6] The development of ultra-scaled InGaAs devices calls for a detailed investigation that can reveal the influence of crystal orientation and size effects on the kinetics of formation, phase, and structural characteristics of compound contacts to InGaAs Fin/nanowire channels.

Compound contacts to III-V channels have been well studied for planar geometries.[7-10] Recent efforts fueled with the desire to develop a suitable self-aligned contact to III-V channels, analogous to saliside (self-aligned silicide) contacts to Si channels, have introduced the Ni-InGaAs compound contact, conventionally named as

Nickelide, as a serious candidate.[11,12] The nickelide contact has a number of attributes that satisfies the stringent requirements for S/D contact technology. First, the nickelide contact is reproducible and stable where the Ni and InGaAs reaction starts at ~ 230 °C, meeting a good thermal budget, and the formed phase is thermally stable between 350 °C and 450 °C.[13] During the formation of crystalline nickelide, Ni is found to be the diffusing species, which provides the feasibility to form metal contact to ultra-thin body devices with controlled Ni supply.[14] Second, the nickelide contact possesses a low specific contact resistance (4×10^{-8} Ω-cm^2)[15] accompanied with a low sheet resistance (20-25 Ω/square)[16,17], and a low Schottky barrier height (SBH)[18-20] to the InGaAs channel. Third, the nickelide contact can be self-aligned to the S/D regions through the selective etching of excess Ni by concentrated HCl,[21] allowing ease of processing to achieve ultra-short nm scale channel lengths[22]. At nanoscale dimensions with Fin and nanowire architectures, the nickelide phase, the epitaxial relationship with InGaAs layer, and the kinetic and thermodynamic effects that are size and orientation dependent and are yet to be determined.

2.2 Summary of Results

This work focuses on nickelide phase formation in $In_{0.53}Ga_{0.47}As$ Fin structures under the influence of a rapid thermal annealing (RTA) process. We observed a strong dependence of the morphology of the formed nickelide segments on the Fin orientation as well as the Fin width. Through systematic studies of different annealing times, temperatures, and Fin widths, we found that the nickelide contact growth behavior is

diffusion-limited and developed a Fin-specific kinetic competition model that strongly agrees with our experimental findings. As the Fin width increased, we observed a transition from a surface diffusion-limited growth to a volume diffusion-limited growth. We carried out detailed transmission electron microscopy (TEM) characterizations of the nickelide phase and interfacial crystalline relationship and developed a crystalline model that explains the uniaxial anisotropic volume expansion of the nickelide contacts observed in experiment. Further, we utilized the cross-sectional TEM images to determine the strain distribution in the channel and relate it to the energy band-edge profiles in the transport direction. These extensive kinetic and structural investigations provide a comprehensive framework to understand and control the formation of nickelide/InGaAs Fin contacts and may inspire new contact engineering opportunities to enhance transport in nickelide-contacted InGaAs channels.

2.3 Experiment

2.3.1 Integration of InGaAs on insulator on Si

Our studies started with a 50 nm $In_{0.53}Ga_{0.47}As$ film on insulator on Si substrate that is accomplished with a novel solid-state wafer bonding approach that we developed in our laboratory as schematically illustrated in **Figure 2.1**.[23]

A 50 nm undoped $In_{0.53}Ga_{0.47}As$ film was MBE grown on (001) InP (by Intelligent Epitaxy Inc., Richardson, Texas). Firstly, 12 nm thick HfO_2 layer was deposited by atomic layer deposition (ALD) on top of the $In_{0.53}Ga_{0.47}As$ layer. This HfO_2 layer can improve the

adhesion to the InGaAs surface and acts as an HF etch stop layer in subsequent processes. Then, a 200 nm thick SiO_2 was grown on top of the HfO_2 layer with a Trion plasma enhanced chemical-vapor-deposition (PECVD) system, followed by 20nm Ti and 100 nm Ni deposition using e-beam evaporation. This sample was then brought in contact with the oxide-free Si sample surface, and the bonding was achieved by applying pressure and thermal annealing at 400 °C for 10 min through a solid-state reaction between Ni atop the dielectric/InGaAs/InP stack and Si wafer to form NiSi. After the wafer bonding, the InP layer was first thinned down by lapping to ~ 100 mm, and then fully removed by selective wet etching with respect to InGaAs in HCl (3:1 diluted in DI H_2O). This integration approach can eliminate the substrate influence (reaction) during thermally driven compound contact formation to III-V channels, and additionally provides a platform to complement and combine the high-performance III-V devices with low-cost Si circuitry underneath.

2.3.2 Fabrication of Horizontal Lying InGaAs Fins

The Fin structures are patterned on top of the $In_{0.53}Ga_{0.47}As$ layer utilizing a 100kV e-beam writer (JEOL JBX-6300FS) with beam size ~ 10 nm. Negative e-beam resist, hydrogen silsesquioxane (HSQ XR-1541–004), was used as the etch mask for a Cl_2/N_2 composite reactive ion etch (RIE)/inductive coupled plasma (ICP) etch of the $In_{0.53}Ga_{0.47}As$ Fin channels. After the RIE/ICP etching step, HSQ atop the Fins is removed with three consecutive cycles of O_2 plasma treatment followed by a short diluted HF dip, which also reduces the plasma-induced surface damage and smoothens the InGaAs surface. During this

surface conditioning process, the height of $In_{0.53}Ga_{0.47}As$ Fin was found to reduce from 50nm to 40nm. A 200 nm Ni film was then evaporated at the two ends of the Fin structures. The nickelide formation was controlled by RTA in the temperature range from 250 °C to 300 °C.

2.3.3 TEM samples preparation with focused ion beam (FIB) milling

The surface topographical measurements were performed with an atomic force microscope (AFM, DI Veeco), and the crystal structure of nickelide phase was characterized by an FEI Tecnai F30 transmission electron microscope (TEM). Cross-sectional lamellas across the Fin length and Fin cross-section were prepared with focused ion beam (FIB, FEI Nova 600) milling and Ar ion post cleaning (Fischione Model 1010 ion mill).

During the TEM samples preparation (shown in **Figure 2.2**), a 500nm wide (limited by the positioning accuracy during FIB milling) $In_{0.53}Ga_{0.47}As$ Fin was fabricated along [110] orientation. Ni pads were deposited at two ends to provide Ni source for nickelide formation. Extended Ni bars were used as an alignment marker for position-controlled FIB milling. Prior to FIB milling, 400nm SiO_2 and 50nm Pt were deposited atop the sample to prevent damage of interested area under ion beams. The FIB and in-situ lift-out (INLO) process utilized here follow conventional procedures[24,25], in which a 30 dKeV Ga beam was used for rough milling and reduced voltage (5KeV) was used for fine milling. Samples were further cleaned with low angle Ar ion milling.

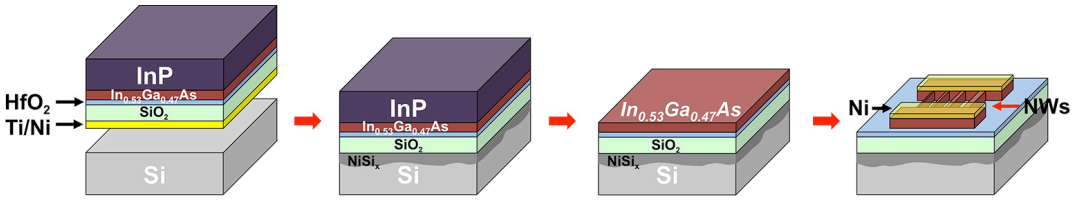

Figure 2.1. Schematic illustration of the fabrication procedure of $In_{0.53}Ga_{0.47}As$ Fin channels on insulator on Si.

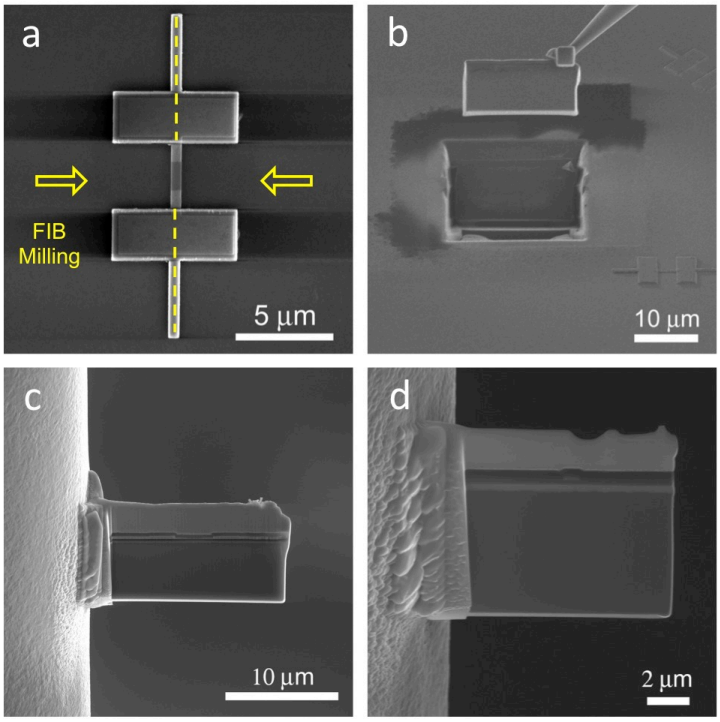

Figure 2.2. SEM images showing the preparation procedure for cross-sectional TEM analysis using FIB and INLO. (a) A 500 nm $In_{0.53}Ga_{0.47}As$ Fin structure with nickelide formation. The Ni bars at two ends were used as an alignment marker for position-controlled FIB milling along the channel direction. (b) The FIB cut lamella was transferred from home substrate to the copper TEM grid. TEM samples were prepared both along the Fin orientation (c) and perpendicular to the Fin orientation (d).

2.4 Results and Discussions

2.4.1 Orientation-Dependent Nickelide Contact Morphologies

Proper investigation of the Nickelide formation mandated the fabrication of the InGaAs Fins in fixed crystallographic orientations. During the wafer-bonding step, the (001) $In_{0.53}Ga_{0.47}As$ /InP was aligned with (001) Si substrate along the cleavage edges that are <110> oriented. The Fin structures were then defined by EBL with <110> orientation parallel to the cleavage edge and <100> orientation rotated 45° with respect to the cleavage edge. These orientations were further validated by detailed TEM characterization, where the misalignment to these crystallographic orientations were within an upper limit of ± 1° for all investigated samples. For both orientations, the Fin heights were 40nm and Fin widths were varied from 30nm to 500nm, with 10nm increment for sub-100nm Fins and 50nm for Fins with 100nm-500nm widths. **Figure 2.3** (a) and (b) show scanning electron microscope (SEM) images of the Ni on $In_{0.53}Ga_{0.47}As$ Fins subjected to an RTA treatment at 250 °C for 20 min for <110> and <100> orientations, respectively. It can be readily observed that the nickelide extension into the $In_{0.53}Ga_{0.47}As$ channels is strongly dependent on the Fin width and that the nickelide and $In_{0.53}Ga_{0.47}As$ segment widths are similar (no lateral nickelide volume expansion). In addition, the nickelide interface is flat for a <110> orientation, and is rough for <100> orientation. AFM topographical measurements shown in **Figure 2.3** (c) and (d) show that the volume expansion is predominant in the vertical <001> direction normal to the substrate surface with a height increase from 40 nm in unreacted regions to around ~ 50 nm-56 nm in nickelide reacted regions. The rough nickelide-InGaAs Fin interface is clearly visible in the AFM topography in **Figure 2.3** (d).

The origin of these dependencies will be further elucidated with the kinetic and structural characterization of nickelide reacted Fins.

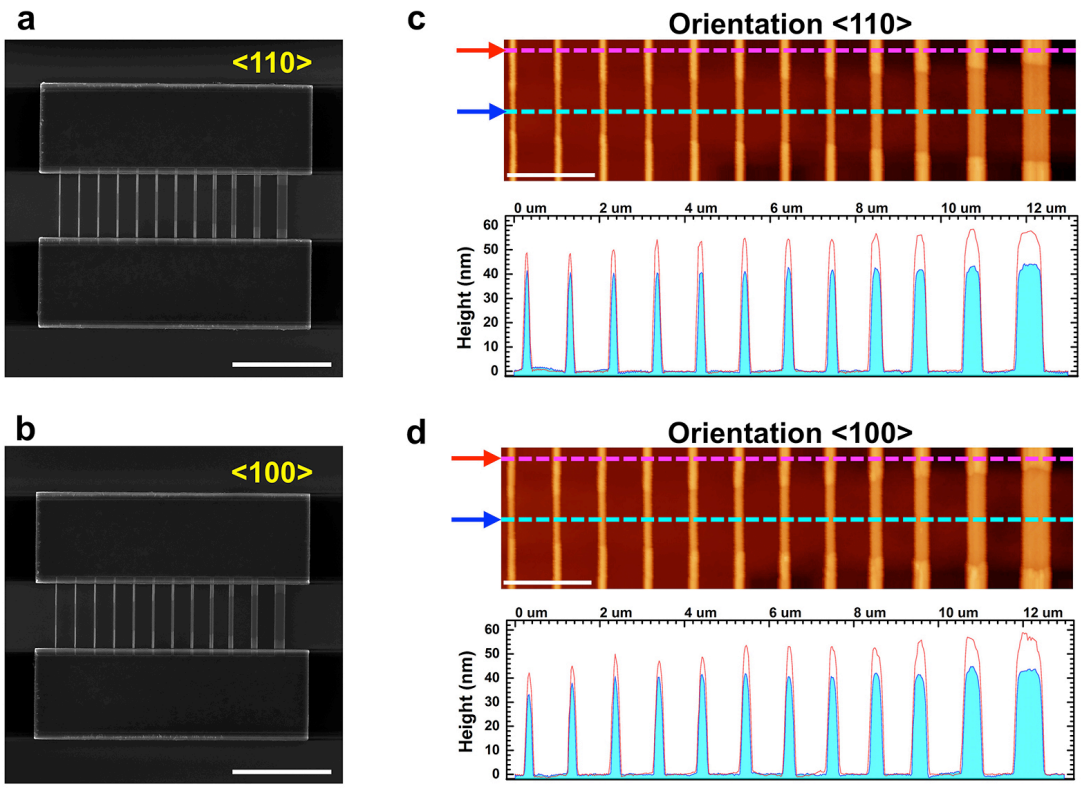

Figure 2.3. Nickelide formation in $In_{0.53}Ga_{0.47}As$ Fin channels. (a)-(b) SEM images illustrating the size-dependent and orientation dependent morphologies for nickelide contacts with $In_{0.53}Ga_{0.47}As$ Fin channels pre-defined in <110> and <100> orientations, respectively. Scale bars are 5 mm. (c)-(d) AFM topography plots of nickelide-InGaAs Fin channels. Scale bars are 2 mm. The brighter portions in the topography images are volume-expanded nickelide regions. The height profiles for nickelide segments (red) and non-reacted $In_{0.53}Ga_{0.47}As$ segments (turquoise), corresponding to the color-marked line cuts, are shown below. The nickelide segments were found to have an increased height of 33% ± 5%. The height profiles don't represent real aspect ratios of each Fin structure, as the units of two axes are different.

2.4.2 Size-Dependent Ni Surface-Diffusion Dominant Kinetic Process

To delve into the details of the Ni and InGaAs reaction, we systematically studied the kinetics of nickelide formation as a function of time (2 min to 95 min) and Fin width (30nm - 500nm) – with a fixed Fin length of 3 mm – for <110> and <100> orientations. The measurements for nickelide lengths and widths were performed post RTA by SEM on 10 Fin sets per single data point to attain average and standard deviation lengths. This procedure was performed multiple times on the same sample for different reaction times in order to avoid sample-to-sample variations. The time-dependent nickelide segment lengths are shown in **Figure 2.4** (a) and (b), with three selected Fin widths and the reference planar film. In both <110> and <100> oriented Fins, the nickelide phase grew faster in narrower Fins and slowest in the planar film. Despite of the slightly larger deviation in measurements for 30nm Fin and at a fixed temperature of 250 °C, the nickelide length as a function of time, t, is well described by a hyperbolic ($t^{1/2}$) dependence. This is further validated at three different temperatures (250 °C, 270 °C, and 300 °C) in **Figure 2.4** (c) and (d), where the nickelide lengths versus $t^{1/2}$ for the narrowest (30nm, **Figure 2.4** (c)) and for the widest (500nm, **Figure 2.4** (d)) displayed linear characteristics for both orientations with a slightly longer nickelide segments for <110> oriented Fins. This $t^{1/2}$ dependence of nickelide growth is characteristic of Ni-diffusion limited growth and was previously observed in nickelide formation in InAs nanowires[26], in GaAs thin films[27], and in nickel silicidation in Si nanowires[28,29]. The insets of **Figure 2.4** (a) and (b) demonstrate an incubation time that is also size dependent for $In_{0.53}Ga_{0.47}As$ Fins and the absence of an incubation time for planar reference films indicating different diffusion paths for the two cases. Next, we will validate that the nickelide growth is surface-diffusion limited in

$In_{0.53}Ga_{0.47}As$ Fins which should explain the faster incubation times for smaller Fins (surface collection area/growth cross-section increases as Fin width decreases) and that volume diffusion of Ni into the growth front in planar films should not encounter any significant incubation time.

The top-down processed Fin structures in our studies present an ideal platform for studying compound metal contact formation with nanoscale channels at precisely defined widths and crystallographic orientations, in contrast to lesser control over such parameters in devices made on vapor-liquid-solid grown nanowires that have been subject to similar studies. For instance, depending on whether or not the Ni pads are in intimate contact with the Si nanowire surface, the kinetics of nickel silicide growth could be dominated by Ni source supply or by Ni diffusion along the silicide segments.[30] The size of nanowires was also found to influence the reaction kinetics, as the diffusion limited process takes over interfacial-reaction limited one in smaller nanowires at elevated temperatures.[31] Even in the Ni diffusion dominant kinetic process, debate still exists in whether Ni diffusion is primarily along the nanowire surface or through its body.[32,33]

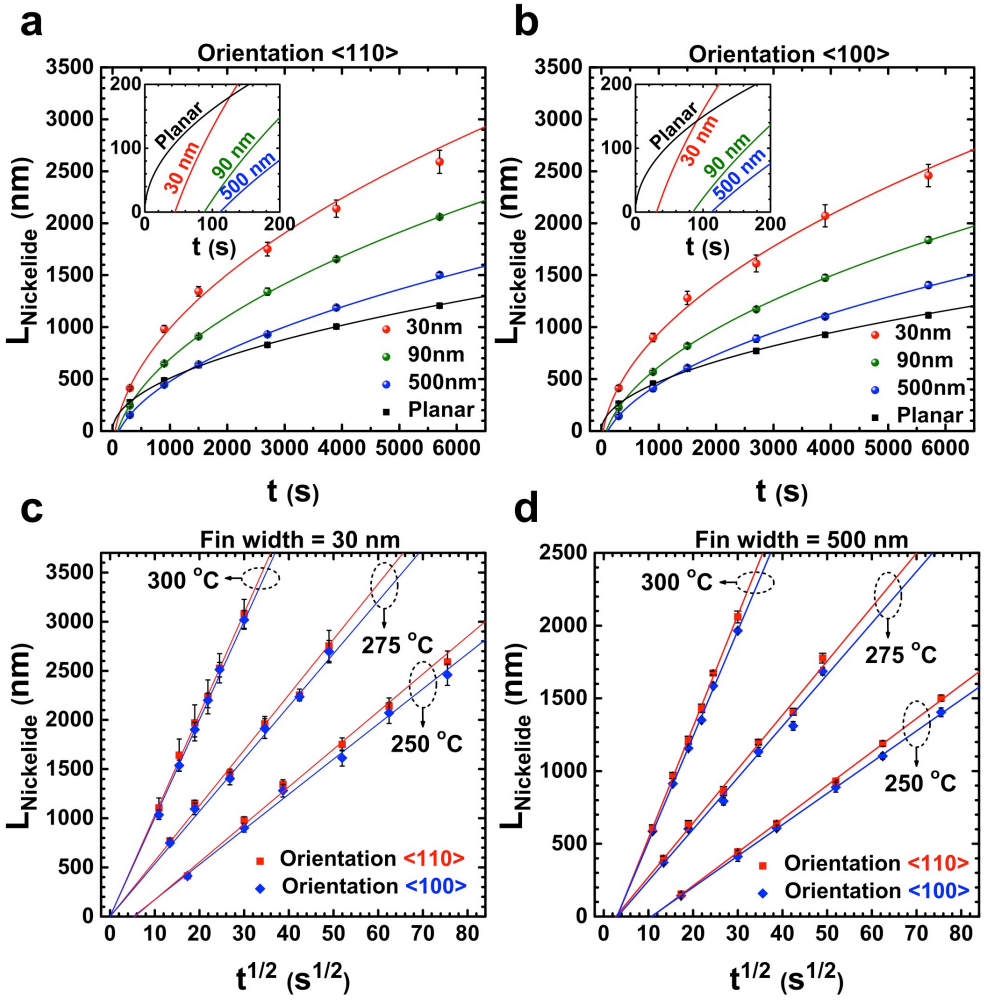

Figure 2.4. Time-dependence of nickelide phase formation. (a) and (b) The length of nickelide segments versus annealing time at 250 °C for <110> and <100> Fin orientations, respectively. In both orientations, the data were well fitted with $t^{1/2}$ dependencies. The insets display $L_{Nickelide}(t)$ for short reaction times where the non-zero intercept indicates an incubation time that is also size dependent. (c) and (d) $L_{Nickelide}(t^{1/2})$ at three different temperatures for 30nm and 500nm Fin widths, respectively. In all cases, the nickelide segment is longer in the <110> orientation.

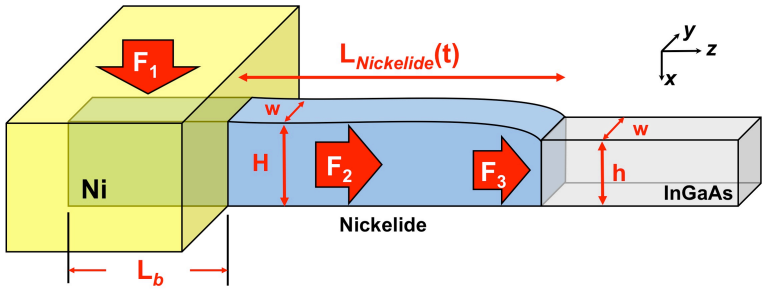

Figure 2.5. A schematic illustration of the rate-limiting processes involved in nickelide formation in InGaAs Fin channel. F_1 is the flux of Ni dissolved from the Ni reservoir to the Fin channel with an effective length, L_b, beneath the Ni pad. F_2 represents the flux of Ni diffusing through the reacted nickelide segment. F_3 is the flux of Ni that will react with fresh InGaAs at the nickelide/InGaAs interface. Due to volume expansion to the Fin channel, the height of InGaAs Fin increases from h to H after nickelide formation. Negligible lateral expansion was observed from AFM measurements, so the Fin width is fixed here as w.

To shed light on the nickelide formation mechanism, we extended previous kinetic models for the reaction of Ni with Si nanowires[29,3] and took account for our Fin-specific rectangular structures and the incurred volume expansion in reacted regions. As shown in **Figure 2.5**, the mass transport of Ni atoms during the nickelide growth involves three steps: (1) Ni dissolution across the Ni/nickelide interface, (2) Ni diffusion along the formed nickelide segment, and (3) Ni and InGaAs reaction at the nickelide/InGaAs interface. The fluxes of Ni atoms in the above three processes can be expressed as:

$$F_1 = k_{dissolve}(C^{eq}_{Ni/Nickelide} - C_0)\cdot(w+2H)\cdot L_b \tag{1-1}$$

$$F_2 = -D_{Ni}\frac{C_L - C_0}{L_{Nickelide}(t)}\cdot X \qquad X = \begin{cases} H\cdot w & Volume\ Diffusion \\ 2(H+w)\cdot\delta & Surface\ Diffusion \end{cases} \tag{1-2}$$

$$F_3 = k_{growth}(C_L - C^{eq}_{Nickelide/InGaAs})\cdot hw \tag{1-3}$$

where $k_{dissolve}$ and k_{growth} are the interfacial reaction rate constants for Ni dissolution into nickelide and for nickelide growth at the reaction front with InGaAs, respectively. At these two interfaces, $C^{eq}_{Ni/Nickelide}$ and $C^{eq}_{Nickelide/InGaAs}$ denote the equilibrium Ni concentrations. C_0 and C_L are the equilibrium Ni concentrations inside the formed nickelide segment, at zero-length position and at a reacted-length position, $L_{Nickelide}(t)$. The flux of Ni atoms diffusing along the formed nickelide segment, F_2, depends not only on the diffusion coefficient of Ni species, but also on the diffusion cross-section X. The diffusion cross-section describes the diffusion path of Ni atoms, with $H \cdot w$ for volume (bulk-like) diffusion and $2(H+w)\cdot\delta$ for surface diffusion, where δ is the thickness of high-diffusivity surface layer, taken conventionally to be one atomic layer high.

By solving the steady-state equation, $F_1 = F_2 = F_3 = F$, F is given by:

$$F = \frac{C^{eq}_{Ni/Nickelide} - C^{eq}_{Nickelide/InGaAs}}{\frac{1}{k_{dissolve}\cdot(w+2H)\cdot L_b} + \frac{L_{Nickelide}(t)}{D_{Ni}\cdot X} + \frac{1}{k_{growth}\cdot hw}} \tag{1-4}$$

The three terms in the denominator represent three rate-limiting mechanisms. In order to solve this equation, the mass conservation of Ni atoms should be considered as follows:

$$Hw\cdot\frac{dL_{Nickelide}(t)}{dt} = F\cdot\frac{M_{Nickelide}}{N_A\cdot\rho_{Nickelide}} \tag{1-5}$$

If these three rate-limiting mechanisms are separately considered, the solutions are given in **Table 2.1** (detailed derivation in ***Appendix I***). From **Table 2.1**, we can find that in both Ni source supply limit and the interfacial kinetic reaction limits, the length of

nickelide segment ($L_{Nickelide}$) is linearly proportional to the annealing time t , which contradicts the experimentally observed $t^{1/2}$ dependence in **Figure 2.4**. This suggested that the nickelide growth witnessed here in InGaAs Fin channels is dominated by the diffusion step of Ni along the formed nickelide segment. Since the volume-diffusion limited growth doesn't incur Fin geometrical terms in contrast to our observation of faster nickelide growth in narrower Fins (**Figure 2.3**), we conclude that Ni diffuses along the surface of the nickelide segment in the Fin channels, as precisely portrayed in the solution for surface-diffusion limited growth dependence in **Table 2.1**.

Table 2.1. Nickelide growth in InGaAs Fin channels for different rate-limiting steps according to equations (1-1) – (1-5).

rate-limiting step	conditions	solution
Ni source supply limit	$k_{dissolve} \ll k_{growth},\ D_{Ni}$	$L_{Nickelide}(t) = k_{dissolve}(\frac{1}{H}+\frac{2}{w})L_b P \cdot t$
surface-diffusion limit ($X = 2(H+w)\cdot\delta$)	$D_{Ni} \ll k_{dissolve},\ k_{growth}$	$L_{Nickelide}(t) = \sqrt{4PD_{Ni}\delta \cdot \left(\frac{1}{w}+\frac{1}{H}\right)} \cdot t^{1/2}$
volume-diffusion limit ($X = H \cdot w$)	$D_{Ni} \ll k_{dissolve},\ k_{growth}$	$L_{Nickelide}(t) = \sqrt{2PD_{Ni}} \cdot t^{1/2}$
interfacial reaction limit	$k_{growth} \ll k_{dissolve},\ D_{Ni}$	$L_{Nickelide}(t) = k_{growth}\frac{h}{H}P \cdot t$

* Here, $P = M_{Nickelide} \cdot (C^{eq}_{Ni/Nickelide} - C^{eq}_{Nickelide/InGaAs}) / (N_A \cdot \rho_{Nickelide})$

To further validate the surface-diffusion limited process, the length of the nickelide segment must follow a linear dependence as a function of $\sqrt{1/w + 1/H}$ and was shown to be the case at 250 °C in **Figure 2.6** for all annealing times (5, 15, 25, 45, 65, and 95 min) and for both Fin orientations. H here was fixed at 53nm, which was measured as the

average height of the reacted nickelide segment. However, for Fin widths larger than 100nm in <110> orientation and Fin widths larger than 150nm in <100> orientation, a second slope with linear dependence was observed (**Figure 2.6**). The slope differences became more eminent across the two segments of linear fitting for annealing times longer than 25min suggesting that certain factors encumbered the nickelide growth in larger Fin widths that resulted in an overall slower growth than a purely surface-diffusion limited process.

In order to better understand the kinetic process accompanying the nickelide formation for all Fin widths, the length of nickelide segment is plotted against both the time and geometrical factors in **Figure 2.7**. Accounting for both geometric and time dependencies, all experimentally measured data for different annealing times and at a single temperature can be linearly fitted for <110> (**Figure 2.7** (a)) and <100> (**Figure 2.7** (b)) orientations validating the surface-diffusion dominant kinetic process. The non-zero intercept with the x-axis indicates an average incubation behavior of all Fins with 250 °C thermal treatment. However, larger Fin nickelide lengths (left-side data points of each data set, color-labeled) fell below the linear trend, indicating a deviation from the surface-diffusion limited model. Interestingly, these deflected data points gradually extend approaching nickelide lengths obtained from growth in $In_{0.53}Ga_{0.47}As$ thin films (black squares in **Figure 2.7** (a) and (b)). Since metal diffusion in crystalline thin films occurs via interstitial diffusion process (volume-like diffusion)[34], the behaviors of nickelide formation in larger Fins could be described as a gradual deviation from surface-dominant to volume-dominant diffusion limited growth process.

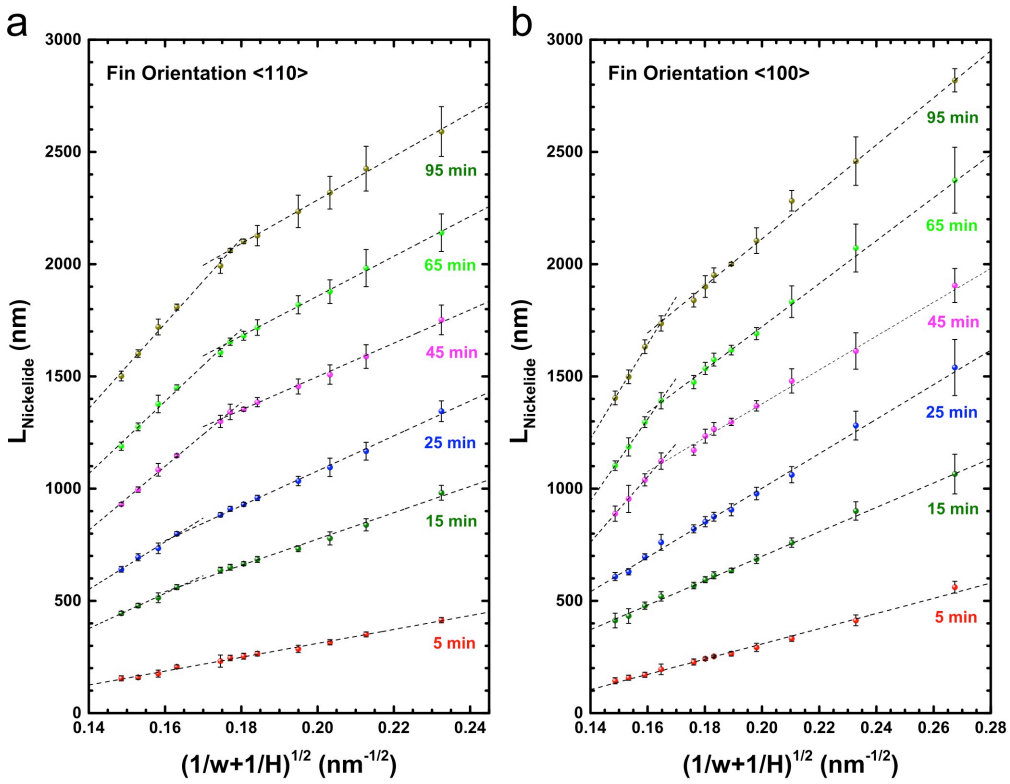

Figure 2.6. Width-dependence of nickelide phase formation. (a) and (b) The length of nickelide segments versus at 250 °C with two different Fin orientations, <110> and <100> respectively. In both orientations, linear fits with two slopes agree well with data measured for each annealing time. The different slopes become more eminent as the annealing time is larger than 25 min. The 'corner' points (deflection points in linear fits) correspond to Fin widths of ~ 100 nm for <110> oriented Fins, and ~ 150 nm for <100> oriented Fins.

The effective surface-diffusion coefficient with Fin-structure measurements, and volume-diffusion coefficient with thin-film measurements, were extracted from **Figure 2.7** (a) and (b) and summarized in **Table 2.2**. One can note from the equation of nickelide growth (**Table 2.1**) that the unit for effective surface-diffusion coefficient is cm^3/s, which excludes the geometric factor, $\sqrt{1/w+1/H}$. For the surface-diffusion coefficients in 30 nm Fins, the values are about one-order of magnitude higher than volume-diffusion coefficients. Moreover, when calculating the surface-diffusion coefficients with infinite Fin width (i.e. $\sqrt{1/w+1/H} \rightarrow \sqrt{1/H}$), the values are still twice as large as those in planar films, validating a distinct Ni diffusion mechanism between Fin structures and thin films. The activation energies were then extracted by using the Arrhenius relationship, $D \propto e^{-E_a/kT}$, for both Fin structures and planar films and in both <110> and <100> orientations (**Figure 2.7** (c) - (f)), where E_a stands for the activation energy, k for Boltzmann's constant, and T is the diffusion temperature. In planar $In_{0.53}Ga_{0.47}As$ films, the calculated activation energy is about 10% larger than in $In_{0.53}Ga_{0.47}As$ Fins.

Table 2.2. Calculated effective surface-diffusion coefficients $D_{Surface}$, excluding the geometric factor $\sqrt{1/w+1/H}$, and volume-diffusion coefficients D_{Volume}, at three different temperatures.

coefficient	orientation	250 °C	275 °C	300 °C
D_{Volume} (10^{-12} cm^2/s)	film <110>	2.59	7.97	28.9
	film <100>	2.24	6.36	23.8
$D_{Surface}$ (10^{-17} cm^3/s)	Fin <110>	2.88 * (1.54×10^{-11} cm^2/s)	6.25 *(3.33×10^{-11} cm^2/s)	24.9 *(13.3×10^{-11} cm^2/s)
	Fin <100>	2.42 *(1.35×10^{-11} cm^2/s)	5.53 *(2.95×10^{-11} cm^2/s)	20.2 *(10.8×10^{-11} cm^2/s)

* The values in parentheses are calculated diffusion coefficients for 30nm fins at corresponding annealing temperatures.

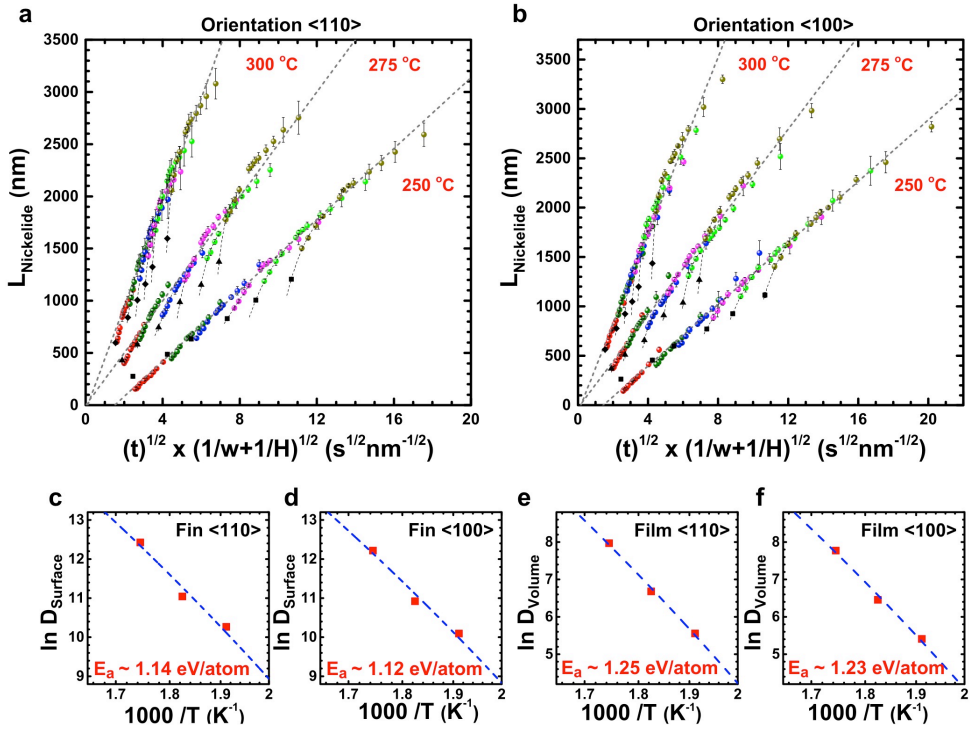

Figure 2.7. Combined plots of nickelide segment length in relation to annealing time and Fin geometrical factors, and extracted kinetic parameters. (a) and (b) $L_{Nickelide}$ versus $\sqrt{t}\cdot\sqrt{1/w+1/H}$ according to the surface-diffusion limited model, at three different growth temperatures and with Fin orientations of <110> and <100> respectively. The data points in black color are nickelide growth in $In_{0.53}Ga_{0.47}As$ thin films, and they were normalized by the factor of $\sqrt{1/H}$ by considering the planar film has an infinite width ($1/w \to 0$). The extracted effective surface-diffusion coefficients $D_{Surface}$ were plotted in semi-logarithmic scale versus inverse temperature to calculate the activation energy of nickelide formation for (c) <110> and (d) <100> oriented $In_{0.53}Ga_{0.47}As$ Fin channels. The extracted volume-diffusion coefficients D_{Volume} were plotted in semi-logarithmic scale versus inverse temperature to calculate the activation energy of nickelide formation for (e) <110> and (f) <100> oriented $In_{0.53}Ga_{0.47}As$ thin films. In these plots, the units for $D_{Surface}$ and D_{Volume} are nm^3/s and nm^2/s, respectively.

With the comprehensive analysis of the kinetics in nickelide formation in $In_{0.53}Ga_{0.47}As$ Fin channels, a deep understanding of the crystalline structure of formed nickelide phases and their interfaces with InGaAs and resultant strains can have far-reaching implications for device performance that utilize such compound contacts. The different crystal phases of compound or alloyed contacts can (1) alter the Schottcky barrier height and contact resistivity;[35-37] (2) strongly influence the reliability of contact properties,[38,39] and (3) induce strain during contact formation that significantly impact the band structure and carrier mobility of the channel material.[40-42] The contact formation in nanoscale channels was proven to be different from that in planar devices[3,43,44,31,45] and can be more sensitive to local microstructures, such as crystalline defects[46] and gate-dielectric layer coatings[44,47].

2.4.3 Crystalline Structure at the Nickelide/InGaAs Interface

Here we carried out the structural analysis for nickelide phase in $In_{0.53}Ga_{0.47}As$ Fin channels and their interfacial correlation. The TEM sample lamellas were prepared with conventional FIB milling with an *in-situ* lift-out (INLO) process[24] (as described in the experimental section), followed by post Ar-ion cleaning that was found essential to remove the FIB damaged surface[25] for clearer imaging. The FIB cut was performed on a 500nm <110> oriented Fin channel, which displayed a flat interface between nickelide and InGaAs segments. As shown in **Figure 2.8** (a), the TEM lamellae of InGaAs was cut along the Fin channel, and the corresponding high resolution TEM (HRTEM) image is shown in **Figure 2.8** (b). The InGaAs phase with zinc blende (ZB) crystal structure was confirmed to be

$In_{0.53}Ga_{0.47}As$ (epitaxially grown on InP) by measuring the lattice constant from fast Fourier transform (FFT) patterns of the HRTEM images.

The HfO_2 layer underneath the $In_{0.53}Ga_{0.47}As$ was found to have monoclinic lattice structure after the thermal process of our wafer bonding at 400 °C. The poly-crystalline nature of this HfO_2 layer didn't seem to induce strain in the $In_{0.53}Ga_{0.47}As$ Fin channels, as no changes of lattice contact for $In_{0.53}Ga_{0.47}As$ has been detected near the interface with HfO_2, which is similar to the case of poly-crystalline HfO_2 formed on Si[48] and GaAs[49]. In order to identify the unknown crystal structure of nickelide phase, the TEM lamellas were cut both along the Fin channel (**Figure 2.8** (c)) and perpendicular to the Fin channel (**Figure 2.8** (d)). The nickelide phase was identified as hexagonal $Ni_4InGaAs_2$ (the slightly stoichiometric difference between In and Ga is not denoted here), where the measured lattice constant agreed well with those reported for Ni reaction with (001) $In_{0.53}Ga_{0.47}As$ film on InP wafer.[50,51] This Ni to As stoichiometric ratio (2:1) was also reported in previous studies of Ni reaction with bulk GaAs.[38,52] The measured lattice constants of $In_{0.53}Ga_{0.47}As$ and $Ni_4InGaAs_2$ are summarized in **Table 2.3**, and the volume expansion after $Ni_4InGaAs_2$ phase formation based on mass conservation was calculated to be ~ 34.2%. This estimated volume expansion agrees well with the height change demonstrated by AFM measurements (**Figure 2.3** (c)-(d)) and further validates that the volume expansion is dominant in the vertical direction, the physical origin of which be discussed in detail next.

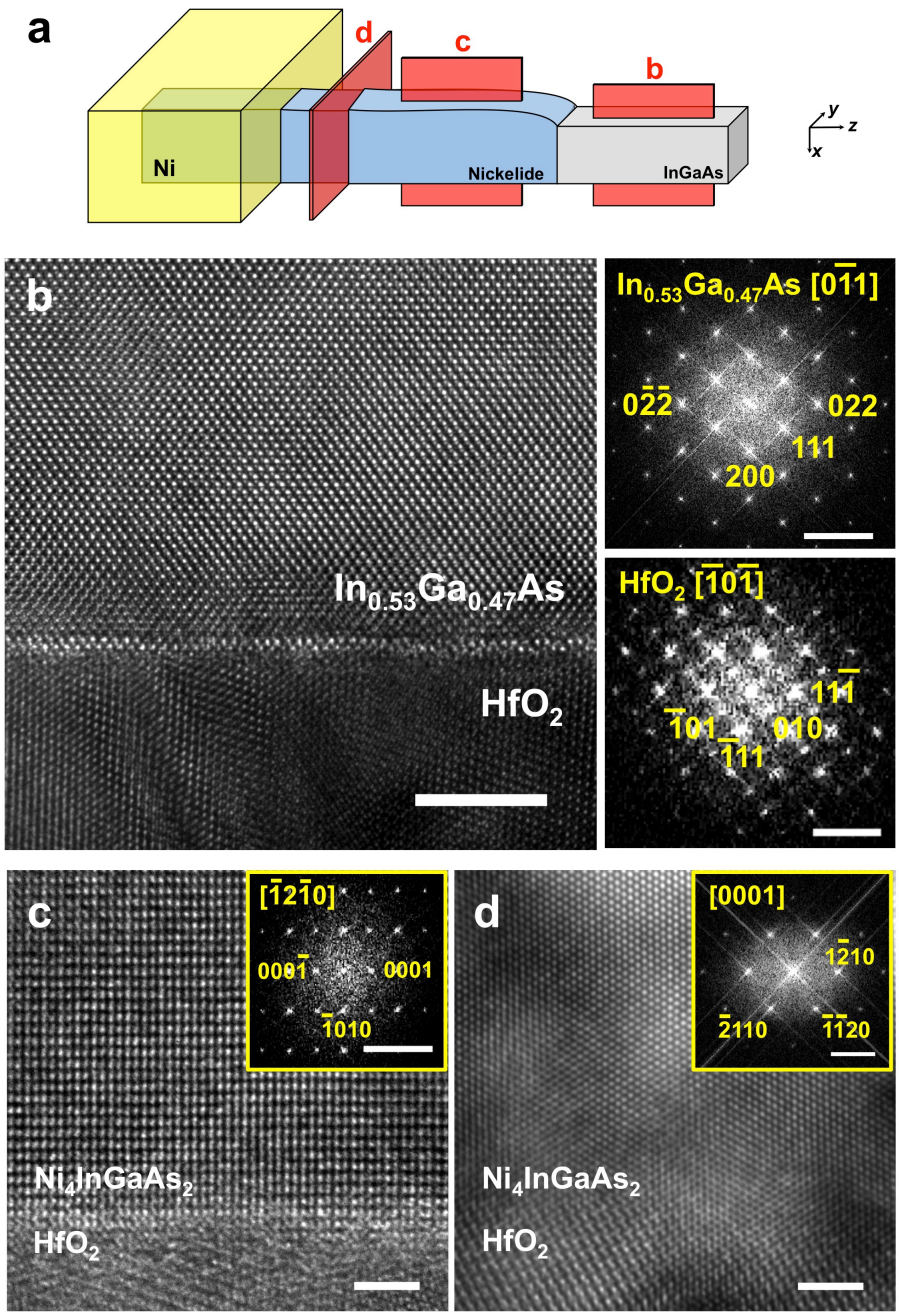

Figure 2.8. Crystal structure analysis of $In_{0.53}Ga_{0.47}As$ and nickelide phases. (a) Schematic illustration of the relative positions of FIB cut lamellas for panels b, c, and d. (b) HRTEM image at the cross-section of the channel for $In_{0.53}Ga_{0.47}As/HfO_2$ and corresponding FFT patterns. The $In_{0.53}Ga_{0.47}As$ composition was confirmed by the lattice constant estimation from the FFT pattern, and the polycrystalline HfO_2 was found to be monoclinic structure. (c)-(d) HRTEM images of nickelide phase with FIB cut lamellas (c) along Fin orientation and (b) perpendicular to the Fin orientation. The nickelide phase was identified as $Ni_4InGaAs_2$ with (0001) plane perpendicular to the Fin orientation. Scale bars are 2 nm for all HRTEM images, and 5 nm^{-1} for all FFT images.

Table 2.3. Summary of the measured lattice constants of $In_{0.53}Ga_{0.47}As$ and $Ni_4InGaAs_2$.

material	lattice structure	literature value	our experiment
$In_{0.53}Ga_{0.47}As$	Zinc Blende (ZB)	a = 5.868 Å	a = 5.88 ± 0.02 Å
$Ni_4InGaAs_2$	Simple Hexagonal	a = 3.96 Å c = 5.16 Å	a = 3.93 ± 0.04 Å c = 5.10 ± 0.03 Å

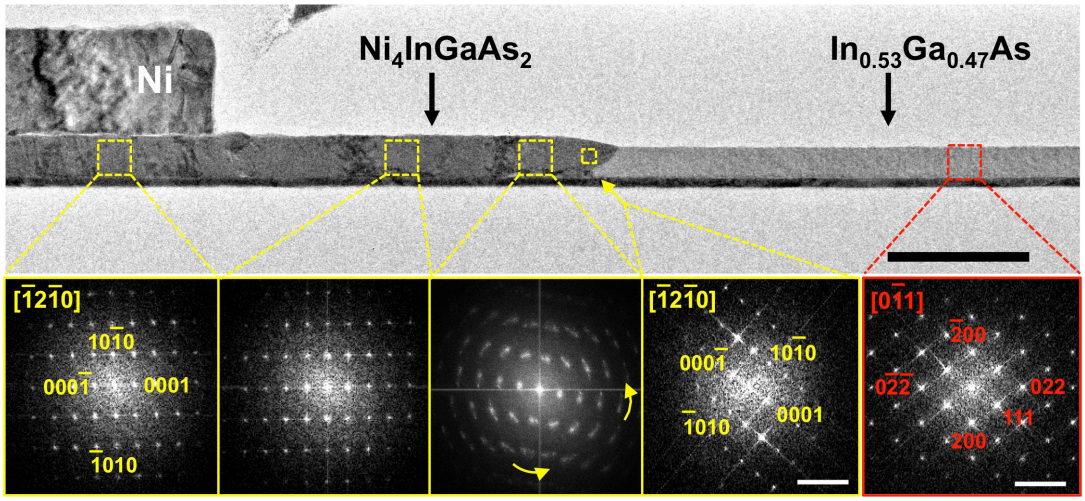

Figure 2.9. Cross-sectional TEM image of a [110] oriented Fin with nickelide formation. The FFT patterns were collected from different regions along the Fin structure. The nickelide FFT and $In_{0.53}Ga_{0.47}As$ FFT are well aligned (details in **Figure 2.10**) at the interface. But away from the interface, there is a gradual rotation of the crystal structure to maintain an equilibrium [0001] nickelide axis parallel to the substrate surface. Scale bars are 200 nm for the TEM image and 5 nm^{-1} for all FFT patterns.

Unlike multiple silicide phases coexisting during the Ni reaction with Si nanochannels, the nickelide segment exhibited a single composition during the Ni and InGaAs solid-state reaction, as shown in **Figure 2.9**. Interestingly, the nickelide crystal undergoes a gradual rotation of the $Ni_4InGaAs_2$ crystal from the reaction interface toward the Ni reservoir. At the nickelide/InGaAs interface, the $Ni_4InGaAs_2$ [0001] direction is aligned with the $In_{0.53}Ga_{0.47}As$ [111] direction. Far away from the interface, the $Ni_4InGaAs_2$ [0001] direction is parallel to the substrate surface and is in the same direction of the [011] Fin channel. The crystal rotation of $Ni_4InGaAs_2$ phase happens within about 200 nm near the nickelide/InGaAs interface, and undergoes a gradual change with defective crystallites (FFT pattern shows continuous arc for each diffraction spot rather than the paired sharp spots for twinned structures). Throughout the whole range of nickelide segment, the zone axis was fixed as $[\bar{1}2\bar{1}0]$, with $Ni_4InGaAs_2$ $[\bar{1}2\bar{1}0]$ || $In_{0.53}Ga_{0.47}As$ $[0\bar{1}1]$. Based on these observations, we speculate that the $Ni_4InGaAs_2$ phase growth starts with the energy preferred epitaxial planar interface of $Ni_4InGaAs_2$ (0001) || $In_{0.53}Ga_{0.47}As$ (111) as is the case for zinc blende or wurtzite III-V semiconductor nanowire growth interfaces,[53-58] and as is reported for Ni reaction with (111) GaAs wafers where Ni_2GaAs (0001) || GaAs (111) interfacial correlation was observed.[38,39] During the continual nickelide formation in InGaAs Fin channels, the $Ni_4InGaAs_2$ away from the interface rotated due to energy-minimization reasons as follows. The rotated $Ni_4InGaAs_2$ crystal away from the interface has its $(10\bar{1}0)$ plane as top surface, which is the preferred facet[59,54] for nanoscale semiconductors with hexagonal structure due to their low surface energy. Further, the [0001] growth axis perpendicular to the growth interface cannot be maintained in such orientation with respect to the $In_{0.53}Ga_{0.47}As$ channel due to the pinned supply of Ni atoms on the

substrate surface (which is not possible to be normal to the slanted nickelide/InGaAs interface). The [0001] growth direction and $(10\bar{1}0)$ facet formation lead to the nickelide segment undergoing a post-growth crystal rotation. The slanted nickelide/InGaAs interfaces were observed in all the prepared TEM samples, and identical morphologies of interfaces were found when nickelide formed from both ends of the Fin channel. From **Figure 2.10** (c), we deduce that the nickelide phase growth follows a layer-by-layer growth sequence from the top surface towards the bottom, as indicated by the yellow arrows in **Figure 2.10** (c). This layer-by-layer growth mechanism, that is observed in experiment to be from top to bottom, leads to an outward volume expansion as observed in **Figure 2.10** (a). These observations suggest that Ni diffusion along the free top surface is faster than that along the nickelide/HfO_2, which leads to a protruded nickelide segment at the top of the $In_{0.53}Ga_{0.47}As$ channel with respect to that near the HfO_2 interface (see **Figure 2.10** (c)).[60]

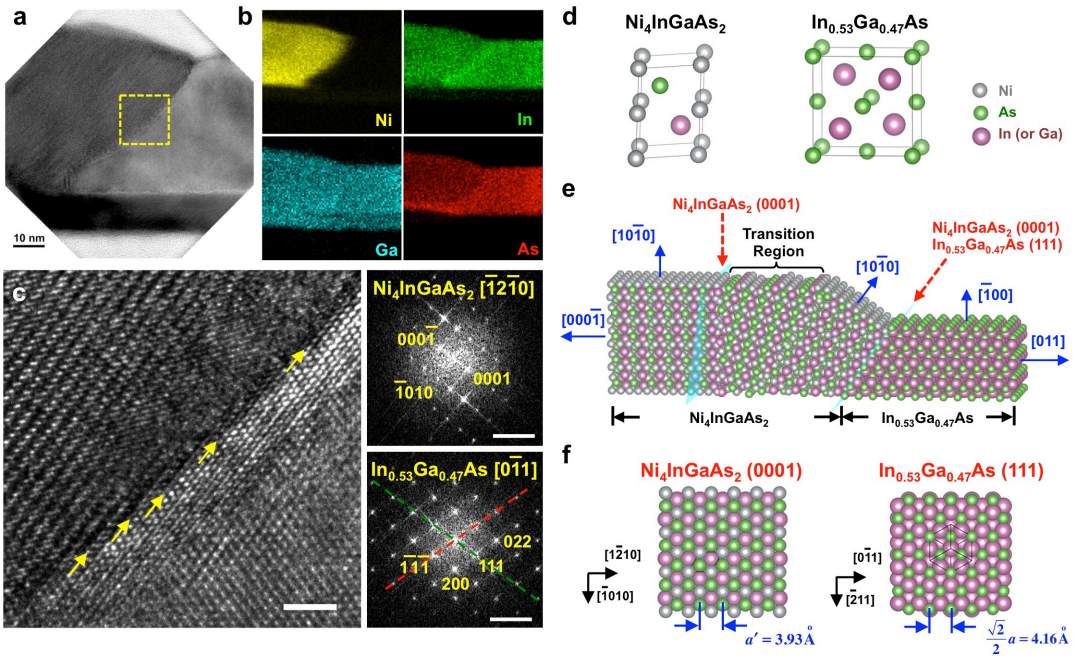

Figure 2.10. TEM characterization and structural analysis of the $Ni_4InGaAs_2/In_{0.53}Ga_{0.47}As$ interface. (a) TEM image of the crystalline structure at the interface. (b) EDX elemental mapping of Ni, In, Ga, and As near the interface. A false Ga signal appears in HfO_2 due to the overlap of Ga (K_α) and Hf (L_β) bands. (c) HRTEM image at the position indicated in yellow square in (a) at the nickelide (dark contrast) InGaAs (bright contrast) interface. The yellow arrows indicate the layered growth of nickelide on a (111) plane of InGaAs from top surface toward interface with HfO_2. Corresponding FFT diffraction patterns show that the (0001) plane of $Ni_4InGaAs_2$ lies in parallel with (111) plane of $In_{0.53}Ga_{0.47}As$. The diffraction spots along $1\bar{1}\bar{1}$ direction (red line) have a slightly different distance than those along 111 direction (green line), indicating the non-uniformity of the in-plane strain and out-of-plane strain. Scale bars are 2 nm for the HRTEM image, and 5 nm^{-1} for all FFT images. (d) Schematic illustration of the simple hexagonal lattice structure of $Ni_4InGaAs_2$ and the zinc blende structure of $In_{0.53}Ga_{0.47}As$. The In and Ga atoms share intermixable locations in the lattice based on their stoichiometric ratio. (e) Atomic stacking that schematically illustrate the crystal relationship between $Ni_4InGaAs_2$ and $In_{0.53}Ga_{0.47}As$. The (0001) $Ni_4InGaAs_2$ plane in parallel with $In_{0.53}Ga_{0.47}As$ (111) plane at the interface, while the $Ni_4InGaAs_2$ (0001) plane in parallel with $In_{0.53}Ga_{0.47}As$ (011) plane far away from the interface. This crystal rotation happens through the formation of a defective transition region. (f) The atomic arrangement in the interfacial plane, for $Ni_4InGaAs_2$ and $In_{0.53}Ga_{0.47}As$ respectively. The hexagonal arrangement of As and In (or Ga) atoms are preserved after nickelide formation, with slight decrease of the distance between two As (or In, Ga) atoms.

The composition of nickelide phase was characterized with the energy-dispersive x-ray (EDX) spectroscopy, and with the elemental mapping under scanning TEM (STEM) mode (**Figure 2.10** (b)). Ni shows an abrupt composition change at the nickelide/InGaAs interface. HRTEM image of the interface (**Figure 2.10** (c)) further validates the $Ni_4InGaAs_2$ (0001) || $In_{0.53}Ga_{0.47}As$ (111) interface. **Figure 2.10** (d)-(e) show the lattice structures for $Ni_4InGaAs_2$ and $In_{0.53}Ga_{0.47}As$, and their crystallographic interfacial relationship. The $Ni_4InGaAs_2$ (0001) and $In_{0.53}Ga_{0.47}As$ (111) interfacial planes have hexagonal atomic arrangements of both As and In (or Ga) atoms for both phases, and that the distance between two As atoms in $Ni_4InGaAs_2$ is 5.6% smaller than that in $In_{0.53}Ga_{0.47}As$. This suggests that during the Ni reaction with $In_{0.53}Ga_{0.47}As$, the As and In (or Ga) atoms keep the close-packed (hexagonal) in-plane arrangement, however, along the $Ni_4InGaAs_2$ [0001] || $In_{0.53}Ga_{0.47}As$ [111] direction, the bonds between As and In (or Ga) are broken and those atoms are separately encaged by Ni atoms. Due to the minimal changes of atomic distances in the interfacial plane, while large separation of atoms is necessary perpendicular to the interfacial plane, the volume expansion mainly happens in the vertical direction normal to the substrate rather than in the lateral direction of Fin channels, as experimentally observed in **Figure 2.3**.

2.4.4 Strain-Induced Energy Band-Edge Structure Near the Interface

We turn now our focus now to the in-plane ($\varepsilon_{\parallel}$) and out-of-plane ($\varepsilon_{\perp}$) strains that have direct influence on the electronic properties of the InGaAs channel. The magnitude and spatial distribution of strain near the InGaAs/nickelide interface shown in **Figure 2.11**

(a)-(d) were obtained from HRTEM utilizing the geometrical phase analysis (GPA) tool[61] within the DigitalMicrograph™(Gatan) package. **Figure 2.11** (a)-(d), the x-axis is selected to be along [111] direction, so the y-axis will be in parallel with the InGaAs (111) interfacial plane. Both of the two strain-tensor components of $In_{0.53}Ga_{0.47}As$, ε_{xx} and ε_{yy}, exhibit negative values near the InGaAs/nickelide interface, indicating a quasi-hydrostatic compressive stress exerted to the $In_{0.53}Ga_{0.47}As$ channel upon nickelide formation. This profile is also validated with another strain mapping, performed along the [011] channel direction. The measured inter-plane spacing along the $In_{0.53}Ga_{0.47}As$ [111] direction from FFT patterns was used to calibrate the $\varepsilon_{\parallel}$ by comparing these values with those measured far from the interface, and the inter-plane spacing along the $[\bar{1}11]$ direction was used to calibrate the $\varepsilon_{\perp}$. Both the $\varepsilon_{\parallel}$ and $\varepsilon_{\perp}$ were measured in multiple locations, from top to bottom surface (with the averaged value shown as one data point in **Figure 2.11** (e)), and from the nickelide/InGaAs interface deep into the $In_{0.53}Ga_{0.47}As$ channel. The $\varepsilon_{\perp}$, introduced by volume expansion, shows a clear trend of relaxation when far from the interface. The $\varepsilon_{\parallel}$, caused by lattice mismatch, exhibits several fluctuations before decreasing to zero. From the trend of $\varepsilon_{\parallel}$, a compressive strain below 3% can be predicted at the nickelide/InGaAs interface. However, this value is smaller than 5.6% (the theoretical lattice mismatch between $In_{0.53}Ga_{0.47}As$ and $Ni_4InGaAs_2$), which is likely to be relaxed by the saw-tooth like steps present at the nickelide/InGaAs interface and the three free surfaces of the $In_{0.53}Ga_{0.47}As$ channel. Under compressive stress from both in-plane and out-of-plane directions, the band structure of $In_{0.53}Ga_{0.47}As$ is significantly altered[62,63], and the strain-

induced shift in band-edge energies can be calculated using well-known elastic theory that incorporates deformation potentials.[64]

Figure 2.11 (f) shows the calculated band-edge energies as a function of distance from the nickelide/InGaAs interface (detailed calculations in ***Appendix II***). The heavy hole (E_{hh}) and light hole (E_{lh}) bands split under the compressive strain, with the E_{hh} slightly higher than E_{lh}, which is different from the conventional cases of uniaxial and bi-axial stresses where band anti-crossing occurs. The E_g gradually increases from the relaxed center of the channel (0.75 eV) toward the strained interface, with a peak value of ~ 1.26 eV at the interface. Such an increase of E_g could lead to an increase in the electron effective mass and reduction of the injection velocities in ultra-scaled sub-10nm channels and may be detrimental for ohmic contact formation with InGaAs Fin channels due to the increased Schottcky barrier height (SBH) with a larger stress-induced bandgap of InGaAs. Possible strategies to mitigate these effects may include the development of heteroepitaxial layers[65] that exert tensile stresses on the Fins/nanowires to zero-balance the strain, and through contact engineering that can allow the formation/piling of higher In composition in InGaAs near the contact region to compensate the stress effects and to lower E_g .

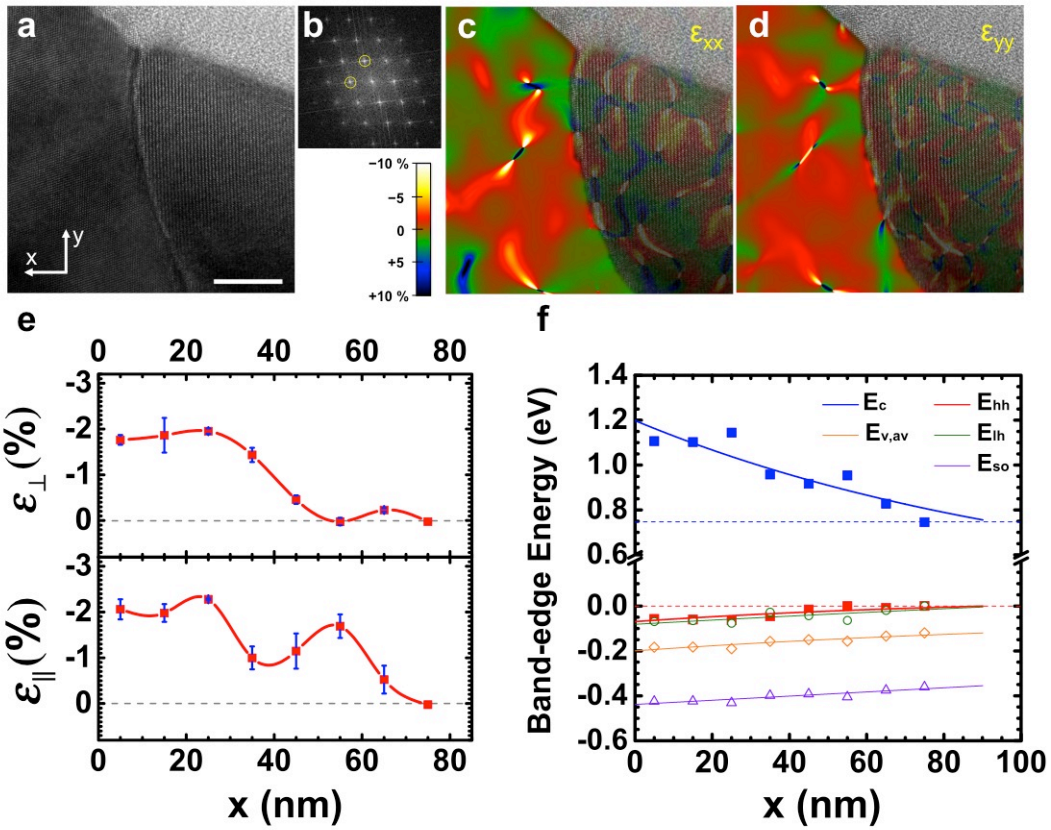

Figure 2.11. Strain induced band-edge shift in $In_{0.53}Ga_{0.47}As$ Fin channels. (a) HRTEM image of a typical InGaAs/nickelide interface, with the $In_{0.53}Ga_{0.47}As$ (111) || $Ni_4InGaAs_2$ (0001) interfacial plane perpendicular to the x direction. Scale bar is 10 nm. (b) The FFT pattern for $In_{0.53}Ga_{0.47}As$ segment (left-side to the interface), and the highlighted two diffraction spots were used for strain mapping. (c) and (d) The mapping of two strain tensor components, ε_{xx} and ε_{yy}, respectively in $In_{0.53}Ga_{0.47}As$ segment. (e) Out-of-plane and in-plane strains of $In_{0.53}Ga_{0.47}As$ as a function of distance from the interface. Those values were calculated by comparing the inter-plane spacing from FFT diffraction patterns (as illustrated in Figure S10, *supporting information*) with the unstrained one. (f) The calculated band-edge energies as a function of distance along x-axis based on elastic theory that incorporates deformation potentials obtained from local-density-functional theory.[64] The estimated bandgap of $In_{0.53}Ga_{0.47}As$ near the InGaAs/nickelide interface is ~ 1.26 eV in this case.

2.5 Conclusions

In summary, this chapter presents the detailed study of solid-state reaction between metal (Ni) and ternary III-V semiconductor ($In_{0.53}Ga_{0.47}As$) nanochannels. Upon nickelide formation, the Fin channel showed a 33% ± 5% height increase with negligible lateral expansion with a flatter interface for <110> oriented Fins compared to <100> ones. Characterization of the nickelide segment lengths as a function of time, temperature and geometrical factors of InGaAs Fin channels, revealed a size-dependent Ni surface diffusion dominant process during the nickelide formation in InGaAs Fin channels that gradually departs to volume diffusion as the Fin width increases. Detailed structural analysis identified the nickelide phase as $Ni_4InGaAs_2$, with $Ni_4InGaAs_2$ $[\bar{1}2\bar{1}0]$ || $In_{0.53}Ga_{0.47}As$ $[0\bar{1}1]$ and $Ni_4InGaAs_2$ (0001) || $In_{0.53}Ga_{0.47}As$ (111), with a peculiar rotation of $Ni_4InGaAs_2$ [0001] axis away from the nickelide/InGaAs interface. The nickelide formation led to both in-plane and out-of-plane compressive strains on the Fin channels that opened up the InGaAs energy band-gap. We believe that these detailed timely observations are likely to benefit the development of self-aligned compound contacts to future electronic devices and inspire new compound contacts and device architectures that can enhance their performance.

Most of chapter 2 was published in *Nano Letters* 2015. R. Chen, S. A. Dayeh. The dissertation author is the first author of this paper.

2.6 References

1. Chau R, Doyle B, Datta S, Kavalieros J, Zhang K (2007) Integrated nanoelectronics for the future. Nature Materials 6 (11):810-812

2. del Alamo JA (2011) The high-electron mobility transistor at 30: impressive accomplishments and exciting prospects. International Conference on Compound Semiconductor Manufacturing Technology:17-22

3. Tang W, Nguyen B-M, Chen R, Dayeh SA (2014) Solid-state reaction of nickel silicide and germanide contacts to semiconductor nanochannels. Semiconductor Science and Technology 29 (5):054004

4. InGaAs is short for InxGa1-xAs, the ternary compound semiconductor that is miscible over the entire compositional range from GaAs (x=0) to InAs (x=1). We will use "InGaAs" in the following text when referening to general InxGa1-xAs cases, while "In0.53Ga0.47As" when discussing the specific parameters in our studies, such as crystal structure, kinetic parameters, energy bandgap, and etc.

5. del Alamo JA (2011) Nanometre-scale electronics with III-V compound semiconductors. Nature 479 (7373):317-323

6. Sanghoon L, Cheng-Ying H, Cohen-Elias D, Thibeault BJ, Mitchell W, Chobpattana V, Stemmer S, Gossard AC, Rodwell MJW (2014) Highly Scalable Raised Source/Drain InAs Quantum Well MOSFETs Exhibiting I_{on}=482μA/μm at I_{off}=100 nA/μm and V_{DD}=0.5V. Electron Device Letters, IEEE 35 (6):621-623

7. Dimoulas A, Toriumi A, Mohney SE (2009) Source and drain contacts for germanium and III–V FETs for digital logic. MRS bulletin 34 (07):522-529

8. Yearsley JD, Lin JC, Hwang E, Datta S, Mohney SE (2012) Ultra low-resistance palladium silicide Ohmic contacts to lightly doped n-InGaAs. Journal of Applied Physics 112 (5):054510

9. Murakami M, Koide Y (1998) Ohmic contacts for compound semiconductors. Critical reviews in solid state and materials sciences 23 (1):1-60

10. Sands T, Palmstrøm CJ, Harbison JP, Keramidas VG, Tabatabaie N, Cheeks TL, Ramesh R, Silberberg Y (1990) Stable and epitaxial metal/III-V semiconductor heterostructures. Materials Science Reports 5 (3):99-170

11. Czornomaz L, El Kazzi M, Caimi D, Machler P, Rossel C, Bjoerk M, Marchiori C, Fompeyrine J Self-aligned S/D regions for InGaAs MOSFETs. In: Solid-State Device Research Conference, 2011. IEEE, pp 219-222

12. Zhang X, Guo H, Lin H-Y, Cheng C-C, Ko C-H, Wann CH, Luo G-L, Chang C-Y, Chien C-H, Han Z-Y, Huang S-C, Chin H-C, Gong X, Koh S-M, Lim PSY, Yeo Y-C

(2011) Self-aligned contact metallization technology for III-V metal-oxide-semiconductor field effect transistors. Journal of Vacuum Science & Technology B: Microelectronics and Nanometer Structures 29 (3):032209. doi:10.1116/1.3592211

13. Czornomaz L, El Kazzi M, Hopstaken M, Caimi D, Mächler P, Rossel C, Bjoerk M, Marchiori C, Siegwart H, Fompeyrine J (2012) CMOS compatible self-aligned S/D regions for implant-free InGaAs MOSFETs. Solid-State Electronics 74:71-76

14. Kim S, Yokoyama M, Taoka N, Iida R, Lee S, Nakane R, Urabe Y, Miyata N, Yasuda T, Yamada H (2011) High Performance Extremely Thin Body InGaAs-on-Insulator Metal-Oxide-Semiconductor Field-Effect Transistors on Si Substrates with Ni-InGaAs Metal Source/Drain. Applied Physics Express 4 (11):4201

15. Abraham M, Yu S-Y, Choi WH, Lee RT, Mohney SE (2014) Very low resistance alloyed Ni-based ohmic contacts to InP-capped and uncapped n+-$In_{0.53}Ga_{0.47}As$. Journal of Applied Physics 116 (16):164506

16. Kim S, Yokoyama M, Taoka N, Iida R, Lee S, Nakane R, Urabe Y, Miyata N, Yasuda T, Yamada H (2010) Self-aligned metal source/drain $In_xGa_{1-x}As$ n-MOSFETs using Ni-InGaAs alloy. Electron Devices Meeting (IEDM):26.26. 21-26.26. 24

17. Zhang X, Guo HX, Gong X, Zhou Q, Yeo Y-C (2012) A Self-Aligned Ni-InGaAs Contact Technology for InGaAs Channel n-MOSFETs. Journal of The Electrochemical Society 159 (5):H511-H515

18. Ivana, Pan J, Zhang Z, Zhang X, Guo H, Gong X, Yeo Y-C (2011) Photoelectron spectroscopy study of band alignment at interface between Ni-InGaAs and $In_{0.53}Ga_{0.47}As$. Applied Physics Letters 99 (1):012105-012103

19. Kim S, Yokoyama M, Taoka N, Iida R, Lee S, Nakane R, Urabe Y, Miyata N, Yasuda T, Yamada H (2011) Self-Aligned Metal Source/Drain InxGa1-xAs n-Metal--Oxide--Semiconductor Field-Effect Transistors Using Ni--InGaAs Alloy. Applied physics express 4 (2):4201

20. Mehari S, Gavrilov A, Cohen S, Shekhter P, Eizenberg M, Ritter D (2012) Measurement of the Schottky barrier height between Ni-InGaAs alloy and $In_{0.53}Ga_{0.47}As$. Applied Physics Letters 101 (7):072103

21. Subramanian S, Zhou Q, Zhang X, Balakrishnan M, Yeo Y-C (2011) Selective Wet Etching Process for Ni-InGaAs Contact Formation in InGaAs N-MOSFETs with Self-Aligned Source and Drain. Journal of The Electrochemical Society 159 (1):H16-H21

22. Kim S, Yokoyama M, Taoka N, Nakane R, Yasuda T, Ichikawa O, Fukuhara N, Hata M, Takenaka M, Takagi S (2012) Sub-60 nm deeply-scaled channel length extremely-thin body $In_xGa_{1-x}As$-on-insulator MOSFETs on Si with Ni-InGaAs metal S/D and MOS interface buffer engineering. VLSI Technology (VLSIT), 2012 Symposium on:177-178

23. Dai X, Nguyen BM, Hwang Y, Soci C, Dayeh SA (2014) Novel Heterogeneous Integration Technology of III–V Layers and InGaAs FinFETs to Silicon. Advanced Functional Materials 24 (28):4420-4426

24. Giannuzzi LA, Kempshall B, Schwarz S, Lomness J, Prenitzer B, Stevie F (2005) FIB lift-out specimen preparation techniques. In: Introduction to focused ion beams. Springer, pp 201-228

25. Mayer J, Giannuzzi LA, Kamino T, Michael J (2007) TEM sample preparation and FIB-induced damage. Mrs Bulletin 32 (05):400-407

26. Chueh Y-L, Ford AC, Ho JC, Jacobson ZA, Fan Z, Chen C-Y, Chou L-J, Javey A (2008) Formation and Characterization of NixInAs/InAs Nanowire Heterostructures by Solid Source Reaction. Nano Letters 8 (12):4528-4533

27. Palmstrom C (1988) Lateral diffusion in Ni-GaAs couples investigated by transmission electron microscopy. J Mater Res 3 (6)

28. Dellas NS, Abraham M, Minassian S, Kendrick C, Mohney SE (2011) Kinetics of reactions of Ni contact pads with Si nanowires. Journal of Materials Research 26 (17):2282-2285

29. Ogata K, Sutter E, Zhu X, Hofmann S (2011) Ni-silicide growth kinetics in Si and Si/SiO 2 core/shell nanowires. Nanotechnology 22 (36):365305

30. Yaish YE, Katsman A, Cohen GM, Beregovsky M (2011) Kinetics of nickel silicide growth in silicon nanowires: From linear to square root growth. Journal of Applied Physics 109 (9):109-116

31. Chen Y, Lin Y-C, Huang C-W, Wang C-W, Chen L-J, Wu W-W, Huang Y (2012) Kinetic Competition Model and Size-Dependent Phase Selection in 1-D Nanostructures. Nano Letters 12 (6):3115-3120. doi:10.1021/nl300990q

32. Appenzeller J, Knoch J, Tutuc E, Reuter M, Guha S Dual-gate silicon nanowire transistors with nickel silicide contacts. In: Electron Devices Meeting (IEDM), 2006. IEEE, pp 1-4

33. Katsman A, Yaish Y, Rabkin E, Beregovsky M (2010) Surface Diffusion Controlled Formation of Nickel Silicides in Silicon Nanowires. Journal of Elec Materi 39 (4):365-370

34. Ciccariello J, Poize S, Gas P (1990) Lattice and grain boundary self‐diffusion in Ni_2Si: Comparison with thin‐film formation. Journal of applied physics 67 (7):3315-3322

35. Tung RT (1984) Schottky-Barrier Formation at Single-Crystal Metal-Semiconductor Interfaces. Physical Review Letters 52 (6):461-464

36. Lavoie C, d'Heurle FM, Detavernier C, Cabral Jr C (2003) Towards implementation of a nickel silicide process for CMOS technologies. Microelectronic Engineering 70 (2–4):144-157

37. Morimoto T, Ohguro T, Momose S, Iinuma T, Kunishima I, Suguro K, Katakabe I, Nakajima H, Tsuchiaki M, Ono M, Katsumata Y, Iwai H (1995) Self-aligned nickel-mono-silicide technology for high-speed deep submicrometer logic CMOS ULSI. Electron Devices, IEEE Transactions on 42 (5):915-922. doi:10.1109/16.381988

38. Lahav A, Eizenberg M, Komem Y (1986) Interfacial reactions between Ni films and GaAs. Journal of Applied Physics 60 (3):991-1001

39. Guivarc'h A, Guérin R, Caulet J, Poudoulec A, Fontenille J (1989) Metallurgical study of Ni/GaAs contacts. II. Interfacial reactions of Ni thin films on (111) and (001) GaAs. Journal of applied physics 66 (5):2129-2136

40. Steegen A, Maex K (2002) Silicide-induced stress in Si: origin and consequences for MOS technologies. Materials Science and Engineering R 38 (1):1-53

41. Ge CH, Lin CC, Ko CH, Huang CC, Huang YC, Chan BW, Perng BC, Sheu CC, Tsai PY, Yao LG, Wu CL, Lee TL, Chen CJ, Wang CT, Lin SC, Yeo YC, Hu C Process-strained Si (PSS) CMOS technology featuring 3D strain engineering. In: Electron Devices Meeting (IEDM), 8-10 Dec. 2003. pp 3.7.1-3.7.4. doi:10.1109/IEDM.2003.1269169

42. Buaud PP, d'Heurle FM, Chevacharoenkul S, Irene EA (1993) In situ strain measurements during the formation of palladium silicide films. Journal of Vacuum Science & Technology B 11 (2):304-310

43. Léonard F, Talin AA (2011) Electrical contacts to one-and two-dimensional nanomaterials. Nature Nanotechnology 6 (12):773-783

44. Lin Y-C, Chen Y, Xu D, Huang Y (2010) Growth of Nickel Silicides in Si and Si/SiOx Core/Shell Nanowires. Nano Letters 10 (11):4721-4726. doi:10.1021/nl103156q

45. Tang W, Dayeh SA, Picraux ST, Huang JY, Tu K-N (2012) Ultrashort Channel Silicon Nanowire Transistors with Nickel Silicide Source/Drain Contacts. Nano Letters 12 (8):3979-3985. doi:10.1021/nl3011676

46. Tang W, Picraux ST, Huang JY, Gusak AM, Tu K-N, Dayeh SA (2013) Nucleation and Atomic Layer Reaction in Nickel Silicide for Defect-Engineered Si Nanochannels. Nano Letters 13 (6):2748-2753. doi:10.1021/nl400949n

47. Chen Y, Lin Y-C, Zhong X, Cheng H-C, Duan X, Huang Y (2013) Kinetic Manipulation of Silicide Phase Formation in Si Nanowire Templates. Nano Letters 13 (8):3703-3708. doi:10.1021/nl401593f

48. Cheynet MC, Pokrant S, Tichelaar FD, Rouvière J-L (2007) Crystal structure and band gap determination of HfO2 thin films. Journal of Applied Physics 101 (5):054101-054101-054108

49. Kim C, Cho S, Cho M-H, Chung K, Suh D, Ko D-H, An C-H, Kim H, Lee H (2009) Changes in the structure of an atomic-layer-deposited HfO_2 film on a GaAs (100) substrate as a function of postannealing temperature. Applied Physics Letters 95 (4):042903-042903-042903

50. Ivana, Lim Foo Y, Zhang X, Zhou Q, Pan J, Kong E, Samuel Owen MH, Yeo Y-C (2013) Crystal structure and epitaxial relationship of $Ni_4InGaAs_2$ films formed on InGaAs by annealing. Journal of Vacuum Science & Technology B 31 (1):012202

51. Shekhter P, Mehari S, Ritter D, Eizenberg M (2013) Epitaxial NiInGaAs formed by solid state reaction on $In_{0.53}Ga_{0.47}As$: Structural and chemical study. Journal of Vacuum Science & Technology B 31 (3):031205

52. Ogawa M (1980) Alloying reaction in thin nickel films deposited on GaAs. Thin Solid Films 70 (1):181-189

53. Dayeh SA, Soci C, Bao X-Y, Wang D (2009) Advances in the synthesis of InAs and GaAs nanowires for electronic applications. Nano Today 4 (4):347-358

54. Ng KW, Ko WS, Lu F, Chang-Hasnain CJ (2014) Metastable Growth of Pure Wurtzite InGaAs Microstructures. Nano Letters 14 (8):4757-4762. doi:10.1021/nl501887f

55. Munshi AM, Dheeraj DL, Fauske VT, Kim D-C, van Helvoort AT, Fimland B-O, Weman H (2012) Vertically aligned GaAs nanowires on graphite and few-layer graphene: generic model and epitaxial growth. Nano letters 12 (9):4570-4576

56. Hjort M, Lehmann S, Knutsson J, Timm R, Jacobsson D, Lundgren E, Dick KA, Mikkelsen A (2013) Direct Imaging of Atomic Scale Structure and Electronic Properties of GaAs Wurtzite and Zinc Blende Nanowire Surfaces. Nano Letters 13 (9):4492-4498. doi:10.1021/nl402424x

57. Dayeh SA, Yu ET, Wang D (2009) Surface Diffusion and Substrate− Nanowire Adatom Exchange in InAs Nanowire Growth. Nano letters 9 (5):1967-1972

58. Dayeh SA, Yu ET, Wang D (2007) III-V nanowire growth mechanism: V/III ratio and temperature effects. Nano letters 7 (8):2486-2490

59. Pankoke V, Kratzer P, Sakong S (2011) Calculation of the diameter-dependent polytypism in GaAs nanowires from an atomic motif expansion of the formation energy. Physical Review B 84 (7):075455

60. However, this slanted interface doesn't alter the validity of our kinetic models discussed above, as the variation of nickelide segment lengths is less than 50 nm

61. Hÿtch MJ, Snoeck E, Kilaas R (1998) Quantitative measurement of displacement and strain fields from HREM micrographs. Ultramicroscopy 74 (3):131-146

62. Stampfl A, Kemister G, Leckey R, Riley J, Orders P, Usher B, Hillebrecht F, Ley L (1990) Effect of strain on the band structure of InGaAs. Physica Scripta 41 (4):617

63. Kuo CP, Vong SK, Cohen RM, Stringfellow GB (1985) Effect of mismatch strain on band gap in III‐V semiconductors. Journal of Applied Physics 57 (12):5428-5432

64. Van de Walle CG (1989) Band lineups and deformation potentials in the model-solid theory. Physical Review B 39 (3):1871

65. Kim S, Yokoyama M, Ikku Y, Nakane R, Ichikawa O, Osada T, Hata M, Takenaka M, Takagi S (2014) Physical understanding of electron mobility in asymmetrically strained InGaAs-on-insulator metal-oxide-semiconductor field-effect transistors fabricated by lateral strain relaxation. Applied Physics Letters 104 (11):113509

Chapter 3: Atomic Scale Dynamics of Contact Formation in the Cross-section of InGaAs Nanowire Channels

3.1 Introduction

As been discussed in chapter 1, the advent of semiconductor nanowires evoked reevaluation of the thermodynamics,[1] kinetics,[2,3] and phases[4,5] in nanoscale metal-semiconductor reactions, which deviate significantly from the behaviors exhibited by their planar counterparts. These efforts captured the evolution of the reaction along the axis of the nanoscale channel,[6-8] but the early stage of the reaction under the metal contact in the radial direction of the nanowire's cross-section is critical and has not been studied until now. From a materials perspective, the early stage of the reaction can govern the channel's final phases and crystalline orientations once the reaction extends into the horizontal segment (forming an end-bond-contact geometry), and can be largely affected by local defects[9] or interfacial properties. From an engineering perspective, the early stage reaction facilitates a side-contact geometry in nanowire devices that is more desirable for self-aligned technology than an end-bond-contact geometry. These issues demand a detailed understanding of the early stage reaction along the nanowire's cross-section.

3.2 Summary of Results

In this chapter, we will talk about the dynamics of the solid-state reaction between metal (Ni) and semiconductor ($In_{0.53}Ga_{0.47}As$), along the cross-section of nanowires that are 15 nm in width. Unlike planar structures where crystalline nickelide readily forms at conventional, low alloying temperatures, nanowires exhibit a solid-state amorphization step that can undergo a crystal regrowth step at elevated temperatures. In this study, we also capture the layer-by-layer reaction mechanism and growth rate anisotropy using in situ transmission electron microscopy (TEM). Our kinetic model depicts this new, in-plane contact formation which could pave the way for engineered nanoscale transistors.

3.3 Experiment

3.3.1 Fabricating InGaAs Nanowires and Preparing TEM Lamellae

In this work, a 50nm-thin undoped $In_{0.53}Ga_{0.47}As$ film (MBE grown on (001) InP by Intelligent Epitaxy Inc., Richardson, Texas) was first transferred on insulator on Si substrate with a solid-state wafer bonding process that has been discussed in section 2.3.1. After the transfer, the stacking layers from top to bottom were 50nm $In_{0.53}Ga_{0.47}As$, 15nm HfO_2, 200nm SiO_2, $NiSi_x$ bonding layer (average thickness of ~ 200nm), and 500μm Si substrate. Secondly, the InGaAs layer was thinned down to ~ 20nm with 15 cycles of digital etching that is alternative oxidation with O_2 plasma treatment (30W 3min), and oxide striping with diluted HCl solution (1:20 diluted in DI, dip for 2min). Thirdly, 20nm wide horizontal-lying nanowire structures were patterned on top of the $In_{0.53}Ga_{0.47}As$ layer

utilizing a 100 kV e-beam writer (JEOL JBX-6300FS) with beam size ~ 8nm. Negative e-beam resist, hydrogen silsesquioxane (HSQ FOx-16), was used as the etch mask for Ar-ion milling (Intlvac) to form the $In_{0.53}Ga_{0.47}As$ nanowire channels. Ar-ion milling was chosen here instead of a chemical dry etch in order to achieve a straight nanowire sidewall. After the Ar-ion milling step, HSQ atop the nanowires was removed with three consecutive cycles of O_2 plasma treatment and a short diluted HF dip, which also reduced the etch-induced surface damage and smoothened the InGaAs surface. This resulted in a nanowire channel cross-section with a squared shape, with an edge width of ~ 15nm. Finally, a 100nm Ni film was deposited onto two types of nanowire samples that were prepared with different surface treatments: (i) a thin layer of $In_{0.53}Ga_{0.47}As$ surface oxide was intentionally introduced with O_2 plasma treatment (30W 3min) before Ni deposition, and (ii) the $In_{0.53}Ga_{0.47}As$ was dipped in diluted HCl solution and immediately loaded into electron-beam evaporator to prevent the formation of a native oxide layer.

To compare the interfacial properties of those two types of specimens after Ni deposition, another set of samples was prepared on a planar InGaAs film with identical interfacial treatments. As shown in **Figure 3.1**, both type (i) specimen (**Figure 3.1** (a)-(c)) and type (ii) specimen (**Figure 3.1** (d)-(f)) showed uniform interfaces over long range. With the interfacial oxide layer, the element Ni and InGaAs were separated sharply, while Ni and InGaAs were readily intermixed upon deposition at room temperature for the sample without the interfacial oxide layer. This can also be observed from elemental line-scans (**Figure 3.1** (g)-(h)) where the type (i) specimen had a sharp change of composition from Ni to InGaAs at the interface, and where the type (ii) specimen had a more graded change of composition from Ni to InGaAs. Inside the intermixing region, the Ni element

maintained a relatively smaller change in composition than that in the InGaAs film. This intermixing nickelide layer that is present for specimens without a interfacial oxide layer was caused by the latent heat during Ni condensation from vapor phase into solid phase as will be discussed in more detail in *Appendix III*.

TEM specimens in this work were prepared by FIB milling on the samples of InGaAs nanowire on insulator on Si substrate, with the method that has been discussed in section 2.3.3.

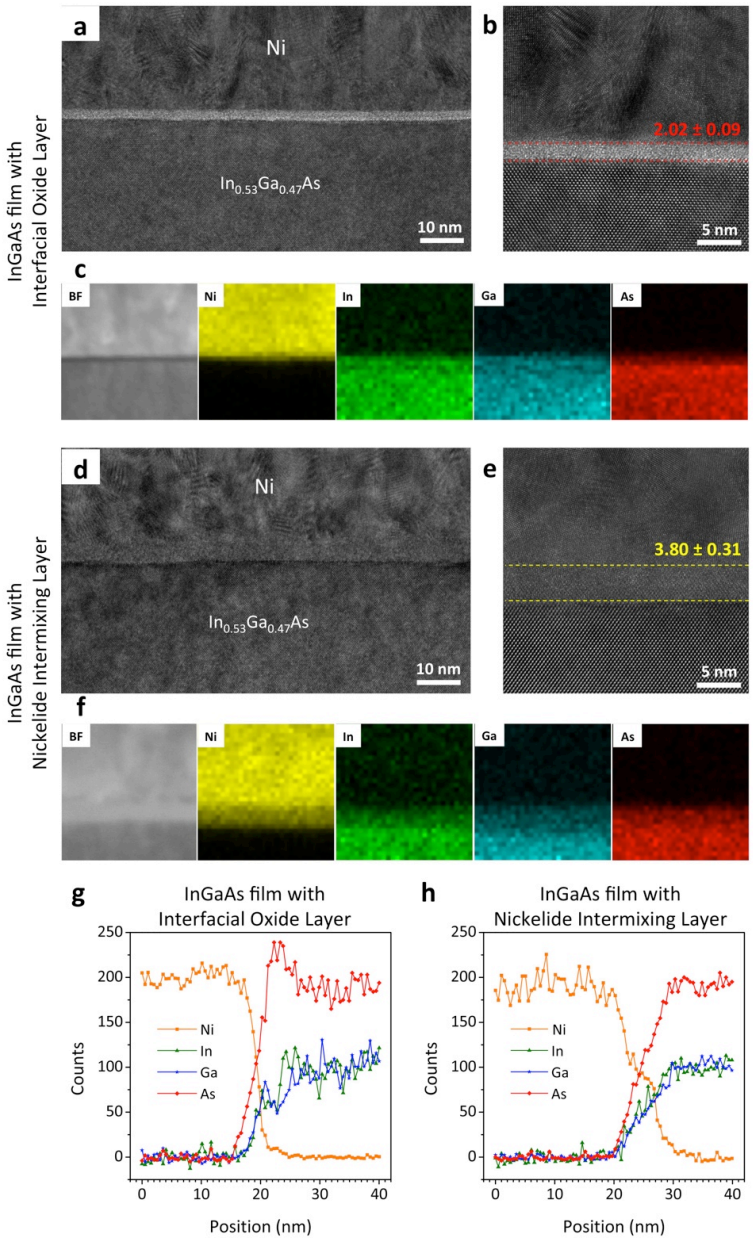

Figure 3.1. Comparison of interfacial structures for two types of specimens on InGaAs thin film. (a)-(c) TEM, HRTEM, and EDS mapping of type (i) specimen at the interface between Ni and InGaAs film. The light contrast layer at the interface, i.e. InGaAs surface oxide layer, has a uniform thickness of 2.02 ± 0.09 nm. The EDS mapping of four elements show the sharp interface between Ni and InGaAs, indicating that the interfacial oxide layer effectively prevents the intermixing of Ni and InGaAs. (d)-(f) TEM, HRTEM, and EDS mapping of type (ii) specimen at the interface between Ni and InGaAs film. The amorphous layer at the interface, i.e. Ni and InGaAs intermixing layer, has a uniform thickness of 3.80 ± 0.31 nm. The EDS mapping of four elements show the clear evidence of intermixing between Ni and InGaAs at the interface. (g)-(h) the EDS line-scan across the interface of type (i) and type (ii) specimens, respectively. Ni and As elemental counts are normalized according to their averaged top flats.

3.3.2 Transferring the Specimen Lamellae on Top of the Thermal E-chips

The process to transfer FIB lamellae onto the TEM window of a thermal E-chip (AHA chip, Protochips Inc.) was shown in **Figure 3.2**, second row. The TEM window was made of conductive ceramic with many manmade circular holes for e-beam transparency. We intentionally drilled a larger rectangular hold for better imaging of our FIB lamellae for the HRTEM video recording of the reaction dynamics. We also deposited two 3 μm tall Pt posts on the edge of the opening region (shown in **Figure 3.2** step 5) to hold the transferred FIB lamellae. These two Pt posts not only helped maintaining the flatness of specimen lamellae during transfer, but also facilitated further thinning and cleaning steps by lifting up the lamellae from the surface of ceramic membrane. Finally, the transferred specimen lamellae was further thinned with FIB with reduced voltage and current (10 kV, 0.1 nA), until the lamellae reached a thickness ~ 60nm.

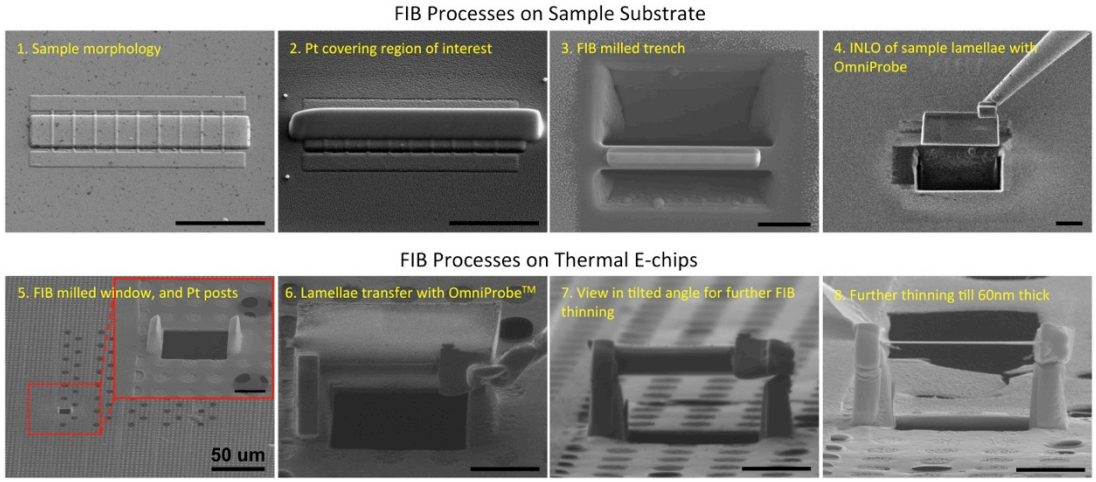

Figure 3.2. Sequences in FIB processes. SEM images show the fabrication sequences to transfer the FIB cut lamellae from the home substrate onto the TEM membrane window of a thermal E-chip™. All the scale bars are 5μm, except the one labeled separately in step 5.

3.3.3 Performing the *in situ* TEM Experiments

We used the FEI Tecnai F30 TEM and Aduro^{TM} 300 double-tilt heating stage (Protochips Inc.) to perform the in-situ heating experiments in this work. We operated TEM at 300 kV with at the minimum electron dose that could still maintain clear imaging at highest magnification (× 1M). The electron beam was never focused on the area of interest in order to minimize possible damage induced by electron beam. Digital video sequences were recorded at 3 frames/s, as the dynamic processes were slowed by well-chosen reaction temperatures. HRTEM images were extracted from the video frames, and processed using the software package DigitalMicrograph where diffraction spots were masked and then inversed to enhance the image clarity. The compatible AHA thermal E-chips^{TM} (SiN_x membranes, from Protochips Inc.) served as the heating platform for our experiments, on top of which a conductive ceramic membrane provided resistive heating and thermocouple feedback temperatures to the controller. Temperatures in this paper were given by the readings on the controller with company-provided temperature calibration files for each thermal E-chip, and through comparison of reaction rates and morphologies with experiments performed ex-situ where temperatures were measured using a thermocouple. We used a 1°C/s ramping rate during the heating experiments, and the stage stabilized within 2min after reaching the desired temperatures. **Figure 3.3** (a)-(b) shows the in-situ heating stage and the compatible thermal E-chip^{TM} that has a thin membrane window for placing our specimen. Temperatures are controlled by resistive heating and are continuously measured on-chip with a thermocouple. Samples that have Ni contacts on $In_{0.53}Ga_{0.47}As$ nanowires were fabricated on a separate substrate and transferred on top of

the membrane window of a thermal E-chip by focused-ion-beam (FIB) milling via the lift-out procedure.

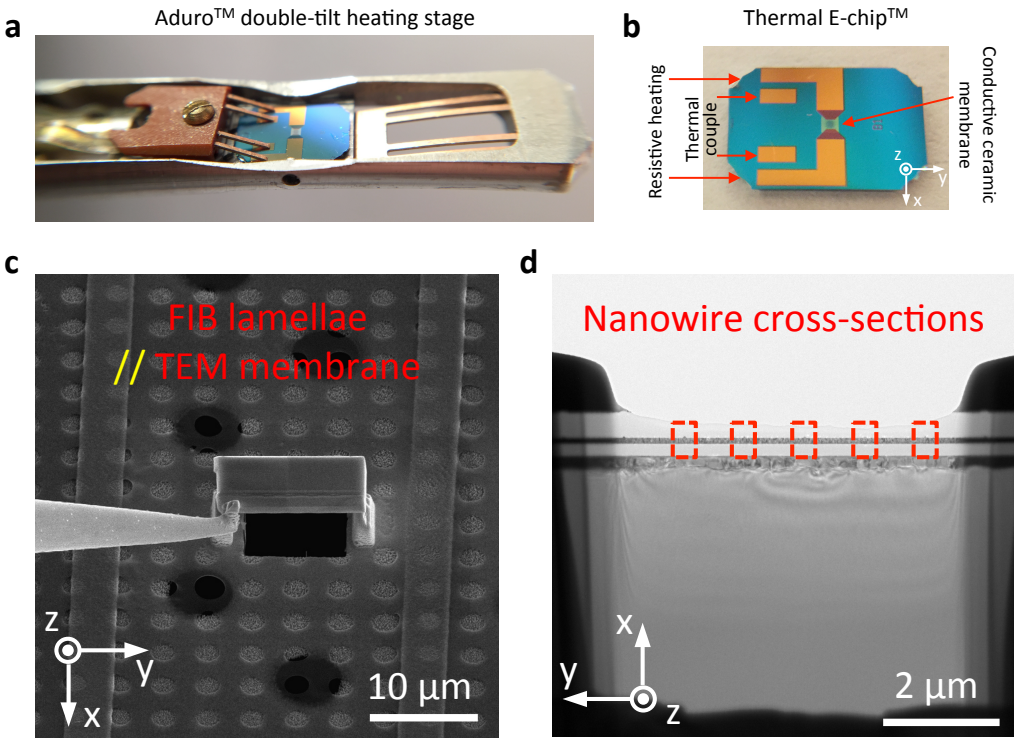

Figure 3.3. In-situ heating TEM platform (a)-(b) photographs of the Protochips Aduro™ heating stage and its compatible thermal E-chip™, respectively. Four probes on the heating stage contacts the metal leads on the thermal E-chip to introduce resistive heating and to read out temperatures. (c) SEM image of the FIB milled specimen lamellae transferred horizontally onto the TEM membrane of the thermal E-chip. (d) TEM image showing an overview of the specimen lamellae and the labeled locations of nanowire cross-sections.

3.4 Results and Discussions

3.4.1 Low-Temperature Solid-State Amorphization Process

In the first set of in-situ heating experiments, we chose a specimen that had a thin (1~2 nm) surface oxide layer in between the Ni contact and $In_{0.53}Ga_{0.47}As$ nanowire (**Figure 3.4** (a)). This was to prevent the intermixing[10] between Ni and $In_{0.53}Ga_{0.47}As$ nanowire upon Ni deposition (as discussed in section 3.3.1). The as-fabricated $In_{0.53}Ga_{0.47}As$ nanowire had a square cross-section with an edge width of ~ 15 nm. At temperatures above 180 °C, Ni diffused through the interfacial oxide layer and reacted with the $In_{0.53}Ga_{0.47}As$ nanowire cross-section to form an amorphous nickelide ($Ni_xIn_{0.53}Ga_{0.47}As$) phase. This is significantly different from the planar case, as the temperature at which the reaction started was reduced by ~ 50 °C and the nickelide phase was amorphous rather than the crystalline $Ni_2In_{0.53}Ga_{0.47}As$ that is usually obtained at or above 230 °C.

To capture the details of this solid-state amorphization process, we recorded the atomic-resolution sequence at 180 °C (**Figure 3.4** (b)). At the onset of the reaction, the Ni diffused through the interfacial oxide layer and along the surface of $In_{0.53}Ga_{0.47}As$ nanowire, quickly forming an amorphous nickelide shell of uniform thickness. Then, the nickelide shell grew evenly along the top and side surfaces of the nanowire (**Figure 3.4** (b), t=4 min), even in regions without intimate contact between Ni and the nanowire sidewall (due to shadowing effects in the metal deposition process). The growth of the surface nickelide shell indicated that surface-diffusion of Ni atoms along the outer few atomic layers of the $In_{0.53}Ga_{0.47}As$ nanowire is much faster than the volume-diffusion rate when Ni

diffuses further into the nanowire cross-section.[11] Following this shell formation (**Figure 3.4** (b), t=8min), the nickelide reaction continued along the bottom region of the nanowire that sits on HfO_2, and then extended across the width of the nanowire isolating the crystalline $In_{0.53}Ga_{0.47}As$ core from the HfO_2 substrate (**Figure 3.4** (b), t=12 min) by an intermediate amorphous nickelide region. This process led to the formation of an isotropic nickelide shell surrounding the entire InGaAs nanowire circumference. At this point the (110) sidewall facets start to disappear by developing multiple {111}-type facets while the top facet remains (001), indicating a faster reaction rate on {110} compared to {111} and {001} surfaces. This process created a stepped interface (**Figure 3.5**) that was gradually eliminated by {111} facets resulting in a rhomboidal core of crystalline $In_{0.53}Ga_{0.47}As$ (**Figure 3.4** (b), t= 24 min).

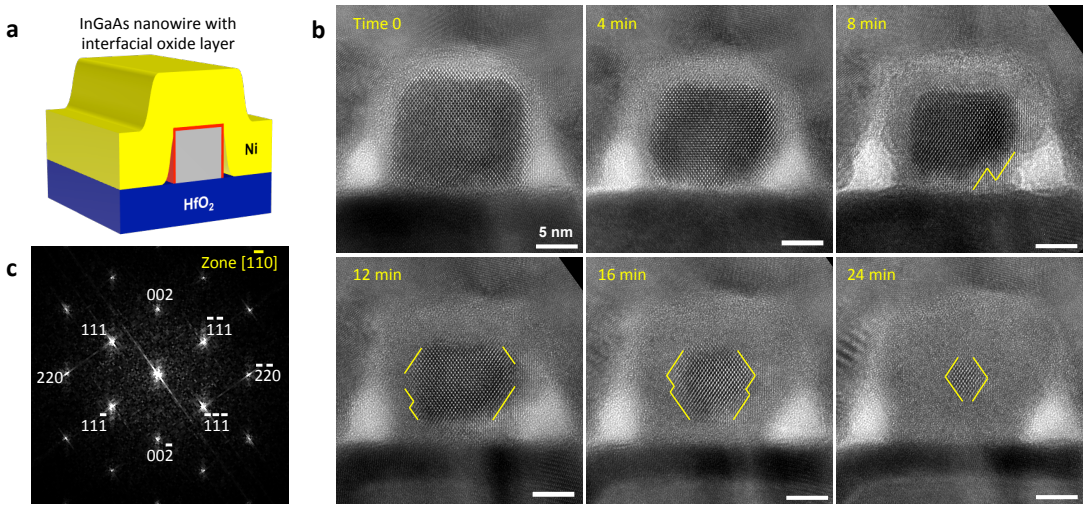

Figure 3.4. (a) schematic of Ni contacting with a $In_{0.53}Ga_{0.47}As$ nanowire cross-section that sits on the HfO_2 dielectric layer. A thin red layer indicates the intentionally introduced $In_{0.53}Ga_{0.47}As$ surface oxide layer before Ni deposition. (b) HRTEM sequences during the in-situ heating experiment at 180 °C. During this process, Ni diffuses through the interfacial oxide layer, reacts with the $In_{0.53}Ga_{0.47}As$ nanowire channel, and results in an amorphous nickelide phase. The nanowire cross-section, started with straight sidewalls, became initially rounded and gradually developed facets with a diamond shape. (c) fast Fourier transform (FFT) image of the corresponding nanowire cross-section, showing the diffraction pattern along the $[1\bar{1}0]$ zone axis (projecting direction in TEM). The developed facets in (b) correspond to the {111} type of facets for $In_{0.53}Ga_{0.47}As$ lattice that has a typical zinc blende structure.

3.4.2 Ledge Formation and Movement Mechanisms in the Nanowire Cross-Sections

The details of the facet evolution and ledge movement are revealed in the still images of the high-resolution TEM recording (**Figure 3.5** (a)) with much shorter time intervals in the time range of 12 min to 16 min shown in Fig. 1f. We observed layer-by-layer Ni reactions on {111} facets with ledge movements that can be characterized by one of the following mechanisms: 1) a step height that eliminates one $In_{0.53}Ga_{0.47}As$ atomic bilayer[12] along a single <112> direction (labeled ① in **Figure 3.5** (a) and shown in the schematic of **Figure 3.5** (c)), 2) a step height that eliminates one atomic bilayer but with the reaction proceeding from both sides of the bilayer in two opposite <112> directions (labeled ② in **Figure 3.5** (a) and shown in the schematic of **Figure 3.5** (d)), 3) the merging of two ledges, each with a single-bilayer step height, into a single ledge with a double-bilayer step height (labeled ③ in **Figure 3.5** (a) and shown in the schematic of **Figure 3.5** (e)) that moves simultaneously after merging, or 4) the split of a double-bilayer step height into two ledges with single-bilayer step heights (labeled ④ in **Figure 3.5** (a) and shown in the schematic of **Figure 3.5** (f)) that moves independently after splitting. These observations imply that there was no shear stress during this nickelide reaction in our current device geometry because a fixed step height of three or more atomic bilayers is necessary in order to compensate for the shear stress during phase transformations,[13] which was not observed in our experiments. Therefore, we believe that these four possible scenarios of ledge movement are general to the Ni/III-V nanowire reaction. We emphasize that **Figure 3.5** not only correlates the nature of ledge movements to the crystal structures

in the nanowire cross-section, but also tracks the time-resolved amorphization reaction in III-V materials at atomic resolution.

The general behavior of the phase transformation in the nanowire cross-section that is exhibited in **Figure 3.5** is valid with or without the presence of the interfacial oxide. The direct deposition of metal on a compound semiconductor surface leads to the formation of an intermixing layer due to the latent heat when the metal atoms condense from the vapor phase to the solid phase.[10] Irrespective of the deposition process (electron beam evaporation or sputtering), we determined that prior to the in-situ heating experiments, our devices exhibited a Ni-$In_{0.53}Ga_{0.47}As$ intermixing surface layer for those that did not have a surface oxide layer (**Figure 3.6** (a)). Ion-beam irradiation intermixing during TEM sample preparation was tested and excluded as being a cause for this behavior (see *Appendix III*). We observed that before the in-situ heating experiment started, the $In_{0.53}Ga_{0.47}As$ core had a rounded top and sidewall surfaces (**Figure 3.6** (b), t=0) due to the formation of the intermixing layer. When heated to 180 °C, Ni diffused through the existing intermixing layer, along the rounded surface of crystalline $In_{0.53}Ga_{0.47}As$, and reacted at the interface between $In_{0.53}Ga_{0.47}As$ and HfO_2 at the bottom of the nanowire, making the $In_{0.53}Ga_{0.47}As$ core even more rounded (**Figure 3.6** (b), t=3 min). As the reaction progressed, many small facets were clearly observed at 6 min, and gradually developed into several {111} type of facets at 9 min. Eventually, the crystalline $In_{0.53}Ga_{0.47}As$ core became rhomboidal shape after 13 min, very similar to that of **Figure 3.3** (b) with the only difference being the relatively lower spatial position of the rhombus due to the initial intermixing layer.

Figure 3.5. Ledge Formation and movement mechanisms at atomic resolution. (a) HRTEM sequences showing the evolution of {110} sidewall facet into multiple {111} type facets, through the layer-by-layer nickelide reactions. Red stars "★" label the identical atoms in each figure. (b) reconstructed $In_xGa_{1-x}As$ lattice structure with the same orientation as the nanowire cross-section. (c)-(f) proposed mechanism of ledge movement on $(11\bar{1})$ plane along $[112]$ or $[\bar{1}\bar{1}2]$ directions. The ledge can move with a step height of one $In_xGa_{1-x}As$ bilayer, from one side (c) or two opposite sides (d) corresponding to the labeled cases of ① and ② in (a). The ledge can also move with a step height of two $In_xGa_{1-x}As$ bilayers together (e) and can separate into two single bilayers afterwards (f) which corresponds to the labeled cases of ③ and ④ in (a).

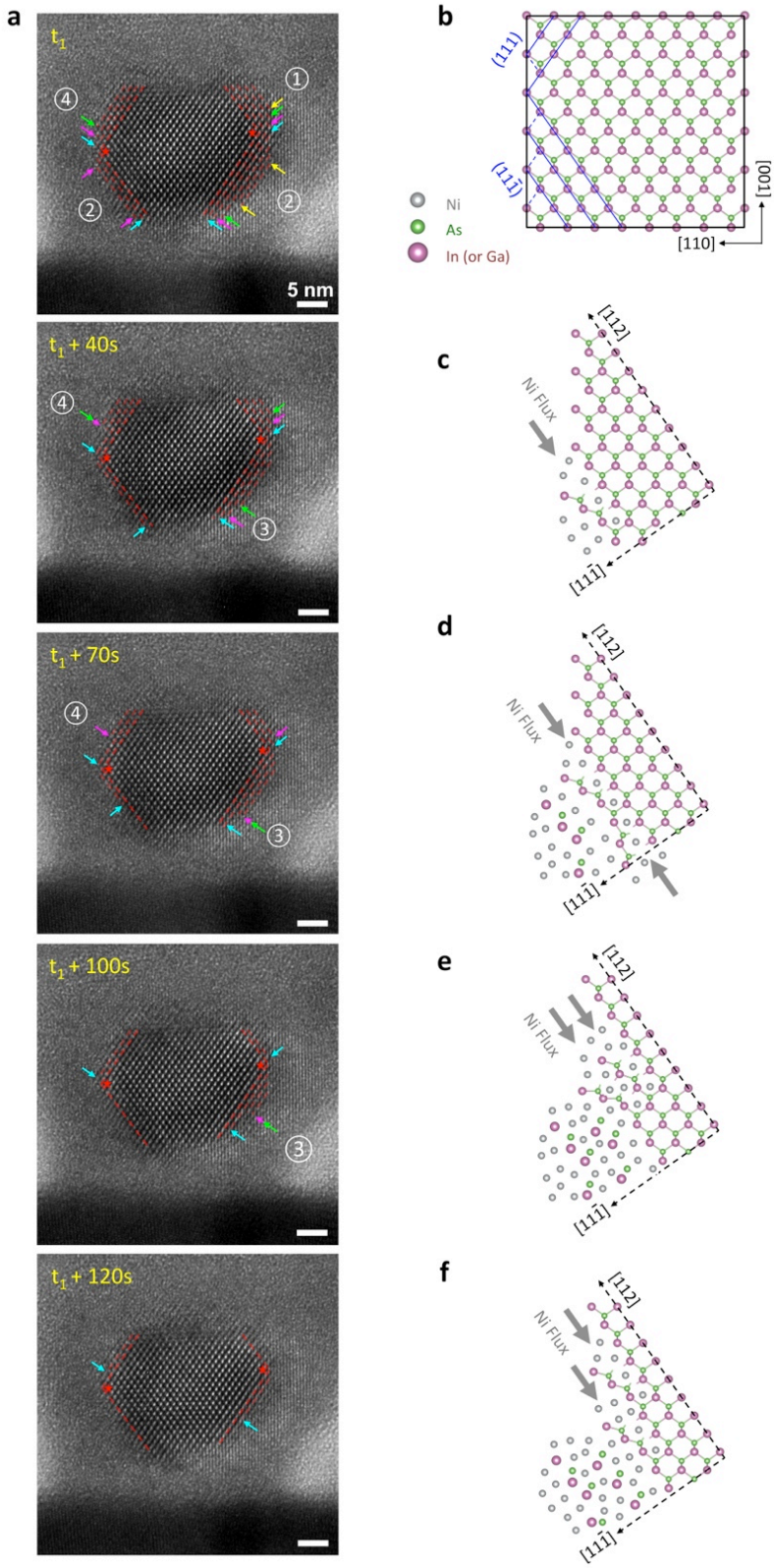
a
t1
5 nm
t1 + 40s
t1 + 70s
t1 + 100s
t1 + 120s
b
(111)
(11$\bar{1}$)
[001]
[110]
Ni
As
In (or Ga)
c
d
e
f
[112]
Ni Flux
[11$\bar{1}$]
[111]

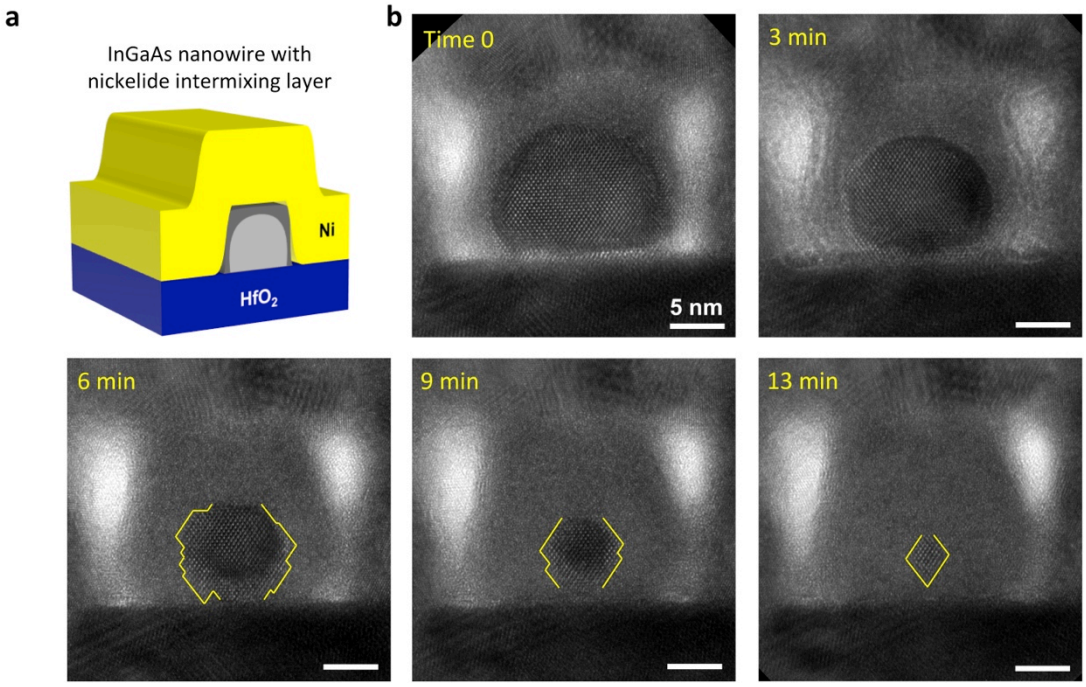

Figure 3.6. Influence of nickelide intermixing layer. (a) schematic of Ni contacting with a $In_{0.53}Ga_{0.47}As$ nanowire cross-section without the introduced oxide interface. An amorphous intermixing layer readily forms upon Ni deposition. (b) high-resolution TEM sequences during the in-situ heating at 180 °C. The non-intermixed $In_{0.53}Ga_{0.47}As$ cross-section, started with rounded structure and gradually developed multiple small facets/steps as highlighted by the yellow lines for t=6min onwards, finally forming an equilateral rhombus-like region.

3.4.3 Modeling the Formation of Radial Contact Alloys

In order to better understand the kinetics and thermodynamics of the nickelide reaction in the radial direction of the nanowire's cross-section, we developed a simple model (**Figure 3.7** (a)) to depict this metallization process. For simplicity, we assumed that (i) the metal contact was an infinite source of Ni since there was no experimentally observed depletion of Ni near the nickelide/nanowire interface; (ii) the unreacted semiconductor core and reacted metallic shell were cylindrical with perimeters, l and L respectively; and (iii) L was fixed which is consistent with our experimental observations in **Figure 3.7** (b)-(c). The fixed perimeter L suggests that the volume expansion due to Ni incorporation occurred in the h direction, and negligible strain was present in the $In_{0.53}Ga_{0.47}As$ core for the present experimental conditions, as was validated from fast Fourier transform (FFT) patterns on the InGaAs regions at various stages of the reaction.

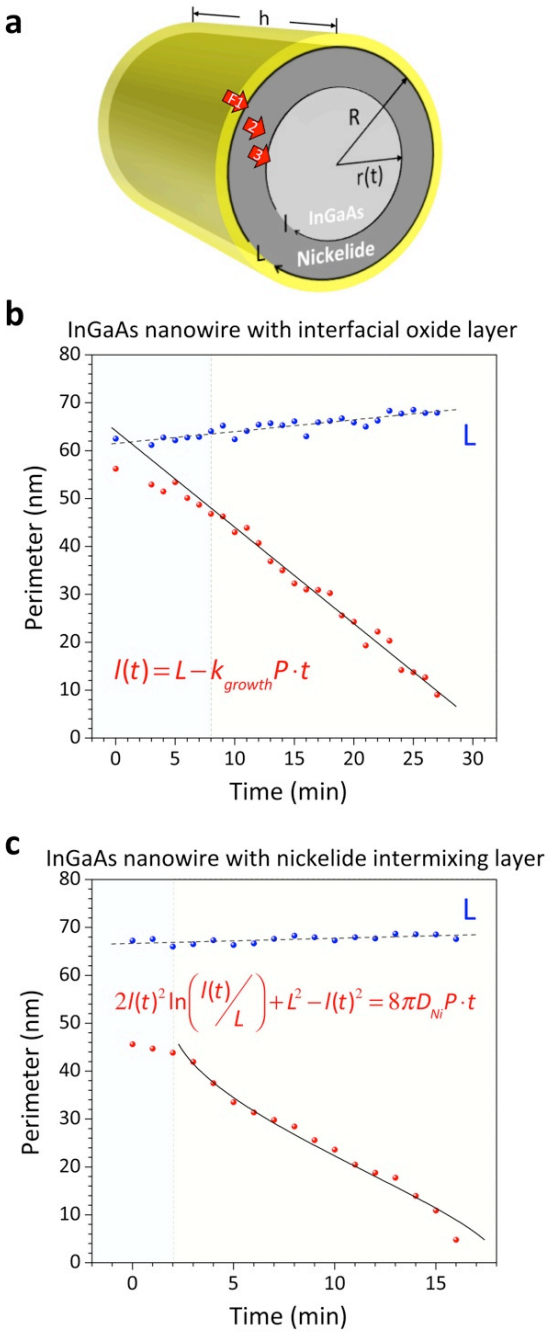

Figure 3.7. Modeling the formation of radial contact alloys. (a) a generalized model for metallic contact formation in the radial direction of a nanowire channel. The metal source is assumed to be unlimited, and the inner and outer perimeters of the reacted regions are labeled with l and L respectively. (b) Plot of the inner and outer perimeters for the specimen that had an interfacial oxide layer, exhibiting a linear dependence with time and indicating a kinetically limited reaction process. (c) Plot of the inner and outer perimeters for the specimen that had no interfacial oxide layer but exhibited an intermixed surface region, with fits that corresponded to a mass-transport limited process.

As shown in **Figure 3.7** (a), the mass transport of Ni atoms in the nickelide reaction involves three steps: (1) Ni dissolution across the Ni/nickelide interface, (2) Ni diffusion through the formed nickelide shell, and (3) solid-state reaction at the nickelide/$In_{0.53}Ga_{0.47}As$ interface, with Ni fluxes denoted as F_1, F_2, and F_3, respectively. If one of the three steps is the rate-limiting step, the correlation between the unreacted perimeter l and time t can be expressed as follows (detailed derivations in *Appendix IV*):

(i) If F_1 is the rate-limiting step:

$$l(t) = \sqrt{L^2 - 2k_{dissolve}LP \cdot t} \quad ; \tag{3-1}$$

(ii) If F_2 is the rate-limiting step:

$$2l(t)^2 \ln\left(l(t)/L\right) + L^2 - l(t)^2 = 8\pi D_{Ni}P \cdot t \quad ; \tag{3-2}$$

(iii) If F_3 is the rate-limiting step:

$$l(t) = L - k_{growth}P \cdot t \quad ; \tag{3-3}$$

where $k_{dissolve}$ and k_{growth} are the rate constants for Ni dissolution and nickelide growth respectively. D_{Ni} is the diffusion coefficient of Ni in $In_{0.53}Ga_{0.47}As$ and P is a constant.

We found that for the first type of specimen that had an interfacial oxide layer in between Ni and $In_{0.53}Ga_{0.47}As$ (**Figures 3.4** and **3.5**), l obeyed a linear dependence on time (**Figure 3.7** (b)) that follows equation (3-3), a behavior that is consistent with F_3 being the rate-limiting step, i.e. kinetically limited growth at the nickelide/$In_{0.53}Ga_{0.47}As$ interface. By

fitting the experimental data in **Figure 3.7** (b) to equation (3-3), we found that the fit line projected to an intercept, L, of 64.2nm with the y-axis, which is in agreement with the external nickelide perimeter within the measurement errors. The slope of the linear fit provided the effective growth rate ($k_{growth}P$) of 2.1 nm/min. Since Ni mainly reacted with three surfaces with the nanowire cross-section but not at the $In_{0.53}Ga_{0.47}As/HfO_2$ lower interface for the first 8 min of the reaction, the experimentally extracted reacted perimeter is lower than the modeled one in **Figure 3.7** (b). For the second type of specimen that had the intermixing layer in between Ni and $In_{0.53}Ga_{0.47}As$ (**Figure 3.7** (c)), l followed a diffusion/mass-transport-limited process (F_2) with a characteristic dependence of equation (3-2). The characteristic shape of equation (3-2) includes rapid decays in unreacted perimeter l at both the beginning and the very end, and an approximate linear segment in between. The fit to the data of Fig. 4c with equation (3-2) included a time-offset term $(t-t_0)$, where t_0 =1.9 min, indicating that the diffusion-limited growth rate became effective after ~ 2 min of reaction. This behavior raises two questions: why did the reaction rate in the second type of specimen change from kinetically limited to diffusion-limited, and what happened in the first 1.9 min before the diffusion-limited process applied? The answer to these two questions lies in the differences in the interfacial properties between Ni and $In_{0.53}Ga_{0.47}As$. In the second type of specimen, an intermixing layer readily formed upon Ni deposition, resulting in a rounded $In_{0.53}Ga_{0.47}As$ cross-section (**Figure 3.6** (b), t=0). The rounded surfaces introduced many kink sites on small steps of nickelide/$In_{0.53}Ga_{0.47}As$ interfaces, facilitating the reaction rate at these interfaces and thereby accelerating the kinetics of the reaction. The rate of arrival of Ni adatoms to the reaction interface became the rate-limiting step and therefore, the nickelide reaction became

mass-transport/thermodynamically limited. It is also worth noting that the initial intermixing layer during metal deposition may not reach an equilibrium concentration (solubility limit) of Ni in $In_{0.53}Ga_{0.47}As$. Upon in-situ heating the sample to 180 °C, Ni must first diffuse through the intermixing layer and reach a point that exceeds the equilibrium concentration within this intermixing layer before Ni supersaturates the interface and nucleation and growth of a nickelide layer can proceed. This is corroborated by the experimentally observed subtle changes in l during the first 2 min (first three red data points in **Figure 3.7** (c)) that became rapid afterwards. We extracted from the fits of the data from **Figure 3.7** (c) an L'=51.3 nm which agreed with the unreacted perimeter before the in-situ experiment started (excluding the intermixing layer), and an effective diffusion coefficient ($8\pi D_{Ni}P$) of 161.4 nm^2/min, which is consistent with the volume diffusion coefficient that can be extracted from an Arrhenius plot in our previous study.[11] For t > 14 min, the measured l of the unreacted $In_{0.53}Ga_{0.47}As$ region fell more quickly than the fitting curve presumably due to interference from surface diffusion of the Ni on the imaging plane which reduced the image contrast of the crystalline core underneath.

3.4.4 High-Temperature Recrystallization Process

During the above in-situ heating experiments, we found that the nickelide reaction resulted in an amorphous phase in the nanowire cross-sections throughout a wide range of reaction temperatures (180 °C ~ 350 °C). Interestingly, when the temperature was elevated to above 375 °C, the amorphized nickelide phase regrew slowly into a crystalline nickelide phase (**Figure 3.8** (a)). During this regrowth, poly-crystallites were observed in the first 5

min followed by a well-aligned single-crystalline nickelide phase that appeared at the top-left corner. At later stages of crystallization, this single-crystalline nickelide phase seeded the regrowth from top-left corner downwards into the cross-section of the nanowire, and then from left side to the right until recrystallizing the entire nanowire cross-section. This crystalline nickelide phase was found to be $Ni_2In_{0.53}Ga_{0.47}As$ by examining the lattice constant (**Figure 3.8** (b)) with known value for this phase.[11] The regrown area of single crystalline $Ni_2In_{0.53}Ga_{0.47}As$ versus the entire nanowire cross-sectional area was plotted as a function of time in **Figure 3.8** (c). We found that the area transition from amorphous to crystalline nickelide can be fit with the Avrami equation,[14] $Y = 1 - \exp\left(-Kt^n\right)$, with n=3.92, which is close to n=4 that is typical for an ideal homogenous phase transformation.[15] Using energy dispersive spectroscopy (EDS) measurements, we found that the Ni concentration at the center of nanowire cross-section increased by 1.6 times after the crystalline regrowth. We hypothesize that during the amorphization step, Ni diffused into the tetrahedral interstitial sites of the $In_{0.53}Ga_{0.47}As$ lattice and formed a metastable nickelide phase (the lattice structure is shown in Figure S6 in the supporting information). This is in agreement with the fact that nickelide reacts faster on {110} facets than on {111} or {100} type of facets, as <110> are usually the net crystal directions for interstitial diffusion.[16] During the crystalline regrowth step, further Ni was supplied from the surrounding contact, gradually forming the thermally stable $Ni_2In_{0.53}Ga_{0.47}As$ phase. Given the shadowing effects during Ni deposition and non-conformal Ni coating (**Figure 3.4** and **3.6**) as well as the thin FIB lamellae examined here, void formation on the sidewall of the reacted nanowire was unavoidable but can be resolved with conformal coating and wider Ni contacts.

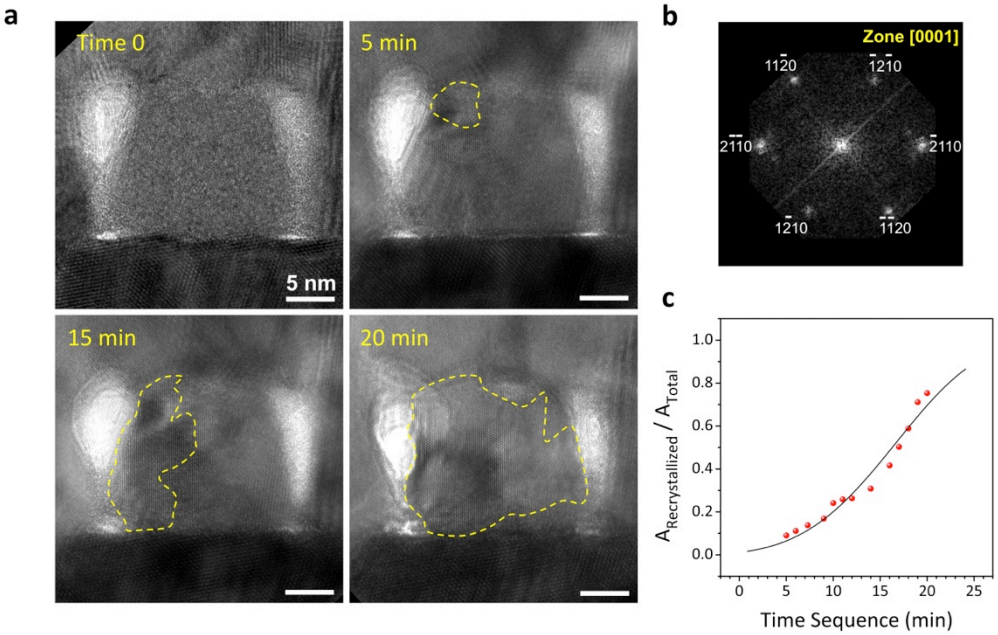

Figure 3.8. Recrystallization at elevated temperature. (a) high-resolution TEM sequences during the in-situ heating at 375 °C. The $In_{0.53}Ga_{0.47}As$ nanowire has fully reacted with Ni to form an amorphous nickelide phase at 180 °C. During the recrystallization growth, well-aligned $Ni_2In_{0.53}Ga_{0.47}As$ phase starts to form at the top-left corner, extends downward and then to the right, and finally recrystallizes the entire nanowire cross-section. (b) FFT image of the corresponding $Ni_2In_{0.53}Ga_{0.47}As$ crystal, showing the diffraction pattern along the [0001] zone axis (projecting direction in TEM). (c) plot of area fraction of recrystallized region over the entire cross-sections as a function of time following the Avrami equation (see text).

3.5 Conclusions

In summary, we report the first direct observation of solid-state reaction dynamics between a metal (Ni) and a semiconductor ($In_{0.53}Ga_{0.47}As$) nanowire along its cross-section. At typical temperatures at which the crystalline $Ni_2In_{0.53}Ga_{0.47}As$ phase grows on planar $In_{0.53}Ga_{0.47}As$ surfaces, the nanowire cross-section experienced a solid-state amorphization step and forms $Ni_xIn_{0.53}Ga_{0.47}As$ ($x<2$). During this amorphization process, nickelide reacts in a layer-by-layer manner proceeding by ledge movements on {111} facets along <112> directions. Nickelide ledge movement events were recorded with time-sequenced high-resolution TEM images. These show that the phase transformation occurs through the evolution of stepped edges on non-{111} facets and their consequent elimination resulted in an equilateral rhombus-like region bounded by {111} planes. The interface between Ni and the $In_{0.53}Ga_{0.47}As$ nanowire was found to significantly influence the reaction kinetics and was captured by a model that we developed specifically for the cross-sectional geometry of nanowire channels. Finally, the amorphous $Ni_xIn_{0.53}Ga_{0.47}As$ ($x<2$) phase regrew into a single crystalline $Ni_2In_{0.53}Ga_{0.47}As$ phase at temperatures above 375 °C by additional incorporation of Ni adatoms from the contact reservoir. Overall, the results presented here provide a general guide for the development of crystalline, self-aligned contacts in nanoscale channels and can be generalized to radial reactions of metallic and other alloys into nanowire cross-sections.

Most of chapter 3 was published in *Nano Letters* 2017. R. Chen, K. L. Jungjohann, W. M. Mook, J. Nogan, S. A. Dayeh. The dissertation author is the first author of this paper.

3.6 References

1. Tang W, Nguyen B-M, Chen R, Dayeh SA (2014) Solid-state reaction of nickel silicide and germanide contacts to semiconductor nanochannels. Semiconductor Science and Technology 29 (5):054004

2. Appenzeller J, Knoch J, Tutuc E, Reuter M, Guha S (2006) Dual-gate silicon nanowire transistors with nickel silicide contacts. Electron Devices Meeting (IEDM):1-4

3. Chen Y, Lin Y-C, Zhong X, Cheng H-C, Duan X, Huang Y (2013) Kinetic Manipulation of Silicide Phase Formation in Si Nanowire Templates. Nano Letters 13 (8):3703-3708

4. Chen Y, Lin Y-C, Huang C-W, Wang C-W, Chen L-J, Wu W-W, Huang Y (2012) Kinetic Competition Model and Size-Dependent Phase Selection in 1-D Nanostructures. Nano Letters 12 (6):3115-3120

5. Tang J, Wang C-Y, Xiu F, Zhou Y, Chen L-J, Wang KL (2011) Formation and device application of Ge nanowire heterostructures via rapid thermal annealing. Advances in Materials Science and Engineering 2011:316513

6. Chueh Y-L, Ford AC, Ho JC, Jacobson ZA, Fan Z, Chen C-Y, Chou L-J, Javey A (2008) Formation and Characterization of NixInAs/InAs Nanowire Heterostructures by Solid Source Reaction. Nano Letters 8 (12):4528-4533

7. Tang W, Dayeh SA, Picraux ST, Huang JY, Tu K-N (2012) Ultrashort Channel Silicon Nanowire Transistors with Nickel Silicide Source/Drain Contacts. Nano Letters 12 (8):3979-3985

8. Fauske VT, Huh J, Divitini G, Dheeraj DL, Munshi AM, Ducati C, Weman H, Fimland B-O, van Helvoort ATJ (2016) In Situ Heat-Induced Replacement of GaAs Nanowires by Au. Nano Letters 16 (5):3051-3057

9. Tang W, Picraux ST, Huang JY, Gusak AM, Tu K-N, Dayeh SA (2013) Nucleation and Atomic Layer Reaction in Nickel Silicide for Defect-Engineered Si Nanochannels. Nano Letters 13 (6):2748-2753

10. Ko DH, Sinclair R (1991) Amorphous phase formation in an as-deposited platinum-GaAs interface. Applied physics letters 58 (17):1851-1853

11. Chen R, Dayeh SA (2015) Size and Orientation Effects on the Kinetics and Structure of Nickelide Contacts to InGaAs Fin Structures. Nano letters 15 (6):3770-3779

12. The atomic bilayer origins from the "zinc blend" structure of InxGa1-xAs lattice, and means the coupled one layer of As atoms and one layer of InxGa1-x atoms.

13. Li N, Yadav SK, Wang J, Liu X-Y, Misra A (2015) Growth and Stress-induced Transformation of Zinc blende AlN Layers in Al-AlN-TiN Multilayers. Scientific Reports 5:18554

14. Jena A, Chaturvedi M (1992) Phase transformation in materials. Prentice Hall,

15. We believe that there exists no preferred heterogeneous nucleation site during this amorphous to crystalline regrowth such that n ~ 4. These poly-crystallites formed over the entire NW cross-section at the onset of the regrowth also referred to as homogeneous phase transformation.

16. Edmonds K, Bogusławski P, Wang K, Campion RP, Novikov S, Farley N, Gallagher B, Foxon C, Sawicki M, Dietl T (2004) Mn Interstitial Diffusion in (G a, M n) A s. Physical review letters 92 (3):037201

Chapter 4: Recordings and Analysis of Atomic Ledge and Dislocation Movements in InGaAs to Nickelide Nanowire Phase Transformation

4.1 Introduction

In chapter 3, we have discussed the metallization process in the cross-section of the InGaAs nanowires, which is the early stage of the reactions that happens underneath the metal contact. If we continue to apply heating, the nickelide reactions will eventually extends into the nanowire channel. Therefore, in this chapter, we are going to look at the nickelide reactions along the nanowire channel directions.

The majority of those nanoscale metallization studies were carried out by *in-situ* heating and imaging inside a transmission electron microscopy (TEM) [1-3] which proved powerful in investigating these thermally driven phase transformations in real-time and at atomic resolutions.[4-7] For instance, it has been found that the ledge nucleation and movement in nanoscale metallization processes can be largely affected by the involved material systems,[8] local defects,[9] metal impurities,[10] dielectric layer coating,[11] and interfacial properties in between the metal contact and the semiconductor[12]. Though prominent discoveries have been made on nanostructures on elemental semiconductors, i.e. Si and Ge nanowires,[13] detailed ledge behaviors have not been uncovered in III-V nanowire channels at atomic resolutions,[8] possibly due to the multifold elements and complicated phases involved in the phase transformation from a binary/ternary compound

semiconductor to a ternary/quaternary compound metallic contact, respectively, even for a single element metal contact (eg. Ni).

Ni has been argued as a suitable alloyed metal contact with $In_{0.53}Ga_{0.47}As$ channels because it forms a metallic nickelide phase ($Ni_xIn_{0.53}Ga_{0.47}As$)[14-16] which is analogous to the nickel silicide (Ni_xSi) to the Si material. For these planar device geometries, it was found that at temperatures as low as ~ 230 °C, a poly-crystalline nickelide phase forms and can be thermally stable up to 450 °C.[17] The $Ni_xIn_{0.53}Ga_{0.47}As$ lattice is of the NiAs (B8) structure with commonly observed stoichiometry of $Ni_2In_{0.53}Ga_{0.47}As$[18,19] or $Ni_3In_{0.53}Ga_{0.47}As$[20,21] at different process conditions. However, the lattice mismatch between $In_{0.53}Ga_{0.47}As$ and the formed $Ni_xIn_{0.53}Ga_{0.47}As$ could introduce large strain in the $In_{0.53}Ga_{0.47}As$ nanowire channels and leads to the formation of defects at the $In_{0.53}Ga_{0.47}As/Ni_xIn_{0.53}Ga_{0.47}As$ interface,[22] which further complicates detailed structural analysis. Therefore, we sought a detailed investigation of the nucleation and ledge propagation behaviors to uncover the origin of these complicated phase-transformation details.

4.2 Summary of Results

Original *in-situ* heating transmission electron microscopy studies are carried out to record and analyze the atomic scale dynamics of contact alloy formation between Ni and $In_{0.53}Ga_{0.47}As$ nanowire channels. It is observed that the nickelide reacts on the $In_{0.53}Ga_{0.47}As$ (111) || $Ni_2In_{0.53}Ga_{0.47}As$ (0001) interface with atomic ledge propagation

along the $Ni_2In_{0.53}Ga_{0.47}As$ $[10\bar{1}0]$ direction. Ledges nucleate as a train of strained single-bilayers and propagate in-plane as double-bilayers that are associated with a misfit dislocation of $\vec{b} = \frac{2c}{3}[0001]$. The atomic structure is reconstructed to explain this phase transformation that involves collective gliding of three Shockley partials in $In_{0.53}Ga_{0.47}As$ lattice to cancel out shear stress and the formation of misfit dislocations to compensate the large lattice mismatch in the newly formed nickelide phase and the $In_{0.53}Ga_{0.47}As$ layers. This work demonstrates the applicability of interfacial disconnection (ledge + dislocation) theory in a nanowire channel during thermally induced phase transformation that is typical in metal/III–V semiconductor reactions.

4.3 Experiment

4.3.1 Preparing the TEM Specimen Lamellae

In this work, we utilized the in-situ TEM heating technique to observe the solid-state reactions between Ni contact and $In_{0.53}Ga_{0.47}As$ nanowire channels. The horizontal $In_{0.53}Ga_{0.47}As$ nanowire channels were fabricated by top-down dry-etch on a separate substrate (the same method as in section 2.3.2 and section 3.3.1), with nanowires sitting on a 15 nm HfO_2 layer. A TEM lamellae prepared by FIB milling usually has a final thickness about 60~80 nm, with positioning accuracy > 100 nm. Therefore, the nanowire arrangement needed to be smartly designed (as shown in **Figure 4.1**) in order to have at least one intact nanowire channel that is fully embedded in the SiO_2 layer and appears in the focused-ion-beam (FIB) milled lamellae. The 120nm wire-to-wire distance in a column

ensures no overlap of two nanowires in a FIB lamellae, and the 30nm column-to-column guarantees 2~3 nanowire channels remain along the FIB lamellae. If 3 nanowires remain, the center one would be the intact nanowire fully embedded by SiO_2 top layer, and the other two would be partially damaged by FIB on the sidewall. If 2 nanowires remain, both of them would be intact nanowires and the in-situ study could be focused on either on them. This design ensures no overlapping of nanowire channels in a FIB milled specimen lamella along the channel direction, and the existence of 2 ~ 3 consecutive nanowire channels in this lamella for in-situ studies.

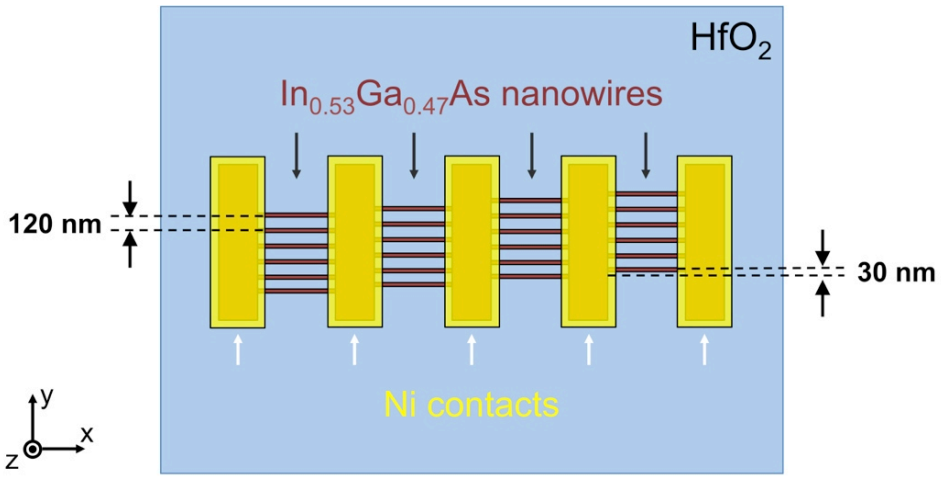

Figure 4.1. Schematic for the top view of $In_{0.53}Ga_{0.47}As$ nanowires arrangement. Each nanowire has a width of 30nm, and a center-to-center distance between two nanowires in a column to be 120nm. The column-to-column group offset was 30nm.

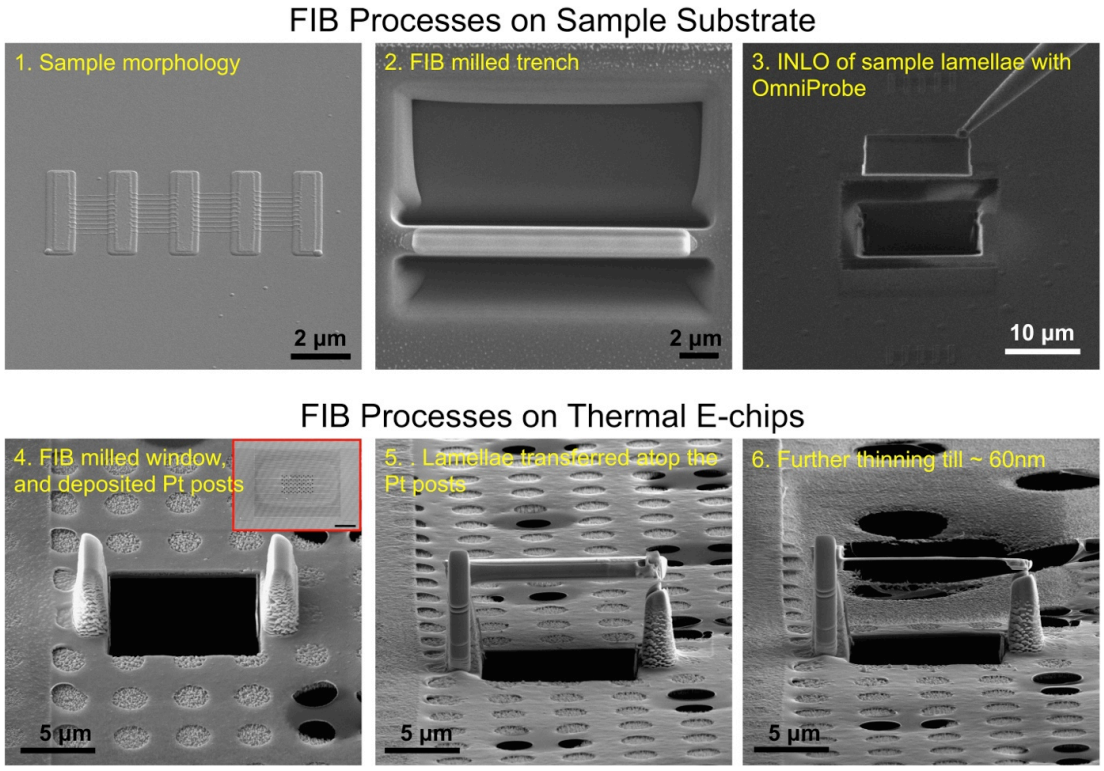

Figure 4.2. SEM images showing the sequences in FIB processes. The fabrication flow exhibits the sequences of transferring the FIB cut lamellae from the home substrate onto the TEM membrane window of a thermal E-chip. The inserted image in step 4 is the overview of TEM membrane with scale bar of 100 µm.

4.3.2 Transferring Specimen Lamellae on Top of Thermal E-Chips

The process to transfer FIB lamellae onto the TEM window of a thermal E-chip^{TM} (AHA chip, Protochips Inc.) was shown in **Figure 4.2**, second row. The TEM window was made of conductive ceramic with many manmade circular holes for electron-beam transparency. We intentionally drilled a larger rectangular hold for better imaging of our

FIB lamellae for the HRTEM video recording of the reaction dynamics. We also deposited two Pt posts on the edge of the opening region (shown in **Figure 4.2** step 4) to hold the transferred FIB lamellae. These two Pt posts not only helped maintaining the flatness of specimen lamellae during transfer, but also facilitated the further thinning and cleaning steps by lifting up the lamellae from the surface of ceramic membrane. Finally, the transferred specimen lamellae was further thinned with FIB with reduced voltage (10 kV), until the lamellae reached a thickness ~ 60nm.

We used the FEI Tecnai F30 TEM and Aduro^{TM} 500 heating stage (Protochips Inc.) to perform the in-situ heating experiments in this work with its compatible AHA thermal E-chips^{TM} (Protochips Inc.) that served as the heating platform (shown in **Figure 4.3** (a)-iv). On top of the chip, the metal leads provided resistive heating through the conductive ceramic membrane underneath and controlled the temperatures with well-calibrated heating current. Then, we again used the FIB to mill an open square on the ceramic membrane and to deposit two Pt posts on opposite sides of the square window (**Figure 4.3** (a)-v, (b)). Subsequently, the specimen lamella was lifted out and transferred on top of the membrane of a thermal E-chip horizontally (schematic in **Figure 4.3** (a)-vi, SEM image in **Figure 4.3** (b)) with an Omniprobe^{TM} inside an SEM (FEI Nova 600) chamber. Finally, this lamella was further thinned to a thickness of 60 ~ 80 nm permitting electron beam transparency. The nanowire channel investigated in our in-situ heating experiment is labeled in the TEM image in **Figure 4.3** (c).

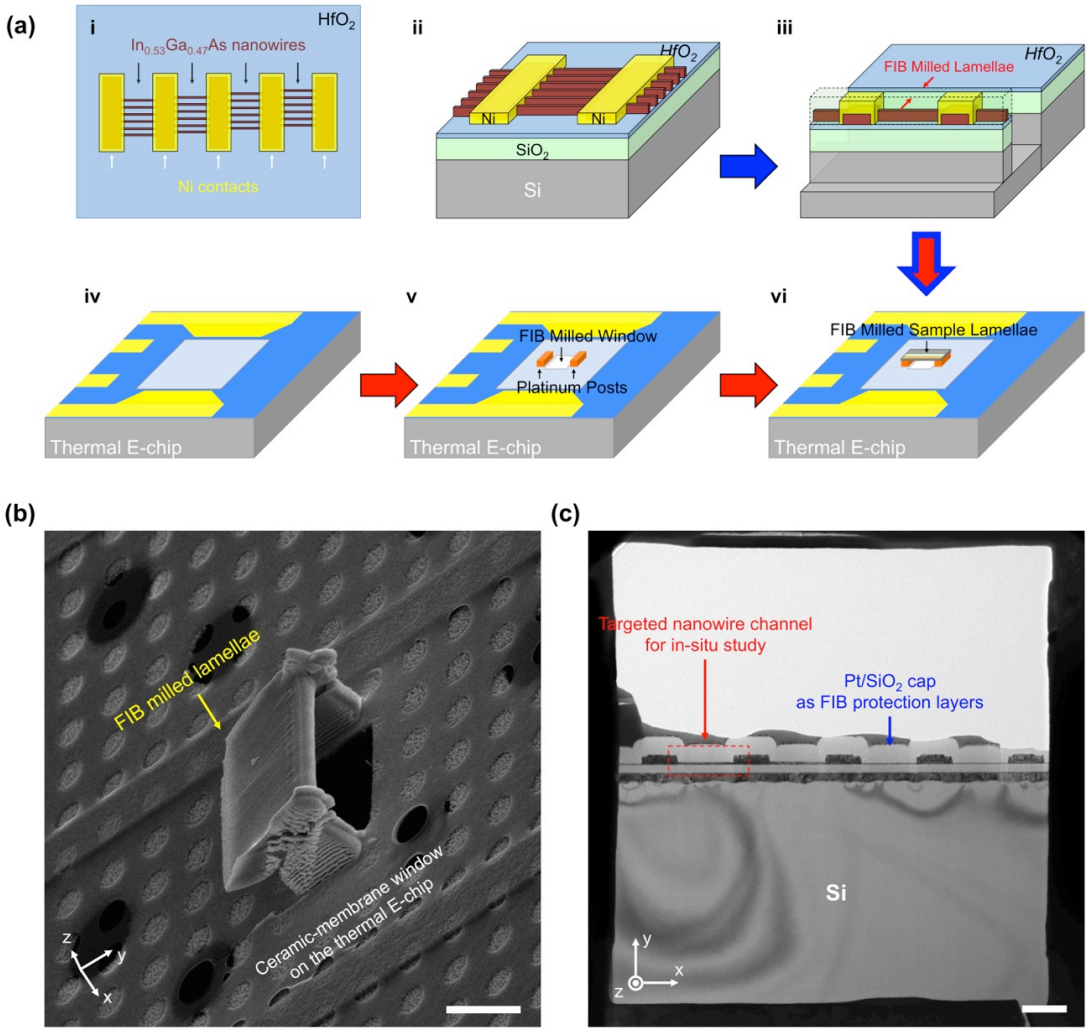

Figure 4.3. Schematics, SEM and TEM images that exhibit the FIB mill and lift-out processes for transferring the specimen lamellae onto the TEM membrane window. (a) Schematics of the process flow, with i-iii representing the FIB process on device substrate and iv-vi representing the transfer process on TEM thermal E-chips™. i) and ii) are the top-view and partial side-view of the fabricated $In_{0.53}Ga_{0.47}As$ nanowire channels with Ni contacts. In each column of nanowires, the center-to-center distance is 120 nm, and the channel length is 1 μm. Between two columns, there is an offset of 30 nm. iii) shows the FIB milling process with the lamellae in parallel with nanowire channel direction. iv) is the schematic for thermal E-chips. Four metal leads on the thermal E-chip will be connected with the probes on Aduro™ TEM heating stage to introduce resistive heating and to read out temperatures. v) shows the FIB milled opening window on the TEM membrane, together with the FIB deposited Pt posts besides. vi) is the lift-out and transfer step that places the specimen lamellae onto the Pt posts atop the thermal E-chip. (c) SEM image of the FIB milled specimen lamellae transferred horizontally onto the TEM membrane on the thermal E-chip. (d) TEM image showing the overview of specimen lamellae and the labeled location of nanowire channel for this in-situ study.

4.3.3 In-situ TEM Movies Recording

In this study, we operated TEM at 300 kV with minimal electron dose that could still maintain clear imaging at highest magnification (× 1M). We blocked the electron beam during the in-situ heating experiments except for imaging and video recording for 1~2 min. The electron beam was never focused on the interested area of the specimen in order to minimize the possible damages induced by electron beam. For over 10 samples that were studied in this work, we didn't observe noticeable beam-effect during the phase transformation from InGaAs to nickelide (detailed discussions in *Appendix V* of the electron beam effect). HRTEM images were extracted from the video frames, and processed in the DigitalMicrograph software where diffraction spots were masked and then inversed to enhance the image clarity.

4.4 Results and Discussions

4.4.1 Ledge Formation and Movement Mechanisms along the Nanowire Channels

Figure 4.4 (a) provides an overview of the interfacial profile between $In_{0.53}Ga_{0.47}As$ nanowire and the reacted nickelide phase after applying the in-situ heating at 320 °C. Debates exist in the literature regarding the stoichiometry of Ni when it forms nickelide compounds with $In_{0.53}Ga_{0.47}As$,[18,21] and the variability of the results can be attributed to the non-equilibrium conditions of short-time annealing, and the sensitivity of the reaction products to the substrates and process temperatures.[19] However, as it will be shown later in this work, the ledge mechanisms for phase transformation is unaffected by the Ni

stoichiometry due to the same hexagonal lattice structure and similar c/a ratios for the different nickelide compounds. Here, we deduced the nickelide phase as $Ni_2In_{0.53}Ga_{0.47}As$ by cross examining the lattice constant (**Figure 4.4** (c)) with known value for this phase.[18]

From the diffraction patterns of two phases across the interface (**Figure 4.4** (b) and (c)), we found that the interface followed the $In_{0.53}Ga_{0.47}As$ (111) || $Ni_2In_{0.53}Ga_{0.47}As$ (0001) atomic planes, in agreement with our earlier *ex-situ* studies.[22] To better understand the interfacial atomic arrangements, ledge formation and movement behaviors, we recorded the nickelide reaction with high-resolution TEM (HRTEM) at × 1M magnification and extracted the time-resolved sequences from the digital video (shown in **Figure 4.4** (d)). To the best of our knowledge, this is the first in-situ observation of solid-state reaction between metal and III-V nanowires with atomic resolution and that clearly exhibits the ledge formation and movement behaviors.

We found that the $Ni_2In_{0.53}Ga_{0.47}As$ ledge formed in a train of single-bilayers[23], as observed near the top surface of the nanowire channel in each time frame of **Figure 4.4** (d). These single-bilayer ledges were under biaxial tensile stresses from inside the interfacial plane ($In_{0.53}Ga_{0.47}As$ (111) || $Ni_2In_{0.53}Ga_{0.47}As$ (0001)) due to lattice mismatch of 5.5%, and a uniaxial compressive stress in the direction that is perpendicular to the interfacial plane due to nickelide volume expansion of 34.2%.[22] These two effects, in principle, add up the compression of $Ni_2In_{0.53}Ga_{0.47}As$ lattice in the out-of-plane directions. While in our case here, the very thin (< 80 nm) TEM sample lamellae in this study facilitate volume expansion laterally perpendicular to the channel and reduces the overall influence of volume expansion on interfacial stresses. Our observations show that these single-bilayer

ledges moved freely along the $[10\bar{1}0]$ direction on the $Ni_2In_{0.53}Ga_{0.47}As$ (0001) surface from the nanowire top surface to the center region, until hindered by a misfit dislocation that is generated to release the compressive stress during the ledge propagation. Those newly generated misfit dislocations were captured in the time duration of 0”0”’~ 14”05”’ and are marked with a cyan colored arrow, the time duration of 9”49”’~14”05”’ with a green colored arrow, and the time duration of 32”39”’~ 36”55”’ with an orange colored arrow. Once a misfit dislocation is formed, the propagation speed of a single-bilayer ledge decreased and another single-bilayer ledge growth can reach the same $Ni_2In_{0.53}Ga_{0.47}As$/ $In_{0.53}Ga_{0.47}As$ of the first single bilayer. The ledge with a double-bilayer height moved together thereafter with a misfit dislocation of $\vec{b} = \frac{2c}{3}[0001]$. Even though double-bilayer ledges could instantly merge and then separate into independent double-bilayer ledges in the following movements (e.g. time duration of 0”0”’~ 9”49”’, ledges related to the two labeled dislocations towards the bottom of the images), a double-bilayer ledge remained stable and never splat into two single-bilayers afterwards. This indicates that double-bilayer is the unit height for a moving $Ni_2In_{0.53}Ga_{0.47}As$ ledge after the generation of a misfit dislocation at the reacting $Ni_2In_{0.53}Ga_{0.47}As$/ $In_{0.53}Ga_{0.47}As$ interface.

Figure 4.4. Ledge formation and movement mechanisms of nickelide phase at atomic resolution. (a) TEM image of the $In_{0.53}Ga_{0.47}As/Ni_2In_{0.53}Ga_{0.47}As$ interface showing a slanted interfacial profile. Scale bar is 20 nm. (b) and (c) Fast Fourier transform (FFT) images of the $In_{0.53}Ga_{0.47}As$ and $Ni_2In_{0.53}Ga_{0.47}As$ segments, respectively, showing the diffraction patterns of $In_{0.53}Ga_{0.47}As$ along the $[0\bar{1}1]$ zone axis (projecting direction in TEM) and of $Ni_2In_{0.53}Ga_{0.47}As$ along the $[\bar{1}2\bar{1}0]$ zone axis. The diffraction patterns indicate that the slanted interface follows the $In_{0.53}Ga_{0.47}As$ (111) || $Ni_2In_{0.53}Ga_{0.47}As$ (0001) atomic planes. (d) HRTEM sequences, showing the ledge formation at the top-surface of nanowire channel and ledge propagations into the nanowire body. The ledges started with a completely strained single-bilayer form and moved with a double-bilayer step height. This double-bilayer step moved together with a misfit dislocation $\vec{b} = \frac{2c}{3}[0001]$ (labeled by the white "$\perp$"), forming a classic "disconnection" at the interface. All these HRTEM images share the same scale bar of 5 nm.

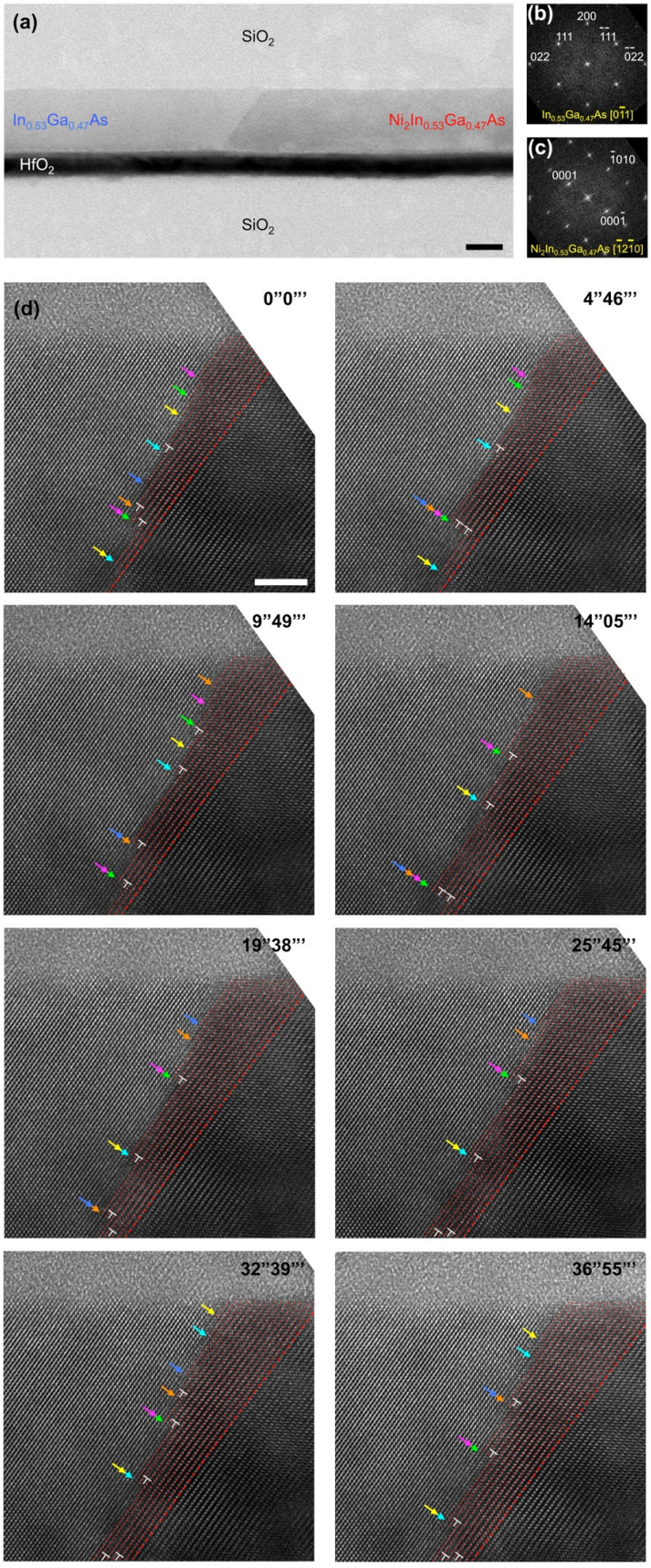
(a)
SiO2
In0.53Ga0.47As
Ni2In0.53Ga0.47As
HfO2
SiO2
(b)
200
111
111
022
022
In0.53Ga0.47As [01̄1]
(c)
1̄010
0001
0001̄
Ni2In0.53Ga0.47As [1̄21̄0]
(d)
0”0”’
4”46”’
9”49”’
14”05”’
19”38”’
25”45”’
32”39”’
36”55”’

4.4.2 Interfacial Disconnection and Atomic Models

These ledge formation and movement behaviors illuminate significant differences with preceding observations made on metal alloying process in elemental semiconductors such as in Si nanowires. When nickel silicide forms in Si nanowire channels, the immediate adjacent phase to pristine Si is $NiSi_2$ that has a cubic lattice structure and a lattice constant that is very close to that of Si.[24,13] Therefore, a coherent heteroepitaxial interface was observed in between Si and $NiSi_2$, and the $NiSi_2$ phase grew by forming ledges of single-bilayer height. However, during the phase transformation in $In_{0.53}Ga_{0.47}As/Ni_2In_{0.53}Ga_{0.47}As$ system, the large lattice mismatch resulted in a misfit dislocation in every two atomic bilayers in $Ni_2In_{0.53}Ga_{0.47}As$ (corresponding to every three atomic bilayers in $In_{0.53}Ga_{0.47}As$, as will be discussed in detail below). The ledges of $Ni_2In_{0.53}Ga_{0.47}As$ moved as a double-bilayer height, coupled with the misfit dislocation. An interface that contains both ledge and misfit dislocation is generally referred to as a "disconnection",[25-27] and our in-situ observations here are the first direct proof of interfacial disconnection in a nanowire channel during thermally induced phase transformation that is typical in metal/III-V semiconductor reactions.

To gain insight into the atomic arrangement at the interfacial disconnection and the motion of the ledges, we developed atomic models to construct the crystal structures at the $In_{0.53}Ga_{0.47}As/Ni_2In_{0.53}Ga_{0.47}As$ interface. Consider the two magnified HRTEM images of the interfacial disconnections (in the same nanowire but at different reaction times) as shown in **Figure 4.5** (a). At time t_1 in **Figure 4.5** (a), one can observe a clear correlation between three layers of $In_{0.53}Ga_{0.47}As$ lattice planes (marked with yellow dashed lines) and two layers of $Ni_2In_{0.53}Ga_{0.47}As$ lattice planes (marked with red dashed lines). Therefore, the

interface is characterized with a misfit dislocation with a Burgers vector $\vec{b} = \frac{a}{3}[111]$, where a = 5.87 Å is the lattice constant of the $In_{0.53}Ga_{0.47}As$ (zinc-blende). For $Ni_2In_{0.53}Ga_{0.47}As$ that has a hexagonal lattice with lattice constants of a = 3.93 Å and c = 5.10 Å,[22] (the Burgers vector defined above is equivalent to $\frac{2c}{3}[0001]$). At time t_2 in **Figure 4.5** (a), we observe the same behavior, where a double-bilayer step height is observed. Shown in **Figure 4.5** (b) are the lattice structures of zinc-blende $In_{0.53}Ga_{0.47}As$ and hexagonal $Ni_2In_{0.53}Ga_{0.47}As$. Along the [111] direction of $In_{0.53}Ga_{0.47}As$ crystal, atomic planes arrange in a A-B-C-A-B-C… manner (shown in **Figure 4.5** (c)), representing a typical fcc stacking. Along the [0001] direction of $Ni_2In_{0.53}Ga_{0.47}As$ crystal, atomic planes arrange in a A-A-A… manner, which is due to the nature of its simple hexagonal lattice (different from typical hexagonal-close-packed (hcp) stacking). Therefore, during the phase transformation from $In_{0.53}Ga_{0.47}As$ to $Ni_2In_{0.53}Ga_{0.47}As$, the atomic bilayers need to glide in each atomic plane in order to transform from A-B-C… type of stacking into A-A-A… type of stacking. Here, we simplified one atomic-bilayer into a lattice plane and depicted the gliding behaviors in **Figure 4.5** (d) and (e). A top-view of the lattice planes is shown in **Figure 4.5** (d), and the top lattice plane has three optional gliding directions to overlap with the bottom lattice plane, i.e. $\frac{1}{6}[11\bar{2}]$, $\frac{1}{6}[1\bar{2}1]$, and $\frac{1}{6}[\bar{2}11]$, corresponding to three Shockley partial dislocations (also referred to as Shockley partials). From a side-view of the lattice planes as shown in **Figure 4.5** (e), three lattice planes need to glide collectively along one of the three Shockley partials in order to eliminate shear stress during phase transformation,[28] as no external shear stress was applied to the NW. Therefore, a group of three (or multiples of three) atomic bilayers in $In_{0.53}Ga_{0.47}As$ crystal will move all together by the collective

gliding of three Shockley partials with a height of $3d_{(111)}$ =10.17 Å which is nearly equivalent to the height of double-bilayer ledge ($2d_{(0001)}$ =10.20 Å) in $Ni_2In_{0.53}Ga_{0.47}As$ crystal with residual strain ≤ 0.3%. This also introduces one misfit-dislocation for each double-bilayer ledge. Finally, the atomic arrangement at the disconnection interface is reconstructed in **Figure 4.5** (f), and both, the single-bilayer nucleus and the double-bilayer ledges are illustrated in the schematic.

Ledges with multilayer height have also been observed during in-situ TEM in other nanowire systems, such as metal-catalyzed growth of Si[29] and GaN[30] nanowires, and phase transformation in InAs nanowire[31] (from wurtzite to zinc-blende). During the metal-catalyzed nanowire growth, the growth species diffuse through the catalyst, supersaturate at the catalyst/nanowire interface, and generate new ledges on the interfacial plane. Since the catalyst has no epitaxial correlation to the nanowire, the number of layers in a ledge largely depends on the supersaturation rate[29,32,33] or the property of nanowire material itself[30]. In the phase transformation of InAs nanowire from wurtzite to zinc-blende phase,[31] the atomic planes changed from A-B-A-B… (hcp) type of stacking to A-B-C… (fcc) type of stacking without elastic strain as the stoichiometry of the InAs and the size of its unit cell are conserved in this phase change. Ledges contained six bilayers by collectively gliding of three Shockley partials that each associated with two atomic bilayers in both the wurtzite and the zinc-blende phases. In our material system of $In_{0.53}Ga_{0.47}As/Ni_2In_{0.53}Ga_{0.47}As$, the phase transformation not only caused an unusual change in atomic stacking (A-B-C… type to A-A-A… type), but also introduced large elastic strain near the interfaces. Therefore, we observed a fixed ledge height of two bilayers in $Ni_2In_{0.53}Ga_{0.47}As$ (three bilayers in $In_{0.53}Ga_{0.47}As$) and a misfit dislocation

associated with the ledge unit. Our observations expound a new type of ledge formation and movement behaviors during contact metallization, that is the phase transformation with large elastic strain in nanowire channels, which serves as a direct proof and in fact the first observation of the applicability of the disconnection theory in nanoscale phase transformation.

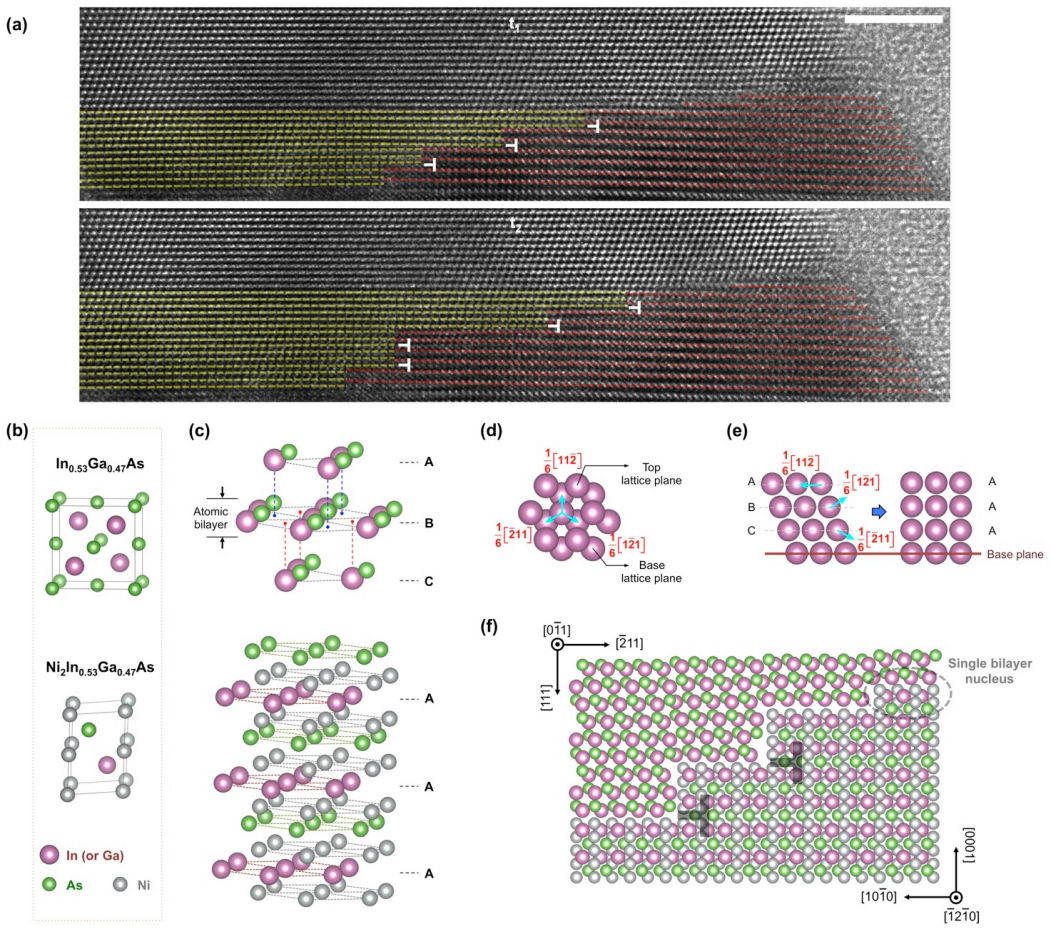

Figure 4.5. Atomic models that reveal the formation of interfacial disconnections during $In_{0.53}Ga_{0.47}As$ to $Ni_2In_{0.53}Ga_{0.47}As$ phase transformation. (a) HRTEM images extracted from two separate time-instant *in-situ* movies in, giving an even closer look at the $In_{0.53}Ga_{0.47}As/Ni_2In_{0.53}Ga_{0.47}As$ interface. Scale bar is 5nm. (b) Lattice structures of $In_{0.53}Ga_{0.47}As$ (zinc blende) and $Ni_2In_{0.53}Ga_{0.47}As$ (simple hexagonal). (c) Atomic arrangements in $In_{0.53}Ga_{0.47}As$ (with [111] direction pointing upwards) and $Ni_2In_{0.53}Ga_{0.47}As$ (with [0001] direction pointing upwards) respectively. In $In_{0.53}Ga_{0.47}As$ crystal, the atomic layers stack in an A-B-C-A-B-C… manner, while in $Ni_2In_{0.53}Ga_{0.47}As$ the stacking is A-A-A…. In $In_{0.53}Ga_{0.47}As$ crystal, an "atomic bilayer" usually refers to the bonded In (or Ga) monolayer and As monolayer. This is also used here for corresponding layers in $Ni_2In_{0.53}Ga_{0.47}As$ crystal after phase transformation. (d) Top-view of two lattice planes in an A-B-C type of stacking, indicating that the top lattice plane has three possible in-plane gliding vectors in order to be overlapping with the bottom lattice plane. (e) Side-view of how the A-B-C stacking of lattice planes shuffle into an A-A-A stacking manner by collective gliding of three lattice planes along three different gliding vectors as shown in (d). (f) The reconstructed atomic structures at the interface in between $In_{0.53}Ga_{0.47}As$ (top left) and $Ni_2In_{0.53}Ga_{0.47}As$ (bottom right). The nature of single-bilayer nucleus and double-bilayer step height is depicted in this schematic, together with the labeled misfit dislocations. We removed one monolayer of As atoms at the interface of $In_{0.53}Ga_{0.47}As$ side, which overlaps with the Ni atoms in $Ni_2In_{0.53}Ga_{0.47}As$, in order to improve the clarity of this structure model at the interface region.

4.4.3 Nucleation Model of the Nickelide Reaction

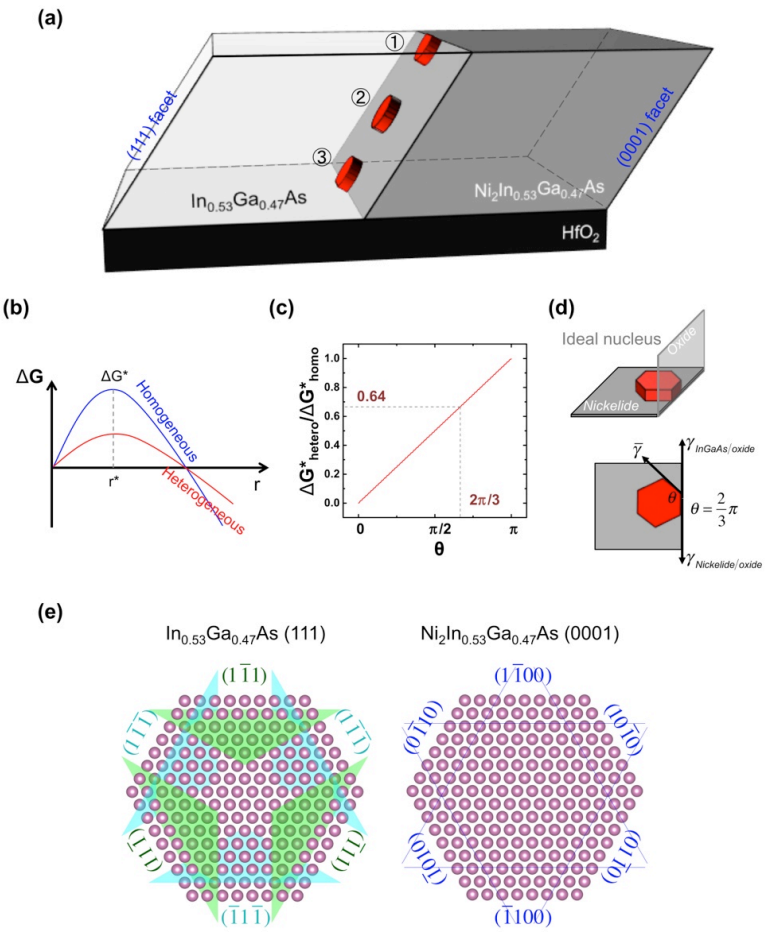

Figure 4.6. Nucleation model of the nickelide reaction in the [011] oriented $In_{0.53}Ga_{0.47}As$ nanowire channel. (a) Schematics of the three possible nucleation sites for nickelide phase on the $In_{0.53}Ga_{0.47}As$/nickelide interface, which are ① heterogeneous nucleation site at $In_{0.53}Ga_{0.47}As$/ nickelide/ SiO_2 triple phase boundary (TPB), ② homogeneous nucleation site at the $In_{0.53}Ga_{0.47}As$/ nickelide interface, and ③ heterogeneous nucleation site at $In_{0.53}Ga_{0.47}As$/ nickelide/ HfO_2 TPB. (b) Plot of free energy of a nucleus as a function of radius for both homogeneous and heterogeneous cases according to the derived thermodynamic model (details in *Appendix VI*). (c) The ratio of energy barriers $\Delta G^*_{\text{hetero}} / \Delta G^*_{\text{homo}}$ as a function of contact angle of the nucleus at the interface of $In_{0.53}Ga_{0.47}As$/dielectric as showing in (b). (d) A hypothesized shape of heterogeneous nucleus that shows a hexagonal shape. This hexagonal disc isn't necessarily equilateral and may contain small facet steps, while the contact angle will be fixed at $\theta = 2\pi/3$ that corresponds to the ratio $\Delta G^*_{\text{hetero}} / \Delta G^*_{\text{homo}} = 0.64$ in (c). (d) An ideal heterogeneous nucleus that shows a hexagonal shape from side and top views. (e) The reason for the hypothesized hexagonal nucleus is illustrated by the atomic arrangements at the $In_{0.53}Ga_{0.47}As$ (111) || $Ni_2In_{0.53}Ga_{0.47}As$ (0001) interface, enclosed by the low-energy facets for both sides of the interface.

We finally provide a qualitative analysis of the nickelide phase nucleation based on thermodynamic and kinetic grounds. This is to explain why the $Ni_2In_{0.53}Ga_{0.47}As$ phase nucleated near the top of the nanowire channel where $In_{0.53}Ga_{0.47}As$ interfaced with SiO_2 layer (as shown in **Figure 4.4** (d)), as opposed to the trimethylalumnium (TMA) treated $HfO_2/In_{0.53}Ga_{0.47}As$ interface. As shown in **Figure 4.6** (a), there are three possible nucleation sites: ① heterogeneous nucleation site near the nanowire top surface, where $In_{0.53}Ga_{0.47}As$ interfaces with SiO_2 cap layer, ② homogeneous nucleation site inside the nanowire channel on the $In_{0.53}Ga_{0.47}As$/nickelide interfacial plane, and ③ heterogeneous nucleation site near the nanowire base, where $In_{0.53}Ga_{0.47}As$ interfaces with HfO_2. Considering the classical case with a disc shaped nucleus (details in *Appendix VI*), the ratio of energy barriers between heterogeneous (truncated disc) and homogeneous (full disc) nuclei is:

$$\frac{\Delta G^*_{hetero}}{\Delta G^*_{homo}} = \frac{\theta - \sin\theta\cos\theta}{\pi} . \qquad (4\text{-}1)$$

where θ is the contact angle of heterogeneous nucleus with the $In_{0.53}Ga_{0.47}As$/oxide interface.

Figure 4.6 (b) schematically illustrates the relation between system free energy and the radius of nucleus, for both homogeneous and heterogeneous cases. The energy barrier for heterogeneous nucleation could be much smaller than the homogeneous nucleation, and the ratio of $\Delta G^*_{hetero}/\Delta G^*_{homo}$ depends on the contact angle θ as can be deduced from equation (1). $\Delta G^*_{hetero}/\Delta G^*_{homo}$ is plotted in **Figure 4.6** (c). In order to determine the ratio of

$\Delta G^*_{hetero} / \Delta G^*_{homo}$, one needs to know each value of the interfacial energies that determine the contact angle θ. However, most of the interfacial energies ($\gamma_{nickelide/oxide}$ and $\overline{\gamma}$) for the $In_xGa_{1-x}As$ system were not measured nor calculated to date. Despite this, we can hypothesize a value for θ by considering the possible shape of nucleus as shown in **Figure 4.6** (d) and (e). We argue that the critical nucleus is preferred to form on coherent interfaces with a shape that is determined by the low energy facets.[34] In our in-situ studies at the temperature range of 280 °C ~ 350 °C, we observed clear facet selectivity of $In_{0.53}Ga_{0.47}As$ (111) on which the $Ni_2In_{0.53}Ga_{0.47}As$ phase preferred to grow. Therefore, it's reasonable to speculate that within our studied kinetic regime, the nucleated $Ni_2In_{0.53}Ga_{0.47}As$ phase should be bound by other equivalent {111} facets as shown in **Figure 4.6** (e). If we consider the other side at the interface, $Ni_2In_{0.53}Ga_{0.47}As$ phase has a hexagonal lattice structure in which $\{1\bar{1}00\}$ are the typically preferred low energy facets.[35,36] Both of these two facet-groups enclose an equivalent hexagonal boundary for the critical nucleus. At the same time, studies of silicide formation in Si nanowires informed that the silicide/oxide interface usually had a larger interfacial energy than Si/SiO_2 interface, resulting in a contact angle $\theta > 90°$.[11] Therefore, for a reasonably speculated contact angle of 120° in the $In_{0.53}Ga_{0.47}As/Ni_2In_{0.53}Ga_{0.47}As$ system under our experimental conditions, the ratio of nucleation barrier is $\Delta G^*_{hetero} / \Delta G^*_{homo} = 0.64$ (labeled in **Figure 4.6** (c)), which is within a typical range of ratios that was found for the more studied silicide growth[37,9]. This indicates the thermodynamic preference of heterogeneous nucleation, but does not account for kinetic considerations. For this, we need to consider the nucleation rate, which can be characterized as,

$$R = \omega C \exp\left(-\frac{\Delta G_D}{kT}\right)\exp\left(-\frac{\Delta G^*}{kT}\right), \tag{4-2}$$

where ω is frequency related to atomic vibrations, C is the concentration of critical sized nucleus, ΔG_D is the activation energy for Ni atoms to diffuse to the reaction interface, and ΔG* is the energy barrier for nucleus. By invoking known values into equation (4-2), (details in *Appendix VI*), we can get,

$$\frac{R_{hetero}}{R_{homo}} \approx 1.26 \exp\left(\frac{\Delta G^*_{homo} - \Delta G^*_{hetero}}{kT}\right). \tag{4-3}$$

Therefore, the nucleation rate is also directly related to the nucleation barrier. Since the nucleation barrier ΔG^*_{homo} is about few electron-volts (eV) for a typical metallization process in nanowires,[11,37] the estimated ratio of nucleation rate $R_{hetero}/R_{homo} \geq 1.5 \times 10^6$. This analysis corroborate our experimental observations that the heterogeneous nucleation is much more favorable both thermodynamically and kinetically.

There are two types of heterogeneous nucleation sites in our model (① and ③ in **Figure 4.6** (a)), which are at the interface with SiO_2 top or with HfO_2 bottom layers. This HfO_2 layer was grown on $In_{0.53}Ga_{0.47}As$ by atomic layer deposition (ALD) with a pretreatment of 5-cycles consecutive pulses of TMA and H_2 plasma. This surface pretreatment was found to introduce an intermediate Al layer and enhance the bonding strength between $In_{0.53}Ga_{0.47}As$ and HfO_2 by forming As-Al-As bonds and Al-O bond on each side respectively.[38,39] It is expected that the abundance of dangling bonds and vacant sites at the sputtered SiO_2 layer on $In_{0.53}Ga_{0.47}As$ (as opposed to ALD deposited

HfO_2) will enhance the diffusion of Ni at that interface since Ni is known to diffuse through interstitial states.[40] We believe that this improved bonding strength between $In_{0.53}Ga_{0.47}As$ and HfO_2 reduces the diffusion rate of Ni at this interface and increases the ΔG_D in equation (4-2), resulting in a reduced nucleation rate. One should not exclude the possibility that the bonding strength increases the elastic strain E_{strain} if $Ni_2In_{0.53}Ga_{0.47}As$ nucleates at the $In_{0.53}Ga_{0.47}As/HfO_2$ interface and then increases the nucleation barrier according to equation S8 (supporting information). Therefore, we believe that the coordinated bonding between $In_{0.53}Ga_{0.47}As$ and HfO_2 limits the heterogeneous nucleation at this interface. Moreover, though the $In_{0.53}Ga_{0.47}As$ nanowire is also covered by SiO_2 on the sides, we believe that once $Ni_2In_{0.53}Ga_{0.47}As$ nucleated from the top surface the fast diffusion of Ni along the sidewalls would only contribute to the ledge propagations by nucleating at the kink sites on the train of ledges instead of nucleating new ledges.

4.5 Conclusions

In summary, we carried out in-situ heating TEM experiments to study the contact metallization process in between Ni contact and $In_{0.53}Ga_{0.47}As$ nanowire channels, and observed the detailed ledge formation and movement behaviors at atomic resolution. We found that the reacted interface followed the $In_{0.53}Ga_{0.47}As$ (111) || $Ni_2In_{0.53}Ga_{0.47}As$ (0001) atomic plane, and the ledges nucleated as a train of strained single-bilayers. Once the strain energy in single-bilayer ledges was relieved in part by forming misfit dislocations, their velocity decreased permitting the formation of associated single-bilayer ledges, the double-bilayer ledges. Consequently, these nickelide ledges moved with a double-bilayer height

that became the unit height of ledges in this phase transformation. Our atomic models depicted the ledge propagation behaviors that are related to collective gliding of three $In_{0.53}Ga_{0.47}As$ single-bilayers along three Shockley partials to cancel out the shear stress during phase transformation. Our analysis for the nucleation of new ledges indicates that the heterogeneous nucleation at the nanowire top surface is favored both kinetically and thermodynamically and is in good agreement with our experimental observations. Our in-situ studies demonstrated for the first time the applicability of interfacial disconnection theory in contact metallization for compound semiconductor nanoscale channels.

Most of chapter 4 was published in *Small* 2017. R. Chen, S. A. Dayeh. The dissertation author is the first author of this paper.

4.6 References

1. Saka H, Kamino T, Ara S, Sasaki K (2008) In situ heating transmission electron microscopy. MRS bulletin 33 (02):93-100

2. Petkov N (2013) In situ real-time TEM reveals growth, transformation and function in one-dimensional nanoscale materials: from a nanotechnology perspective. ISRN Nanotechnology 2013:893060

3. Zheng H, Meng YS, Zhu Y (2015) Frontiers of in situ electron microscopy. MRS Bulletin 40 (01):12-18

4. Boston R, Schnepp Z, Nemoto Y, Sakka Y, Hall SR (2014) In Situ TEM Observation of a Microcrucible Mechanism of Nanowire Growth. Science 344 (6184):623-626

5. Wang S-C, Lu M-Y, Manekkathodi A, Liu P-H, Lin H-C, Li W-S, Hou T-C, Gwo S, Chen L-J (2014) Complete Replacement of Metal in Metal Oxide Nanowires via Atomic Diffusion: In/ZnO Case Study. Nano Letters 14 (6):3241-3246

6. Panciera F, Chou YC, Reuter MC, Zakharov D, Stach EA, Hofmann S, Ross FM (2015) Synthesis of nanostructures in nanowires using sequential catalyst reactions. Nat Mater 14 (8):820-825

7. Yu Q, Mao M-M, Li Q-J, Fu X-Q, Tian H, Li J-X, Mao SX, Zhang Z (2016) In Situ Observation on Dislocation-Controlled Sublimation of Mg Nanoparticles. Nano letters 16 (2):1156-1160

8. Fauske VT, Huh J, Divitini G, Dheeraj DL, Munshi AM, Ducati C, Weman H, Fimland B-O, van Helvoort ATJ (2016) In Situ Heat-Induced Replacement of GaAs Nanowires by Au. Nano Letters 16 (5):3051-3057

9. Tang W, Picraux ST, Huang JY, Gusak AM, Tu K-N, Dayeh SA (2013) Nucleation and Atomic Layer Reaction in Nickel Silicide for Defect-Engineered Si Nanochannels. Nano Letters 13 (6):2748-2753

10. Tang W, Picraux ST, Huang JY, Liu X, Tu K, Dayeh SA (2013) Gold catalyzed nickel disilicide formation: a new solid–liquid–solid phase growth mechanism. Nano letters 13 (12):6009-6015

11. Chou Y-C, Wu W-W, Chen L-J, Tu K-N (2009) Homogeneous Nucleation of Epitaxial CoSi2 and NiSi in Si Nanowires. Nano Letters 9 (6):2337-2342

12. Chen R, Jungjohann KL, Mook WM, Nogan J, Dayeh SA (2017) Atomic Scale Dynamics of Contact Formation in the Cross-section of InGaAs Nanowire Channels. Nano letters. doi:10.1021/acs.nanolett.6b04713

13. Tang W, Nguyen B-M, Chen R, Dayeh SA (2014) Solid-state reaction of nickel silicide and germanide contacts to semiconductor nanochannels. Semiconductor Science and Technology 29 (5):054004

14. Kim S, Yokoyama M, Taoka N, Iida R, Lee S, Nakane R, Urabe Y, Miyata N, Yasuda T, Yamada H (2010) Self-aligned metal source/drain $In_xGa_{1-x}As$ n-MOSFETs using Ni-InGaAs alloy. Electron Devices Meeting (IEDM):26.26. 21-26.26. 24

15. Zhang X, Guo HX, Gong X, Zhou Q, Yeo Y-C (2012) A Self-Aligned Ni-InGaAs Contact Technology for InGaAs Channel n-MOSFETs. Journal of The Electrochemical Society 159 (5):H511-H515

16. Abraham M, Yu S-Y, Choi WH, Lee RT, Mohney SE (2014) Very low resistance alloyed Ni-based ohmic contacts to InP-capped and uncapped n+-$In_{0.53}Ga_{0.47}As$. Journal of Applied Physics 116 (16):164506

17. Czornomaz L, El Kazzi M, Hopstaken M, Caimi D, Mächler P, Rossel C, Bjoerk M, Marchiori C, Siegwart H, Fompeyrine J (2012) CMOS compatible self-aligned S/D regions for implant-free InGaAs MOSFETs. Solid-State Electronics 74:71-76

18. Ivana, Lim Foo Y, Zhang X, Zhou Q, Pan J, Kong E, Samuel Owen MH, Yeo Y-C (2013) Crystal structure and epitaxial relationship of $Ni_4InGaAs_2$ films formed on InGaAs by annealing. Journal of Vacuum Science & Technology B 31 (1):012202

19. Shekhter P, Mehari S, Ritter D, Eizenberg M (2013) Epitaxial NiInGaAs formed by solid state reaction on $In_{0.53}Ga_{0.47}As$: Structural and chemical study. Journal of Vacuum Science & Technology B 31 (3):031205

20. Zhiou S, Nguyen-Thanh T, Rodriguez P, Nemouchi F, Rapenne L, Blanc N, Boudet N, Gergaud P (2016) Reaction of Ni film with $In_{0.53}Ga_{0.47}As$: Phase formation and texture. Journal of Applied Physics 120 (13):135304

21. Perrin C, Ghegin E, Zhiou S, Nemouchi F, Rodriguez P, Gergaud P, Maugis P, Mangelinck D, Hoummada K (2016) Formation of $Ni_3InGaAs$ phase in Ni/InGaAs contact at low temperature. Applied Physics Letters 109 (13):131902

22. Chen L-J, Wu W-W (2015) Metal silicide nanowires. Japanese Journal of Applied Physics 54 (7S2):07JA04

23. In InGaAs crystal, an "atomic bilayer" usually refers to the bonded In (or Ga) monolayer and As monolayer. This name is also used here in this manuscript for corresponding layers in nickelide crystal after phase transformation.

24. Tang W, Dayeh SA, Picraux ST, Huang JY, Tu K-N (2012) Ultrashort Channel Silicon Nanowire Transistors with Nickel Silicide Source/Drain Contacts. Nano Letters 12 (8):3979-3985

25. Hirth JP (1994) Dislocations, steps and disconnections at interfaces. Journal of Physics and Chemistry of Solids 55 (10):985-989

26. Hirth J (1994) Ledges and dislocations in phase transformations. Metallurgical and Materials Transactions A 25 (9):1885-1894

27. Hirth JP, Hoagland RG, Kurtz RJ (1998) The motion of multiple height ledges and disconnections in phase transformations. Metallurgical and Materials Transactions A 29 (8):2033-2038

28. Li N, Yadav SK, Wang J, Liu X-Y, Misra A (2015) Growth and Stress-induced Transformation of Zinc blende AlN Layers in Al-AlN-TiN Multilayers. Scientific Reports 5:18554

29. Hofmann S, Sharma R, Wirth CT, Cervantes-Sodi F, Ducati C, Kasama T, Dunin-Borkowski RE, Drucker J, Bennett P, Robertson J (2008) Ledge-flow-controlled catalyst interface dynamics during Si nanowire growth. Nat Mater 7 (5):372-375

30. Gamalski AD, Tersoff J, Stach EA (2016) Atomic Resolution in Situ Imaging of a Double-Bilayer Multistep Growth Mode in Gallium Nitride Nanowires. Nano letters 16 (4):2283-2288

31. Zheng H, Wang J, Huang JY, Wang J, Zhang Z, Mao SX (2013) Dynamic Process of Phase Transition from Wurtzite to Zinc Blende Structure in InAs Nanowires. Nano Letters 13 (12):6023-6027

32. Wen CY, Tersoff J, Reuter MC, Stach EA, Ross FM (2010) Step-Flow Kinetics in Nanowire Growth. Physical Review Letters 105 (19):195502

33. Cui H, Lü YY, Yang GW, Chen YM, Wang CX (2015) Step-Flow Kinetics Model for the Vapor–Solid–Solid Si Nanowires Growth. Nano Letters 15 (5):3640-3645

34. Porter DA, Easterling KE, Sherif M (2009) Phase Transformations in Metals and Alloys, (Revised Reprint). CRC press,

35. Pankoke V, Kratzer P, Sakong S (2011) Calculation of the diameter-dependent polytypism in GaAs nanowires from an atomic motif expansion of the formation energy. Physical Review B 84 (7):075455

36. Ng KW, Ko WS, Lu F, Chang-Hasnain CJ (2014) Metastable Growth of Pure Wurtzite InGaAs Microstructures. Nano Letters 14 (8):4757-4762

37. Chou Y-C, Wu W-W, Lee C-Y, Liu C-Y, Chen L-J, Tu K-N (2011) Heterogeneous and Homogeneous Nucleation of Epitaxial NiSi2 in [110] Si Nanowires. The Journal of Physical Chemistry C 115 (2):397-401

38. Melitz W, Shen J, Kent T, Kummel AC, Droopad R (2011) InGaAs surface preparation for atomic layer deposition by hydrogen cleaning and improvement with high temperature anneal. Journal of Applied Physics 110 (1):013713

39. Cai G, Sun Q, Jia Y, Liang E (2016) Al passivation effect at the HfO2/GaAs interface: A first-principles study. Materials Science in Semiconductor Processing 41:1-5

40. Ciccariello J, Poize S, Gas P (1990) Lattice and grain boundary self‐diffusion in Ni2Si: Comparison with thin‐film formation. Journal of applied physics 67 (7):3315-3322

Chapter 5: *In-situ* Control of Synchronous Germanide/Silicide Reactions with Ge/Si Core/Shell Nanowires to Monitor Formation and Strain Evolution in Abrupt 2.7nm Channel Length

5.1 Introduction

Besides the homogeneous nanowires that we have discussed in chapter 2-4, semiconductor heterostructured transistors also play a pivotal role in advanced high-speed analog telecommunications circuits and amplifiers.[1,2] The performance of these analog devices and that of logic devices is enhanced at shorter channel lengths and can be tailored by strain engineering through compositional change parallel to or in the direction of current transport, such as in the SiGe source/drain regrowth for Si channels.[3,4] The standard practice in obtaining short channel devices is enabled by the solid-state reaction of self-aligned contacts.[5,6] The combination of heterostructure engineering and self-aligned contacts at atomic to nano-scales is expected to refine the benefits of the two approaches. However, despite macroscopic studies on forming short transistor channels in heterostructured nanowires,[7-10] detailed metallurgical studies on solid-state reaction with heterostructured nanowires and the morphology of the contact/semiconductor interface have not been pursued thus far. Prior detailed efforts in this field have primarily focused on metallic contact formation in homogeneous semiconductor nanowires, such as in Si,[11,12] Ge,[13,14] and III-V[15,16] NWs.

We focus in this work on Ge/Si core/shell NWs because they have several advantages including alleviated surface scattering and accumulated holes in the core due to type-II band alignment between Ge and Si,[17] and therefore larger hole-mobility in the Ge core. Additionally, the lower strain in the Si shell – due to strain sharing in core/shell NW geometry – than its thin-film counterpart,[18,19] leads to the growth of more uniform Si layers on Ge. Therefore, we used the Ge/Si core/shell NW as a model system to investigate the compound contact formation between metal (Ni) and semiconductor heterostructures *in situ* inside a transmission electron microscope (TEM).

5.2 Summary of Results

In this work, we found that the solid-state reactions between Ni and Ge/Si core/shell nanowires resulted in a protruded and a leading $NiSi_y$ segment into the channel. A single $Ni_2Ge/NiSi_y$ to Ge/Si core/shell interface was achieved by the selective shell removal near the Ni source/drain contact areas. Using in situ transmission electron microscopy, we measured the growth rate and anisotropic strain evolution in ultra-short channels. We found elevated compressive strains near the interface between the compound contact and the NW and relatively lower strains near the center of the channel which increased exponentially below the 10 nm channel length to exceed 10% strain at 3 nm lengths. These compressive strains are expected to result in a non-homogeneous energy band structure in Ge/Si core/shell NWs below 10 nm and potentially benefit their transistor performance.

5.3 Experiment

The Ge, Si, and Ge/Si core/shell NWs in this work were grown in a low pressure, cold wall chemical vapor deposition (CVD) system.[20,21] The diameters of Ge cores ranged from 10 ~ 35 nm and the Si shells had an average thickness of 2 nm, both measured by high-resolution TEM (HRTEM).

For imaging the compound contacts formation, NWs were sonicated and suspended in isopropyl alcohol (IPA) and then drop-casted on top of a 50 nm thin Si_3N_4 window of the commercial Si TEM apertures (Norcada Inc). After recording the locations of dispersed NWs, e-beam lithography was used to define the source/drain contacts followed by 120 nm Ni deposition. Prior to Ni deposition, a 30s buffered oxide etch (BOE, 1:20 in deionized water) dip was applied to each sample to ensure an oxide free interface between metal and NW. For some devices, a rapid thermal annealing (RTA) furnace provided the *ex-situ* heating prior to loading the samples into a Tecnai F30 TEM. For other devices, *in-situ* heating was performed by a single-tilt Gatan heating-holder with temperatures applied and read out by a hot-stage controller (Model 628). Energy-dispersive X-ray spectroscopy (EDX) was collected for elemental analysis under scanning TEM (STEM) model. Finally, the recoded HRTEM images were processed in the DigitalMicrograph software to extract the reciprocal lattice by fast-Fourier transform (FFT).

5.4 Results and Discussions

5.4.1 Control of Synchronous Nickel Germanide Core and Silicide Shell Growth

Under the same fabrication and imaging conditions, we found distinct growth-rate behaviors and interface morphology in the Ni reaction with Ge, Si, and Ge/Si core/shell NWs that have similar diameters (**Figure 5.1**). The three samples underwent a simultaneous *ex situ* rapid thermal anneal (RTA) process at 300 °C for 30 s with a forming gas (N_2/H_2) flow at a chamber pressure of 1 Torr. We observed that the nickel germanide/germanium (Ni_xGe/Ge) interface remained flat during the reaction as shown in **Figure 5.1** (a), similar to the nickel silicide/Si ($NiSi_y/Si$) interface in **Figure 5.1** (b). However, for the Ge/Si core/shell NW (**Figure 5.1** (c)), the Ni_xGe/Ge and $NiSi_y/Si$ interfaces each remained flat in the core and shell respectively, while the reaction front of $NiSi_y$ shell lead the Ni_xGe core by ~ 20 nm. We then investigated the origin of this behavior in order to control the morphology of the compound contact to the Ge/Si core/shell NW.

Numerous studies on the Ni reaction with homogeneous semiconductor NWs (i.e. Si, Ge) have demonstrated Ni as the dominant diffusion species into NWs and a Ni-diffusion limited (mass-transport limited) growth.[22-24] Ni has a much higher estimated diffusivity in Ge (~8×10^{-9} cm^2/s, at 300 °C)[25] than that in Si (~1×10^{-10} cm^2/s, at 300 °C)[26] due to the larger atomic spacing in Ge lattice.[27] Therefore, the rate of arrival for Ni atoms to the growth interface are less inhibited in Ge than in Si and the reaction rate is consequently faster in Ge leading to a longer Ni_xGe segment (**Figure 5.1** (a)) in Ge NW channels than the $NiSi_y$ segment (**Figure 5.1** (b)) in Si NW channels under the same reaction conditions. In Ge/Si NWs, the Ge core and Si shell share the strain due to the

nearly 4.2% lattice mismatch between the tensile strained Si core and the compressive strained Ge shell. Since the Ge core dominates the volume of the entire NW body, it experiences less strain than the Si shell. Therefore, the Ni diffusivity in Ge/Si core/shell NWs is expected to be little influenced by strain and the reacted Ni_xGe length in Ge/Si core/shell NWs (**Figure 5.1** (c)) was very close to that in Ge NWs. Here, the protruded $NiSi_y$ phase cannot be well explained with the change of Ni diffusivity in the strained Si shell, and other factors may play roles in this phenomenon as we will discuss next.

From separate observations on Ni reaction with other NW materials, we observed distinct ledge nucleation and movement behaviors under the metal pad than in the NW cross-section.[28] In InGaAs, we found that a nickelide shell is quickly formed on the NW surface as the reaction started, and then grew evenly but slowly into the NW core with multiple nucleation sites and reaction interfaces under the metal pad. This is different from the single interface in elementary NW channels when the reaction extends outside the metal pad.[29,30] In the case of Ge/Si nanowire, as the reaction starts underneath the source/drain Ni pads, the Si shell will firstly be reacted to form a $NiSi_y$ shell before the Ge core is completely reacted to form a Ni_xGe core. As a result, the $NiSi_y$ shell protrudes into the channel earlier than the Ni_xGe core extends outside the Ni pad, resulting in a leading $NiSi_y$ reaction front (**Figure 5.1** (c)). We therefore concluded that the Ni_xGe core needs to protrude outside the metal pad and into the channel simultaneously with the $NiSi_y$ shell in order to balance and simultaneously grow the Ni_xGe and $NiSi_y$ fronts. To validate this hypothesis, we carried out *in situ* heating experiments and monitored the dynamic reactions between Ni and Ge/Si NWs inside TEM as is schematically shown in **Figure 5.2** (a)-(b). **Figure 5.2** (c) shows the sequence of reactions near the Ni contact area. The Si shell had

been removed prior to Ni deposition by five cycles of oxidation (ambient environment, 1h) and oxide stripping (BOE 1:20 in deionized water, dip for 30s). We found that the left portion of the NW had a smaller diameter than its right portion due to the Si shell removal on the left. The reaction happened first in the Ge core and then gradually extended into the Ge/Si core/shell region. During this process, $Ni_xGe/NiSi_y$ initially did not have a fixed interface on certain atomic planes of Ge/Si NW and the upper portion of the reacted NW extended further into the channel. Later, the $Ni_xGe/NiSi_y$ compounds gradually started to react uniformly across the entire NW body, and the reaction fronts became flat for both Ni_xGe and $NiSi_y$ at time t_0+14 min. To validate that the reacted $Ni_xGe/NiSi_y$ phases still had a flat front at very short channel lengths, we monitored the reaction in another Ge/Si NW at a channel length below 30 nm as shown in **Figure 5.2** (d). The $Ni_xGe/NiSi_y$ phases nucleated heterogeneously from one side of the NW near the surface and the nucleuses had a step height of multiple atomic layers on the Ge (111) planes as shown in the colored arrows overlaid on **Figure 5.2** (d) panels. The $Ni_xGe/NiSi_y$ reaction front remained flat during further reactions.

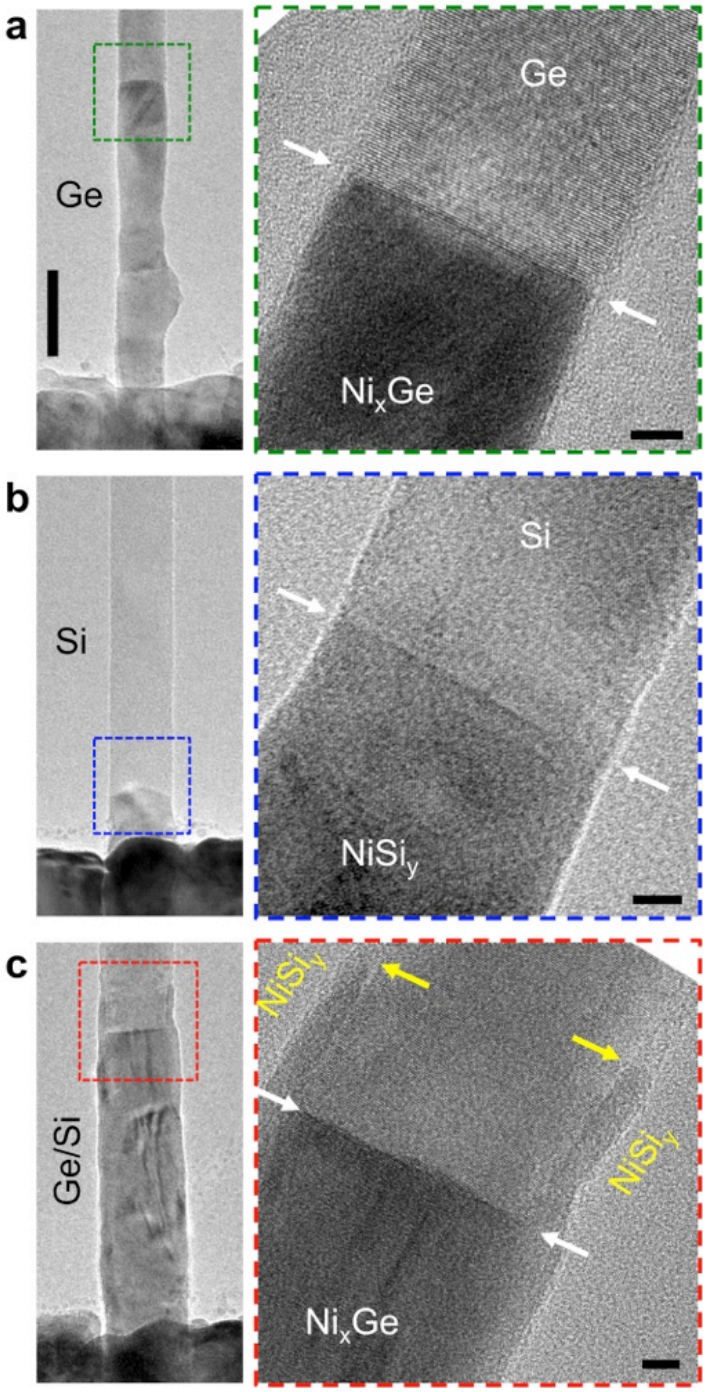

Figure 5.1. (a) TEM image of nickel germanide formation in a Ge NW, with high magnification TEM (HRTEM) image showing the Ni_xGe/Ge interface. (b) TEM image of nickel silicide formation in a Si NW, with HRTEM image showing the $NiSi_y$/Si interface. (c) TEM image of nickel germanide/silicide formation in a Ge/Si core/shell NW, with HRTEM image showing the protruded silicide shell than the germanide core. All three samples were annealed in RTA with forming gas (N_2/H_2) at 300 °C for 30 s. Low magnification TEM images share the same scale bar of 50 nm, and the scale bars for all HRTEM images are 5 nm.

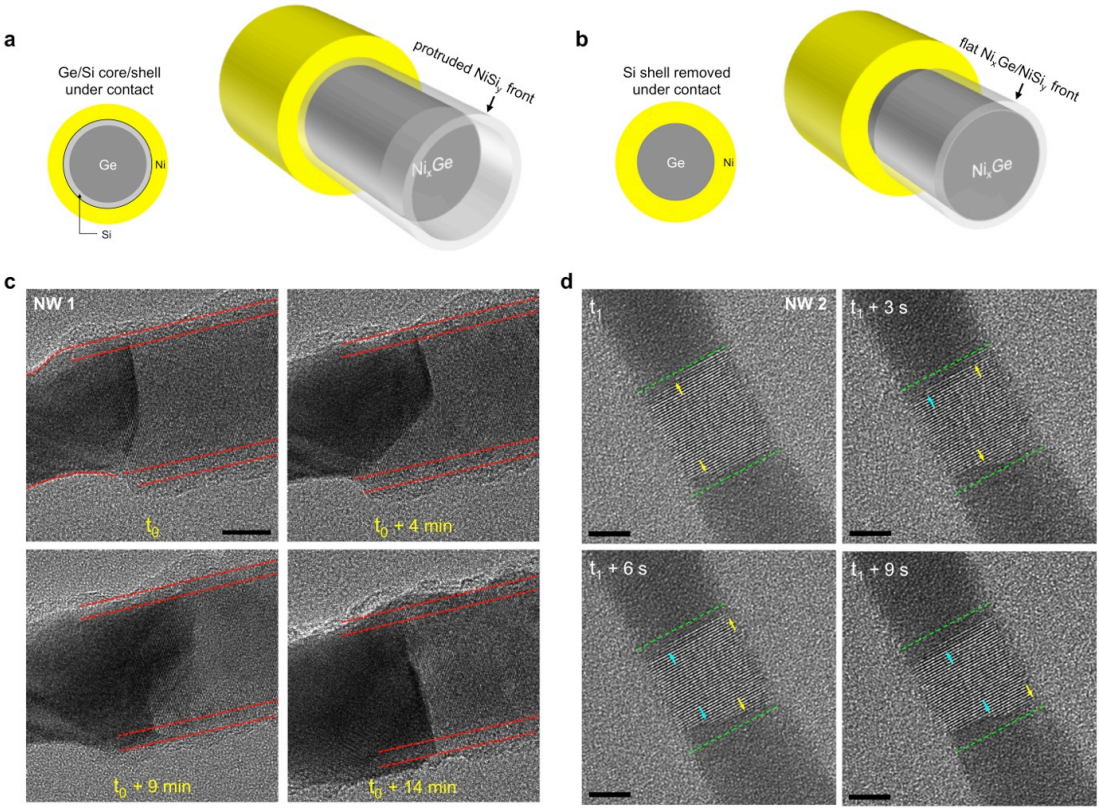

Figure 5.2. (a)-(b) Schematics of $Ni_xGe/NiSi_y$ contact formation in the Ge/Si NW before and after removing the Si shell at the metal contact area prior to Ni deposition, respectively. (c) HRTEM sequences from a Ge/Si NW showing the $Ni_xGe/NiSi_y$ formation near the contact where the Si shell has been removed. (d) HRTEM sequences from another Ge/Si NW showing the flat $Ni_xGe/NiSi_y$ front when approaching very short channel lengths. Scale bars are 5 nm.

5.4.2 Abrupt 2.7nm Ge/Si Channel and the Strain Evolution

Using this fabrication process (**Figure 5.2** (b)) and the *in situ* heating and monitoring method, we were able to control the reacted $Ni_xGe/NiSi_y$ segment lengths and achieved a channel length of 2.7 nm that corresponds to 7 layers of Ge (111) atomic planes as shown in **Figure 5.3** (a). Ultra-small channel lengths have been demonstrated in elementary NWs by similar compound contact reactions monitored *in situ* by TEM, such as 8nm-channel in PtSi/Si/PtSi NW,[31] 15nm-channel in $Cu_3Ge/Ge/Cu_3Ge$ NW,[32] and 2 nm-channel in NiSi/Si/NiSi NW[33] but not in heterostructured NWs. EDX line-scan across the NW diameter in the reacted segment is summarized in **Figure 5.3** (b). The high-angle annular dark-field (HAADF) image is shown as an inset and its contrast contour is also plotted in **Figure 5.3** (b) with the peak intensity normalized with the height of Ni signal counts. The profile width of the Ni signal-counts was close to that of the HAADF contour indicating the full reaction of the NW body with Ni. The profile width of Ge signal was narrower than that of Ni, suggesting that the Ge element was still limited to the core without any intermixing with the Si shell during the reaction with Ni, and that the shell had a thickness of ~ 2nm on each side. The EDX signal of the thin Si shell was barely detected and the Si_3N_4 TEM window underneath provided large background Si counts to which we performed the subtraction of the baseline thus resulting in nearly zero Si counts.

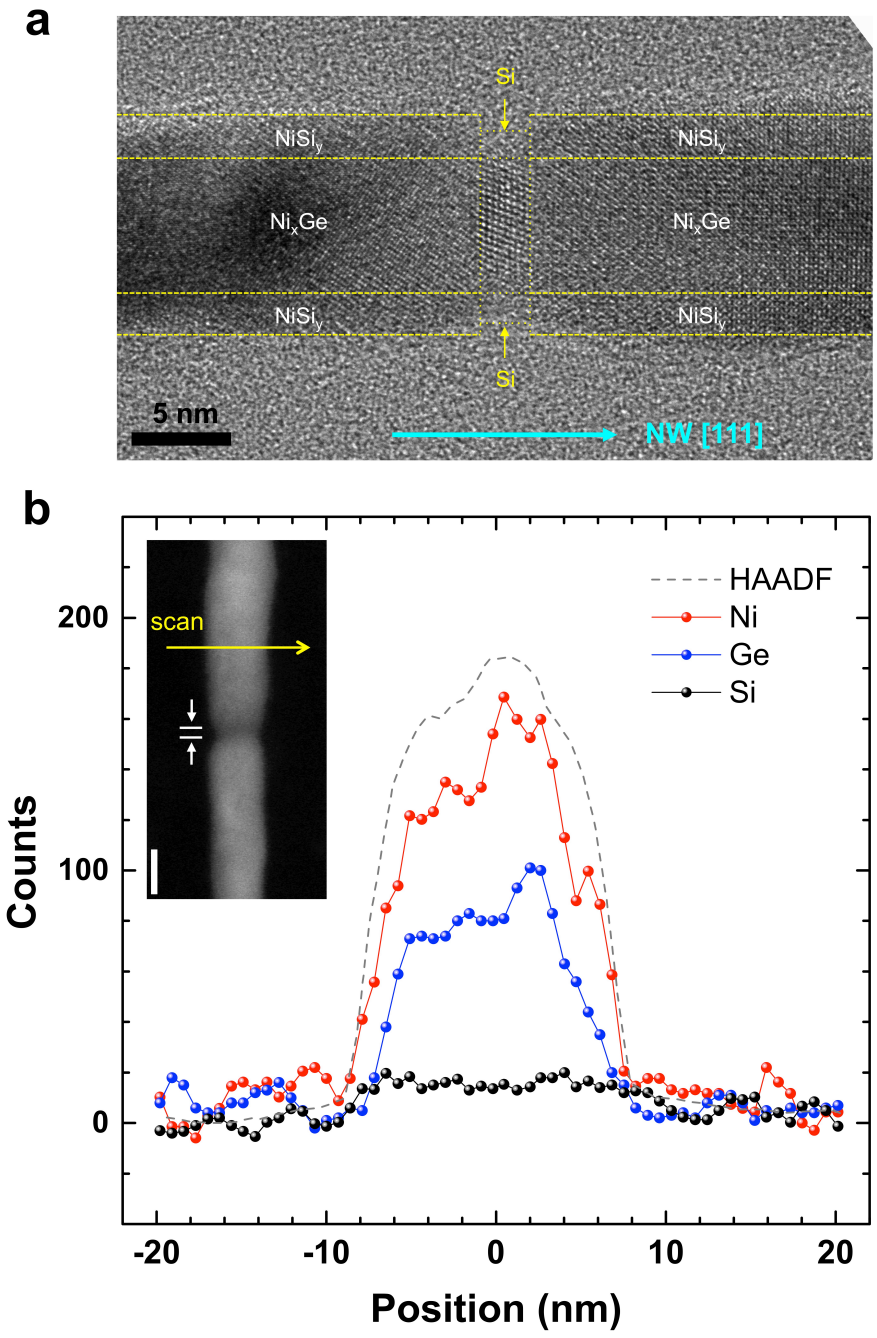

Figure 5.3. (a) HRTEM image of an ultra-short Ge/Si channel of 2.7 nm with $Ni_xGe/NiSi_y$ contacts at both ends. (b) The EDX spectrum with line-scan across the $Ni_xGe/NiSi_y$ contact, and insertion is the HAADF image.

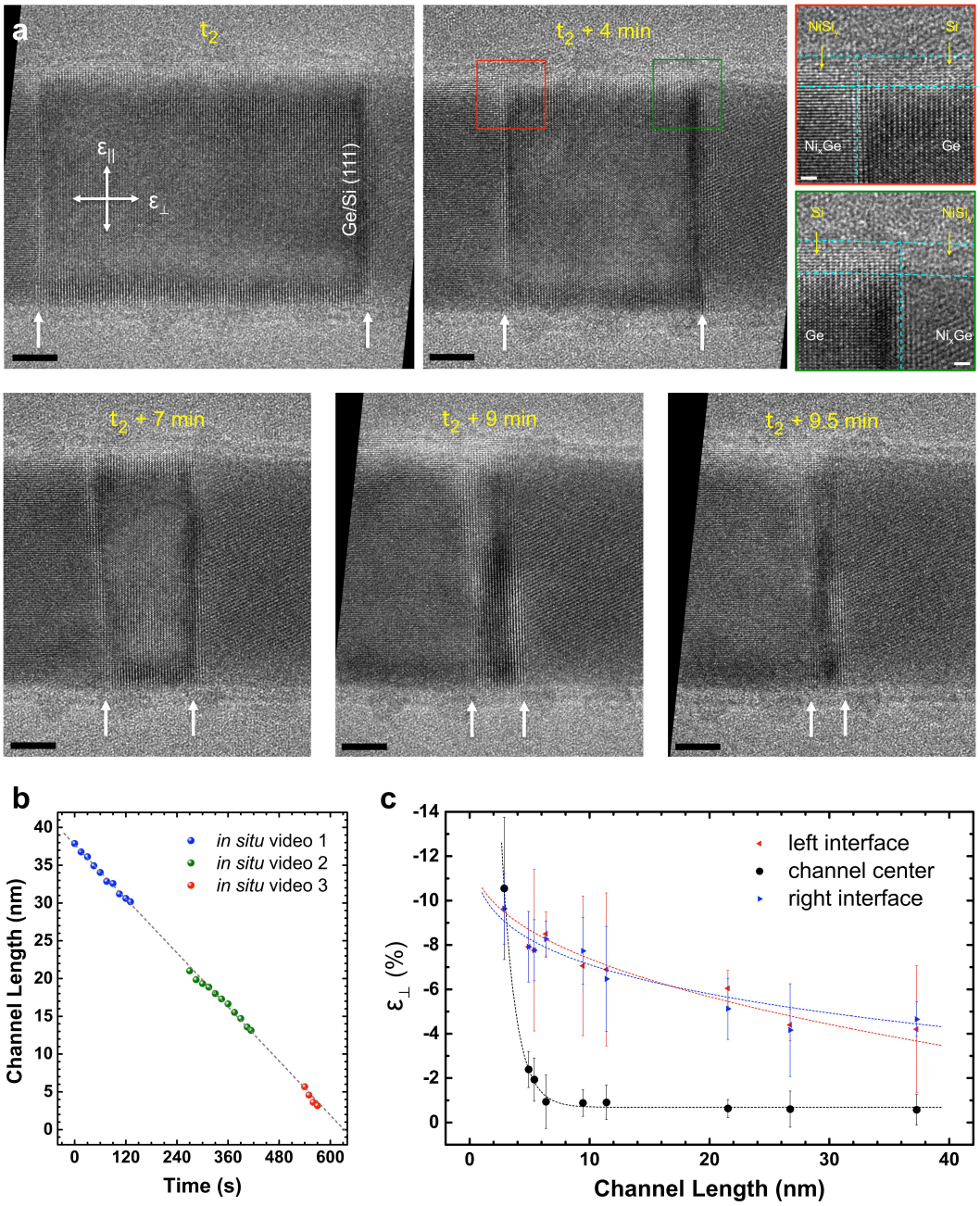

Figure 5.4. (a) HRTEM sequences that show the consecutive formation of $Ni_xGe/NiSi_y$ contacts from both ends of the channel for reaching a very short-channel length. Scale bars are 5 nm. The highlighted HRTEM images show the flat reaction front of Ni_xGe and $NiSi_y$. Scale bars are 1 nm. (b) Plot of channel length as a function of time from the recorded *in situ* videos. (c) Plot of channel strain ($\varepsilon_{\perp}$) as a function of channel length with measurements from left interface, channel center, and right interface, respectively.

At a few nanometer channel lengths, unprecedented levels of strains (along the channel direction) are expected from the 57% volume expansion due to the phase transformation from Ge to Ni_2Ge, a phase that we will discuss its validation later in this work. To systematically investigate the channel strains at different lengths and their influence on the $Ni_xGe/NiSi_y$ growth, we captured *in-situ* videos of the reactions at very short channel lengths with HRTEM as shown in **Figure 5.4** (a). We noticed that the reaction fronts of $Ni_xGe/NiSi_y$ remained aligned on Ge/Si (111) atomic planes and were perpendicular to the channel direction. Labeled on the left-most figure are the directions of the in-plane ($\varepsilon_{\parallel}$) and the out-of-plane ($\varepsilon_{\perp}$) uniaxial strains along the [111] channel direction.[34,35] The non-reacted channel length as a function of time exhibited a linear dependence (**Figure 5.4** (b)) indicating that the kinetic reaction rate remains constant even with strain accumulation at the reaction front for such nanoscale channel lengths. The $\varepsilon_{\perp}$ were analyzed by measuring the inter-plane distances, both near the left and right interfaces of Ge/Si with $Ni_xGe/NiSi_y$ compound contacts and at the center of Ge/Si channel, which are plotted in **Figure 5.4** (c). Each data point was the average of three measurements (top, center and bottom) at the same distance (within 2 nm) from the $Ni_xGe/NiSi_y$ interfaces or at the channel center. The interfacial $\varepsilon_{\perp}$ showed an average value of 5% of compression at a channel length of 40 nm and gradually increased to ~ 10% of compression at a channel length of 3 nm. However, the $\varepsilon_{\perp}$ at Ge/Si channel center showed a different behavior than the interfacial strains and remained below 1% of compression when channel length was larger than 10 nm. As the channel length reached 10 nm and smaller, the center of the overall channel saw a dramatic increase of compressive $\varepsilon_{\perp}$, and reaches to ~ 10.5% at 3 nm channel length. Such a high channel strain is possible in nanowire channels due to the

greatly reduced Young's modulus of the material in nanoscale.[36,37] Very high channel strain up to 12% of compression was also reported in 2 nm channels of NiSi/Si/NiSi NW.[33] Uniaxial strain is known to lift the valence-band degeneracy and lead to the crossover of heavy-hole (HH) and light-hole (LH) bands under compressive stresses.[38,39] As more holes populate the LH bands, the effective mass of holes is reduced leading to an enhanced hole mobility that boosts transistor performance. Mapping and evaluating the stress distributions within short NW transistor channel length becomes inevitable to design nanowire transistor channels below 10 nm. Future efforts will focus on the electrical characterization to quantify the strain effects and to improve the gate-modulation over such small channel lengths.

Finally, we examined the evolution of the compound phase formation and its interfacial correlation with the NW by analyzing the $Ni_xGe/NiSi_y$ phases at different locations of a Ge/Si NW as shown in **Figure 5.5**.

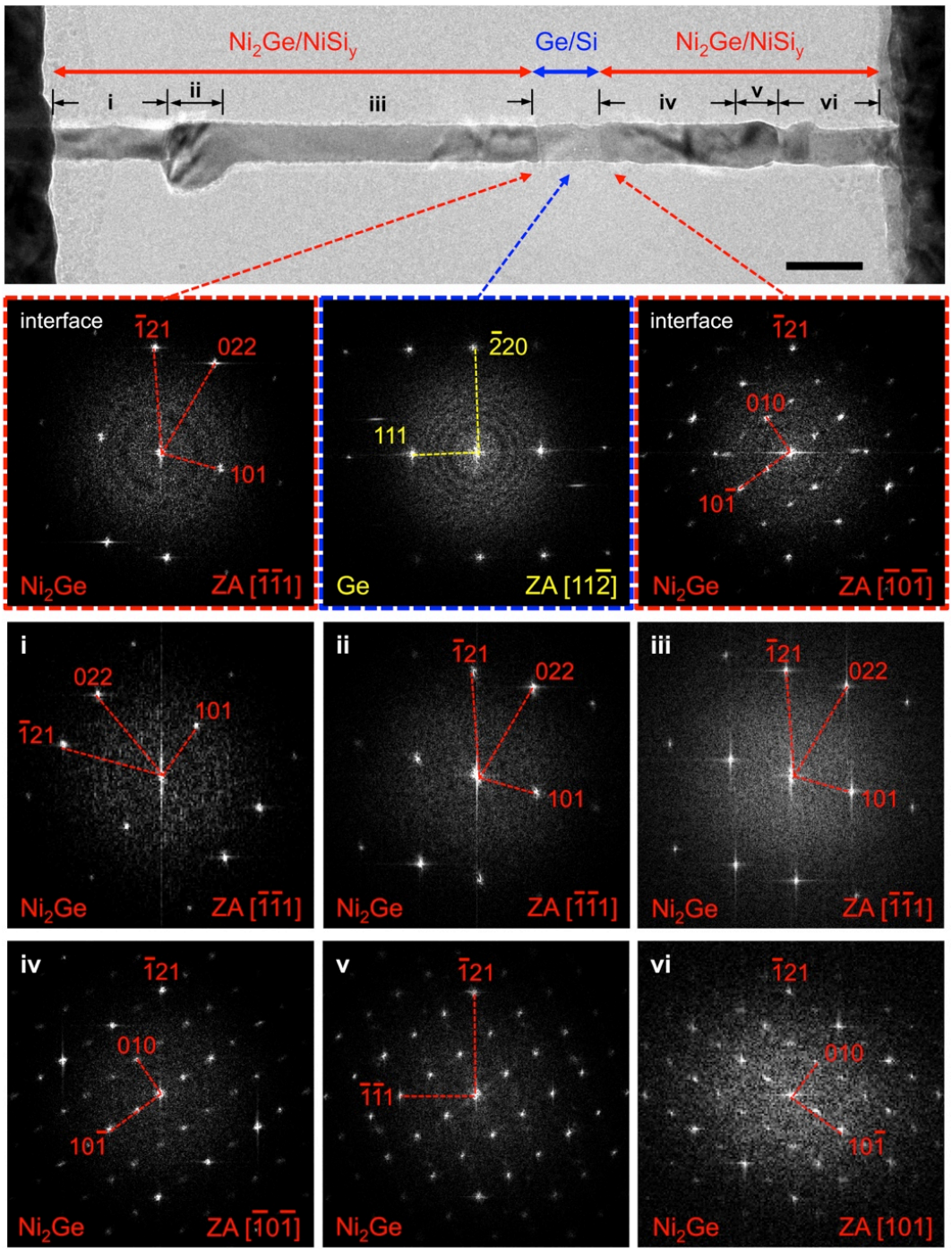

Figure 5.5.TEM image of $Ni_2Ge/NiSi_y$ contact formation in a Ge/Si core/shell NW, and the fast-Fourier transform (FFT) images showing the diffraction patterns at different locations of the nanowire that have been label on the TEM image. The scale bar is 50 nm.

To determine the phase of the formed germanide phase, we compared their lattice constants that were extracted from the FFT patterns with the known lattice constants of common Ni_xGe and $NiSi_y$ phases.[40] We found that over this entire Ge/Si NW the germanide preserved the Ni_2Ge phase that has an orthorhombic crystal structure with lattice constants of a=3.83 Å, b= 5.11 Å, c=7.26 Å. This Ni_xGe (x=2) composition was also confirmed by EDX analysis on more than 5 NWs, which gave an average value of x = 2.09 ± 0.24. The Ni_2Ge segments were generally polycrystalline with the crystal orientations slightly varying at different locations. As shown in **Figure 5.5 (i-iii)**, when the crystal orientation changed from location **i** to location **ii**, the NW was accompanied by an abrupt change of diameter at location **ii**, while at location **iii** the NW diameter in unaltered as no further crystal-rotation happened. This similar behavior happened at transitions from location **vi** to location **iv**. The only difference is that transition **i→iii** occured inside the projected plane rotating along the zone axis of $[\bar{1}\bar{1}1]$, while transition **vi→iv** occurred out of the projected plane rotating along the $[\bar{1}21]$ direction that pointed upward. This **i→iii** crystal rotation was associated with an abrupt diameter change that could be observed in the projected NW image on the screen whereas the **vi→iv** crystal rotation was expected to also have a large diameter change in the direction that was normal to the projected NW image and therefore couldn't be seen. Prior studies have shown that in Ni reaction with Si NWs, the diameter changes were observed in the reacted $NiSi_y$ regions due to the different compositions (y values, and therefore different volume expansions) in each segment.[11,41,42] In contrast, for the Ni reaction with Ge NWs, segregated nano-particles as opposed to diameter changes were observed at the surface of reacted Ni_xGe region that are likely due to the instable native germanium oxide and the large lattice mismatch

between Ni_xGe and Ge.[43] The interfacial correlations between Ni_2Ge and Ge were also found to be different at the two sides of the Ge/Si channel. On the left side, the Ni_2Ge/Ge followed a crystallographic relationship of $Ni_2Ge[\bar{1}21] \parallel Ge[\bar{2}20]$ and $Ni_2Ge[\bar{1}\bar{1}1] \parallel Ge[11\bar{2}]$, while on the right side, the interface followed a different crystallographic relationship of $Ni_2Ge[\bar{1}21] \parallel Ge[\bar{2}20]$ and $Ni_2Ge(11\bar{1}) \parallel Ge(111)$. In both cases, the $[\bar{1}21]$ direction of Ni_2Ge was in parallel with Ge $[\bar{2}20]$ direction, due to the fact that the $(\bar{1}21)$ Ni_2Ge inter-plane distance (2.04 Å) is very close to $(\bar{2}20)$ Ge inter-plane distance (2.00 Å) with a lattice mismatch of 2%. Here, the $NiSi_y$ shell layer was too thin (~ 2 nm) to collect any diffraction patterns or to accurately measure the lattice spacing from HRTEM images for phase analysis. It is worth noting that the polycrystalline segments and abrupt diameter changes in the Ni_2Ge are likely to reduce if the Ni pads were made closer in a shorter channel device.

5.5 Conclusions

In summary, we reported the systematic analysis of solid-state reactions between metal (Ni) and heterostructured (Ge/Si core/shell) NWs that exhibited a uniform and abrupt $Ni_2Ge/NiSi_y$ to Ge/Si core/shell interface with an unreacted channel length of 2.7 nm. The *in situ* monitoring this thermally driven reaction under HRTEM allowed us to evaluate and monitor the strain evolution in ultra-short channel Ge/Si core/shell NWs. The interfacial strains between Ge/Si and $Ni_xGe/NiSi_y$ compounds showed different ascending behaviors than the strains at the channel center, both of which exceeded 10% of compression below 3

nm unreacted Ge/Si core/shell NW. The formed $Ni_xGe/NiSi_y$ compounds exhibited no intermixing between Ge and Si elements, and the phase of the reacted core is identified as Ni_2Ge with polycrystalline structures. The high compressive strain may benefit the hole-mobility for Ge/Si core/shell NW-FETs and the measured strain anisotropy could inform the design of sub 10 nm transistor channels.

Most of chapter 5 was published in *Applied Physics Letters* 2017. R. Chen, B.-M. Nguyen, W. Tang, Y. Liu, J. Yoo, S. A. Dayeh. The dissertation author is the first author of this paper.

5.6 References

1. Whall T, Parker E (1995) Silicon-germanium heterostructures—advanced materials and devices for silicon technology. Journal of Materials Science: Materials in Electronics 6 (5):249-264

2. Paul D (1998) Silicon germanium heterostructures in electronics: the present and the future. Thin Solid Films 321 (1):172-180

3. Ueno T, Rhee HS, Lee SH, Lee H, Shin DS, Jin Y-S, Maeda S, Lee N-I Dramatically enhanced performance of recessed SiGe source-drain pmos by in-situ etch and regrowth technique (InSERT). In: VLSI Technology, 2005. Digest of Technical Papers. 2005 Symposium on, 2005. IEEE, pp 24-25

4. Eneman G, Verheyen P, Rooyackers R, Nouri F, Washington L, Schreutelkamp R, Moroz V, Smith L, De Keersgieter A, Jurczak M (2006) Scalability of the $Si_{1-x}Ge_x$ source/drain technology for the 45-nm technology node and beyond. IEEE Transactions on Electron Devices 53 (7):1647-1656

5. Liu E-S, Jain N, Varahramyan KM, Nah J, Banerjee SK, Tutuc E (2010) Role of Metal–Semiconductor Contact in Nanowire Field-Effect Transistors. IEEE Transactions on Nanotechnology 9 (2):237-242

6. Léonard F, Talin AA (2011) Electrical contacts to one-and two-dimensional nanomaterials. Nature Nanotechnology 6 (12):773-783

7. Lu W, Xiang J, Timko BP, Wu Y, Lieber CM (2005) One-dimensional hole gas in germanium/silicon nanowire heterostructures. Proceedings of the National Academy of Sciences of the United States of America 102 (29):10046-10051

8. Xiang J, Lu W, Hu Y, Wu Y, Yan H, Lieber CM (2006) Ge/Si nanowire heterostructures as high-performance field-effect transistors. Nature 441 (7092):489-493

9. Hu Y, Kuemmeth F, Lieber CM, Marcus CM (2012) Hole spin relaxation in Ge-Si core-shell nanowire qubits. Nature nanotechnology 7 (1):47-50

10. Nguyen B-M, Taur Y, Picraux ST, Dayeh SA (2014) Diameter-independent hole mobility in Ge/Si core/shell nanowire field effect transistors. Nano letters 14 (2):585-591

11. Tang W, Dayeh SA, Picraux ST, Huang JY, Tu K-N (2012) Ultrashort Channel Silicon Nanowire Transistors with Nickel Silicide Source/Drain Contacts. Nano Letters 12 (8):3979-3985

12. Tang W, Picraux ST, Huang JY, Gusak AM, Tu K-N, Dayeh SA (2013) Nucleation and Atomic Layer Reaction in Nickel Silicide for Defect-Engineered Si Nanochannels. Nano Letters 13 (6):2748-2753

13. Dellas N, Minassian S, Redwing J, Mohney S (2010) Formation of nickel germanide contacts to Ge nanowires. Applied Physics Letters 97 (26):263116

14. Tang J, Wang C-Y, Xiu F, Lang M, Chu L-W, Tsai C-J, Chueh Y-L, Chen L-J, Wang KL (2011) Oxide-confined formation of germanium nanowire heterostructures for high-performance transistors. ACS nano 5 (7):6008-6015

15. Chueh Y-L, Ford AC, Ho JC, Jacobson ZA, Fan Z, Chen C-Y, Chou L-J, Javey A (2008) Formation and Characterization of NixInAs/InAs Nanowire Heterostructures by Solid Source Reaction. Nano Letters 8 (12):4528-4533

16. Chen R, Dayeh SA (2015) Size and Orientation Effects on the Kinetics and Structure of Nickelide Contacts to InGaAs Fin Structures. Nano letters 15 (6):3770-3779

17. Picraux ST, Dayeh SA, Manandhar P, Perea DE, Choi SG (2010) Silicon and germanium nanowires: Growth, properties, and integration. Jom 62 (4):35-43

18. Dayeh SA, Tang W, Boioli F, Kavanagh KL, Zheng H, Wang J, Mack NH, Swadener G, Huang JY, Miglio L (2012) Direct measurement of coherency limits for strain relaxation in heteroepitaxial core/shell nanowires. Nano letters 13 (5):1869-1876

19. Nguyen B-M, Swartzentruber B, Ro YG, Dayeh SA (2015) Facet-selective nucleation and conformal epitaxy of Ge shells on Si nanowires. Nano letters 15 (11):7258-7264

20. Dayeh SA, Mack NH, Huang JY, Picraux S (2011) Advanced core/multishell germanium/silicon nanowire heterostructures: The Au-diffusion bottleneck. Applied Physics Letters 99 (2):023102

21. Dayeh S, Gin A, Picraux S (2011) Advanced core/multishell germanium/silicon nanowire heterostructures: Morphology and transport. Applied Physics Letters 98 (16):163112

22. Appenzeller J, Knoch J, Tutuc E, Reuter M, Guha S (2006) Dual-gate silicon nanowire transistors with nickel silicide contacts. Electron Devices Meeting (IEDM):1-4

23. Yaish YE, Katsman A, Cohen GM, Beregovsky M (2011) Kinetics of nickel silicide growth in silicon nanowires: From linear to square root growth. Journal of Applied Physics 109 (9):094303

24. Tang W, Nguyen B-M, Chen R, Dayeh SA (2014) Solid-state reaction of nickel silicide and germanide contacts to semiconductor nanochannels. Semiconductor Science and Technology 29 (5):054004

25. Giese A, Bracht H, Stolwijk N, Mehrer H Diffusion of nickel and zinc in germanium. In: Defect and Diffusion Forum, 1997. Trans Tech Publ, pp 1059-1066

26. Spit F, Gupta D, Tu K (1989) Diffusivity and solubility of Ni (63 Ni) in monocrystalline Si. Physical Review B 39 (2):1255

27. Heitjans P, Kärger J (2006) Diffusion in condensed matter: methods, materials, models. Springer Science & Business Media,

28. Chen R, Jungjohann KL, Mook WM, Nogan J, Dayeh SA (2017) Atomic Scale Dynamics of Contact Formation in the Cross-section of InGaAs Fin/Nanowire Channels. Nano letters:in acceptance

29. Chou Y-C, Wu W-W, Cheng S-L, Yoo B-Y, Myung N, Chen LJ, Tu KN (2008) In-situ TEM Observation of Repeating Events of Nucleation in Epitaxial Growth of Nano $CoSi_2$ in Nanowires of Si. Nano Letters 8 (8):2194-2199

30. Chou Y-C, Wu W-W, Chen L-J, Tu K-N (2009) Homogeneous Nucleation of Epitaxial CoSi2 and NiSi in Si Nanowires. Nano Letters 9 (6):2337-2342. doi:10.1021/nl900779j

31. Lin Y-C, Lu K-C, Wu W-W, Bai J, Chen LJ, Tu KN, Huang Y (2008) Single Crystalline PtSi Nanowires, PtSi/Si/PtSi Nanowire Heterostructures, and Nanodevices. Nano Letters 8 (3):913-918

32. Burchhart T, Lugstein A, Hyun Y, Hochleitner G, Bertagnolli E (2009) Atomic scale alignment of copper-germanide contacts for ge nanowire metal oxide field effect transistors. Nano letters 9 (11):3739-3742

33. Lu K-C, Wu W-W, Wu H-W, Tanner CM, Chang JP, Chen LJ, Tu KN (2007) In situ Control of Atomic-Scale Si Layer with Huge Strain in the Nanoheterostructure NiSi/Si/NiSi through Point Contact Reaction. Nano Letters 7 (8):2389-2394. doi:10.1021/nl071046u

34. Callister WD, Rethwisch DG (2007) Materials science and engineering: an introduction, vol 7. Wiley New York,

35. Greaves GN, Greer A, Lakes R, Rouxel T (2011) Poisson's ratio and modern materials. Nature materials 10 (11):823-837

36. Li X, Ono T, Wang Y, Esashi M (2003) Ultrathin single-crystalline-silicon cantilever resonators: fabrication technology and significant specimen size effect on Young's modulus. Applied Physics Letters 83 (15):3081-3083

37. Han X, Zheng K, Zhang Y, Zhang X, Zhang Z, Wang ZL (2007) Low‐Temperature In Situ Large‐Strain Plasticity of Silicon Nanowires. Advanced Materials 19 (16):2112-2118

38. Fischetti MV, Laux SE (1996) Band structure, deformation potentials, and carrier mobility in strained Si, Ge, and SiGe alloys. Journal of Applied Physics 80 (4):2234-2252

39. Xihong P, Fu T, Paul L (2011) Band structure of Si/Ge core–shell nanowires along the [110] direction modulated by external uniaxial strain. Journal of Physics: Condensed Matter 23 (11):115502

40. Tang J, Wang C-Y, Xiu F, Hong AJ, Chen S, Wang M, Zeng C, Yang H-J, Tuan H-Y, Tsai C-J (2010) Single-crystalline Ni2Ge/Ge/Ni2Ge nanowire heterostructure transistors. Nanotechnology 21 (50):505704

41. Chen Y, Lin Y-C, Huang C-W, Wang C-W, Chen L-J, Wu W-W, Huang Y (2012) Kinetic Competition Model and Size-Dependent Phase Selection in 1-D Nanostructures. Nano Letters 12 (6):3115-3120

42. Chen Y, Lin Y-C, Zhong X, Cheng H-C, Duan X, Huang Y (2013) Kinetic Manipulation of Silicide Phase Formation in Si Nanowire Templates. Nano Letters 13 (8):3703-3708

43. Tang J, Wang C-Y, Xiu F, Zhou Y, Chen L-J, Wang KL (2011) Formation and device application of Ge nanowire heterostructures via rapid thermal annealing. Advances in Materials Science and Engineering 2011

Chapter 6: Ongoing and Future Work

6.1 The Ohmic Contacts to InGaAs with Solid-Phase-Regrowth Method

In chapter 2 to chapter 4, we have discussed the nickelide contact formation in InGaAs Fin and nanowire channels. However, when fabricating and measuring the InGaAs FinFETs with nickelide contacts, my senior labmates have realized a low on-current which is limited by the high contact resistance, though the overall device performance was decent.[1] The reason of the high contact resistance here is related to three reasons: firstly, the as deposited Ni usually formed an amorphous intermixing layer in between the contact and the nanochannels, which has much higher contact resistance than a crystalline compound contact, as having been discussed in chapter 3.[2] Secondly, the crystalline nickelide contacts after annealing introduced compressive strains to the InGaAs channel, which opens up the energy band-gap at the interface and significantly reduces the tunneling currents, as discussed in chapter 2.[3] Thirdly, the nanoscale contact geometries also affect the energy band bending near the contact interface (chapter 1, section 1.3.1), which can also increase the contact resistance at low dimensions. Here, we adopted a method, called solid-phase-regrowth (SPR),[4-8] in order to form Ohmic contacts to nanoscale InGaAs channels by introducing higher n-type dopants at the contact interface. This SPR contact formation process is schematically illustrated in **Figure 6.1**.

During this SPR process, the contacting metal layer (usually Ni or Pd) first reacts with the underlying semiconductor material (usually III-V, and here InGaAs) at a fairly low

temperature (< 200 °C), forming a ternary or quaternary phase, depending on the III-V material. At a higher temperature (> 300 °C), this phase becomes unstable and decomposes, consequently having the out-diffusion metal atoms reacting with an adjacent group IV material (usually Si or Ge) to form a stable compound in contact with the III-V channel. This consumption of the reacting metal causes the regrowth of the III-V material, during which, the excess Ge or Si can act as n-type dopant to heavily dope the surface layer of this III-V channel. And the reaction formulas can be expressed as bellows:

1st step of thermal anneal at a low temperature (< 200 °C)

$$Pd + InGaAs \rightarrow Pd_xInGaAs \quad (6\text{-}1)$$

$$Pd + Si \rightarrow Pd_2Si \quad (6\text{-}2)$$

2nd step of thermal anneal at a higher temperature (> 300 °C)

$$Pd_xInGaAs + Si \rightarrow Pd_2Si + InGaAs\ [Si] \quad (6\text{-}3)$$

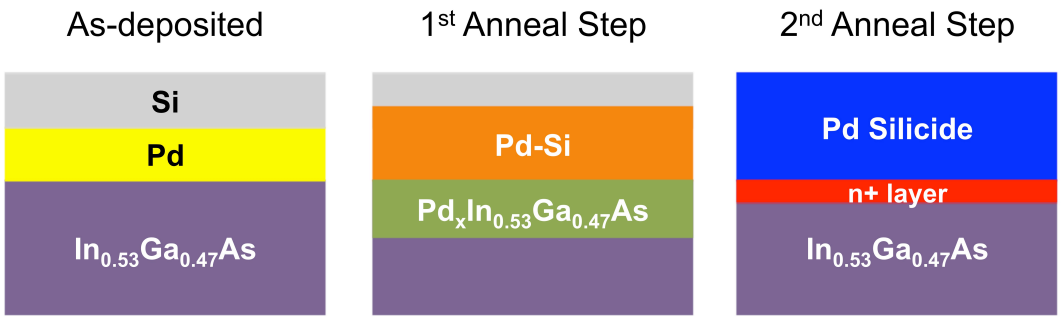

Figure 6.1 Schematics of the two-step anneal processes of solid-phase-regrowth (SPR) contact formation to InGaAs.

In order to directly prove the SPR reactions and to optimize the contact formatting conditions, we carried out the *in-situ* heating TEM studies on InGaAs thin films with Pd and Si contacts. Firstly, a 50nm InGaAs film was transferred on insulator on Si substrate with the method described in chapter 2 and 3. Then, we deposited 20nm Pd and 50nm Si on top of the InGaAs film. Before depositing the Pd layer, we prepared two types of InGaAs surfaces, with or without removing the 1nm native oxide layer (shown schematically in **Figure 6.2** (a)). TEM images in **Figure 6.2** (b) and (c) show the cross-sectional views of these two types of sample. Without the native oxide layer (**Figure 6.2** (b)), the Pd layer intermixed with InGaAs during e-beam deposition step due to the latent heat generated by the condensation of Pd atoms.

While applying the heating *in-situ* on the InGaAs samples inside the TEM chamber, we were able to characterize the reactions at various temperatures (**Figure 6.3**). As shown in **Figure 6.3** (a), the intermixed Pd_xInGaAs layer is amorphous, and there is no further reactions between Pd and InGaAs at 100 °C. In **Figure 6.3** (e), the interfacial oxide layer prevents the intermixing to happen, and also blocks the Pd and InGaAs reaction at 100 °C. At 175 °C, the Pd_xInGaAs layer starts to grow thicker (**Figure 6.3** (b)) with the non-reacted Pd diffusing into InGaAs layer. At the same time, Pd can also diffuse through the native oxide barrier and react with the InGaAs layer in the second type of sample (**Figure 6.3** (f)). At the temperature of 300 °C, Pd_xInGaAs layers in both of samples start to decompose and regrow into crystalline InGaAs that is epitaxial with the non-reacted InGaAs substrate (**Figure 6.3** (c) and (g)). However, when the temperature is elevated to 350 °C and above, the decomposing and regrowth rate significantly increases, and defects start to form in the regrown InGaAs layer (**Figure 6.3** (d) and (h)).

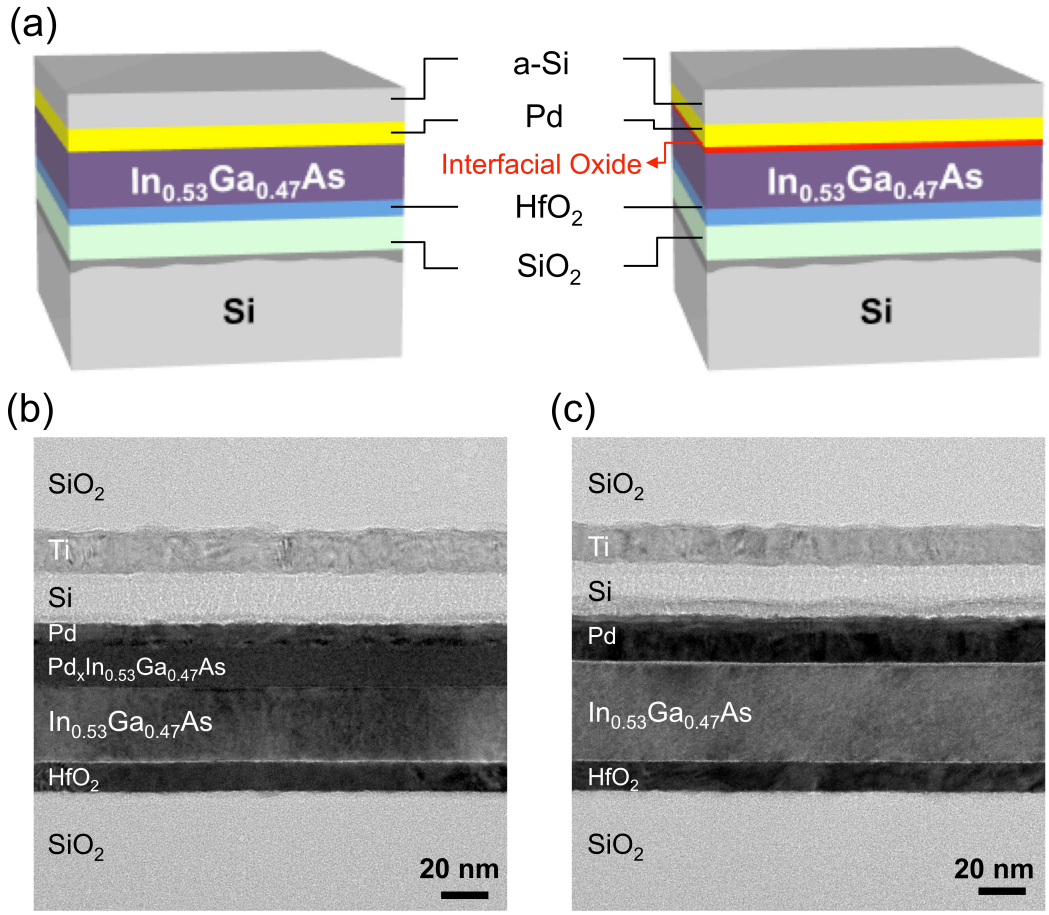

Figure 6.2 (a) Schematics and (b)-(c) TEM images of SPR contacts (Pd and Si) on the transferred InGaAs thin film on Si substrate. There is an intestinally introduced interfacial oxide layer in between Pd and InGaAs in (c), not in (b).

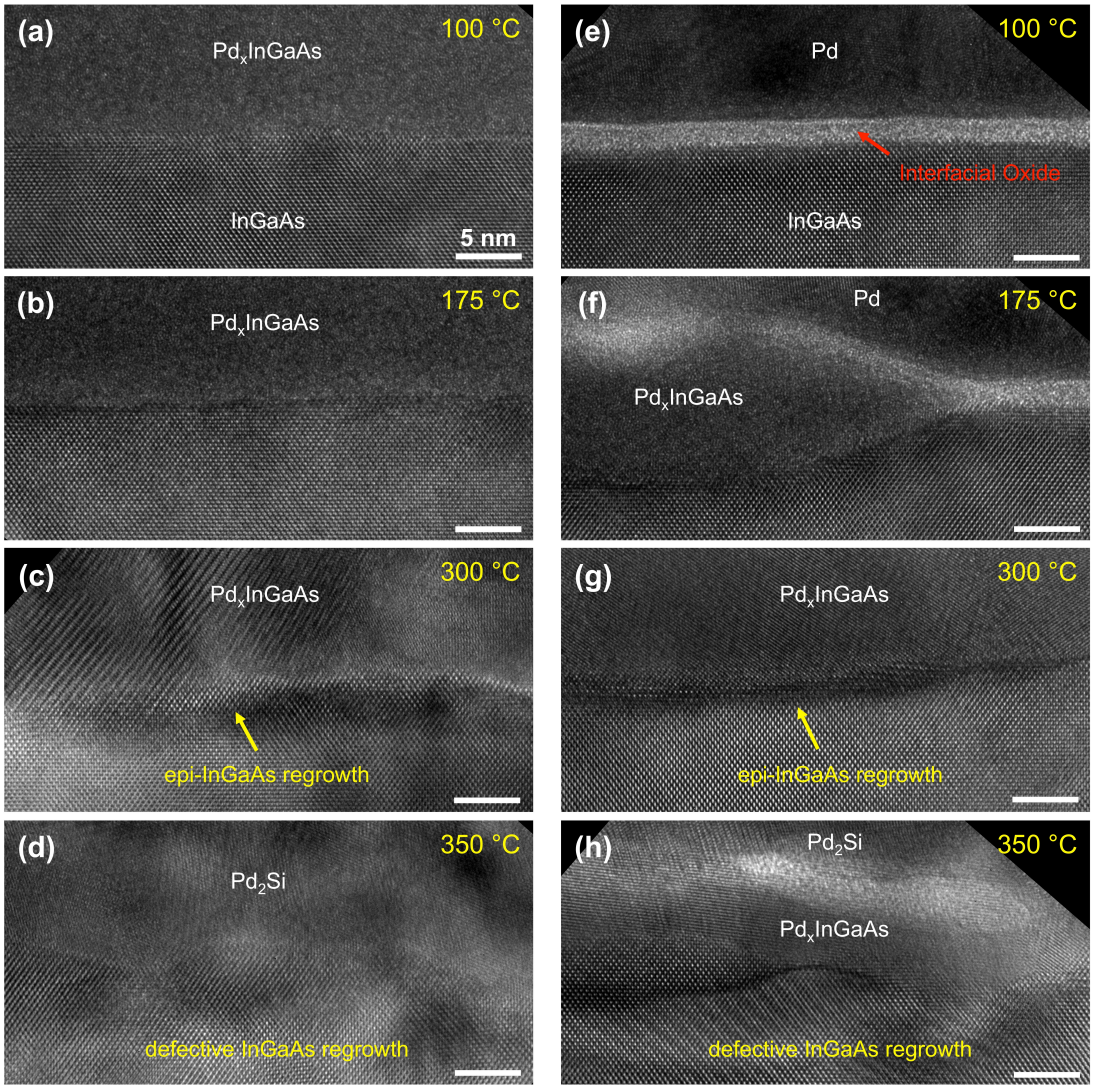

Figure 6.3 Cross-sectional HRTEM images at different temperatures during the SPR contact reactions. (a)-(d) The sample without the interfacial oxide layer in between Pd and InGaAs. (e)-(h) The sample with the interfacial oxide layer in between Pd and InGaAs.

Table 6.1 Summary of the specific contact resistance (ρ_C) with various contact metals and annealing conditions.

Metal Stacking	Annealing Condition	Electrical Measurements	
		ρ_C (Ω-cm²)	R_{sheet} (Ω/□)
Ni 120 nm	non-annealed	1.78 x 10^{-3}	63008
	350°C for 60s	3.20 x 10^{-2}	156571
Pd/Si/Pd/Ti/Au 5/20/15/80/30 nm	non-annealed	1.25 x 10^{-1}	42507
	150°C 60s, 250°C 60s, and 330°C 60s	5.90 x 10^{-3}	80263
Pd/Ti/Au 60/40/90 nm	non-annealed	9.65 x 10^{-5}	1073
	150°C 5min (Si cover)	2.83 x 10^{-5}	880
Pd/Ge/Pd/Ti/Au 5/27.5/25/40/90 nm	150'C 5min, 250'C 10min, and 350'C 20min	4.68 x 10^{-5}	1188
	150'C 5min, 250'C 10min, and 350'C 20min (Ar)	--	--
	200'C 30s, 380'C 40s (Si cover)	8.67 x 10^{-5}	1971
	150'C 5min, 250'C 10min, and 380'C 5min (Si cover)	1.70 x 10^{-4}	1407
Pd/Si/Pd/Ti/Au 5/27.5/25/40/90 nm	150'C 5min, 250'C 10min, and 350'C 5min (Si cover)	4.86 x 10^{-5}	1047
	200'C 10min, and 350'C 5min (Si cover)	2.94 x 10^{-5}	1042
	200'C 20min, and 350'C 10min (Si cover)	8.46 x 10^{-6}	1042
	200'C 20min, and 350'C 10min (Si cover, repeated)	6.33 x 10^{-6}	1091
Pd/Si/Pd/Ti/Au 10/27.5/20/40/90 nm	200'C 20min, and 350'C 10min (Si cover)	4.00 x 10^{-6}	1497
	200'C 20min, and 350'C 10min (Si cover, repeated)	8.37 x 10^{-6}	1354
Pd/Si/Pd/Ti/Au 15/27.5/15/40/90 nm	200'C 20min, and 350'C 10min (Si cover)	6.99 x 10^{-6}	1714
	200'C 20min, and 350'C 10min (Si cover, repeated)	8.40 x 10^{-6}	1452

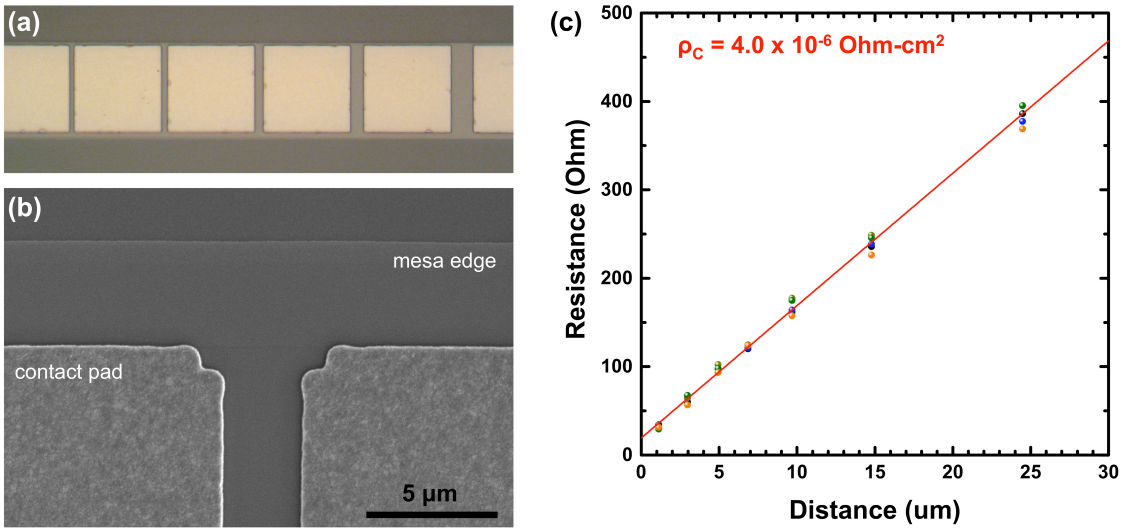

Figure 6.4 Transmission line measurement (TLM) of the SPR contacts on InGaAs. The (a) microscope image and (b) SEM image of the TLM metal pads with very smooth surface after annealing. (c) TLM characterization of 5 devices and the linear fitting of the resistance as a function of the gap distances.

We also studied the electrical properties of the SPR contacts using the transmission line measurement (TLM) method, in comparison to other metal contacts, such as Ni and Pd (**Table 6.1**). So far, the lowest specific contact resistance (ρ_C) was achieved in a SPR contact with the metal stacking layers of Pd/Si/Pd/Ti/Au = 10/27.5/20/40/90nm, after annealing at 200 °C for 20min and then 350 °C for 10min in forming gas ambient (5% H_2 in N_2), with the value of $\rho_C = 4 \times 10^{-6}$ Ω-cm^2 (**Figure 6.4** (c)). As shown in **Figure 6.4** (a) the metal surface looks shinning and smooth after annealing under the microscope. The SEM image in **Figure 6.4** (b) also demonstrates the smooth metal surface, and there are no protruded Pd_xInGaAs reactions near the edge of the metal pads. Our next steps of work will be to further optimize the thicknesses of Pd and Si layers and the annealing conditions to reach a ρ_C in the range of $10^{-8} \sim 10^{-9}$ Ω-cm^2.

In the meanwhile, we also did the TLM characterizations in InGaAs nanowire channels, because the nanoscale contacts are our ultimate goal. However, upon thermal anneal under the same condition as the planar devices, the metal Pd diffuses into the NW channel after the 2nd step of anneal, as shown in the segments of InGaAs NWs with brighter contrast in **Figure 6.5** (a). To understand the reason and figure out the solutions, we prepare the cross-sectional TEM sample underneath the metal contact. As shown in **Figure 6.5** (b), the NW has a nearly square-shaped cross-section, which is the Pd_xInGaAs without any regrowth of crystalline InGaAs. This is because, the lower Pd layer have relatively infinite supply than the finite InGaAs NW and therefore can continually diffuse into the InGaAs NW from places far away, which can be approved by the voids formed in the lower Pd layer in **Figure 6.5** (b).

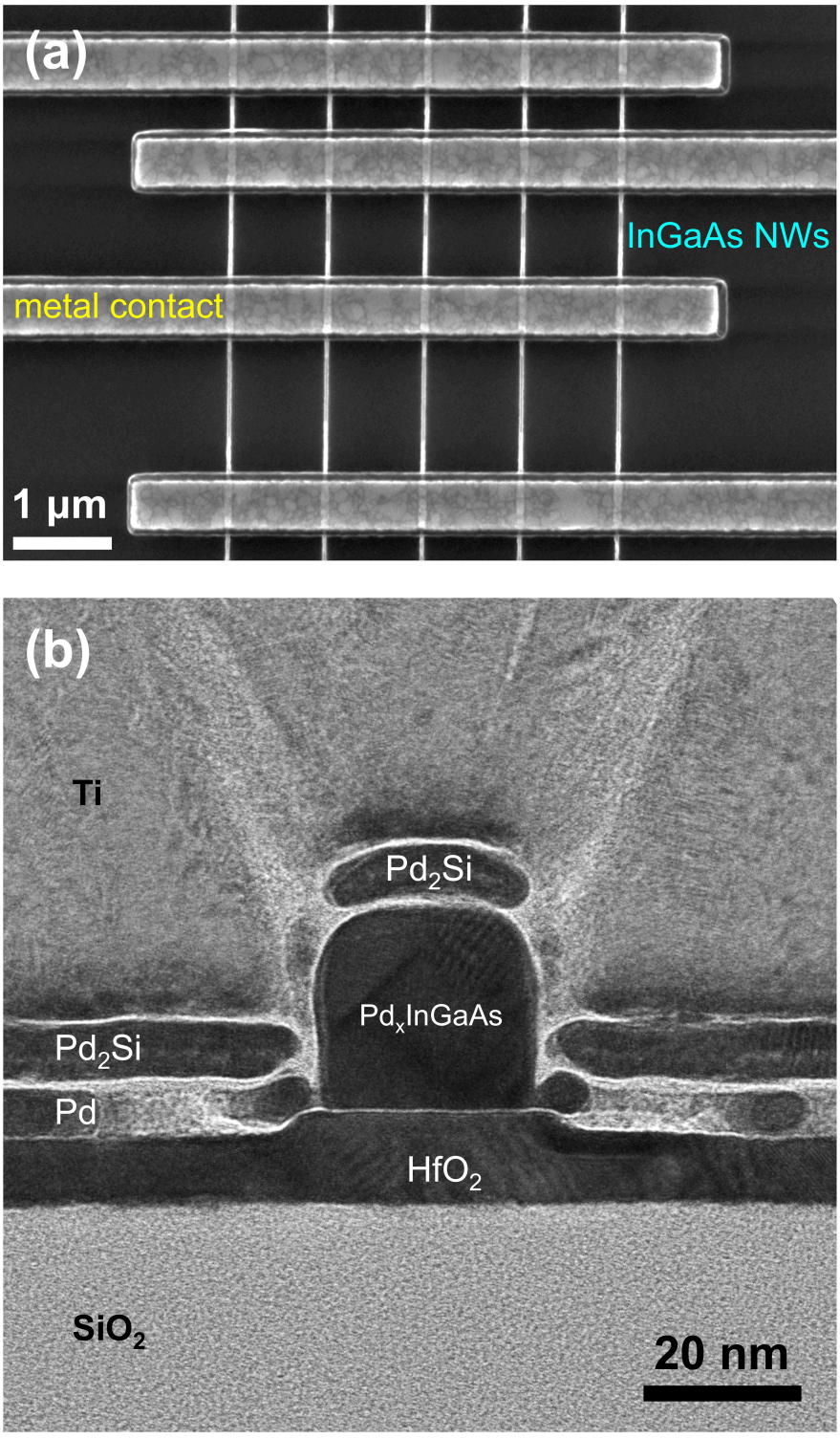

Figure 6.5 (a) SEM and (b) cross-sectional TEM images of the SPR contact on InGaAs NWs after annealing.

In order to achieve the successful regrowth in InGaAs NWs, we need to eliminate the infinite supply of Pd contact. One possible way is to pattern the very narrow SPR contact metals just on top of the NW channel, while to cover them with Ti and Au for the metal leads and for reducing the contact sheet resistance. However, we did multiple tests for these narrow SPR contacts, but none of them were successful. A directly patterning on to of the NWs requires extremely good alignment, and very good metal filling into the e-beam resist pockets. A deposition and dry etching step was found to resulted in tapered SPR contacts and the underneath InGaAs NWs. Our next step of work is to try out a much thinner lower Pd layer and relatively thicker Si and top Pd layers, which holds promise in reducing the diffusion of lower Pd layer into the InGaAs NW.

Future work of this project also includes optimizing the SPR contact layers and annealing conditions for the InGaAs NWs, to carry out the in-situ heating TEM studies of the SPR reactions in the NW cross-sections, and to correlate the structural studies with the electrical performance of these devices.

6.2 Improving the Intrinsic Linearity of AlGaN/GaN Fin MOS-HEMTs

This is a collaborated project leading by my advisor, Prof. Shadi A. Dayeh, and my labmate, Woojin Choi. My role in this work focuses on developing the fabrication process for those FinFET devices.

The objective of this project is to develop a novel intrinsically tunable high linearity AlGaN/GaN multi-Fin MOS-HEMT device that can deliver wideband linearity at low DC biases. The intrinsic device characteristics as a function of gate-source voltage in the novel device can be controllably synthesized in order to provide the desired linearity, along with high f_t, f_{max} and low noise performance.

Prof. Dayeh and Woojin have proposed this device scheme that comprises of multiple Fin channels whose threshold voltage can be individually tuned by width of the Fin-channel, W_{Fin}. **Figure 6.6** (a) shows an exemplary schematic of the proposed device. For such a multi-Fin device, one can write:

$$I(V_{GS}) = \alpha_1 I_1(V_{GS}-V_{T1}) + \alpha_2 I_2(V_{GS}-V_{T2}) + \ldots + \alpha_n I_n(V_{GS}-V_{Tn}) \quad (6\text{-}4)$$

$$g_m(V_{GS}) = \alpha_1 g_{m1}(V_{GS}-V_{T1}) + \alpha_2\, g_{m2}(V_{GS}-V_{T2}) + \ldots + \alpha_n g_{mn}(V_{GS}-V_{Tn}) \quad (6\text{-}5)$$

where α_n is the number of channels for a family of Fins, n, with width $W_{Fin\text{-}n}$, and threshold voltage, V_{Tn}, where $V_{Tn} > V_{Tn\text{-}1}$ d. Therefore, two simple engineering knobs are present in the current device scheme to control the device linearity: W_{Fin} which controls the shift in the threshold voltage, V_T, and the amplitude α_n which controls the current output beyond a V_T point.

Recently, there is a rise in interest in utilizing Fin HEMT devices to reduce the source access resistance and enhance the linearity,[9-11] but this linearity is not accessible at gate voltages beyond those at which the gate Schottky diode turns on (~ 2V). In contrast, our group proposed Fin MOS-HEMT devices permit flexible engineering of the device threshold voltage and attaining linearity over a wider V_{GS} range. The concept is illustrated in **Figure 6.6** (b) and (c), which show typical non-linear I_{DS} (V_{GS}) characteristics for individual Fins but a linearized transfer characteristics when a combination of Fins with different widths as outlined above.

Noting that the I_{DS} does not saturate beyond the g_m roll-off voltage, especially for Fins, it would be required therefore to have multiple elements of larger current carrying Fins (wide), a few Fins with intermediate current capacity, and the largest number of small current capacity Fins (narrow). This situation is illustrated in **Figure 6.6** (c) where such a combination can lead to linearization of the g_m curve over $\Delta V_{GS} = 8V$.

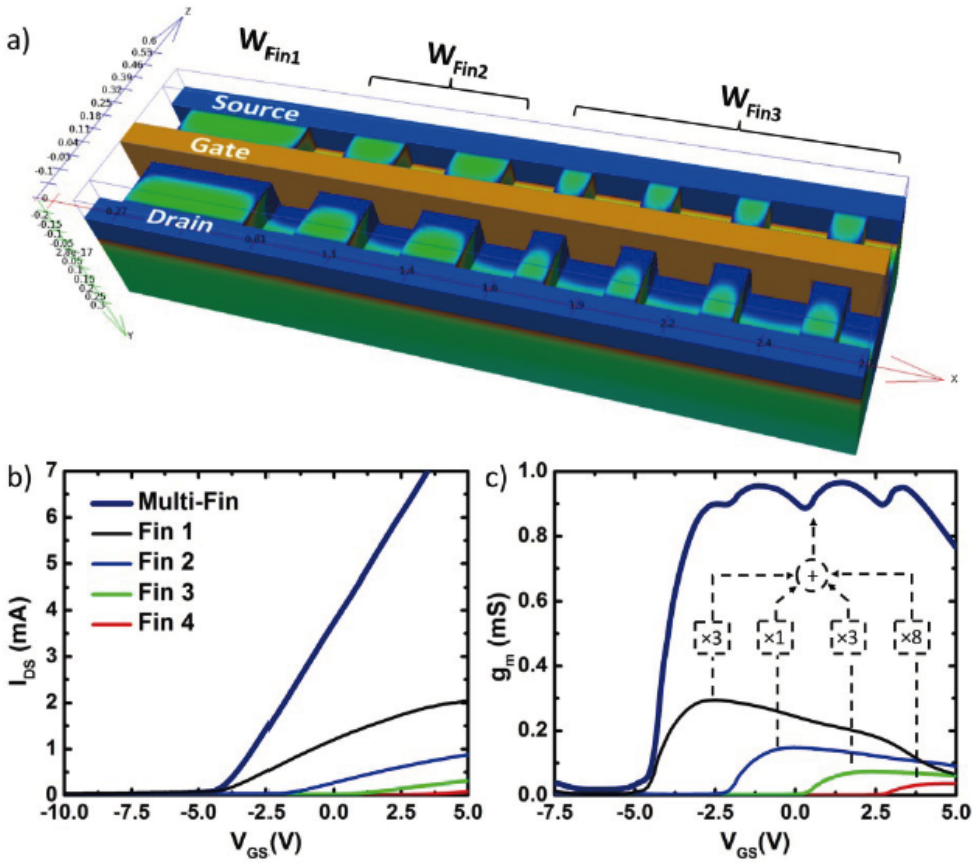

Figure 6.6 Schematic illustration (Silvaco thermal equilibrium electrostatic simulation) of combining different Fin widths into a single device to achieve linear transfer characteristics in (b) and flattened transfer characteristics in (c).

To fabricate the AlGaN/GaN FinFETs, we start with a commercial wafer that has 20nm undoped $Al_{0.23}Ga_{0.77}N$ and 2um undoped GaN epitaxially grown on a Si (111) substrate through a GaN buffer layer, as shown in **Figure 6.7** (a). Firstly, the Ohmic contacts of Ti/Al/Ni/Au were patterned on the wafer by photolithography and deposited by e-beam evaporation. Prior to the deposition, the AlGaN layer was removed by dry etching in the source/drain contact areas. Then, a thermal anneal was performed at 875 °C in N_2 ambient for 30s in order to reduce the contact resistance. Secondly, we used the e-beam lithography (EBL) to pattern the Fin channels with the e-beam resist of HSQ, which turned into SiO_2 under e-beam exposure and acted as etching masks for the Fins. Then we etched the Fins by BCl_3 and Cl_2 based ICP/RIE process, with a targeted etching depth of 50nm. After removing the HSQ masks, we deposited 5nm of Al_2O_3 with ALD as the gate dielectric layer. Then, the metal gate lines were patterned by EBL with a gate length of 50nm and deposited with 30nm of Ni and 70nm of Au. Finally, the other bigger contact pads were patterned by photolithography and deposited with Ti/Au.

During this fabrication, several challenges were faced and successfully resolved. For example, this fabrication process involves multiple steps of photolithography and e-beam lithography and therefore requires extremely good alignment in between each step. However, in our first several attempts, we noticed that any conventionally used metal markers diffused into GaN during the Ohmic metal anneal at 875 °C. This challenge was resolved by etching cross-shaped grooves into the AlGaN/GaN substrate (shown in **Figure 6.8** (a)), and by using these etched grooves as the alignment markers in all the following steps. Another challenge during the device fabrication is related to the uniformity of Fin structures in the EBL step. As shown in **Figure 6.8** (b), the test EBL structures were well

patterned with Fin widths varying from 40nm to 300nm. However, when patterning multiple Fins in between large source and drain pads, the results were not as desired. With a smaller dose, Fins were bared found in between the source/drain pads, while with a larger dose, source and drain pads merged together. To solve this problem, we utilized the approximate effect correction (PEC) function in the BEAMER software to assign different e-beam dosages at different locations according to their approximate positions. Finally, the EBL writing gave very uniform Fin structures over a large region.

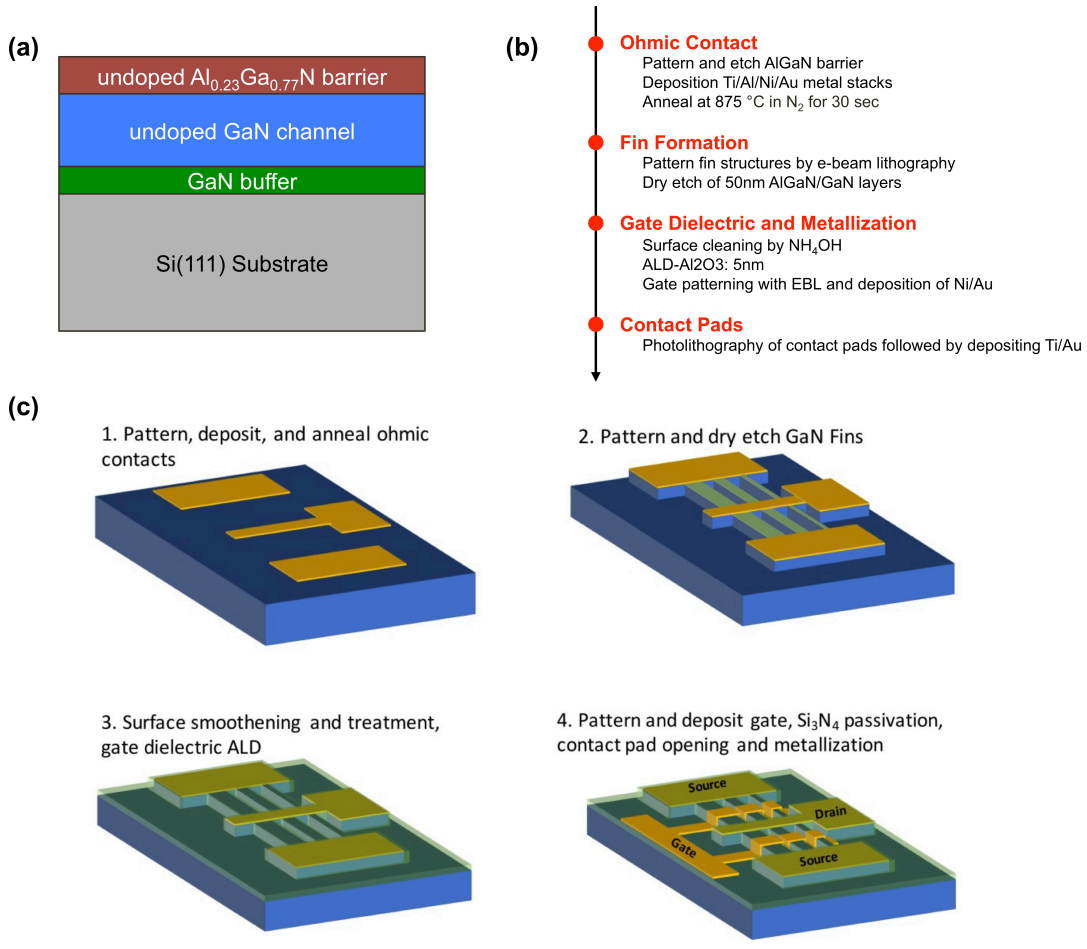

Figure 6.7 (a) Cross-sectional schematic of the AlGaN/GaN epitaxial layers grown on Si substrate. (b) The fabrication flow and (c) the schematics of fabrication steps.

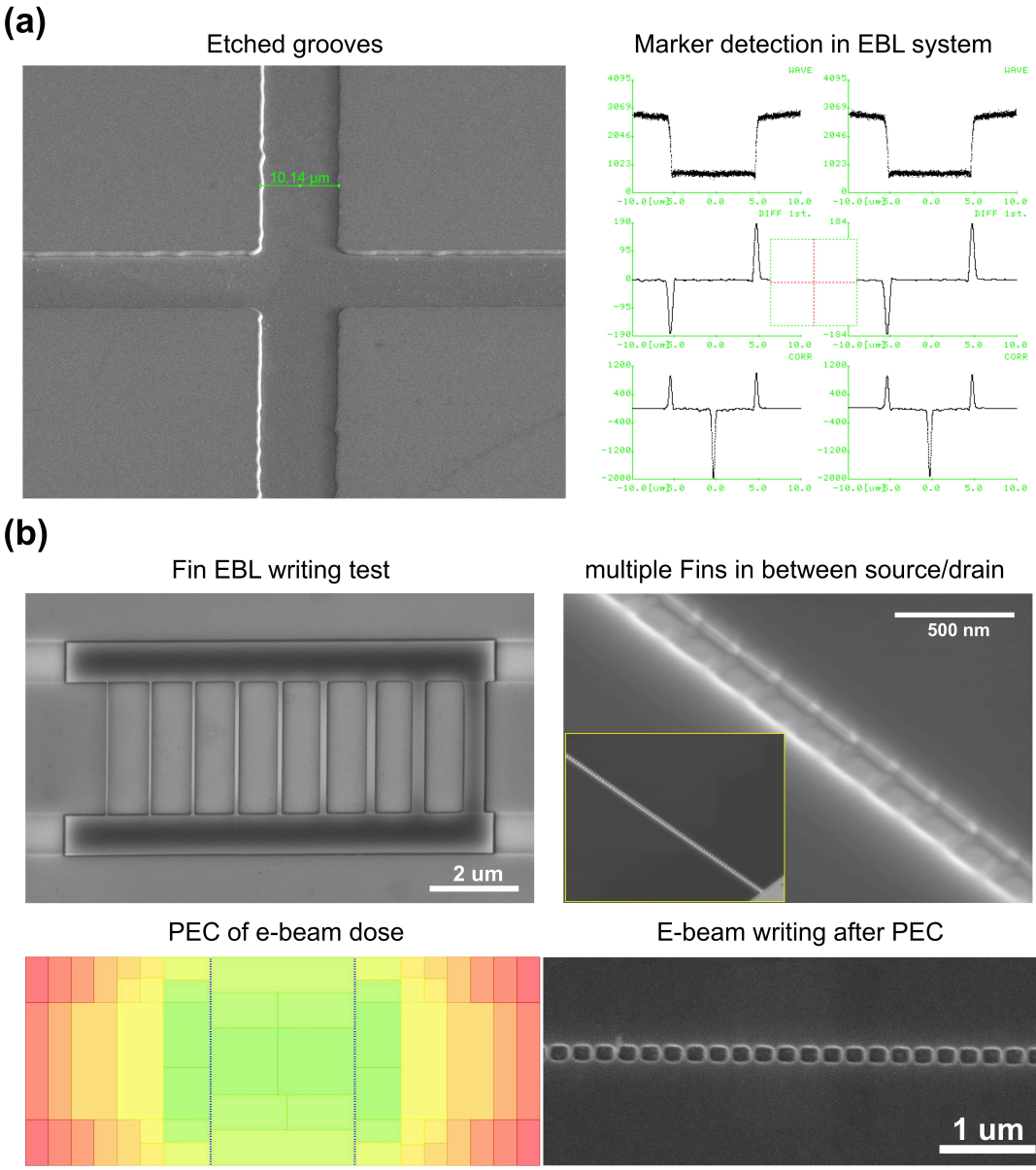

Figure 6.8 Challenges and corresponding solutions during the AlGaN/GaN FinFETs fabrications. (a) Etched grooves on AlGaN/GaN layers as alignment markers. (b) The proximate effect correction (PEC) of the e-beam writing dosage for uniform patterning of multiple Fins.

After successfully fabricating those FinFETs, we firstly investigated the Fin width dependence of the device performance. As we can see from **Figure 6.9** (a), the threshold voltage (V_t) increases at smaller Fin widths following a hyperbola trend, which can be fitted with $y \propto 1/x^{1.22}$. For planar device geometry, the V_t = -4.62V, and there is no much differences between the horizontal devices and the vertical devices. Similarly, in **Figure 6.9** (b), the maxim transconductance ($g_{m\text{-}max}$) also increases at smaller Fin widths, with the fitting curve close to $y \propto 1/x^{1.44}$. All those measurements were done at V_{ds} = 4V, and those devices were found to have very small values of the inversed sub-threshold slopes (SS^{-1}), which are in the range of 77.7 ± 11.6 mV/dec, as shown in **Figure 6.9** (c).

On the other hand, we also studied the effects of Fin widths and gate positions on the g_m flatness. Shown in **Figure 6.10** (a) is the overall layout of the device, with source, drain and gate labeled on the figure. The gate-to-source length (L_{gs}) characterizes the distance in between the source Ohmic metal and the gate metal line (**Figure 6.10** (b)), and is designed to be 500nm in comparison to the 2um source-to-drain distance, in order to reduce the source access resistance. The Fin channels are lying underneath the gated area. As shown in **Figure 6.10** (c), the normalized current (I_{ds}) and g_m for smaller Fin channels are generally larger, and that the g_m peaked at a higher gate voltage (V_{gs}). This limits the flatness of g_m under our defined V_{gs} range from -6V to 4V, above which the gate dielectric may break down. At the same time, for much larger Fin channels (> 200nm), we saw a rapid decrease of the g_m curve after its peak value. For the 100nm wide Fins, we found the widest g_m flatness across the gate voltages of $\Delta V_{gs} \approx 5V$.

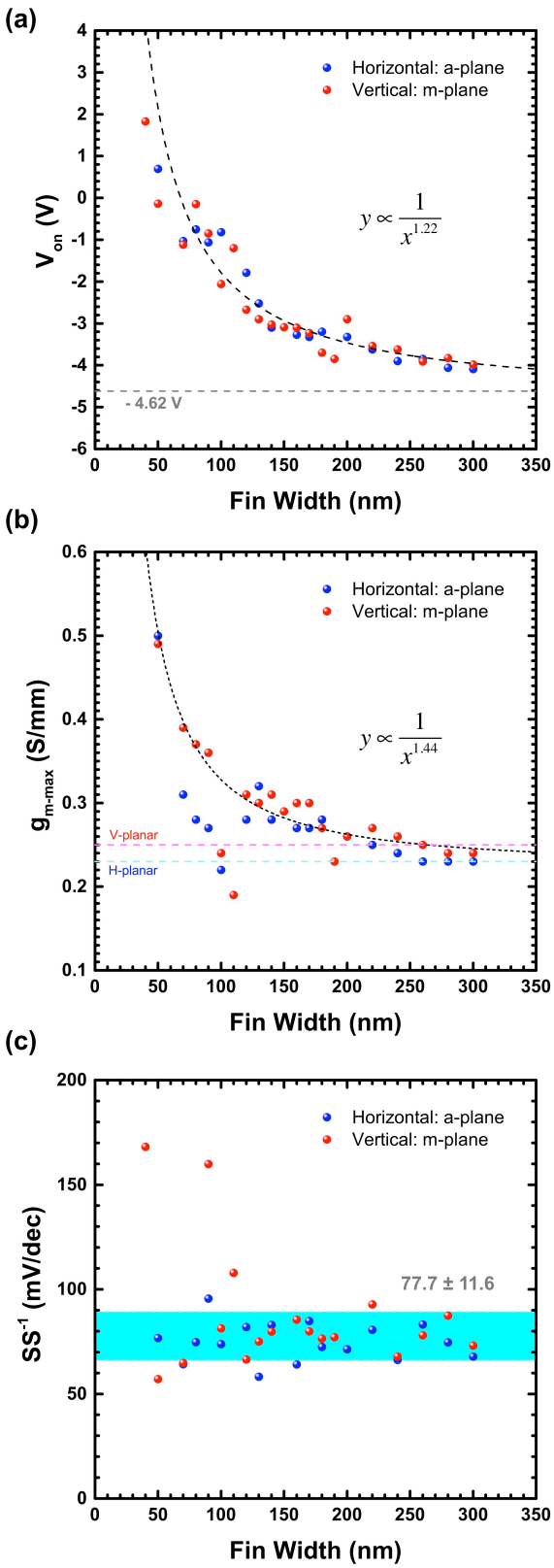

Figure 6.9 Device characteristics, including (a) V_t, (b) $g_{m\text{-}max}$, and (c) SS^{-1} as a function of Fin widths. All measurements were done at V_{ds} = 4 V.

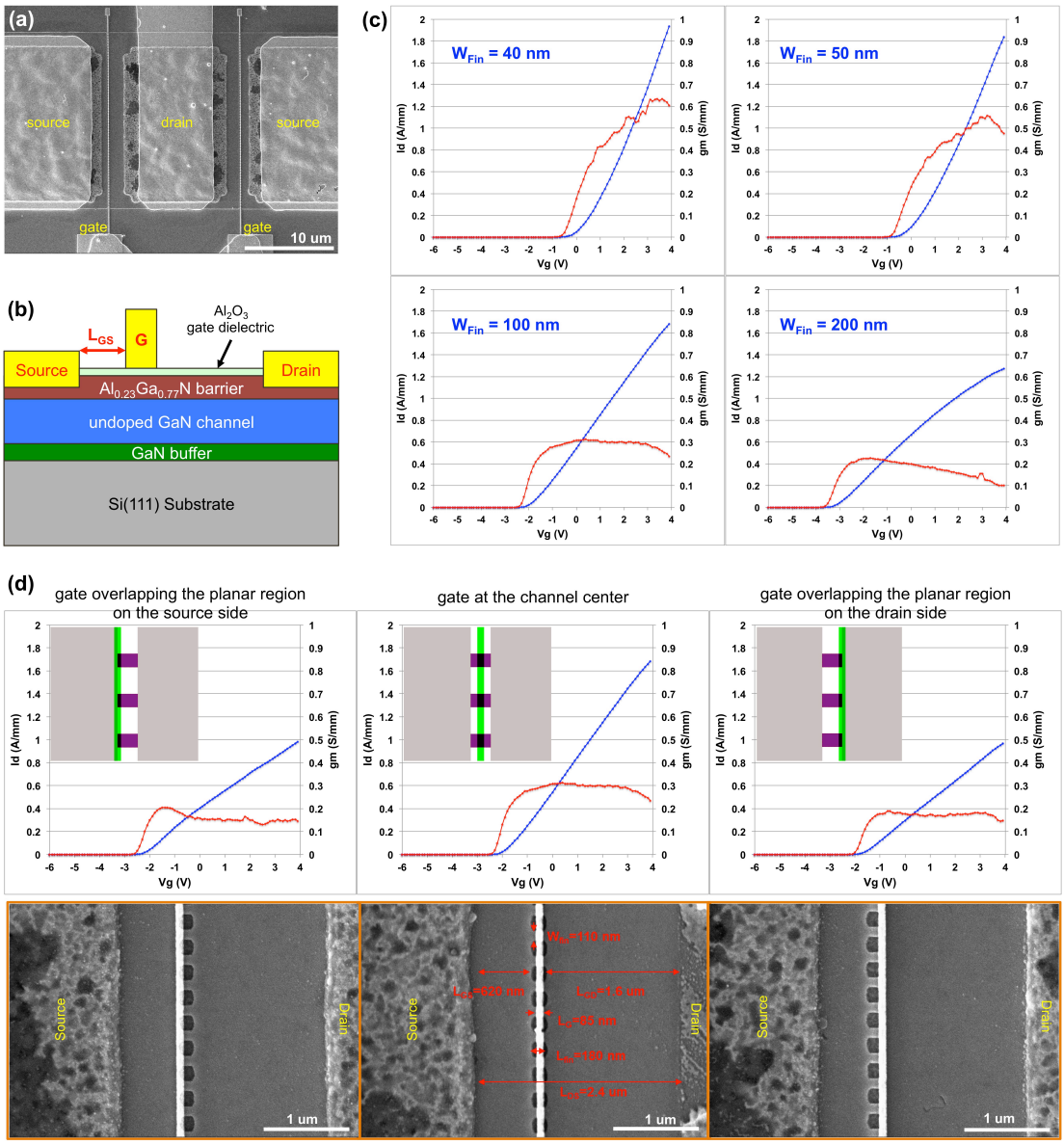

Figure 6.10 The effects of Fin widths and gate positions on the g_m flatness. (a) SEM image and (b) schematic of the overall device structure. (c) I_d-V_g (blue curves) and g_m-V_{gs} (red curves) characteristics with different Fin widths. (d) I_{ds}-V_g (blue curves) and g_m-V_{gs} (red curves) characteristics with different gate positions. All these measurements were done at V_{ds} = 4V with L_{gs} = 500nm, and the I_d and g_m values are normalized to the Fin widths and the number of Fins.

We also designed the metal gate lines at different positions on the Fin channels, as shown in **Figure 6.10** (d). If the gate is overlapping with the planar region on either the source or drain side, the $g_{m\text{-}max}$ will decrease, due to the less electro-statistic control to the channel. However, the g_m flatness is good for samples with gate positions at either the center location or the drain overlapping location. Considering both the flatness and the magnitude of g_m curves, the center gate position will be favorable. In the future designs, it will be good to further minimize the L_{gd} lengths.

For the future work of this project, my labmate, Woojin, is working on synthesizing the linear g_m by the combination of several different Fin widths with certain weighting of their numbers, as illustrated in equation 6-4 and 6-5, and in in **Figure 6.6**. With to the synthesized results, we will work on the design and fabrication of these AlGaN/GaN multi-Fin MOS-HEMT devices, in order to achieve wideband linearity at low DC biases.

6.3 References

1. Dai X, Nguyen BM, Hwang Y, Soci C, Dayeh SA (2014) Novel heterogeneous integration technology of III–V layers and InGaAs finFETs to silicon. Advanced Functional Materials 24 (28):4420-4426

2. Chen R, Jungjohann KL, Mook WM, Nogan J, Dayeh SA (2017) Atomic Scale Dynamics of Contact Formation in the Cross-Section of InGaAs Nanowire Channels. Nano letters 17 (4):2189-2196

3. Chen R, Dayeh SA (2015) Size and Orientation Effects on the Kinetics and Structure of Nickelide Contacts to InGaAs Fin Structures. Nano letters 15 (6):3770-3779

4. Lau SS (1993) Case studies of metal-III–V compound interactions. Applied Surface Science 70–71, Part 2 (0):488-495

5. Marshall ED, Lau SS, Palmstrøm CJ, Sands T, Schwartz CL, Schwarz SA, Harbison JP, Florez LT (1989) Ohmic Contact Formation Mechanism in the Ge/Pd/N-GaAs System. MRS Online Proceedings Library 148:null-null

6. Sands T, Marshall ED, Wang LC (1988) Solid-phase regrowth of compound semiconductors by reaction-driven decomposition of intermediate phases. Journal of Materials Research 3 (05):914-921

7. Wang LC, Hao PH, Cheng JY, Deng F, Lau SS (1996) Ohmic contact formation mechanism of the Au/Ge/Pd/n-GaAs system formed below 200'C. Journal of Applied Physics 79 (8):4216-4220

8. Yearsley JD, Lin JC, Hwang E, Datta S, Mohney SE (2012) Ultra low-resistance palladium silicide Ohmic contacts to lightly doped n-InGaAs. Journal of Applied Physics 112 (5):054510-054518

9. Palacios T, Rajan S, Chakraborty A, Heikman S, Keller S, DenBaars SP, Mishra UK (2005) Influence of the dynamic access resistance in the g_m and f_T linearity of AlGaN/GaN HEMTs. IEEE Transactions on Electron Devices 52 (10):2117-2123

10. DiSanto DW, Bolognesi C (2006) At-bias extraction of access parasitic resistances in AlGaN/GaN HEMTs: Impact on device linearity and channel electron velocity. IEEE transactions on electron devices 53 (12):2914-2919

11. Trew RJ, Liu Y, Bilbro L, Kuang W, Vetury R, Shealy JB (2006) Nonlinear source resistance in high-voltage microwave AlGaN/GaN HFETs. IEEE Transactions on Microwave Theory and Techniques 54 (5):2061-2067

Appendix

Appendix I. Derivation of Diffusion Model

The fluxes of Ni atoms in the three processes as shown in **Figure 2.5**, can be expressed as:

$$F_1 = k_{dissolve}(C^{eq}_{Ni/Nickelide} - C_0)\cdot(w+2H)\cdot L_b \tag{AI.1}$$

$$F_2 = -D_{Ni}\frac{C_L - C_0}{L_{Nickelide}(t)}\cdot X \qquad X = \begin{cases} H\cdot w & \textit{Volume Diffusion} \\ 2(H+w)\cdot\delta & \textit{Surface Diffusion} \end{cases} \tag{AI.2}$$

$$F_3 = k_{growth}(C_L - C^{eq}_{Nickelide/InGaAs})\cdot hw \tag{AI.3}$$

Under steady state condition, F_1=F_2=F_3=F:

$$F = k_{dissolve}(C^{eq}_{Ni/Nickelide} - C_0)\cdot(w+2H)\cdot L_b = -D_{Ni}\frac{C_L - C_0}{L_{Nickelide}(t)}\cdot X = k_{growth}(C_L - C^{eq}_{Nickelide/InGaAs})\cdot hw \tag{AI.4}$$

Hence:

$$F = \frac{C^{eq}_{Ni/Nickelide} - C^{eq}_{Nickelide/InGaAs}}{\frac{1}{k_{dissolve}\cdot(w+2H)\cdot L_b} + \frac{L_{Nickelide}(t)}{D_{Ni}\cdot X} + \frac{1}{k_{growth}\cdot hw}}. \tag{AI.5}$$

Because of mass conservation,

$$Hw \cdot \frac{dL_{Nickelide}(t)}{dt} = F \cdot \frac{M_{Nickelide}}{N_A \cdot \rho_{Nickelide}}, \tag{AI.6}$$

and assuming that $P = \frac{M_{Nickelide}}{N_A \cdot \rho_{Nickelide}} \cdot (C^{eq}_{Ni/Nickelide} - C^{eq}_{Nickelide/InGaAs})$, (AI.7)

we can write,

$$\frac{dL_{Nickelide}(t)}{dt} = \frac{P}{\frac{Hw}{k_{dissolve}(w+2H)L_b} + \frac{Hw}{D_{Ni} \cdot X} \cdot L_{Nickelide}(t) + \frac{H}{k_{growth}h}}. \tag{AI.8}$$

To gain intuitive insights into the functional dependence of the dominant growth-limiting step, we solve the time-dependent equation by considering each limiting step separately. Namely,

(i) If Ni dissolution at the Ni/nickelide interface is the rate limiting step:

$$\frac{dL_{Nickelide}(t)}{dt} \approx P \cdot k_{dissolve}(\frac{1}{H} + \frac{2}{w})L_b, \text{ therefore: } L_{Nickelide}(t) = k_{dissolve}(\frac{1}{H} + \frac{2}{w})L_b P \cdot t. \tag{AI.9}$$

(ii) If nickelide growth at the nickelide/InGaAs interface is the rate limiting step:

$$\frac{dL_{Nickelide}(t)}{dt} \approx P \cdot k_{growth}\frac{h}{H}, \text{ therefore: } L_{Nickelide}(t) = k_{growth}\frac{h}{H}P \cdot t. \tag{AI.10}$$

(iii) If the Ni diffusion in the reacted nickelide region is the rate limiting step:

$\frac{dL_{Nickelide}(t)}{dt} \approx P \cdot \frac{D_{Ni} \cdot X}{Hw} \cdot L_{Nickelide}(t)$, and this can be evaluated in for two regimes:

(a) a volume diffusion regime for which:

$$L_{Nickelide}(t) = \sqrt{2PD_{Ni}} \cdot t^{1/2} . \qquad \text{(AI.11)}$$

(b) and a surface diffusion regime for which:

$$L_{Nickelide}(t) = \sqrt{4PD_{Ni}\delta \cdot \left(\frac{1}{w} + \frac{1}{H}\right)} \cdot t^{1/2} \quad . \qquad \text{(AI.12)}$$

Appendix II. Strain-induced Energy Band-edge Shift

Based on deformation potentials obtained from local-density-functional theory, the strain-induced shift in band-edge energies can be calculated according to:[1]

$$E_c = E_c^0 + a_c \frac{\Delta\Omega}{\Omega},\ E_{v,av} = E_{v,av}^0 + a_v \frac{\Delta\Omega}{\Omega} \tag{AII.1}$$

$$E_v^0 = E_{v,av}^0 + \frac{\Delta_0}{3} \tag{AII.2}$$

where, the E_c and $E_{v,av}$ are conduction band-edge energy and averaged valence band-edge energy (considering light hole E_{lh}, heavy hole E_{hh}, and the split-off E_{so} bands). a_c and a_v are the deformation potentials for conduction band and valence band respectively, and Δ_0 is the spin-orbit split-off energy. $\frac{\Delta\Omega}{\Omega}$ is the fractional volume change, and can be expressed as:

$$\frac{\Delta\Omega}{\Omega} = Tr(\ddot{\varepsilon}) = \varepsilon_{xx} + \varepsilon_{yy} + \varepsilon_{zz} = 2\varepsilon_{\parallel} + \varepsilon_{\perp}. \tag{AII.3}$$

In the presence of shear strain, ε_{xy}, the degeneracy of E_{hh} and E_{lh} at the Γ-point is lifted. For strain along [111] direction, E_{hh}, E_{lh}, and E_{so} can be calculated with respect to the $E_{v,av}$ according to:

$$E_{hh} = E_{v,av} + \frac{1}{3}\Delta_0 - \frac{1}{2}\delta E_{111}, \tag{AII.4}$$

$$E_{lh} = E_{v,av} - \frac{1}{6}\Delta_0 + \frac{1}{4}\delta E_{111} + \frac{1}{2}\sqrt{\Delta_0^2 + \Delta_0 \delta E_{111} + \frac{9}{4}(\delta E_{111})^2}\ , \tag{AII.5}$$

and,

$$E_{so} = E_{v,av} - \frac{1}{6}\Delta_0 + \frac{1}{4}\delta E_{111} - \frac{1}{2}\sqrt{\Delta_0^2 + \Delta_0 \delta E_{111} + \frac{9}{4}(\delta E_{111})^2}\ . \tag{AII.6}$$

In these equations, δE_{111} is given by:

$$\delta E_{111} = 2\sqrt{3} d \cdot \varepsilon_{xy} \tag{AII.7}$$

where *d* is the shear deformation potential.

We designate the unstrained valence band-edge as the reference energy such that $E_c^0 = E_g^0 = 0.75eV$ and $E_v^0 = 0eV$ for $In_{0.53}Ga_{0.47}As$.[2] The values of $\varepsilon_{\parallel}$ and $\varepsilon_{\perp}$ are imported from Figure 8e, as a function of position along the channel. a_c, a_v, *d*, and Δ_0 can be obtained by linear interpolation from those of InAs and GaAs as listed in the table below. The resulting band-edge energies for E_c, E_v, E_{hh}, E_{lh}, and E_{so} are then calculated and plotted in **Figure 2.11** (f).

Table AII.1. Deformation potentials of $In_{0.53}Ga_{0.47}As$, calculated by linear interpolation from well know values for InAs and GaAs.[1]

	a_c (eV)	a_v (eV)	Δ_0 (eV)	d (eV)
GaAs	-7.17	1.16	0.34	-4.23
InAs	-5.08	1.0	0.38	-3.1
$In_{0.53}Ga_{0.47}As$ (Calculated)	-6.062	1.075	0.361	-3.631

Appendix III. Origin of the Intermixing Layer in Between As-deposited Ni and InGaAs

There are several possible reasons that may cause the intermixing between as-deposited Ni and InGaAs, including chamber overheating during evaporation, ion-beam-induced metal-semiconductor reaction,[3,4] or latent heat released from the condensation of metal atoms from vapor phase,[5,6] which we validated to be the cause below.

Firstly, we deposited the Ni in our experiments with an electron-beam evaporator with a total thickness of 100nm. Ni was deposited slowly (0.7 Å/s) to prevent exaggerated stress and overheating, and the chamber was cooled down for 30min halfway after the deposition of the first 50nm of Ni. We also did a control experiment by depositing Ni by sputtering at room temperature where the surface pre-deposition treatments for InGaAs were similar to those samples that underwent electron-beam evaporation. The results are shown in **Figure AIII.1**, with very similar interfacial structures as those with e-beam evaporated Ni, indicating that the Ni-InGaAs intermixing layer was not introduced by over-heating in the electron-beam evaporation chamber.

Similarly, we excluded the possibility of ion-beam-induced metal-semiconductor reaction, also called ion-beam mixing, by processing FIB milling in a tilted angle (shown in **Figure AIII.2**). Here, the Ni layer was deposited on two ends of InGaAs channel with HCl treated surface (no surface oxides present). After FIB milling, the interface structures were characterized under TEM. We found that the Ni-InGaAs intermixing layers were identical on both sides, and that both of them extended slightly out of the edge of Ni contacts. Ion-beam mixing is usually caused by penetrating energetic ions through the interface between

a metal-film and semiconductor, overcoming equilibrium constraints in localized regions, and forcing atomic rearrangement, which will be localized and directional. This is contradictory to our observations here.

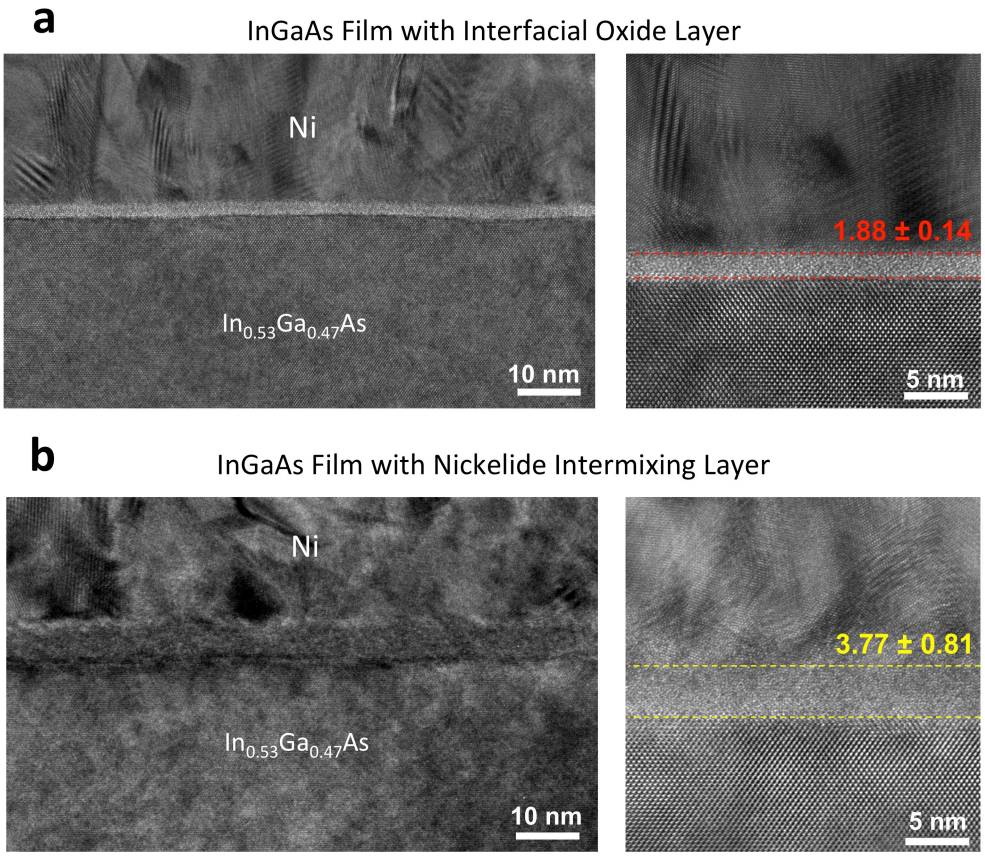

Figure AIII.1. Comparison of interfacial structures when Ni deposited by sputtering. a, TEM and HRTEM images of type (i) specimen at the interface between Ni and InGaAs film. The light contrast layer at the interface, i.e. InGaAs surface oxide layer, has a uniform thickness of 1.88 ± 0.14 nm. b, TEM and HRTEM images of type (ii) specimen at the interface between Ni and InGaAs film. The amorphous layer at the interface, i.e. Ni and InGaAs intermixing layer, has a nearly uniform thickness of 3.77 ± 0.81 nm.

The third possibility is that the latent heat released from the condensation of metal atoms from vapor phase. In fact, when a metal and a semiconductor are brought in contact at room temperature, an intermixing layer can be readily formed between them due to the screening coulomb interaction by free electrons in the metal, which weakens the covalent bonding energy at the semiconductor surface.[7,8] However, the intermixing layer due to electron screening is usually a monolayer or two thick. It has been previously observed that the as-deposited metal on semiconductor can introduce thicker (few nanometers) amorphous intermixture caused by the negative heat (latent heat) from metal condensation. The amorphous interfacial layers between the deposited metal and semiconductor were also observed in other metal/III-V systems.[9,10]

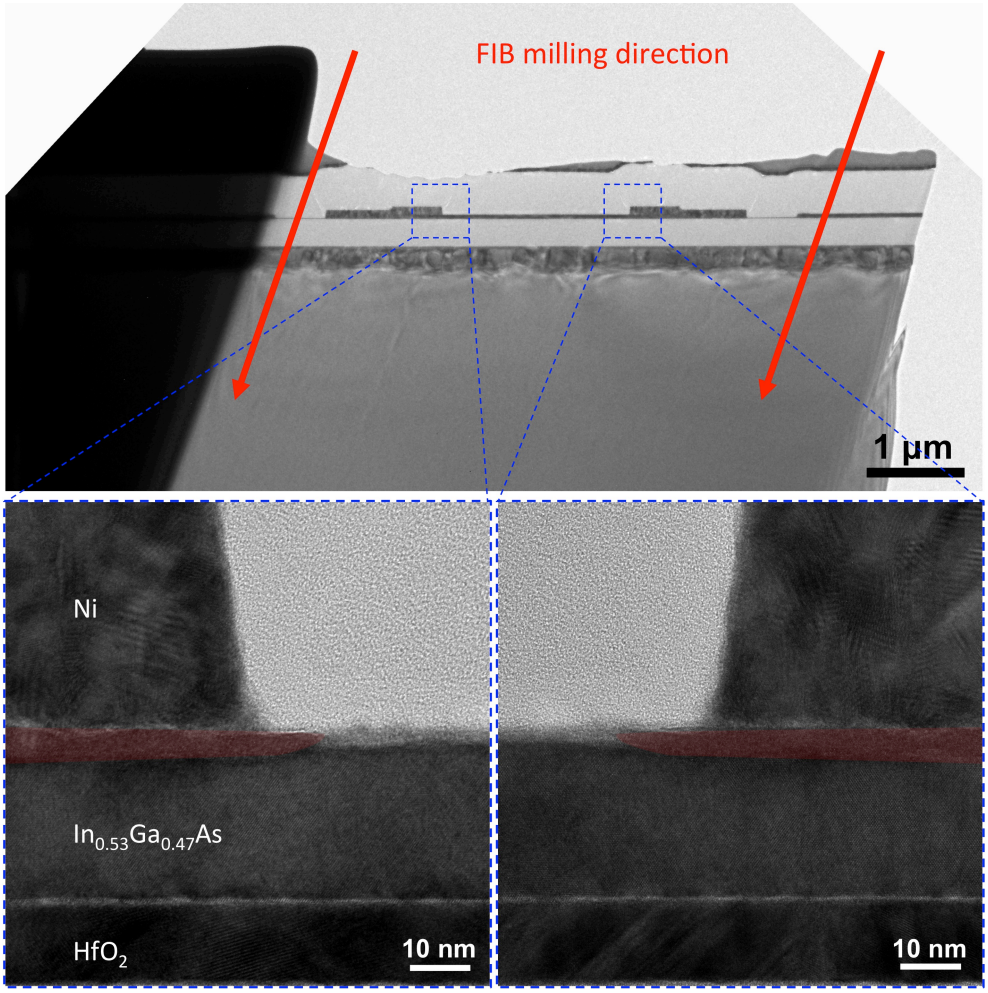

Figure AIII.2. Interfacial structures when specimen is milled by FIB in a tilted angle. TEM images of a type (ii) specimen in which Ni contacts were deposited at two ends of the InGaAs channel. The specimen was milled by FIB in a tilted angle in the direction of the red arrows in the top panel. Zoomed in TEM images show identical Ni-InGaAs intermixing layers on both sides, and both intermixing layers extended slightly out of the edge of Ni contacts. The evolution of the nickelide extended region to the right from the left contact indicates that the Ni-InGaAs intermixing is not introduced by the directional ion-beam induced mixing (directed to the left of the sample).

Appendix IV. Derivation of the Diffusion Model in Nanowire Cross-section

The fluxes of Ni atoms in the three processes as shown in **Figure 3.7**, can be expressed as:

$$F_1 = k_{dissolve}(C^{eq}_{Ni/Nickelide} - C_R)\cdot 2\pi Rh = k_{dissolve}(C^{eq}_{Ni/Nickelide} - C_R)\cdot hL \quad \text{(AIV.1)}$$

$$F_2 = D_{Ni}\left(C_r - C_R\right)\cdot 2\pi h\cdot\left[\ln\left(r(t)/R\right)\right]^{-1} = D_{Ni}\left(C_r - C_R\right)\cdot 2\pi h\cdot\left[\ln\left(l(t)/L\right)\right]^{-1} \quad \text{(AIV.2)}$$

$$F_3 = k_{growth}(C_r - C^{eq}_{Nickelide/InGaAs})\cdot 2\pi r(t)h = k_{growth}(C_r - C^{eq}_{Nickelide/InGaAs})\cdot hl(t) \quad \text{(AIV.3)}$$

where $k_{dissolve}$ and k_{growth} are the rate constants for Ni dissolution and nickelide growth respectively. $C^{eq}_{Ni/Nickelide}$ and C_R represents the equilibrium and instant Ni concentrations across the Ni/nickelide interface. C_r and $C^{eq}_{Nickelide/InGaAs}$ denotes the instant and equilibrium Ni concentrations across the nickelide/$In_{0.53}Ga_{0.47}As$ interface.

Derivation of equitation F_2:

Considering Fick's first law of diffusion in cylindrical coordinates, we can write:

$\vec{J} = -D\dfrac{dC}{dr}\vec{r}$.

The Ni atomic flux can be expressed as $F = D\dfrac{dC}{dr}\cdot 2\pi rh$, pointing to the core.

Integration of the equation $\dfrac{F}{2\pi rh\cdot D}dr = dC$ across the entire nickelide region yields:

$$\int_R^r \frac{F}{2\pi rh\cdot D}dr = \int_{C_R}^{C_r} dC$$

Therefore, we can write:

$$\frac{F}{2\pi h\cdot D}\ln\left(r/R\right) = C_r - C_R,\ \Rightarrow F = D\left(C_r - C_R\right)\cdot 2\pi h\cdot\left[\ln\left(r/R\right)\right]^{-1}$$

Under steady state condition, $F_1=F_2=F_3=F$, we can obtain a characteristic equation of the reaction as follows:

$$F = k_{dissolve}(C^{eq}_{Ni/Nickelide} - C_R)\cdot hL = D_{Ni}\left(C_r - C_R\right)\cdot 2\pi h\cdot\left[\ln\left(l(t)/L\right)\right]^{-1} = k_{growth}(C_r - C^{eq}_{Nickelide/InGaAs})\cdot hl(t),$$

(AIV.4)

hence:

$$F = \frac{C^{eq}_{Ni/Nickelide} - C^{eq}_{Nickelide/InGaAs}}{\frac{1}{k_{dissolve}\cdot hL} - \frac{\ln\left(l(t)/L\right)}{D_{Ni}\cdot 2\pi h} + \frac{1}{k_{growth}\cdot hl(t)}}. \quad \text{(AIV.5)}$$

Because of mass conservation,

$$F\cdot\frac{M_{Nickelide}}{N_A\cdot\rho_{Nickelide}} = -2\pi r(t)h\cdot\frac{dr(t)}{dt} = -\frac{hl(t)}{2\pi}\cdot\frac{dl(t)}{dt} \quad \text{(AIV.6)}$$

and assuming that $P = \frac{2\pi M_{Nickelide}}{N_A\cdot\rho_{Nickelide}}\cdot(C^{eq}_{Ni/Nickelide} - C^{eq}_{Nickelide/InGaAs})$ (AIV.7)

we can write,

$$\frac{dl(t)}{dt} = -\frac{P}{\frac{l(t)}{k_{dissolve}L} - \frac{l(t)\cdot\ln\left(l(t)/L\right)}{2\pi D_{Ni}} + \frac{1}{k_{growth}}} \quad \text{(AIV.8)}$$

Here, the three terms in the denominator represent three rate-limiting mechanisms. If these three rate-limiting mechanisms are separately considered, the differential equation can be solved.

(i) If Ni dissolution at the Ni/nickelide interface is the rate-limiting step, we obtain:

$$\frac{dl(t)}{dt} \approx -\frac{P \cdot k_{dissolve} L}{l(t)}, \qquad \text{therefore: } l(t) = \sqrt{L^2 - 2k_{dissolve} LP \cdot t}\ . \qquad \text{(AIV.9)}$$

(ii) If nickelide growth at the nickelide/InGaAs interface is the rate-limiting step, we obtain:

$$\frac{dl(t)}{dt} \approx -P \cdot k_{growth}, \qquad \text{therefore: } l(t) = L - k_{growth} P \cdot t\ . \qquad \text{(AIV.10)}$$

(iii) If the Ni diffusion in the reacted nickelide region is the rate-limiting step, we obtain:

$$\frac{dl(t)}{dt} \approx P \cdot \frac{2\pi D_{Ni}}{l(t) \cdot \ln\left(l(t)/L\right)}, \qquad \text{therefore: } 2l(t)^2 \ln\left(l(t)/L\right) + L^2 - l(t)^2 = 8\pi D_{Ni} P \cdot t\ .$$

(AIV.11)

Solution of the Differential equation AIV.11:

To solve the equation $l(t) \cdot \ln\left(l(t)/L\right) dl(t) = 2\pi D_{Ni} P dt$,

we can assume $y = l(t)/L$, and then obtain $L^2 y \ln y dy = 2\pi D_{Ni} P dt$.

We then perform integration of this equation across the entire nickelide region:

$\int_1^{l/L} L^2 y \ln y \, dy = \int_0^t 2\pi D_{Ni} P \, dt$

Using known integrals for logarithmic functions, $\int x \ln x \, dx = x^2 \left(\frac{\ln x}{2} - \frac{1}{4} \right)$, we obtain:

$$L^2 y^2 \left(\frac{\ln y}{2} - \frac{1}{4} \right) \Bigg|_1^{l/L} = 2\pi D_{Ni} P \cdot t\ , \Rightarrow 2l(t)^2 \ln\left(l(t)/L\right) + L^2 - l(t)^2 = 8\pi D_{Ni} P \cdot t$$

Appendix V. Discussions of the potential beam-effects on our in-situ TEM observations

The incident beam in TEM carries energetic electrons that can interact with specimen materials through elastic and inelastic scatterings.[11] During these interactions, electrons may cause momentum change of specimen atoms, leading to atomic displacement and structural defects, or transfer energy to the specimen materials. The typically concerned beam effects during TEM imaging and recording include knock-on damage, beam-induced coalescence, and local heating.[12]

The knock-on damages are generally observed as defects (e.g. dislocations, voids, and bubbles) and structural changes (e.g. crystalline-to-amorphous or order-to-disorder phase transitions).[13] In order to see these phenomena, most of the (electron or ion) irradiation studies were carried out under very high voltages (1~3 MV).[14] Here in our in-situ study, the TEM system was operated at 300kV and a minimal electron dose for HRTEM imaging. The electron beam was never focused on the interested area of the specimen. Therefore, none of these beam-induced damages were observed.

Beam-induced coalescence and local heating effect are largely concerned for specimen in liquid phases,[15] and reactions can be stimulated by electron-beam in liquid-cell TEM studies though energy transfer in between electron-beam and the specimen.[16,17] However, in in-situ TEM studies of solid-state reactions (as in our case), such beam effects have not been found to influence the reaction under moderate imaging conditions.[18,19] Though beam-heating may raise the local temperatures, calculations indicate only a small temperature rise (a few degrees or less) on solid specimens with good

thermal conductivities.[11] This small temperature variations in a local area will be alter our observed phase transformations, as the nickelide phase was generally reported stable over a large temperature range (230 ~ 450 °C).[20]

Ex-situ reactions are generally used as a validation to exclude the beam effect.[21] In our prior ex-situ heating study,[22] the same nickelide phase ($Ni_2In_{0.53}Ga_{0.47}As$) was observed at a RTA temperature of 300 °C, in which however, no detailed ledge movement behaviors could be observed without in-situ observations. Therefore, we conclude that the reported InGaAs to nickelide phase transformation in this work was mainly dominated by the thermally driven Ni-InGaAs solid-state reaction, with negligible effect from the electron-beam irradiations.

Appendix VI. Derivation of the Nucleation Model at Nanowire/Nickelide Interface

Considering a classic nucleus with disc shape on the InGaAs/nickelide interface, heterogeneous and homogeneous nuclei are schematically illustrated in **Figure AVI.1**.

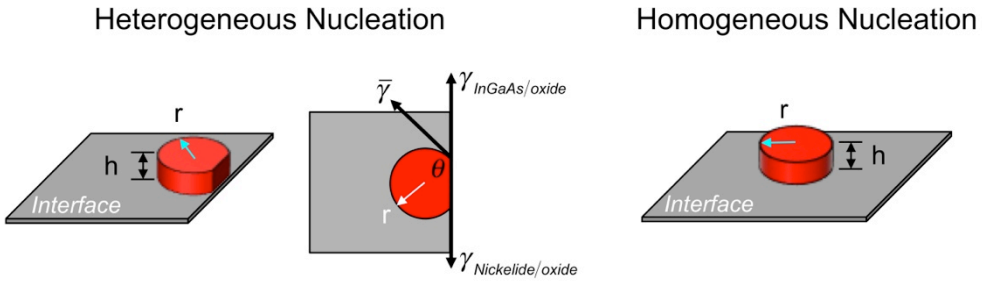

Figure AVI.1. Schematics of heterogeneous and homogeneous nuclei with disc shape with interfacial forces that determine the contact angle θ.

(1) Thermodynamic considerations

In the heterogeneous nucleation situation, the total change in the system free energy is:

$$\Delta G_{hetero} = -\Delta g \cdot V_{disc} + \bar{\gamma} \cdot S_{disc-side} + (\gamma_{nickelide/oxide} - \gamma_{InGaAs/oxide}) \cdot S_{flat-side} + E_{strain} \cdot V_{disc} \qquad \text{(AVI.1)}$$

where Δg is the nickelide formation energy, $\bar{\gamma}$ is the average InGaAs/nickelide interfacial energy, $\gamma_{nickelide/oxide}$ and $\gamma_{InGaAs/oxide}$ are the interfacial energies of nickelide/oxide and InGaAs/oxide respectively, and E_{strain} is the elastic strain energy for the nickelide nucleus.

Here,

$$V_{disc} = \pi r^2 h \cdot \frac{2\theta}{2\pi} + r^2 \sin(\pi - \theta)\cos(\pi - \theta)h = r^2 h \cdot (\theta - \sin\theta\cos\theta) \quad \text{(AVI.2)}$$

$$S_{disc-side} = 2\pi rh \cdot \frac{2\theta}{2\pi} = 2\theta rh \quad \text{(AVI.3)}$$

$$S_{flat-side} = 2rh\sin(\pi - \theta) = 2rh\sin\theta \quad \text{(AVI.4)}$$

We also have the Young's equation of:

$$\gamma_{nickelide/oxide} - \gamma_{InGaAs/oxide} = \overline{\gamma} \cdot \cos(\pi - \theta) \quad \text{(AVI.5)}$$

Therefore,

$$\Delta G_{hetero} = (E_{strain} - \Delta g) \cdot r^2 h \cdot (\theta - \sin\theta\cos\theta) + \overline{\gamma} \cdot 2rh \cdot (\theta - \sin\theta\cos\theta) \quad \text{(AVI.6)}$$

As critical nucleus size can be calculated at the peak of the energy barrier,

$$\left.\frac{\partial \Delta G_{hetero}}{\partial r}\right|_{r=r^*} = 0 \text{, and therefore } r^* = \frac{\overline{\gamma}}{\Delta g - E_{strain}} . \quad \text{(AVI.7)}$$

By substituting r* into equation AV.6, the energy barrier for heterogeneous nucleation can be obtained as,

$$\Delta G^*_{hetero} = \frac{\overline{\gamma}^2 h}{\Delta g - E_{strain}} \cdot (\theta - \sin\theta\cos\theta) . \quad \text{(AVI.8)}$$

Homogeneous nucleation is equivalent to the case when $\theta = \pi$, for which,

$$\frac{\Delta G^*_{hetero}}{\Delta G^*_{homo}} = \frac{\theta - \sin\theta\cos\theta}{\pi} . \quad \text{(AVI.9)}$$

(2) Kinetic considerations

The nucleation rate[23] can be characterized as:

$$R = \omega C \exp\left(-\frac{\Delta G_D}{kT}\right)\exp\left(-\frac{\Delta G^*}{kT}\right) \quad \text{(AVI.10)}$$

where ω is the frequency related to atomic vibrations, C is the concentration of critical sized nucleus, ΔG_D is the activation energy for Ni atoms to diffuse to the reaction interface, and ΔG* is the energy barrier for nucleus.

Therefore,

$$\frac{R_{hetero}}{R_{homo}} = \frac{C_{hetero}}{C_{homo}}\exp\left(\frac{\Delta G_D^{volume} - \Delta G_D^{surface}}{kT}\right)\exp\left(\frac{\Delta G^*_{homo} - \Delta G^*_{hetero}}{kT}\right) \quad \text{(AVI.11)}$$

In our previous study,[22] we extracted the value of activation energy for volume diffusion and surface diffusion from Arrhenius plots and obtained:

$\Delta G_D^{volume} = 1.25\ eV$, and $\Delta G_D^{surface} = 1.14\ eV$

We also know that the surface diffusion is related to the mono-layer atoms at the surface, while the volume diffusion is related to the entire channel cross-section. Therefore,

$$\frac{C_{hetero}}{C_{homo}} \approx \frac{30nm \times 0.588nm}{30nm \times 35nm} = 0.0168\,. \quad \text{(AVI.12)}$$

Also, $$\frac{R_{hetero}}{R_{homo}} \approx 1.26\exp\left(\frac{\Delta G^*_{homo} - \Delta G^*_{hetero}}{kT}\right) \quad \text{(AVI.13)}$$

References:

1. Van de Walle CG (1989) Band lineups and deformation potentials in the model-solid theory. Physical review B 39 (3):1871

2. Goetz KH, Bimberg D, Jürgensen H, Selders J, Solomonov AV, Glinskii GF, Razeghi M (1983) Optical and crystallographic properties and impurity incorporation of $Ga_xIn_{1-x}As$ ($0.44<x<0.49$) grown by liquid phase epitaxy, vapor phase epitaxy, and metal organic chemical vapor deposition. Journal of Applied Physics 54 (8):4543-4552

3. Lau S, Tsaur B, Von Allmen M, Mayer J, Stritzker B, White C, Appleton B (1981) Ion-beam mixing of metal-semiconductor eutectic systems. Nuclear Instruments and Methods 182:97-105

4. Nastasi M, Mayer J (1994) Ion beam mixing in metallic and semiconductor materials. Materials Science and Engineering: R: Reports 12 (1):1-52

5. Sands T, Keramidas V, Yu A, Yu K, Gronsky R, Washburn J (1987) Ni, Pd, and Pt on GaAs: A comparative study of interfacial structures, compositions, and reacted film morphologies. Journal of Materials Research 2 (02):262-275

6. Ko DH, Sinclair R (1992) Amorphous phase formation and initial interfacial reactions in the platinum/GaAs system. Journal of applied physics 72 (5):2036-2042

7. Hiraki A, Shuto K, Kim S, Kammura W, Iwami M (1977) Room‐temperature interfacial reaction in Au‐semiconductor systems. Applied Physics Letters 31 (9):611-612

8. Hiraki A (1980) A Model on the Mechanism of Room Temperature Interfacial Intermixing Reaction in Various Metal‐Semiconductor Couples: What Triggers the Reaction? Journal of The Electrochemical Society 127 (12):2662-2665

9. Sands T, Keramidas V, Washburn J, Gronsky R (1986) Structure and composition of NixGaAs. Applied physics letters 48 (6):402-404

10. Ko DH, Sinclair R (1991) Amorphous phase formation in an as-deposited platinum-GaAs interface. Applied physics letters 58 (17):1851-1853

11. Egerton R, Li P, Malac M (2004) Radiation damage in the TEM and SEM. Micron 35 (6):399-409

12. Taheri ML, Stach EA, Arslan I, Crozier P, Kabius BC, LaGrange T, Minor AM, Takeda S, Tanase M, Wagner JB (2016) Current status and future directions for in situ transmission electron microscopy. Ultramicroscopy 170:86-95

13. Lian J, Wang L, Sun K, Ewing RC (2009) In situ TEM of radiation effects in complex ceramics. Microscopy research and technique 72 (3):165-181

14. Carter CB, Williams DB (2016) Transmission electron microscopy. Springer-Verlag US,

15. De Jonge N, Ross FM (2011) Electron microscopy of specimens in liquid. Nature nanotechnology 6 (11):695-704

16. Liang W-I, Zhang X, Zan Y, Pan M, Czarnik C, Bustillo K, Xu J, Chu Y-H, Zheng H (2015) In Situ Study of Fe3Pt–Fe2O3 Core–Shell Nanoparticle Formation. Journal of the American Chemical Society 137 (47):14850-14853

17. Liang W-I, Zhang X, Bustillo K, Chiu C-H, Wu W-W, Xu J, Chu Y-H, Zheng H (2015) In Situ Study of Spinel Ferrite Nanocrystal Growth Using Liquid Cell Transmission Electron Microscopy. Chemistry of Materials 27 (23):8146-8152

18. Liu XH, Wang JW, Huang S, Fan F, Huang X, Liu Y, Krylyuk S, Yoo J, Dayeh SA, Davydov AV (2012) In situ atomic-scale imaging of electrochemical lithiation in silicon. Nature nanotechnology 7 (11):749-756

19. Tang W, Picraux ST, Huang JY, Gusak AM, Tu K-N, Dayeh SA (2013) Nucleation and Atomic Layer Reaction in Nickel Silicide for Defect-Engineered Si Nanochannels. Nano Letters 13 (6):2748-2753

20. Czornomaz L, El Kazzi M, Hopstaken M, Caimi D, Mächler P, Rossel C, Bjoerk M, Marchiori C, Siegwart H, Fompeyrine J (2012) CMOS compatible self-aligned S/D regions for implant-free InGaAs MOSFETs. Solid-State Electronics 74:71-76

21. Han L, Meng Q, Wang D, Zhu Y, Wang J, Du X, Stach EA, Xin HL (2016) Interrogation of bimetallic particle oxidation in three dimensions at the nanoscale. Nature Communications 7

22. Chen R, Dayeh SA (2015) Size and Orientation Effects on the Kinetics and Structure of Nickelide Contacts to InGaAs Fin Structures. Nano letters 15 (6):3770-3779

23. Porter DA, Easterling KE, Sherif M (2009) Phase Transformations in Metals and Alloys, (Revised Reprint). CRC press,